

UC Davis

UC Davis Electronic Theses and Dissertations

Title

Comprehensive Rotorcraft Broadband Noise Prediction

Permalink

<https://escholarship.org/uc/item/0pp5r0x4>

Author

Li, Sicheng

Publication Date

2022

Peer reviewed|Thesis/dissertation

Comprehensive Rotorcraft Broadband Noise Prediction

By

SICHENG (KEVIN) LI
DISSERTATION

Submitted in partial satisfaction of the requirements for the degree of

DOCTOR OF PHILOSOPHY

in

Mechanical and Aerospace Engineering

in the

OFFICE OF GRADUATE STUDIES

of the

UNIVERSITY OF CALIFORNIA

DAVIS

Approved:

Prof. Seongkyu Lee, Chair

Prof. Nesrin Sarigul-Klijn

Prof. Eric Greenwood

Committee in Charge

2022

Copyright © 2022 by

Sicheng (Kevin) Li

All rights reserved.

ABSTRACT

The research objective of this dissertation is to advance the understanding of rotorcraft broadband noise and reduce the noise impacts. Rotorcraft broadband noise has recently become a critical topic for vertical take-off and landing (VTOL) aircraft, due to the rapid progresses in Advanced Air Mobility (AAM) technologies. However, the current noise assessment tools of VTOL broadband noise rely heavily on semi-empirical models, which are short of both prediction accuracy and flow physics. To close this gap, a state-of-the-art prediction tool, namely UCD-QuietFly, is developed to assess rotor broadband noise using physics-based approaches. Extensive validations of UCD-QuietFly are performed against experiments. The effects of rotor design parameters on broadband noise are studied. Broadband noise impacts are investigated on Urban Air Mobility (UAM) conceptual designs, quiet helicopter designs, and small-scale drones. Finally, the noise reduction technique using trailing-edge serrations is analyzed.

The first part of this dissertation investigates the effects of rotorcraft design and operating parameters on trailing-edge noise. A rotor trailing-edge noise prediction method is first developed. It is found that helicopter broadband noise scales with the 4.5th to 5.0th power of the tip Mach number in which the range is determined by the typical helicopter collective pitch angle in operation. Detailed trend analyses of noise levels as a function of frequency are presented in terms of the collective pitch angle, twist angle, rotor solidity, rotor radius, disk loading, and number of blades.

Second, broadband noise of multi-rotor UAM vertical take-off and landing (VTOL) vehicles is studied. The multi-rotor broadband noise prediction capability is developed. It is

found that UAM VTOL vehicles' broadband noise is important in the high-frequency range. For the same mission specifications, broadband noise is found to be higher for VTOL designs with more rotors. Multi-rotor vehicles at the same rotational speeds have weaker amplitude modulations than a single rotor, which demonstrates the benefits of using multiple rotors in terms of noise annoyance.

Third, tonal and broadband noise are studied for rotor designs used on UAM vehicles. The rotor aerodynamics in edge-wise forward flight is calculated by an in-house code. With the forward flight capability developed in UCD-QuietFly, it is found that broadband noise is the dominant noise source for the rotor designs with low tip speeds and fewer blades, while tonal noise is dominant for the high-tip-speed designs. A low tip speed and more blades are found to be the preferable design features in terms of psychoacoustic metrics.

Fourth, a physics-based broadband noise prediction approach is applied for small-scale drone rotors. LBL-VS noise is found to be an important noise source for untripped blades. The effect of leading-edge back-scattering in broadband noise is found to be important for small-scale rotors at low frequencies. Finally, at the same thrust, the ideally twisted rotor generates slightly higher broadband noise than the linearly twisted rotor, while the tapered blade tip is shown to reduce the broadband noise levels significantly.

Fifth, machine learning-based fast-predicting models of rotorcraft trailing-edge broadband noise are developed, using artificial neural network (ANN) and linear regression. It is found that the ANN model accurately captures the variations of the noise levels, and the linear regression models are also capable of predicting the general trends of noise levels.

This dissertation is dedicated to my parents,

Jianhong Li and Yun Yue,

and my wife,

Di Jody Zhou,

for their constant support and inspiration throughout my graduate study.

CONTENTS

Abstract	i
List of Figures	xi
List of Tables	xxii
Acknowledgments	xxiv
List of Symbols	xxv
1 Introduction	1
1.1 Rotorcraft Noise	1
1.2 Outline of Chapters	7
1.3 Multi-Rotor Broadband Noise	8
1.4 Rotor Trailing-Edge Noise	11
1.5 Rotor Tonal and Broadband Noise in Forward Flight	13
1.6 Broadband Noise Predictions of Small-Scale Rotors	18
1.7 Noise Reduction Using Trailing-Edge Serrations	22
1.8 Airfoil-Turbulence Interaction Noise	25
1.9 Machine-Learning Based Rotor Broadband Noise Predictions	26
2 Acoustic Theories and Derivations	28
2.1 Wave Equation	28
2.2 Lighthill's Acoustic Analogy	30
2.3 Curle's Solution	32
2.4 Prandtl-Glauert Coordinate Transformation	35

2.5	Acoustic Power Spectral Density	36
2.6	Amiet’s Trailing-Edge and Leading-Edge Noise Theories	37
2.7	Airfoil-Self Noise	38
3	Methods and Formulations in Rotor Broadband Noise Predictions: UCD- QuietFly	41
3.1	Multi-Rotor Trailing-Edge Noise Predictions in Hovering Flight	42
3.2	Amplitude Modulation of Rotor Broadband Noise	52
3.3	Rotor Airloads and Inflow Predictions in Forward Flight	54
3.4	Tonal Noise Prediction	56
3.5	Rotor Broadband Noise Predictions in Forward Flight	58
3.6	Psychoacoustic Metrics	60
3.7	Broadband Noise Predictions of Small-Scale Rotors	61
3.8	Predictions of Other Airfoil-Self Noise Sources	64
3.9	Trailing-Edge Noise Due to Serrated Edges	64
3.10	Airfoil-Turbulence Interaction or Leading-Edge Noise	68
3.11	Machine-Learning Based Rotor Noise Prediction Model	70
4	Validations of Rotorcraft Noise Predictions	74
4.1	Airfoil Sections	74
4.1.1	Case 1: BANC case airfoil section	74
4.1.2	Case 2: NACA0012 airfoil section	76
4.2	Full-Scale Helicopter Rotors	76
4.2.1	Case 1: Leverton full-scale model rotor	76

4.2.2	Case 2: UH-1B helicopter rotor	78
4.3	Mid- and Small-Scale Rotors	79
4.3.1	Cases 1 and 2: APC drone rotor and BO-105 model rotor	79
4.3.2	Cases 3: NASA Ideally-Twisted rotor	82
4.3.3	Cases 4: SUI Endurance drone rotor	87
4.3.4	Cases 5: DJI-CF rotor	89
4.4	Rotor Inflow Distribution	92
4.4.1	Case 1: 2MRTS rotor	92
4.4.2	Case 2: SUI Endurance drone rotor	93
4.5	Tonal Noise	94
4.6	Turbulence-Ingestion Noise	96
4.7	Summary	97
5	Parameter Sensitivity Study of Rotorcraft Broadband Trailing-Edge Noise	99
5.1	Rotor Parameters Trend Analysis	99
5.1.1	Effect of rotor tip Mach number:	101
5.1.2	Effect of blade collective pitch	106
5.1.3	Effect of blade twist	107
5.1.4	Effect of rotor solidity	107
5.1.5	Effect of rotor radius	108
5.1.6	Effect of rotor ascending speed	108
5.1.7	Effect of disk loading	109
5.1.8	Effect of number of blades	111

5.2	Rotor Geometric Attenuation and Directivity	111
5.3	Summary	115
6	Broadband Noise Predictions of VTOL Multi-Rotors in Urban Air Mo-	
	bility	118
6.1	Prediction of UAM VTOL Aircraft	118
6.2	Amplitude Modulation	124
6.3	Vertiport	129
6.4	Summary	129
7	Forward Flight Rotor Tonal Noise, Broadband Noise, and Psychoacous-	
	tics	132
7.1	Tonal and Broadband Noise Comparison	134
7.2	Effect of Advance Ratio	145
7.3	Broadband Noise Amplitude Modulation and Psychoacoustics	146
7.4	Summary	150
8	Effects of Rotor Blade Ideal Twist and Tip Taper on Broadband Noise	153
8.1	Ideal Twist and Tip Taper	153
8.2	Summary	157
9	Applications of Trailing-Edge Serrations	160
9.1	Validations	160
	9.1.1 Serrated Wing Section	161
	9.1.2 Serrated Rotor	164

9.2	Results	166
9.2.1	Effects of Serration Parameters	167
9.2.2	Noise Reduction on an eVTOL Quadcopter	173
9.2.3	Noise Reduction of a Helicopter in Cruise	176
9.3	Summary	176
10	Machine Learning Model on Rotorcraft Broadband Noise Predictions	179
10.1	Artificial Neural Network Model	179
10.2	Linear Regression Model	181
10.3	Validations of the ANN model and the linear regression model	183
10.4	Summary	187
11	Concluding Remarks and Future Directions	188
11.1	Summary of Research Work	188
11.1.1	Validations of Rotorcraft Noise Predictions	188
11.1.2	Parameter Sensitivity Study of Rotorcraft Broadband Trailing-Edge Noise	190
11.1.3	Broadband Noise Predictions of VTOL Multi-Rotors in Urban Air Mobility	191
11.1.4	Forward Flight Rotor Tonal Noise, Broadband Noise, and Psychoa- coustics	191
11.1.5	Effects of Rotor Blade Ideal Twist and Tip Taper on Broadband Noise	192
11.1.6	Applications of Trailing-Edge Serrations	192
11.1.7	Machine Learning Model on Rotorcraft Broadband Noise Predictions	193

11.2 Contributions	194
11.3 Recommendations for Future Work	195
A Expanded Terms	198
B Calculation of Sound Pressure Level	200
C Training Statistics	202
References	205

LIST OF FIGURES

1.1	VTOL community noise sources and classifications	3
1.2	Schematic A-weighted noise spectrum of UAM VTOL rotors. Note that the relative importance of each noise component can vary with the operating condition.	4
1.3	Typical rotorcraft noise in frequency domain. [5]	5
1.4	Typical rotorcraft noise directivity. [10]	6
1.5	NASA’s six-passenger UAM VTOL conceptual designs [37]: (a) side-by-side, (b) lift+cruise, and (c) quadcopter.	10
1.6	Quiet helicopter (a) configuration and (b) rotor geometry for various design tip speeds. [45]	15
1.7	Dominate noise sources at various rotor conditions. [113]	25
2.1	1-D wave propagation. [119]	29
2.2	Turbulent flow in a stationary medium. [120]	31
2.3	Monopole, dipole, and quadrupole sources. [120]	33
2.4	Airfoil local coordinate. [16]	37
2.5	Airfoil self-noise sources. [24]	39
3.1	Airfoil local and global coordinates for an observer [16]. Positive elevation angle is defined as above the rotor.	43
3.2	Rotor broadband noise prediction code UCD-QuietFly flowchart.	44

3.3	Blade collective pitch and twist. Collective pitch angle (θ_0) measures from the rotor hub plane to the root chord plane, and twist angle (θ) measures from the root chord plane to the section chord plane, with positive angles in the counter-clockwise direction.	46
3.4	Multi-rotor vehicle coordinates: (a) Rotor coordinate (X_1, Y_1, Z_1) and vehicle coordinate (X_2, Y_2, Z_2). The distance from rotor hub to vehicle hub is described by (l_x, l_y, l_z) , and (b) Rotor hub plane, vehicle hub plane, and geographical ground.	49
3.5	Retarded time effect on amplitude modulation from each blade section as a noise source.	53
3.6	Top view of a two-bladed rotor in forward flight.	59
3.7	Incident and scattered pressure field theories in (a) original Amiet's model [28] and (b) Roger and Moreau's modification [84].	62
3.8	Observer distance and angle in the blade local coordinates.	64
3.9	Trailing-edge serrated geometries. The $\eta - F$ serration coordinate has the origin at the lower-left corner, with the serration wavelength of l	66
3.10	Serrated rotor blade geometry.	67
3.11	ANN model configuration.	72
4.1	Validation of airfoil trailing-edge noise prediction against measurement [128].	75
4.2	Predictions of airfoil trailing-edge noise using the current model compared to the experimental data in Ref. 130.	77

4.3	Comparison of UCD-QuietFly prediction with measurement by Johnson and Katz [131] and prediction by Kim and George [31]	78
4.4	Comparison of UCD-QuietFly prediction with measurement by Leverton [132]	79
4.5	Validations of UCD-QuietFly on rotors. (a) APC Slow Flyer 11×4.7 , RPM=3600, $\mu = 0.0$, (b) BO-105 40% scale, RPM=1050, $\mu = 0.0$, $\alpha_{tpp} = -20^\circ$, $C_T = 0.0$, (c) BO-105 40% scale, RPM=1050, $\mu = 0.086$, $\alpha_{tpp} = -20^\circ$, $C_T = 0.0044$, and (d) BO-105 40% scale, RPM=525, $\mu = 0.173$, $\alpha_{tpp} = -10^\circ$, $C_T = 0.044$	83
4.6	Predictions of angle of attack and induced velocity from the blade element momentum theory (BEMT) on the ideally twisted rotor.	84
4.7	Broadband noise predictions of the ideally twisted small rotor at 3000 RPM using UCD-QuietFly for: (a) rough blade surface, and (b) smooth blade surface. The experiment data is given in Ref. 5.	85
4.8	Broadband noise predictions of the ideally twisted small rotor at 5500 RPM using UCD-QuietFly for: (a) rough blade surface, and (b) smooth blade surface. LBL-VS noise model is limited to $R_c < 1.8 \times 10^5$. The experiment data is given in Ref. 5.	86
4.9	Comparisons of the effects of the leading-edge back-scattering correction. The experiment data and BPM predictions are given in Ref. 25.	87
4.10	Broadband noise predictions of the SUI Endurance rotor using UCD-QuietFly. The experiment data and BPM predictions are given in Ref. 25.	88
4.11	Broadband noise predictions of the SUI rotor in forward flight using UCD-QuietFly. $\alpha_{sh} = -10^\circ$, $M_\infty = 0.045$, $\phi_o = -90$, $r_o = 3.54$ m. The experiment data is given in Ref. 25.	89

4.12	Broadband noise predictions of the DJI-CF rotor using UCD-QuietFly at the rotational speeds of (a) 4800 RPM, (b) 5400 RPM, and (c) 6000 RPM. The experiment data is given in Ref. 9.	91
4.13	Validation of rotorcraft forward flight inflow distributions on 2MRTS rotor at $\mu = 0.15$: (a) prediction, and (b) measurement [78, 135].	93
4.14	Predictions of the SUI rotor forward flight angle of attack distribution at $\alpha_{sh} = -10^\circ$ and $M_\infty = 0.045$ using: (a) in-house BET code, and (b) CAM-RAD II [25].	94
4.15	Validations of tonal noise predictions, compared with the measurements of Brooks et al. [4] and Snider et al. [7]. Rotor specifications and observer locations are given in Table 4.5.	95
4.16	Validation of the predictions of turbulence-ingestion noise on an airfoil section with the observer at 2.25 m directly above. Experimental data are given in Ref. [115]	96
5.1	OASPL trend with parameters: (a) tip Mach number, (b) collective pitch angle, (c) blade linear twist slope, (d) rotor solidity, (e) rotor radius, (f) rotor ascending speed, (g) disk loading, (h) number of blades, and (i) sectional noise contribution from one blade.	101
5.2	Narrow-band SPL trends with design parameters: (a) tip Mach number, (b) collective pitch angle, (c) twist slope, and (d) chord length.	103

5.3	Boundary layer parameters measured near the trailing edge ($x/c = 0.99$) at 90% rotor radius: (a) M_{tip} vs. C_f , (b) M_{tip} vs. U_e , (c) θ_0 vs. δ^* , (d) θ_0 vs. U_e , (e) θ vs. δ^* , and (f) σ vs. δ^*	104
5.4	Scaled SPL with tip Mach number: (a) $\theta_0 = 13.52^\circ$, (b) $\theta_0 = 10.0^\circ$, and (c) scaling factor for various collective pitch angles with blade twist fixed at -10° .	106
5.5	Narrow-band SPL trends with design parameters: (a) rotor radius, (b) rotor ascending speed, (c) disk loading, and (d) number of blades.	109
5.6	Boundary layer parameters measured near the trailing edge ($x/c = 0.99$) at 90% rotor radius: (a) R vs. δ^* , (b) R vs. U_e , (c) V_c vs. δ^* , (d) V_c vs. U_e .	110
5.7	OASPL obtained from UCD-QuietFly on: (a) X_1Z_1 plane, and (b) X_1Y_1 plane.	112
5.8	OASPL calculated from rotor attenuation equation, and its difference to UCD-QuietFly: (a) OASPL calculated by Eq. (5.3) on the X_1Z_1 plane, (b) OASPL calculated by Eq. (5.3) on the X_1Y_1 plane, (c) absolute difference between Fig. 5.8(a) and Fig. 5.7(a) on the X_1Z_1 plane, and (d) absolute difference between Fig. 5.8(b) and Fig. 5.7(b) on the X_1Y_1 plane. .	114
5.9	Comparison of UCD-QuietFly and Eq. (5.3): (a) OASPL vs. observer distance, (b) OASPL vs. elevation angle.	115
6.1	Quadrotor VTOL broadband noise prediction from UCD-QuietFly compared to community background noise [23]. Peak-level frequency = 6 kHz.	120
6.2	Side-by-side VTOL broadband noise prediction from UCD-QuietFly compared to community background noise [23]. Peak-level frequency = 7 kHz. .	121

6.3	Lift+cruise VTOL broadband noise prediction from UCD-QuietFly compared to community background noise [23]. Peak-level frequency = 3 kHz.	122
6.4	Equivalent sound exposure level measurement and overall sound pressure level prediction for: (a) community background noise [23], (b) quadrotor, (c) side-by-side, and (d) lift+cruise.	123
6.5	Comparisons of UAM VTOL designs: (a) effect of changing the number of rotors by keeping the same tip Mach number and the same total swept area from multiple rotors, and (b) broadband noise of conventional helicopter Bell 430 compared to multi-rotor UAM VTOLs.	124
6.6	Broadband noise spectrum of a UH-1B helicopter in time history for observer distances at an elevation angle of -45 deg: (a) 2R, (b) 4R, (c) 10R, and (d) 20R.	125
6.7	Broadband noise spectrum of multi-rotor vehicles in time history: (a) quadcopter, (b) side-by-side, and (c) lift+cruise.	126
6.8	Predicted UH-1B helicopter amplitude modulation: (a) peak-to-peak amplitude vs. observer distance, and (b) OASPL in time history for different observer distances.	128
6.9	Predicted amplitude modulations of different vehicle designs: (a) peak-to-peak amplitudes for four designs, and (b) OASPL in time history for four designs.	128
6.10	Predicted broadband noise OASPL from the 4-FATO Gannett Fleming [40] vertiport: (a) quadcopter, (b) side-by-side, and (c) lift+cruise.	130

7.1	Aerodynamic predictions for seven designs over one revolution of the single blade at the 75% radial section: (a) loading force, and (b) loading derivative.	133
7.2	Predictions of tonal and broadband noise of the quiet air taxi designs at -90° elevation angle and 492 ft observer-hub distance: (a) OASPL, and (b) A-weighted OASPL.	136
7.3	The loading noise acoustic pressure time histories from each blade and from the entire rotor (total) for the design tip speed of 600 ft/s. The observer is at -90° elevation angle and 492 ft observer-hub distance.	137
7.4	The loading noise acoustic pressure time histories from each blade and from the entire rotor (total) for the design tip speed of 650 ft/s. The observer is at -90° elevation angle and 492 ft observer-hub distance.	138
7.5	Narrow-band SPL predictions of broadband noise for the seven design cases at the elevation angle of -90° and 492 ft observer-hub distance.	139
7.6	Predictions of tonal and broadband noise of the quiet air taxi designs at -45° elevation angle and 492 ft observer-hub distance: (a) OASPL, and (b) A-weighted OASPL.	139
7.7	Narrow-band SPL predictions of broadband noise for the seven design cases at the elevation angle of -45° and 492 ft observer-hub distance at the forward position of the vehicle.	140
7.8	Noise directivity in the vehicle downward region of the design tip speed of 450 ft/s and the observer-hub distance of 5 rotor radii, with elevation angle in the longitudinal and lateral directions shown in the polar angle: (a) port side view, and (b) rear view.	141

7.9	Sectional OASPL contours at the observer-hub distance of 492 ft and the elevation angle of -90° : (a) 700 ft/s, (b) 650 ft/s, (c) 600 ft/s, (d) 550 ft/s, (e) 500 ft/s, (f) 450 ft/s, and (g) 400 ft/s.	142
7.10	Contours of the boundary layer parameters taken at 99% of the blade chord length for the 700 ft/s tip speed case: (a) boundary layer edge velocity on the upper surface, (b) displacement thickness on the upper surface, (c) chord-wise pressure gradient on the upper surface, (d) boundary layer edge velocity on the lower surface, (e) displacement thickness on the lower surface, (f) chord-wise pressure gradient on the lower surface, (g) skin friction coefficient on the upper surface, and (h) skin friction coefficient on the lower surface.	144
7.11	Predictions of tonal and broadband noise of the 450 ft/s tip speed design for varied advance ratios at -90° elevation angle and 492 ft observer-hub distance: (a) OASPL, and (b) A-weighted OASPL.	146
7.12	Narrow-band SPL predictions of broadband noise of the 450 ft/s tip speed design for varied advance ratios at -90° elevation angle and 492 ft observer-hub distance.	147
7.13	Time variation of the broadband noise spectrum at 5 rotor radii observer distance and -45° forward elevation angle for the design tip speeds of: (a) 700 ft/s, (b) 650 ft/s, (c) 600 ft/s, (d) 550 ft/s, (e) 500 ft/s, (f) 450 ft/s, and (g) 400 ft/s.	149
7.14	Fluctuation strengths of the rotor designs at 5 rotor radii observer distance and -45° forward elevation angle.	150

7.15	Roughness of the rotor designs at 5 rotor radii observer distance and -45° forward elevation angle.	151
8.1	Spanwise distributions of pitch angle for the three rotor cases.	156
8.2	Comparisons of the acoustic effects of the blade ideal twist, linear twist, and taper on the rotor at a constant thrust: (b) sound pressure level (SPL) spectrum, and (c) overall sound pressure level (OASPL) contributions of the radial sections.	158
8.3	Comparisons of the boundary layer displacement thickness at a 0.99 chord location for the blade ideal twist, linear twist, and taper on the rotor at a constant thrust for: (b) suction side, and (b) pressure side.	159
9.1	Comparison of Amiet’s model and Lyu and Ayton’s model on a straight wing section at different observer distances.	162
9.2	Effect of the spanwise wavenumber in Lyu & Ayton’s model on a straight wing section.	163
9.3	Noise reduction validation of the serrated trailing-edge noise model on the wing section. The serration shape is sawtooth, $2h = 0.04$ m, and $l = 0.02$ m. Experiment data is given in Ref. [145]	163
9.4	Validation of UCD-QuietFly on the serrated drone rotor. Experiment data is given in Ref. [104], with broadband components extracted.	165
9.5	Validation of UCD-QuietFly on the serrated drone rotor in forward flight. Experiment data is given in Ref. [105], with broadband components extracted.	166

9.6	The effect of the number of serrations on rotor broadband noise: (a) sound pressure level spectrum and (b) noise reduction compared to the straight-blade rotor.	167
9.7	The effect of starting radial locations of the serrations on rotor broadband noise: (a) sound pressure level spectrum and (b) overall sound pressure level reduction compared to the straight-blade rotor.	168
9.8	The effect of serration heights on rotor broadband noise: (a) sound pressure level spectrum and (b) overall sound pressure level reduction compared to the straight-blade rotor.	170
9.9	The effect of serration shapes on rotor broadband noise: (a) (b) sound pressure level spectrum of the shapes in Eq. (3.43), and (c) overall sound pressure level reduction compared to the straight-blade rotor.	171
9.10	The effect of starting radial locations of the serrations on rotor broadband noise: (a) sound pressure level spectrum and (b) overall sound pressure level reduction compared to the straight-blade rotor.	172
9.11	Conceptual design of an electric quadrotor [77].	172
9.12	Effects of using serrated blades on broadband noise of a eVTOL quadrotor, with various design tip speeds and numbers of blades. The observer is located at 492 ft directly underneath the vehicle. The serration height is $2h=0.0702$ m and the serration wavelength is $l=0.0351$ m. The community background noise is given in [23]. (a) sound pressure level spectrum and (b) overall sound pressure level reduction compared with the straight-blade rotor.	174

9.13	Hemispheric directivity of broadband noise OASPL (0.1-13 kHz) of the UAM eVTOL quadrotor with three blades and the tip speed of 700 ft/s: (a) straight blade, (b) serrated blade, and (c) noise reduction.	175
9.14	Hemispheric directivity of broadband noise OASPL (0.1-13 kHz) of a quiet helicopter design in forward flight with three blades and the tip speed of 700 ft/s: (a) straight blade, (b) serrated blade, and (c) noise reduction.	177
10.1	Number of points in data vs. mean absolute error of OASPL, which shows the convergence of the model's accuracy with an increasing data size.	181
10.2	Convergence study of the number of epochs in the training of the ANN model: (a) overall sound pressure level, and (b) narrow-band sound pressure level.	181
10.3	Distribution of validation errors: (a) Comparison between true OASPL and predicted OASPL, (b) Histogram of OASPL validation error distribution, (c) Comparison between true SPL and predicted SPL, and (d) Histogram of SPL validation error distribution.	182
10.4	The OASPL validation of the ANN model and the linear regression model for the parameters: (a) Tip Mach number, (b) Collective pitch angle, (c) Twist angle, (d) Rotor solidity, and (e) Rotor radius.	185
10.5	The narrow-band SPL validation of the for the ANN model and the linear regression model in frequency domain: (a) $M_{tip}=0.67$, $\theta_0=13.52^\circ$, $\theta=-10^\circ$, $\sigma=0.0506$, and $R=6.71m$, and (b) $M_{tip}=0.45$, $\theta_0=13.52^\circ$, $\theta=-10^\circ$, $\sigma=0.0853$, and $R=6.71m$	186

LIST OF TABLES

1.1	Parameters of UH-1B helicopter and six-passenger UAM VTOL conceptual designs [37].	11
3.1	Variables and Constants	71
4.1	Conditions of airfoil section validations.	75
4.2	Conditions of Helicopter Rotor validations.	77
4.3	Specifications of the rotors used for UCD-QuietFly validation.	79
4.4	Parameters of small-scale rotors	84
4.5	Validation rotor cases.	95
5.1	Constant Conditions.	100
5.2	Range of Parameters.	100
5.3	Geometric Attenuation and Directivity.	112
7.1	Quiet air taxi rotor design configurations [45].	134
8.1	Parameters of twisted and tapered rotors	155
9.1	Parameters for Validation of Trailing-Edge Noise from a Wing Section	161
9.2	Hovering Rotor Validation Parameters	164
9.3	Forward Rotor Validation Parameters	165
9.4	UAM eVTOL Quadrotor Parameters ([77]	173
9.5	Quiet helicopter design [45].	176

10.1	Statistics of the linear regression model (Continued)	183
A.1	Statistics of the OASPL linear regression model	203
A.2	Statistics of the SPL linear regression model	204

ACKNOWLEDGMENTS

I want to thank everyone who has supported me in completing this Ph.D. research. First, I would like to express deep gratitude to my advisor, Dr. Seongkyu Lee, for providing me the opportunities to study challenging research problems. I have learned an extensive amount of knowledge from him in rotorcraft and acoustics, and my expertise in those research areas has become the most valuable asset in my career. He always encourages my critical thinking to challenge myself and conduct groundbreaking research. Dr. Lee has provided me with tremendous support in my career development. Second, I would like to thank Dr. Nesrin Sarigul-Klijn and Dr. Eric Greenwood for serving my dissertation committee and supporting me in securing the next position in my career. Third, I would like to thank my lab mates, especially Dr. Zhongqi Henry Jia for his valuable career advice.

This journey would not have been possible without the support of my family. My parents have given me significant support throughout my graduate study. My wife always encourages me to believe in myself, and she has taught me to think from the liberal art perspective.

This research was partially supported by Hyundai Motor Company.

List of Symbols

A_{cs}	airfoil cross-sectional area
c	chord length, m
c_0	speed of sound in the undisturbed medium, m/s
C_f	skin friction coefficient
C_T	rotor thrust coefficient
D_ϕ	directivity term
dP/dx	boundary layer pressure gradient, Pa/m
E^*	complex conjugate of a Fresnel integral
E_n	serration shape coefficient
f	frequency, Hz
f_{mod}	modulations frequency, Hz
F	fluctuation strength, vacil
$F(\eta)$	serration geometry function
G	Green's function
$2h$	serration height, m
H_j^r	factorial combination
i	blade section index
k	acoustic wavenumber, ω/c_0
K	aerodynamic wavenumber, ω/V
\bar{K}_x	normalized streamwise wavenumber, $\omega c/2V_c$
L	effective lift function, N/m

l	serration wavelength, m
l_y	spanwise turbulence lengthscale, $1.6V_c/\omega$, m
\vec{l}	blade surface loading vector, N/s
l_r	blade surface loading in the radiation direction, $\vec{l} \cdot \hat{r}$, N/m
l_M	blade surface loading in the motion direction, $\vec{l} \cdot \hat{M}$, N/m
L_{BBN}	broadband noise level, dB
$[L]$	influence matrix
L_i^q	lift on the q_{th} blade i_{th} section, N
ΔL	overall modulation depth, dB
ΔL_E	specific modulation depth, dB/Bark
m	modulation factor
M	blade sectional flow Mach number
M_∞	rotor forward Mach number
M_r	March number in the radiation direction, $\vec{M} \cdot \hat{r}$
$[M]$	apparent mass matrix
M_{β_p}	flapping motion matrix
M_t	rotor tilt motion matrix
M_{tip}	tip Mach number
M_θ	blade twist and collective pitch matrix
M_ϕ	azimuth motion matrix
N_B	number of blades per rotor
N_R	number of rotors

N_S	number of sections per blade
$(n)!!$	double factorial of n, (n)(n-2)(n-4)...
p'	tonal acoustics pressure, Pa
p'_L	loading noise acoustic pressure, Pa
p'_T	thickness noise acoustic pressure, Pa
q	blade index
R	rotor radius, m
R_o	observer-vehicle hub distance, m
R_s	observer-blade section distance, m
R_c	chord Reynolds number
R	roughness, asper
r	blade radial location, m
\hat{r}	unit vector in the radiation direction
\bar{r}	non-dimensional blade radial location
r_o	observer distance, m
r, m	harmonic number
j, n	polynomial number(shape function index)
S_{pp}	acoustic PSD, Pa ² /Hz
St	Strouhal number, $f\delta_p/V$
\bar{S}_{pp}	instantaneous acoustic PSD
t	observer time, s
\bar{t}	non-dimensional time, Ωt

t_r	rotor tilt, deg
t_v	vehicle tilt, deg
U_e	boundary layer edge velocity, m/s
u_τ	friction velocity, $(\tau_w/\rho)^{1/2}$
V	blade sectional freestream velocity, m/s
V_c	convection velocity, $0.7V$, m/s
V_i	inflow velocity, m/s
V_∞	rotor forward velocity, m/s
w	inflow ratio, $V_i/\Omega R$
\vec{x}	observer position, m
X, Y, Z	source local coordinate system
X_1, Y_1, Z_1	rotor coordinate system
X_2, Y_2, Z_2	observer global coordinate system
\vec{y}	sound source position, m

Greek Symbols

α_j^r, β_j^r	induced flow coefficients
α^*	effective angle of attack, deg
α_{sh}	rotor shaft angle of attack, deg
α_{tpp}	rotor tip-path-plane angle of attack, deg
β_p	blade flap, deg
δ	boundary layer thickness, m

Δr	blade section span, m
λ_i	inflow ratio
μ	advance ratio
ν	local fluid velocity on the blade surface, m/s
ν_n	normal component of fluid velocity, m/s
δ^*	boundary layer displacement thickness, m
δ_p	pressure side boundary layer thickness, m
Ω	rotational speed, rad/s
ω	angular frequency, rad/s
Φ_{pp}	surface pressure spectrum, Pa ² /Hz
ϕ_j^r	radial expansion function
ψ	rotor blade azimuth angle, deg
ϕ_o	observer elevation angle, deg
ψ_o	observer azimuth angle, deg
ρ_∞	air density in the undisturbed medium, kg/m ³
σ	rotor solidity
τ	retarded time, s
τ_w	wall shear stress, Pa
Θ	momentum thickness, m
τ_n^m	loading coefficients
θ_{tw}	blade linear twist rate, deg
θ_0	collective pitch angle, deg

Acronyms

OASPL	overall sound pressure level, dB
SPL	sound pressure level, dB
$SPL_{i(U/L)}$	blade section (upper or lower surface) sound pressure level, dB
SPL_{rotor}	rotor sound pressure level, dB
SPL_{vehicle}	vehicle sound pressure level, dB
RPM	revolution per minute

Chapter 1

Introduction

1.1 Rotorcraft Noise

Rotors are commonly used to achieve vertical take-off and landing (VTOL). In addition to conventional helicopters, recent development in Urban Air Mobility (UAM) has broadened the usage and capabilities of rotorcraft. For such UAM vehicles, achieving low noise levels is one of the major challenges in employing them in the market, since loud noise will not be accepted by the communities.

The constitution of VTOL/UAM noise sources is shown in Fig. 1.1. While VTOL/UAM community noise consists of various sources, such as the flow, mechanical vibration, and motor/engine, the dominant noise pertinent to the community acceptance mainly comes from aerodynamically induced noise or flow noise. Flow noise is dominated by noise emitted from the rotor blades, although airframe also marginally contributes [1]. Generated from the blades, tonal noise dominates at low frequencies while the broadband noise dominates at mid to high frequencies. While Jia and Lee [2, 3] investigated VTOL tonal blade-vortex-interaction (BVI) noise, this dissertation will focus on broadband noise of rotorcraft, including conventional helicopters, UAM multi-rotors, and small-scale drone rotors. Although

broadband blade-wake-interaction (BWI) noise is dominant at low and mid frequencies in descending flight, broadband airfoil-self noise is dominant at mid to high frequencies in hover and forward flight [4], in which blade-wake interaction is weak. An exemplary A-weighted noise spectrum containing UAM VTOL noise sources is shown in Fig. 1.2. Among the airfoil-self noise sources, trailing-edge noise is dominant, which makes it a good representation of mid- to high-frequency UAM VTOL noise.

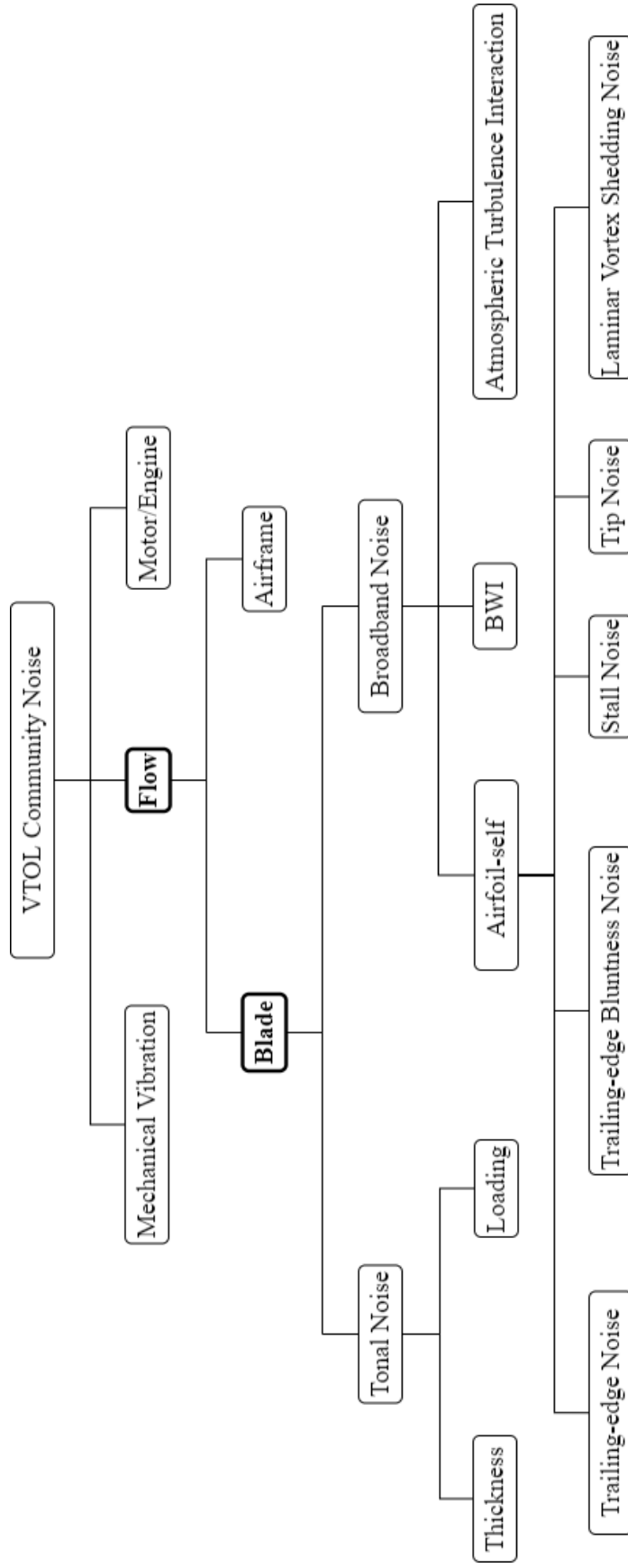


Figure 1.1: VTOL community noise sources and classifications

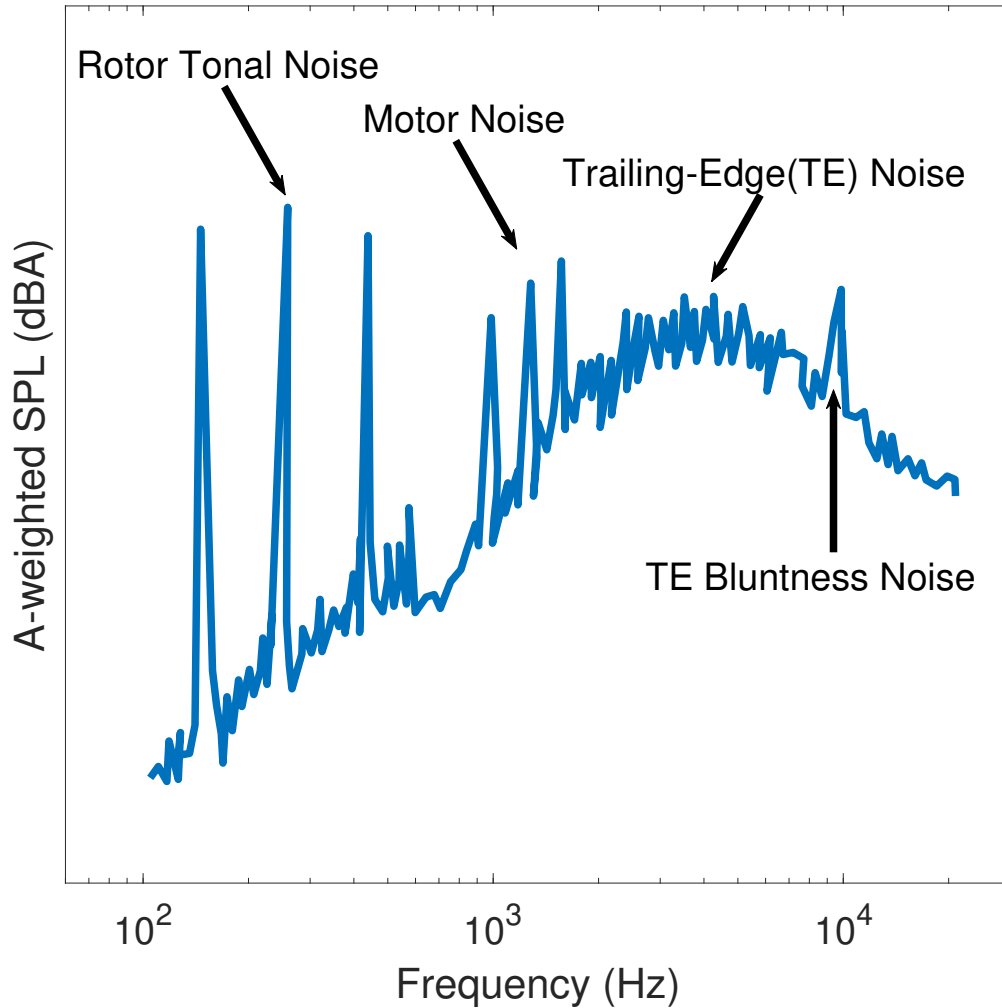


Figure 1.2: Schematic A-weighted noise spectrum of UAM VTOL rotors. Note that the relative importance of each noise component can vary with the operating condition.

Aerodynamically induced noise from rotorcraft can be categorized into tonal noise and broadband noise by its nature. While rotorcraft tonal noise is typically dominant at low- and mid- frequencies, broadband noise covers a wide frequency range, including high frequency to which human ears are sensitive. Fig. 1.3 shows the acoustic wind tunnel measurements of a NASA’s ideally-twisted drone rotor [5]. On this exemplary rotor noise spectrum, loading noise is observed in the low-frequency range as the discrete frequency peaks (tonal peaks). The mid-frequency range (1-5 kHz) is dominated by blade-wake-interaction noise [6], which

is also commonly referred to as leading-edge noise. In the mid- to high-frequency range (2-30 kHz), turbulent boundary layer trailing-edge noise is typically the dominant source. When laminar flows separate from the surface, laminar boundary layer vortex-shedding noise can generate a broadband noise peak. Trailing-edge bluntness noise is typically a high-frequency hump on a noise spectrum. For this specific experiment, facility background noise associated with the acoustic wind tunnel occupies the frequencies below 0.3 and above 30 kHz [5].

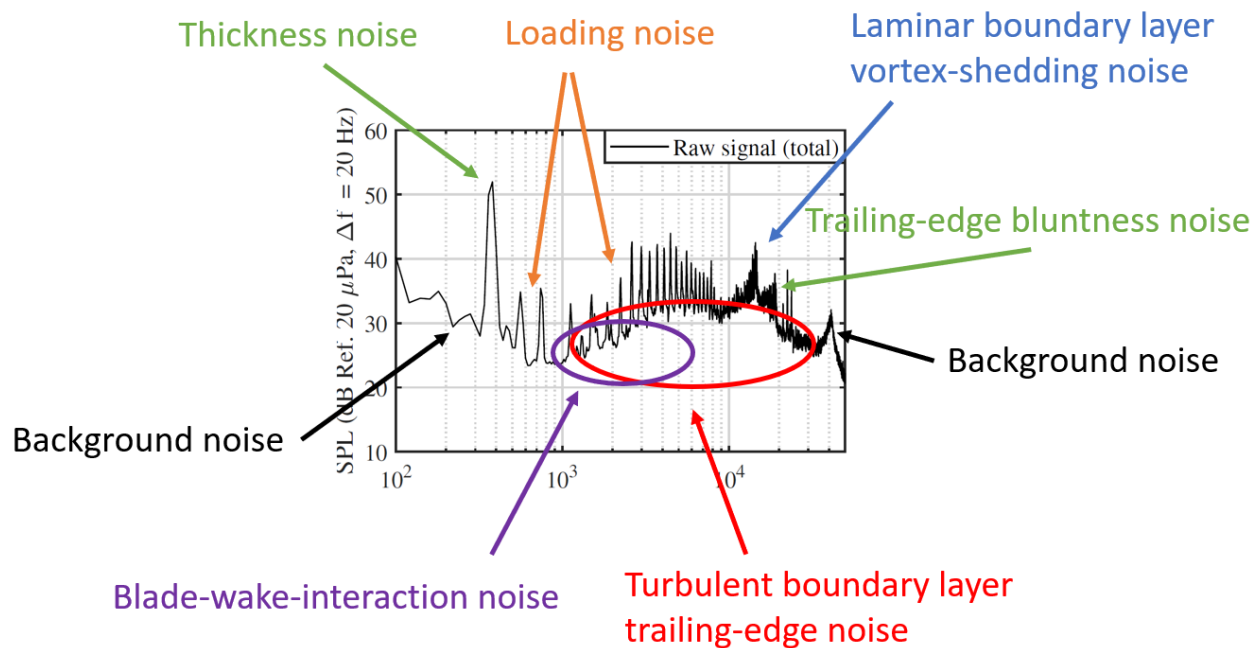


Figure 1.3: Typical rotorcraft noise in frequency domain. [5]

Historically, less research effort has been devoted to rotorcraft broadband noise compared to its tonal noise. However, rotorcraft broadband noise becomes important when the tonal noise is weak. Recently, interest in broadband noise has been raised with the broader use of rotorcraft and the emergence of UAM vehicle concepts. Broadband noise from rotorcraft is characterized by its wide frequency range and high-frequency dominance. To demonstrate the importance of rotor broadband noise on traditional helicopters, Snider et al. [7] measured helicopter fly-over noise and found that rotor broadband noise is important when it

approaches or flies overhead, which significantly contributes to Effective Perceived Noise Level (EPNL). For small-scale rotors, Intaratep et al. [8] experimentally showed that broadband noise of a DJI Phantom rotor, especially trailing-edge noise, not only dominates at mid- and high-frequency ranges but also considerably increases from a single rotor to multi-rotors. In addition, the acoustic measurements by Zawodny et al. [9] showed that quadcopter rotors generate significant broadband noise above 1 kHz frequency, and the A-weighted spectrum [1] indicated the human ear’s high sensitivity at such a frequency range.

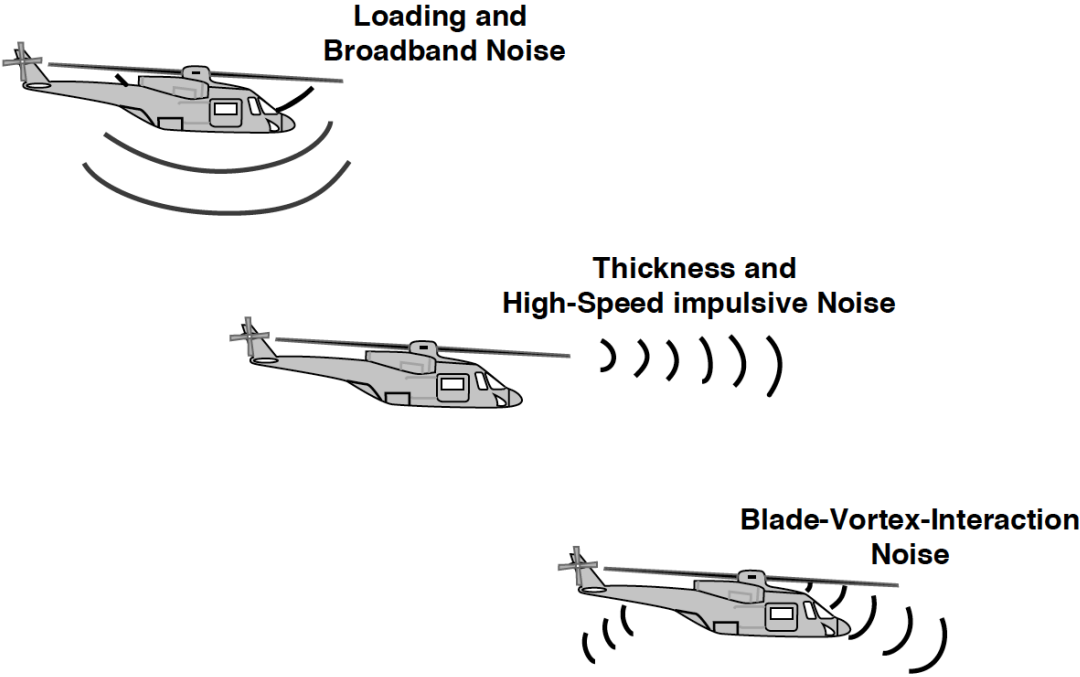


Figure 1.4: Typical rotorcraft noise directivity. [10]

Besides their different characteristics on a frequency spectrum, the noise sources on a rotor have distinct directivity patterns. The typical rotorcraft noise directivity is given in Fig. 1.4 [10]. Tonal noise, occurring at discrete frequencies in the low-frequency range, is the dominant noise source in the forward and rearward directions [10], while broadband noise is important in the downward direction [7]. The strong tonal noise results from the aerodynamic

characteristics of conventional helicopters. For instance, a transonic rotor blade tip generates high-speed impulsive noise propagating in the forward direction [11]. Strong tip vortices are formed to create blade-vortex-interaction (BVI) noise that is dominant during descent flight or for multi-rotors [3, 12–14]. The variation of the blade loading creates unsteady loading noise at high forward speed. Thickness noise is also important for high-speed rotor blades.

1.2 Outline of Chapters

This dissertation includes 11 chapters that summarize the author’s published works [15–22]. Chapter 1 gives an introduction of rotorcraft noise prediction methods, including rotor aerodynamics, broadband noise, tonal noise, psychoacoustics, noise reduction techniques, and machine learning. Chapter 2 begins with the fundamentals of airfoil-self noise and wave equation, and the derivations of the acoustic Amiet’s model are included. Chapter 3 provides the methods and formulations used in each research topic in Chapters 4-11. Chapter 4 presents the validations of UCD-QuietFly on various designs and operations, and the validations of rotor forward flight aerodynamics and tonal noise are also included. Chapter 5 investigates the effects of rotor parameters on broadband noise [15]. Chapter 6 studies UAM VTOL broadband noise in the urban environment, including the comparisons to community background noise, the amplitude modulation, and broadband noise from vertiports [16]. Chapter 7 investigates tonal and broadband noise of the quiet air taxi designs in cruise, and the psychoacoustic metrics are presented [17]. Chapter 8 studies the effects of rotor blade twist and taper on broadband noise [18]. Chapter 9 explores the rotor broadband noise reductions using trailing-edge serrations, where serrated-blade UAM aircraft and drone rotors are

studied for their noise reduction potentials [18, 22]. Chapter 10 develops a machine-learning based prediction model for rotor broadband noise, where the Artificial Neural Network and linear regression are used to develop fast-predicting models [20]. Chapter 11 summarizes the research topics presented in this dissertation, and the recommendations for future work are given. More research background and motivations that associated with specific chapters are described in the following sections.

1.3 Multi-Rotor Broadband Noise

Broadband noise has grown to receive more interest due to its annoyance on urban residents underneath rotorcraft. On drone rotors, Zawodny and Boyd [1] showed human ears' high sensitivity to broadband noise on the A-weighted noise spectrum. Regarding the perception of UAM vehicles operating in urban environment, Begault [23] showed that low-frequency tonal noise from eVTOL aircraft is inaudible as it is likely to be masked by street noise; however, eVTOL broadband noise may not be masked at mid to high frequencies, at which street traffic noise is weak.

When external turbulence or wake turbulence interacting with blades are not present, rotorcraft broadband noise is essentially airfoil self-noise that occurs on rotating blades, which includes airfoil trailing-edge noise, trailing-edge bluntness noise, etc. Rotor broadband noise can be predicted by empirical models or theoretical models. Brooks et al. [24] developed a semi-empirical airfoil self-noise prediction model, known as a BPM model, by performing scaling on the noise measurement of a NACA0012 airfoil; the output from this model is one-third octave band sound pressure level ($SPL_{1/3}$). The BPM model was implemented on

drones by Pettingill and Zawodny [25]. Theoretically, Ffowcs Williams and Hall [26] provided a trailing-edge noise solution to the Lighthill [27] acoustic analogy equation. Likewise, Amiet [28] developed a theoretical model to predict airfoil trailing-edge noise based on the theory of Curle [29]. Using Amiet's model, Schlinker and Amiet [30] predicted trailing-edge noise on helicopters, but some simplifications were made in their approach. For example, helicopter blades were modeled as flat plates and the induced velocity on the rotor is not included. Kim and George [31] predicted rotor trailing-edge noise using Ffowcs Williams and Hawkings [32] equation along with Amiet's loading function [28]. In their method, however, each blade was modeled as a point source of a flat plate, and the angle of attack effect was neglected. Modeling rotor blades as actual airfoil sections, Blandeau and Joseph [33] predicted propeller trailing-edge noise based on Amiet's model [28], but the wall pressure spectrum model, Goody's model [34], used in their approach was not accurate for airfoil adverse pressure gradient flows, and the noise source was modeled as a point source located at 75% of the blade radius. Li and Lee [15] developed the rotor broadband noise prediction code UCD-QuietFly, which combines Amiet's trailing-edge noise model [28], BPM trailing-edge bluntness noise and stall noise model [24], XFOIL panel method [35], Lee's wall pressure spectrum model [36], Blade Element Momentum Theory (BEMT), and rotor blades' full motions. Multi-rotor noise prediction capability has also been added to UCD-QuietFly [16].

Regarding the noise characteristics, Christian et al. [38] used a synthesizing method with the BPM model to simulate the amplitude modulated broadband noise from a helicopter, which became more identifiable by its periodic features. However, the importance of such features has not been studied for the multi-rotor VTOL vehicles.

Regarding the VTOL designs, Johnson et al. [39] made conceptual designs of single-

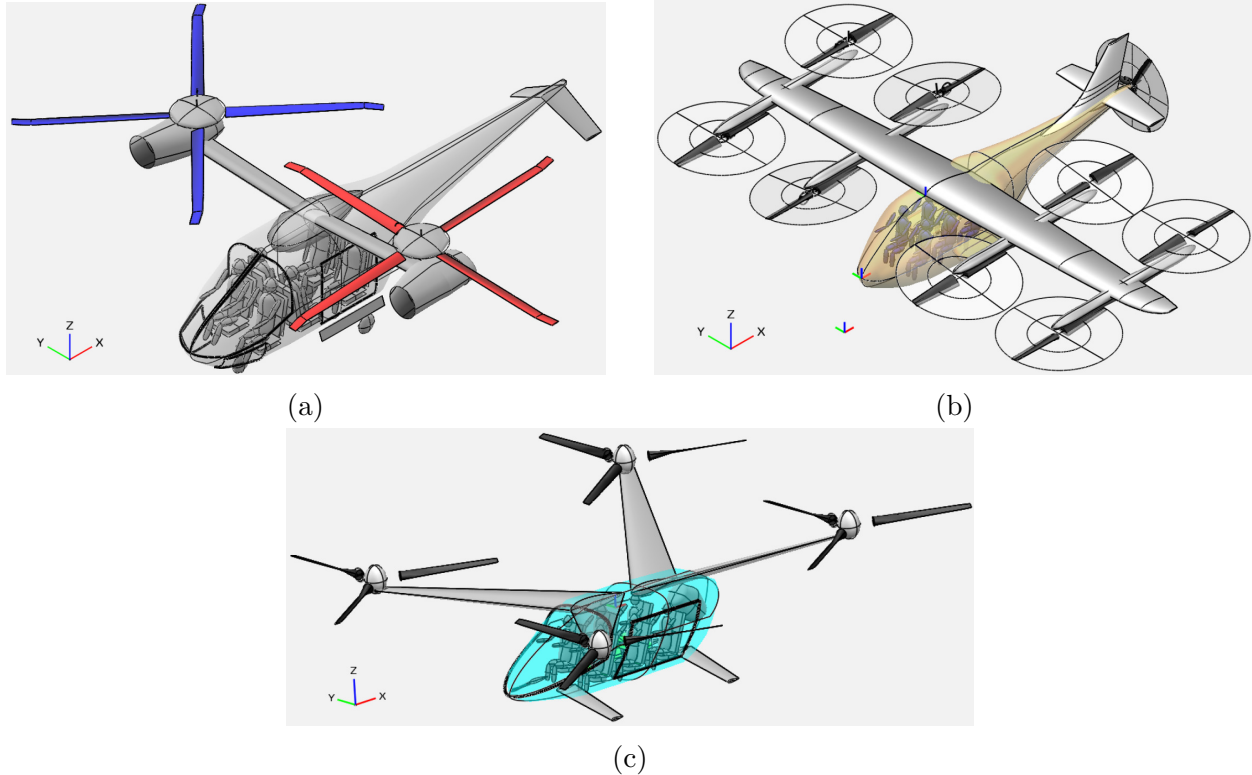


Figure 1.5: NASA’s six-passenger UAM VTOL conceptual designs [37]: (a) side-by-side, (b) lift+cruise, and (c) quadcopter.

passenger quadrotor, six-passenger side-by-side helicopter, and fifteen-passenger tilt-wing and turbo-electric aircraft. Based on these designs, Silva et al. [37] produced three new designs, quadcopter, side-by-side, and lift+cruise, with the same mission specifications of carrying six passengers. These conceptual designs are given in Fig. 1.5. The specifications of the three conceptual designs are shown in Table 1.1 along with UH-1B helicopter for comparison. Silva et al. [37] presented the electric and turbo-electric versions of each VTOL design, and in Chapter 6, the electric versions are only shown. This dissertation will investigate the broadband noise of these vehicles.

To investigate such topics, the author developed a new rotor broadband noise prediction software named UCD-QuietFly [16]. This program is used to predict broadband noise of the VTOL conceptual designs [37] in Fig. 1.5; the importance of VTOL broadband noise

Table 1.1: Parameters of UH-1B helicopter and six-passenger UAM VTOL conceptual designs [37].

Parameter	UH-1B	Quadrotor	Side-by-side	Lift+cruise
Rotor radius (ft)	22	13.1	14.9	5.0
Number of rotors	1	4	2	8
Blades per rotor	2	3	4	2
Tip speed (ft/s)	748.031	550	550	585
Rotor speed (RPM)	325	400	353	1117
Disk loading (lb/ft ²)	4.74	3.0	3.5	13.1
Solidity, thrust-weighted	0.0036	0.055	0.058	0.267
Airfoils	NACA0012	VR-12 (r/R<0.85)/SSC-A09 (r/R>0.95)		

is studied by comparing to the urban community noise measurements [23]. Furthermore, the significance of periodic features of VTOL broadband noise is studied at various observer locations. Finally, broadband noise of multiple operating VTOLs at one of Uber’s considered vertiport design [40] is predicted. It is important to note that rotor broadband noise considered in this dissertation includes trailing-edge noise, trailing-edge bluntness noise, and airfoil stall noise, which are important at mid- to high-frequency range. In this dissertation, other broadband noise sources, such as blade wake interaction noise or turbulence ingestion noise, which are apparent in a low frequency region, are not considered.

1.4 Rotor Trailing-Edge Noise

Trailing-edge noise is a type of broadband noise that contributes significantly to mid- and high-frequency noise. This noise is generated by the interaction between a turbulent boundary layer flow and a trailing-edge corner on an airfoil section or a flat plate. Trailing-edge noise models on an airfoil have been empirically and theoretically developed. A semi-empirical BPM model was developed by Brooks et al. [24] and has been widely used to

predict airfoil self-noise. Although Zawodny et al. [9] and Pettingill and Zawodny [25] have predicted broadband noise from small-scale rotors using the semi-empirical BPM model [24], broadband noise from the passenger-size electric vertical takeoff and landing (eVTOL) vehicles has not been predicted, nor has the vehicle designs been studied for their effects on the broadband noise.

As for the method of accounting for the blade sections as the noise sources, Burley and Brooks [41] used coordinate transformations to locate the noise source locations on the blade by including the rotor tilt angle, sectional radius, blade segment pitch angle, and blade azimuthal angle. They applied these coordinate transformations on the BPM airfoil self-noise model [24] to predict rotor broadband noise. However, their transformations did not include the blade flapping motion, and the semi-empirical BPM model was scaled based on symmetrical NACA0012 airfoils.

This dissertation presents multiple coordinate transformations during the motions of rotor blades to account for each blade section as a noise source and individually compute each blade section's noise contribution to a given observer. The blade twist angle, collective pitch angle, flapping angle, azimuthal angle, sectional radius, and rotor tilt angle are included in the coordinate transformation. This method relates the flow physics at the trailing edge noise to sound propagation. The new model combines Blade Element Momentum Theory (BEMT), XFOIL boundary-layer panel code, and a recently developed empirical wall pressure spectrum model [36] to accurately obtain the source of trailing-edge noise at given flight conditions of rotorcraft. Following its development, UCD-QuietFly is validated against airfoil trailing-edge noise and rotor noise measurements in hover.

For the airfoil section, the effects of flow Mach number, angle of attack, and chord length

on the trailing-edge noise come from studies by other researchers. Hutcheson and Brooks [42] computationally and experimentally showed that airfoil trailing edge noise is well scaled with the 5.0th power of the flow Mach number and that the angle of attack only affects low-frequency noise. For the same effective angle of attack, Brooks et al. [24] experimentally showed, with a boundary-layer tripped airfoil, that a larger chord length increased the noise level and shifted the level peak to a lower frequency. Lee [43] also studied the effect of the airfoil shape on trailing-edge noise using a TNO-Blake model. He identified the noise source region for different airfoils at different conditions and showed that the suction side contributes to the low-frequency noise and the pressure side contributes to the high-frequency noise. On rotorcraft, Chou and George [44] found that collective pitch angle has a large effect on low-frequency and mid-frequency noise while it has a negligible effect on high-frequency noise.

In the second part of Chapter 5, UCD-QuietFly is used to study the effects of rotor tip Mach number, collective pitch, blade twist, rotor solidity, rotor radius, ascending speed, disk loading, and number of blades on rotor trailing-edge noise. Finally, the rotor noise directivity is analyzed, and a semi-analytic equation is proposed to represent the geometric attenuation and the directivity of rotorcraft trailing-edge noise.

1.5 Rotor Tonal and Broadband Noise in Forward Flight

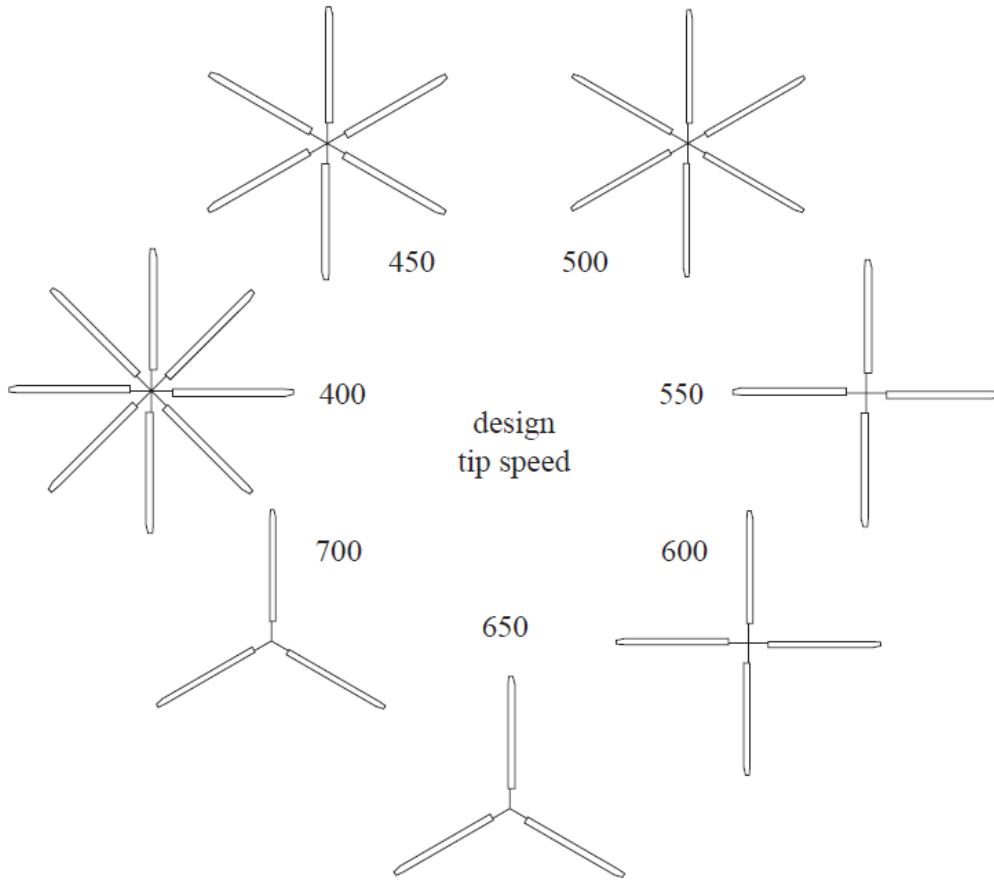
Although many UAM aircraft designs have multi-rotor configurations with a distributed power system, Johnson [45] presented a quiet single-rotor helicopter for urban air taxi operations, as shown in Fig. 1.6. A quiet helicopter was designed with variations of the number

of blades, solidity, and RPM. Key attributes of this quiet helicopter are the muffled propulsion system and a NOTAR-style tailboom to eliminate high-frequency tail rotor noise. Scott [46] investigated eVTOL aircraft configurations for military mission requirements. He found that a traditional low disk loading configuration, such as a coaxial rotor, provides the best operational benefits among various eVTOL configurations including multirotors and ducted fans. Johnson’s and Scott’s studies provide different perspectives on eVTOL configurations and reinforce the importance of traditional low disk loading helicopter, although multi-rotor configurations are still a dominant choice being developed by many companies [47, 48]. However, there are limited understanding and studies on noise, sound quality, and annoyance levels of this quiet helicopter in the context of urban air mobility and public acceptance.

NASA UAM market study [49] presented that noise is one of the top potential barriers to a successful UAM market due to its negative public acceptance. Uber [50] suggested that UAM VTOL vehicles should have a noise level (L_{Amax}) less than 62 dB(A) at an altitude of 500 ft or 67 dB(A) at 250 ft, and it has been demonstrated that these noise targets can be challenging to meet with the current VTOL aircraft designs [13, 14, 16]. Numerous computational studies have been performed recently to analyze multi-rotor VTOL aircraft and drone noise. Tonal noise of quadrotor and side-by-side configurations of VTOL aircraft were studied using high-fidelity CFD [2, 3, 14]. Pettingill and Zawodny [25] investigated broadband noise of small-scale drone rotors using the BPM model [24]. Thurman et al. [51] used the lattice-Boltzmann method–very-large-eddy simulation (LBM-VLES) to predict noise from a DJI-9450 drone rotor in hover, and they found that broadband noise is the dominant noise source above 1 kHz. Smith et al. [52] studied the effect of increasing the number of rotors on multicopter tonal noise using the rotor aerodynamics software Rensselaer



(a)



(b)

Figure 1.6: Quiet helicopter (a) configuration and (b) rotor geometry for various design tip speeds. [45]

Multicopter Analysis Code (RMAC) [53] and the acoustics software PSU-WOPWOP [54, 55].

By its frequency characteristics, rotorcraft noise can be categorized into tonal and broadband noise, where rotor tonal noise is important in the forward direction [12], while rotor broadband noise mainly propagates in the downward (or plane-normal) direction [15]. Rotor tonal noise is the dominant noise source at the low- and mid-frequency ranges and has discrete-frequency characteristics. It consists of various sources, such as steady loading noise, thickness noise, unsteady Blade-Vortex-Interaction (BVI) noise, and high-speed impulsive noise. Loading noise is generated by the forces to the fluid caused by the moving body, while thickness noise is generated by the displacement of fluid due to the body motion. Loading and thickness noise can be solved by the computation of Farassat's Formulation 1A [10, 56] of the Ffowcs Williams and Hawkings (FW-H) equation [32]. This method is widely used in acoustic simulation software, including PSU-WOPWOP [54, 55] and ANOPP [57]. At the onset of BVI noise, it becomes the most dominant tonal noise, so the accurate prediction of the blade and vortex interaction is critical to assessing UAM noise. High-speed impulsive noise associated with shock waves and the nonlinear sound propagation are important at high Mach number flows [58], but this type of noise can be easily avoided on the low-tip-speed UAM aircraft. In general, it is straightforward and feasible to predict rotor tonal noise with low or medium fidelity solvers when BVI noise is not present.

Rotorcraft tonal noise has been studied through experiments and computations. Thickness noise and loading noise were measured in the acoustics wind tunnel [4], and the blade-vortex-interaction (BVI) noise was studied in the flight test [59]. High-fidelity computational fluid dynamics (CFD) has the capability of investigating tonal noise on the complex vehicle configurations, such as the rotor-to-rotor and rotor-to-wing interactions [12, 60]. On the

other hand, the low-fidelity approaches are shown to capture tonal noise and thickness noise with low computational costs. The free-wake model and vortex-particle method were used to calculate the rotor blade loading for the FW-H solver [61–63]. The finite state dynamic inflow model was used to calculate rotor forward flight aerodynamics that was used in the FW-H solver to predict tonal noise at the blade passing frequency [64, 65]. Blade element theory, coupled with the FW-H solver, was also used on an axial flight propeller to predict tonal noise [66].

Historically, more research efforts have been devoted to tonal noise compared to broadband noise in the rotorcraft community, since conventional helicopters operate at high tip Mach numbers where tonal noise is important. However, the thriving UAM market has brought to the rotorcraft community a significant interest in broadband noise due to the reduced tip speeds and close proximity to residential areas [7]. Rotor broadband noise in large scale typically dominates at the mid- to high-frequency range [8] (1-5 kHz), which is in a sensitive frequency range in human hearing, as manifested in the A-weighting [1].

The prediction models of rotorcraft broadband noise are mainly based on two different approaches: the physics-based acoustics model and the empirical noise model. First, the physics-based acoustics models, such as the Amiet model [28] and the Howe model [67], are developed from the theories of edge-scattering of pressure fluctuations on an airfoil. As for their advantages, these models account for fundamental physics of noise generation mechanism [68], which provides the ability to accurately predict noise in general airfoils, such as cambered airfoils, and flow conditions as well as the flexibility to investigate complicated acoustic scattering processes, such as the serrated trailing-edge [69]. However, the physics-based models still depend on the input of the wall pressure spectrum [36] near the trailing

edge. The Amiet model has been used to study broadband noise on helicopters, propellers, axial fans, and wind turbines [15, 70–73]. Second, the empirical broadband noise models are determined by curve-fitting the measured broadband noise in conjunction with a proper scaling, such as the semi-empirical BPM model [24]. These empirical models tend to accurately predict broadband noise for the airfoils that were used in the model development, but they reveal little noise mechanisms and require additional measurements for different airfoils, such as cambered airfoils. Based on the BPM model, rotor broadband noise has been predicted and validated against the experiments [1, 5, 74–77].

In Chapter 7, the recent developments in UCD-QuietFly are presented to predict rotorcraft broadband noise in trimmed forward flight with the applications to UAM aircraft. The trimmed rotor forward flight aerodynamics is calculated using the Peters-He dynamic inflow model [78], the force-moment balance trim solution [79], and the blade element theory. With the updated UCD-QuietFly capabilities, we are able to investigate NASA’s newly designed quiet helicopter noise in forward flight with varying tip speeds and blade numbers at various operating conditions. The relative importance between tonal noise and broadband noise is investigated in this chapter. The psychoacoustic metrics of time-varying broadband noise are also studied.

1.6 Broadband Noise Predictions of Small-Scale Rotors

In recent years, the industry of small unmanned aircraft systems (sUAS) or drones has rapidly emerged for both civil and defense applications [80–82]. Powered by small-scale rotors, these

aircraft are widely used for logistics, surveillance, and recreation. However, noise is one of the top barriers to the wider deployment of the UAS aircraft, which involves different noise characteristics from full-scale helicopter rotors.

Regarding broadband noise on full-scale rotors, fully turbulent boundary layer flows occur in the rotor tip regions at high Reynolds number [15]. Therefore, turbulent boundary layer flow trailing-edge noise is the dominant broadband noise source in hovering and forward flights, while blade-wake-interaction (BWI) noise is a vital broadband noise source in descending flight [4].

On the contrary, small-scale rotors have different noise characteristics from conventional helicopters, due to their low tip speeds and small blade sizes. Experiments have shown that the importance of tonal noise is reduced while the broadband noise becomes more critical on small-scale rotors [9]. In addition, the A-weighted sound pressure level (SPL) shows that the broadband noise is more important on drone rotors at high frequencies considering human perception [1]. The reduced rotor tip speed considerably lowers the tonal noise strength, while the tip speed reduction has weaker effects on broadband noise [83]. For example, on a mid-scale BO-105 rotor [4] with the rotor radius of 2 m and the tip Mach number of 0.32, the tip Reynolds number is 1 million; however, on a small drone rotor [5] with the rotor radius of 0.16 m and the tip Mach number of 0.15, its tip Reynolds number is about 0.1 million. It is seen that the fully turbulent boundary layer flow can be developed in the tip regions of the BO-105 rotor, while the drone rotor can have a laminar boundary layer on the entire blade, where vortex-shedding noise becomes a critical broadband noise source at moderate or high angles of attack. In addition, due to the short chord length of the small-scale rotors, the effect of leading-edge back-scattering can be important with the small reduced frequency kc

[84]. Thus, the broadband noise prediction methods specialized for small-scale rotors must be developed and validated.

Turbulent boundary layer trailing-edge (TBL-TE) noise [68] is still one of the most important broadband noise sources for small-scale rotors. Amiet's trailing-edge noise model [28] was developed to predict this trailing-edge noise based on Curle's acoustics analogy [29] in conjunction with Schwartzchild's solution [85] for acoustic scattering. Amiet's original model only included the trailing-edge scattering, but the leading-edge back-scattering and the subcritical gusts were incorporated later in Roger and Moreau's model [84]. The improved trailing-edge boundary condition for Amiet's model was proposed based on new interpretations of the Kutta condition [86]. While the original Amiet model [87] supposed that the pressure around the trailing edge on each side of the wake is equal to half of the incident pressure, the modified Roger and Moreau's theory [84] suggested that the wake pressure on both the upper and lower sides of the wake should be zero. Although both theories satisfied the Kutta condition as the pressure difference between the upper and lower sides is zero, the large eddy simulation (LES) [88] indicated that the latter was closer to the flow physics. The strengths of these physics-based models, such as Amiet's model [28] or Howe's model [89], have been demonstrated by their capabilities to investigate the noise reduction techniques, including the trailing-edge serrations [69, 90] and the swept blades [72]. Regarding the rotorcraft applications, Amiet's model was recently used to study broadband noise of UAM vehicles [16].

The prediction methods of small-scale rotors have been explored through different approaches. First, Lattice-Boltzmann Method / Very Large Eddy Simulation (LBM/VLES) was used to capture the boundary layer transition and laminar separation bubble accurately.

LBM/VLES method was also used to predict the BWI noise of a small rotor in hover [6]. Broadband noise was obtained using the Ffowcs-Williams and Hawkings (FW-H) equation and validated on a low Reynolds number propeller [91]. Regarding tonal noise, the low-fidelity tools, such as the BEMT/FW-H method, were proved to provide accurate results for small-scale rotors [91]. Second, broadband noise of a small ideally twisted rotor was predicted using the NASA Aircraft Noise Prediction Program (ANOPP), which was based on the semi-empirical Brooks-Pope-Marcolini (BPM) model developed based on NACA0012 airfoil [5, 25]. Third, broadband noise of a drone rotor with the tripped boundary layer was predicted using a physics-based tool, UCD-QuietFly [15], which used Amiet’s trailing-edge noise model [28] and Lee’s wall pressure spectrum model [36]. High-fidelity computational fluid dynamics (CFD) was coupled with UCD-QuietFly to predict broadband noise on an APC drone rotor [70]. UCD-QuietFly was shown to be a feasible method to predict small-scale rotors, but improvement needs were identified for more consistent predictions in small-scale rotors[20].

In Chapter 4, an improved approach to predict broadband noise of small-scale rotors is presented using the rotor-broadband noise prediction tool UCD-QuietFly [16]. The effects of leading-edge back-scattering, the importance of laminar-boundary-layer vortex-shedding (LBL-VS) noise, and an improved Amiet’s model are studied. The new method is validated against various small-scale rotor experiments.

1.7 Noise Reduction Using Trailing-Edge Serrations

Rotorcraft noise reductions can be achieved by the operation and the design. During a rotorcraft operation, noise can be reduced by adjusting the flight path and vehicle attitude [92–94], including increasing the flight altitude, avoiding populated areas, and decreasing the descending flight angle. On the other hand, noise reduction can be incorporated in the rotorcraft design phase. Rotor tip speed and number of blades can be varied to reduce tonal and broadband noise [45, 77, 83]. The tail rotor noise can be eliminated by the NOTAR-style tailboom system [95]. Swept and tapered blades at the rotor tip are widely adopted to reduce the BVI noise [96, 97]. In addition, turbulent boundary layer trailing-edge broadband noise [68] can be attenuated by turbulent hydrodynamic energy reduction or acoustic scattering modification. These modifications include active flow controls [98], finlets [99], porous material [100], acoustics liners [101], and edge serrations [69].

Among the aforementioned broadband noise reduction techniques, serrated blades are preferred on vertical flight rotors. The serrations are easy to manufacture, and the rotor performance remains unchanged after adding the serrated edges [102]. Regarding the mechanism of the noise reduction, on properly designed serrations, destructive interference can be achieved between the serration root and tip, and the acoustic energy is redistributed to the high cut-off modes [69]. Although serrations have been widely used on wind turbines to reduce trailing-edge noise [103], the application of this idea to vertical flight rotors is still limited. The drone rotors with serrated trailing edges are experimentally shown to have noise reductions at high frequencies [104, 105]. However, rapid design tools with proper analytical models to investigate the potential to reduce rotor broadband noise are still lack-

ing. Therefore, Chapter 9 will focus on the analytical predictions of rotor broadband noise reduction with serrated trailing edges. We note that the exact reason of noise reduction with serrated trailing edges is controversial. Experiments [106] and high-fidelity numerical simulations [107] were performed to show that the wall pressure spectrum can be significantly varied upstream a trailing edge with the serrations, which results in trailing-edge noise. It is possible that the both source and scattering effects may play a role in noise reduction. However, in Chapter 9, we focus on the acoustic scattering effect by serrations rather than the noise source effect, which has been more traditionally accepted.

The early work of Howe used the tailored Green's function to theoretically predict trailing-edge noise of the serrated blade [89], but this method was shown to over-predict the noise reduction [108]. Using the Schwarzschild method [85] and the Wiener-Hopf method [109], Lyu et al. [108] and Huang [110] derived more recent serrated trailing-edge noise models, respectively. However, these two models cannot be solved exactly, and require extensive computational time for the entire rotor blade. Using the Wiener-Hopf method, Ayton [69] developed a new model that can be solved exactly with the infinite number of the scattering modes, where any serrated shape can be expressed in a 2-D function. To further reduce the computational cost, Lyu and Ayton [90] simplified Ayton's model [69] by implementing the finite number of cut-on and cut-off modes.

In Chapter 9, Lyu and Ayton's model [90] will be used to predict trailing-edge noise from the serrated rotor. This model requires the wall pressure fluctuations upstream the trailing edge, which can be obtained from Lee's wall pressure spectrum model [36] that is designed for adverse pressure gradient flows. An underlying assumption in Lyu and Ayton's model is that the boundary layer formation upstream a trailing-edge is not affected by the appearance

of the serration structures. This was confirmed from Direct Numerical Simulation (DNS) showing that the wall pressure spectrum change upstream a trailing edge is negligible with the addition of the serrations [111, 112]. The boundary layer parameters used to calculate the wall pressure spectrum are obtained from the low-fidelity XFOIL panel method [35], where the two-equation boundary layer formations are used to calculate a turbulent boundary layer flow around an airfoil surface. As for the rotor aerodynamics, the hovering flight is solved using the blade element momentum theory (BEMT), while the forward flight is solved by coupling the blade element theory (BET), Peters-He dynamic inflow model [78], and the moment-balance trim solution [79].

The current study extends the capabilities of the rotorcraft broadband noise prediction tool, UCD-QuietFly [16], from a straight trailing edge to a serrated trailing edge. For the straight blade sections, Amiet’s model [28] is transformed into the rotor blade coordinates [15] to predict trailing-edge noise. Amiet’s model uses the Schwarzschild method [85] to solve an acoustic scattering problem by a trailing edge [27]. For the serrated sections, Lyu and Ayton’s model is used. Note that a user-defined blade geometry accepts a blend of straight and serrated shapes on a rotor blade.

The dissertation will first validate this developed toolchain for serrated wing sections and serrated rotor blades against existing experimental data. Second, the importance and mechanism of serrated trailing edges used on rotorcraft will be addressed. Third, various parameters including serration number, shapes, and locations will be compared for their broadband noise reductions capabilities. Finally, quiet helicopter and quadrotor designs will be used to demonstrate the effectiveness of noise reduction with trailing-edge serrations in the context of UAM operations.

1.8 Airfoil-Turbulence Interaction Noise

Apart from airfoil-self noise that was mainly discussed in the previous sections, an airfoil also generates noise when it interacts with external turbulence. Depending on the source of the external turbulence, there are two types of airfoil-turbulence interaction noise: turbulence ingestion (TI) noise that is associated with atmospheric turbulence and blade-wake-interaction (BWI) noise that is associated with the wake turbulence from the preceding blades. With the same acoustic mechanism but more complex flows, BWI noise is associated with significant variations of streamwise velocities in the radial direction due to the blade-induced wake, which also creates strong spanwise flows. The turbulence is associated with blade inboard wake and tip vortices. Figure 1.7 shows that BWI noise is the dominant noise source in flow-speed level and shallow descent flights [113].

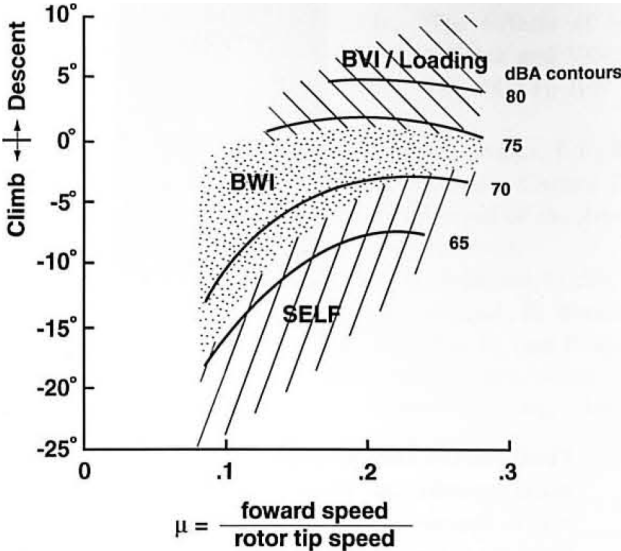


Figure 1.7: Dominate noise sources at various rotor conditions. [113]

An analytic model to predict airfoil-turbulence interaction noise or leading-edge noise was developed by Amiet [114], which took a similar approach as Amiet’s trailing-edge noise model [28]. This leading-edge noise model was validated by Paterson and Amiet [115] using

measured turbulence spectrum at the leading edge. Rotor BWI noise was predicted using Amiet's model with turbulence measured at the rotor blade leading edge [113]. Recently, lattice-Boltzmann method-very-large-eddy-simulation (LBM-VLES) was used to calculate blade wake, and BWI noise was predicted by the Ffowcs Williams and Hawkings (FW-H) equation [6, 32].

1.9 Machine-Learning Based Rotor Broadband Noise Predictions

Although the aforementioned approaches are much faster than computational fluid dynamics (CFD)-based approaches, they still require large computational cost and complexity to obtain accurate results. Specifically, UCD-QuietFly takes about 60 seconds to obtain the predicted noise at one observer location for a single-rotor configuration, and it also requires users' basic knowledge about rotor aerodynamics and aeroacoustics. A low-noise design optimization or design of experiment (DOE) requires an order of hundreds or thousands of simulations at multiple observers. Even with semi-analytical or reduced-order models, the computational cost is too prohibitive. Chapter 10 aims to develop data-driven machine learning and linear regression models to achieve fast computations of rotor broadband noise based on the data collection generated by UCD-QuietFly. As the outcome, the trained machine learning model and a simple polynomial equation will be useful for rotorcraft engineers in preliminary design.

Regarding the applications of the machine learning approach on rotorcraft applications, Greenwood [93] developed a machine-learning model to predict the noisy helicopter operating conditions based on the training data of NASA Langley Research Center's flight tests. Based

on the high-fidelity computational fluid dynamics (CFD) simulation results on a UH-60 rotor, Martinez et al. [116] used the convoluted neural network (ANN) to develop a mid-fidelity model that predicted the rotor blade loading from the given flow conditions. In addition, Ren et al. [117] developed a fast-predicting model for the fatigue life of a rotorcraft component using TensorFlow [118], based on the data of high-fidelity simulations. To the best of authors knowledge, however, no one has used machine-learning models or data-driven models to predict rotorcraft broadband noise.

Chapter 2

Acoustic Theories and Derivations

This section will briefly discuss the fundamental theories and mechanisms of the airfoil surface noise generation and propagation, starting from the fluid mechanics and deriving the acoustic model achieved by Amiet [28], which serves as the primary acoustic theory in the proposed research. The detailed implementations of the theories into the computer program will be described in Chapter 3.

2.1 Wave Equation

Before diving into more complicated sound generation and propagation problems on a lifting surface, it is essential to understand the 1-dimensional wave equation below, where y represents the acoustic pressure or any amplitude in a wave propagation problem, and c is the phase speed.

$$\frac{\partial^2 y}{\partial x^2} - \frac{1}{c^2} \frac{\partial^2 y}{\partial t^2} = 0 \quad (2.1)$$

The solution to this equation consists of two parts, where y_1 travels to the right and y_2

travels to the left.

$$y(x, t) = y_1(ct - x) + y_2(ct + x) \quad (2.2)$$

As shown in Fig. 2.1 by Kinsler et al. [119], the distance traveled by the wave can be described as $c(t_2 - t_1)$, since the peak value $y_1(ct_1 - x_1) = y_1(ct_2 - x_2)$, and $ct_1 - x_1 = ct_2 - x_2$.

This also demonstrates the propagating nature of the wave equation.

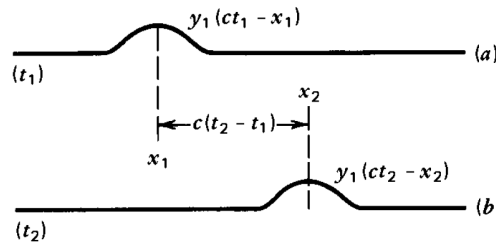


Figure 2.1: 1-D wave propagation. [119]

For example, a string extending to the right has a driving force of $F e^{j\omega t}$ requires the solution at the boundary $x = 0$ to be Eq. (2.3), where \mathbf{A} is a complex constant depending on the forcing function [119].

$$y(x = 0, t) = \mathbf{A} e^{i\omega t} \quad (2.3)$$

The solution in terms of the wavenumber $k = \omega/c$ for all x becomes

$$y(x, t) = \mathbf{A} e^{jk(ct-x)} = \mathbf{A} e^{j(\omega t - kx)} \quad (2.4)$$

2.2 Lighthill's Acoustic Analogy

This section reviews the theories to model the noise source and wave propagating from a rigid surface. The approximations and assumptions for the propagation will be included. Finally, a simplified source will be justified to replace the exact one.

The aerodynamically-generated noise theories began with the aeroacoustics pioneer Lighthill's acoustic analogy that was derived using fluid mechanics in Eq. (2.5), where the first equation is the time derivative of the continuity equation, and the second is the divergence of the momentum equation.

$$\begin{aligned}\frac{\partial}{\partial t} \left(\frac{\partial \rho}{\partial t} + \frac{\partial \rho v_i}{\partial x_i} \right) &= 0 \\ \frac{\partial}{\partial x_i} \left(\frac{\partial \rho v_i}{\partial t} + \frac{\partial (\rho v_i v_j + p_{ij})}{\partial x_j} \right) &= 0\end{aligned}\tag{2.5}$$

Subtracting these two equations and adding the term $c_\infty^2 \partial^2 \rho' / \partial x_i^2$ give the Lighthill's acoustic analogy [27], where the left-hand side is the wave equation of propagation, and the right-hand side is the source terms represented by the Lighthill stress tensors T_{ij} .

$$\frac{\partial^2 \rho'}{\partial t^2} - c_\infty^2 \frac{\partial^2 \rho'}{\partial x_i^2} = \frac{\partial^2 T_{ij}}{\partial x_i \partial x_j}\tag{2.6}$$

$$T_{ij} = \rho v_i v_j + (p - p_\infty) - (\rho - \rho_\infty) c_\infty^2 \delta_{ij} - \sigma_{ij}$$

Equation (2.6) models the sound generation and propagation from turbulent flows in the stationary medium, such as jet noise in Fig. 2.6. Although Lighthill's analogy does not take any approximations, accurately obtaining all the terms in the stress tensor requires

high-fidelity computations.

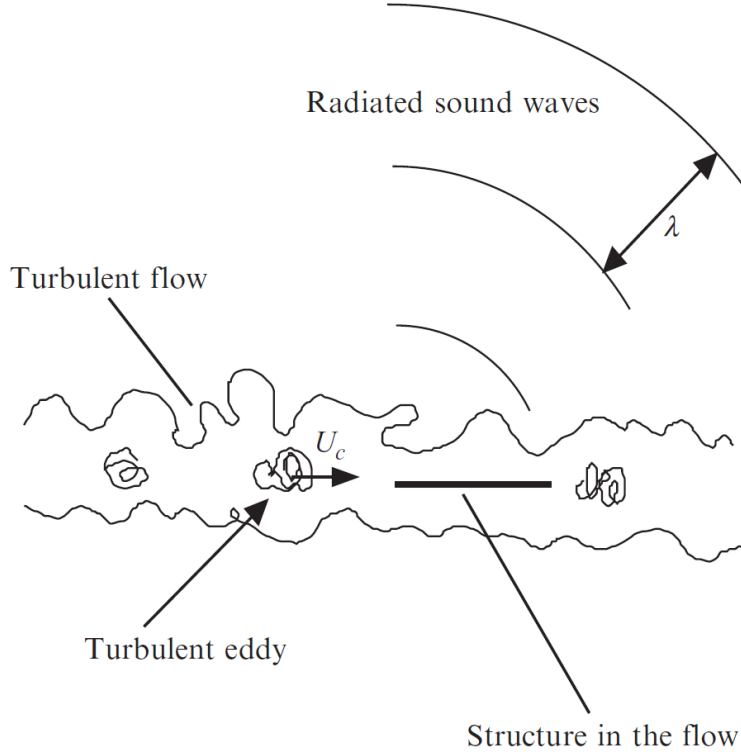


Figure 2.2: Turbulent flow in a stationary medium. [120]

The inhomogeneous wave equation can be solved analytically using Green's function to give the solution in Eq. (2.7), which specifies that the acoustic pressure is associated with the surface normal pressure p_{ij} , the momentum across the surface $\rho v_i v_j$, the mass across the surface ρv_j , and the Lighthill's stress tensor T_{ij} inside the source volume. The surface "S" in Eq. (2.7) is represented by the structure in the flow in Fig. 2.2.

$$\rho' c_\infty^2 = \int_{-T}^T \int_S \left((p_{ij} + \rho v_i v_j) \frac{\partial G}{\partial y_i} + G \frac{\partial(\rho v_j)}{\partial \tau} \right) n_j dS(\mathbf{y}) d\tau + \int_{-T}^T \int_V \left(\frac{\partial^2 G}{\partial y_i \partial y_j} \right) T_{ij}(\mathbf{y}, \tau) dV(\mathbf{y}) d\tau \quad (2.7)$$

The free field Green's function G_0 is shown below as a function of the source position,

receiver position, and receiver time. $\mathbf{x} = [x_1, x_2, x_3]$ is the position vector of the receiver in Cartesian coordinate, while \mathbf{y} is the position vector of the source.

$$G_o(\mathbf{x}, t|\mathbf{y}, t) = \frac{\delta(t - \tau + |\mathbf{x} - \mathbf{y}|/c_\infty)}{4\pi|\mathbf{x} - \mathbf{y}|} \quad (2.8)$$

2.3 Curle's Solution

Extending Lighthill's acoustic analogy of a jet stream, Curle [29] extended the solution to model noise propagation from a rigid surface. By substituting the free-field Green's function into Eq. (2.7), a solution is obtained to describe the directivity of each source term explicitly. In Eq. (2.9), the three terms are shown to have the monopole, dipole, and quadrupole directivities, respectively.

For the monopole term, the receiver noise strength is a function of distance $|\mathbf{x} - \mathbf{y}|$ in omni-direction, which demonstrates that the decrease of noise strength only depends on the receiver distance. The dipole term has the directivity characterized by the partial differentiation $\partial/\partial x_i$ in one direction that is different from the normal force direction n_j ; therefore, the two dipole circles shown in Fig. 2.3 have the same direction as the normal force since the differentiation is taken in the normal directions. Similar to the dipole term, the quadrupole term has the partial differentiation in both i and j directions, and its directivity is shown in Fig. 2.3 for a combination of two perpendicular dipoles. Note that the directivity of the quadrupole term depends on the arrangement of the source (+) and sink (-).

$$\rho' c_\infty^2 = \int_S \left[\frac{\partial(\rho v_j)}{\partial \tau} \right] \frac{n_j dS(\mathbf{y})}{4\pi|\mathbf{x} - \mathbf{y}|} - \frac{\partial}{\partial x_i} \int_S [p_{ij} + \rho v_i v_j] \frac{n_j dS(\mathbf{y})}{4\pi|\mathbf{x} - \mathbf{y}|} + \frac{\partial^2}{\partial x_i \partial x_j} \int_V [T_{ij}(\mathbf{y}, \tau)] \frac{dV(\mathbf{y})}{4\pi|\mathbf{x} - \mathbf{y}|} \quad (2.9)$$

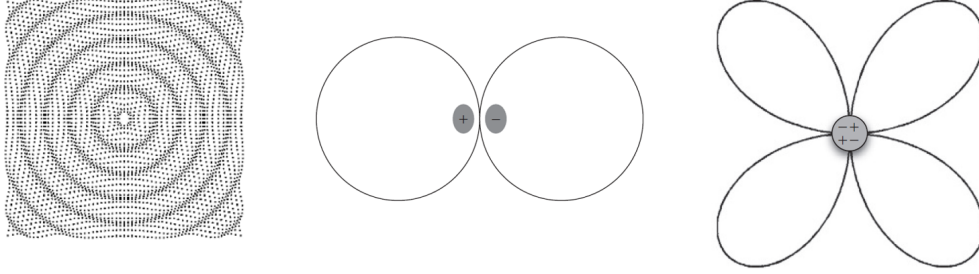


Figure 2.3: Monopole, dipole, and quadrupole sources. [120]

Since we are interested in noise generated from a lifting surface, according to the mathematical characteristics of each term, the dipole term related to the normal pressure on a lifting surface is important. Although the monopole term is also related to the surface, the mass flow across a stationary rigid surface is physically impossible, so this term is neglected for stationary lifting surface noise. For a moving surface, the monopole term becomes important, especially for a high-speed moving source. The quadrupole term involves the volume integral, which can be important when the surrounding volume of a lifting surface has non-linear source terms, such as a shock wave. However, this type of volume noise source associated with shock waves is not the focus of this dissertation. As a result, lifting surface noise is formulated in Eq. (2.10), and taking the differentiation of $\partial/\partial x_i$ with chain rule gives Eq. (2.11).

$$(\rho'(\mathbf{x}, t)c_\infty^2)_{dipole} = -\frac{\partial}{\partial x_i} \int_S [p_{ij} + \rho v_i v_j] \frac{n_j dS(\mathbf{y})}{4\pi|\mathbf{x} - \mathbf{y}|} \quad (2.10)$$

$$(\rho'(\mathbf{x}, t)c_\infty^2)_{dipole} = \int_S \left[\frac{\partial p_{ij} + \rho v_i v_j}{\partial \tau} + \frac{\partial (p_{ij} + \rho v_i v_j)c_\infty}{\partial |\mathbf{x} - \mathbf{y}|} \right] \frac{(x_i - y_i)n_j dS(\mathbf{y})}{4\pi|\mathbf{x} - \mathbf{y}|^2 c_\infty} \quad (2.11)$$

In Eq. (2.11), the second term inside the bracket is the near-field term because of its differentiation with respect to the observer distance in the source term, and it can be neglected for acoustic far-field applications. The momentum flux $\rho v_i v_j$ can be ignored on a rigid surface. For a compact source, the source region is assumed to be small, which is the case for an airfoil when the receiver is in the far-field, i.e., $|\mathbf{x}| \gg |\mathbf{y}|$. Therefore, the final equation that relates the far-field acoustic pressure to the lifting surface pressure in the time domain is given in Eq. (2.12).

$$(\rho'(\mathbf{x}, t)c_\infty^2)_{dipole} = \frac{x_i}{4\pi|\mathbf{x}|^2 c_\infty} \int_S \left[\frac{\partial (p_{ij} n_j)}{\partial \tau} \right] dS(\mathbf{y}) \quad (2.12)$$

Taking the Fourier transform of Eq. (2.12) gives the acoustic pressure in the frequency domain shown in Eq. (2.13), where $\Delta \tilde{p}$ is the wavenumber spectrum of the lifting surface pressure fluctuation.

$$\begin{aligned} \tilde{p}(\mathbf{x}, \omega) = (\tilde{p}'(\omega, t)c_\infty^2)_{dipole} &= \frac{-i\pi\omega x_2 \Delta \tilde{p}(k_1, k_3, \omega) e^{ik|\mathbf{x}|}}{c_\infty |\mathbf{x}|^2} \\ \Delta \tilde{p}(k_1, k_3, \omega) e^{ik|\mathbf{x}|} &= \frac{1}{2\pi} \int_{-c}^0 \Delta \tilde{p}(\mathbf{y}, \omega) e^{-ik_1 y_1} dy_1 \end{aligned} \quad (2.13)$$

2.4 Prandtl-Glauert Coordinate Transformation

Equation (2.13) was derived for a stationary medium. Adding the mean flow results in the convective wave equation in Eq. (2.14), where the mean flow is added in the fixed-frame Green's function, $G_e(\mathbf{x} + V_\infty t, t | \mathbf{y} + V_\infty \tau, \tau)$.

$$\frac{1}{c_\infty^2} \frac{D_\infty^2 G_e}{D\tau^2} - \Delta^2 G_e = \delta(t - \tau) \delta(\mathbf{x} - \mathbf{y}) \quad (2.14)$$

Equation (2.15) is used to transform the convective wave equation into a regular wave equation, whose analytic solution can be obtained.

$$G_e(\mathbf{x}, t | \mathbf{y}, \tau) = G_g(\xi, t_g | \zeta, \tau_g) \quad (2.15)$$

where $\xi = (x_1, \beta x_2, \beta x_3)$, $\zeta = (y_1, \beta y_2, \beta y_3)$, $t_g = t + Mx_1/\beta^2 c_\infty$, and $\tau_g = \tau + My_1/\beta^2 c_\infty$

The wave equation in Prandtl-Glauert coordination is given as

$$\frac{1}{\beta^4 c_\infty^2} \frac{\partial^2 G_g}{\partial t_g^2} - \frac{\partial^2 G_g}{\partial \xi_i^2} = -\delta(\xi - \zeta) \delta(t_g - \tau_g) \quad (2.16)$$

To account for this mean flow effect, the Prandtl-Glauert transformation is used to perform the coordinate transformation in the acoustic wave numbers k_1 and k_3 by the following equations.

$$k_1 = k_0 \left(\frac{x_1}{r_e} - M \right), \quad k_2 = k_0 \beta^2 \left(\frac{x_2}{r_e} \right), \quad k_0 = \frac{\omega}{\beta^2 c_\infty} \quad \beta^2 = 1 - M^2, \quad r_e = \sqrt{x_1^2 + \beta^2(x_2^2 + x_3^2)} \quad (2.17)$$

2.5 Acoustic Power Spectral Density

Taking the expected value of the acoustic pressure and its conjugate gives the acoustic power spectral density in Eq. (2.18), where the two integrals represent the inclusion of all pressure fluctuations over the entire chord of an airfoil.

$$S_{pp}(\mathbf{x}, \omega) = \frac{\pi}{T} E[\tilde{p}^*(\mathbf{x}, \omega) \tilde{p}(\mathbf{x}, \omega)] = \left(\frac{\omega x_3}{2c_\infty r_e^2} \right)^2 \frac{b}{2\pi} \int_{-c}^0 \int_{-c}^0 \phi_{qq}(y_1, y'_1, k_3, \omega) e^{-ik_1(y'_1 - y_1)} dy_1 dy'_1 \quad (2.18)$$

The flow passes on one side of a plate. Since the Kutta condition ($\Delta p = 0$) must be satisfied at the trailing edge, and there is a sudden change in the boundary condition at the trailing edge, an acoustic pressure must be generated to account for the sudden change in the pressure. The pressure fluctuation on the airfoil can be given in Eq. (2.19), which gives two components of the noise sources: the first term in the bracket specifies the pressure fluctuation carried in the boundary layer. The second term specifies the scattering of this fluctuation for trailing-edge noise, when an edge suddenly disappears, that eventually propagates to the far field. To obtain the scattered pressure or g_{te} , Schwartzschild's solution [85] is used to model the pressure jump at the trailing edge.

$$\begin{aligned} \phi_{qq}(y_1, y'_1, 0, \omega) &= \frac{2\pi^2}{TR_\infty} E[\tilde{p}^* \tilde{p}] \\ \tilde{p}(y_1, k_3, \omega) &= \tilde{p}_{bl}(k_3, \omega) [e^{iK_1 y_1} + g_{te}(y_1, k_1, k_3)] \end{aligned} \quad (2.19)$$

The leading-edge response to the incoming turbulence can also be calculated using the

similar approach as the trailing-edge response. The surface pressure fluctuation at a leading edge in Eq. (2.13) is expressed as

$$\Delta\tilde{p} = \frac{1}{2}\rho_0 c \tilde{w}_3 L_{te} \quad (2.20)$$

where \tilde{w}_3 is the wavenumber transform of the of the upwash velocity, which can be calculated in turbulent spectrum in Eq. (2.21). L_{te} is related to the nondimensional lift on the airfoil surface.

$$\phi_{ww}(k_1, k_2) = \frac{\pi^2}{R_\infty^2} E \left[|\tilde{w}_3(k_1, k_2)|^2 \right] \quad (2.21)$$

2.6 Amiet's Trailing-Edge and Leading-Edge Noise Theories

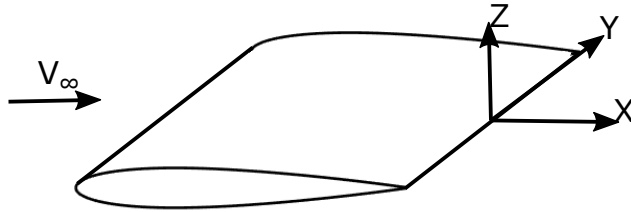


Figure 2.4: Airfoil local coordinate. [16]

Amiet [28] obtained the acoustic power spectrum for trailing-edge noise using Schwartzschild's solution that was originally applied to the scattering problem in an electromagnetic field. The Amiet theory given in Eq. (2.22) conveniently related the measurable quantities, such as the wall pressure spectrum Φ_{pp} of the boundary layer, to the acoustic power spectrum. Δr is the span of the airfoil, z is the coordinate shown in Fig. 2.4, L is the lifting function

derived by Amiet, ω is the angular frequency, and Φ_{pp} is the wall pressure spectrum, which can be obtained using empirical equations, such as Lee's [36] model.

$$S_{pp}(x, y, z, \omega) = \frac{1}{32\pi^2} \left(\frac{\omega cz}{c_0 r_e^2} \right)^2 \Delta r |L|^2 l_r \Phi_{pp} \quad (2.22)$$

Amiet's leading-edge noise [114], which was published earlier than Amiet's trailing-edge noise, is given as

$$S_{pp}(x, y, z, \omega) = \left(\frac{\rho_0 k c x_3}{2S_0^2} \right)^2 \pi V_\infty \frac{L}{2} \Phi_{ww} |L_{le}|^2 \quad (2.23)$$

As a result, the sound pressure level for either trailing-edge noise or leading-edge noise is obtained in Eq. (2.24) with the appropriate S_{pp} .

$$\text{SPL}(x, y, z, \omega) = 10 \log_{10} \left(\frac{2\pi S_{pp}(x, y, z, \omega)}{P_{ref}^2} \right), \quad P_{ref} = 2 \times 10^{-5} Pa \quad (2.24)$$

2.7 Airfoil-Self Noise

A type of airfoil broadband noise is airfoil-self noise generated by the interactions between the airfoil geometry and the turbulent/laminar flows produced by itself. Figure 2.5 shows some common airfoil self-noise sources and the mechanism [24], including trailing-edge noise, vortex-shedding noise, trailing-edge bluntness noise, stall noise, and tip noise. Trailing-edge noise is generally the dominant broadband noise source for the fully turbulent or transition flow conditions, which is typical for aircraft operations. Due to the unsteadiness of the turbulent flow, the boundary layer passing through the airfoil surface has pressure fluctua-

tions. As the surface discontinues, such as the appearance of a trailing edge, the pressure fluctuation is perturbed and scattered by the trailing edge. Theoretically, to meet the Kutta condition in the wake downstream of the trailing edge, a scattered pressure propagating to the far-field must appear to account for the pressure deficit in the wake due to the incident pressure upstream [18, 28, 84, 86]. Vortex-shedding noise is dominant for laminar flow [6], which is associated with the feedback mechanism of instability waves. Trailing-edge bluntness noise typically covers a narrow range of frequency [25], which is caused by the vortex generated by a finite thickness at the trailing edge. For a stalled airfoil with flow separation, the vortices are formed by the leading-edge separation and act as the noise sources. Finally, due to the pressure difference between the upper and lower surfaces, the vortices are formed at the blade tip and produce pressure fluctuations.

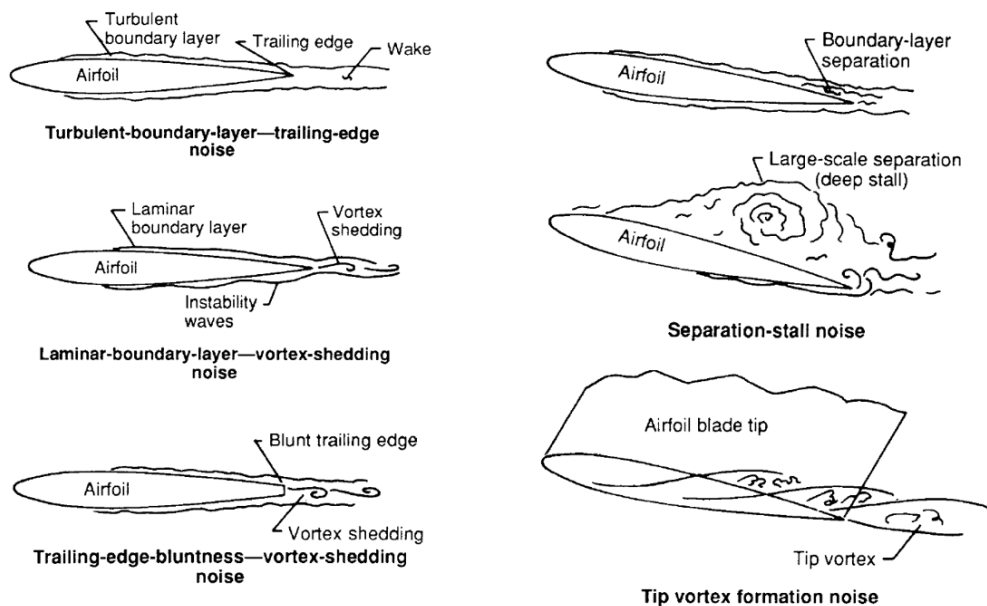


Figure 2.5: Airfoil self-noise sources. [24]

Airfoil self-noise has many applications, especially for rotorcraft because rotorcraft has many operations close to humans. Blandeau and Joseph [33] predicted the broadband noise of

an airplane propeller using the theoretical approach. Snider et al. [7] experimentally justified that broadband noise is more important than tonal noise when a helicopter operates at the overhead position. Li and Lee applied the noise theories to predict the broadband noise of conventional helicopters [15, 20, 83], multi-rotor conceptual vehicles [16], small-scale drone rotors [18], and serrated rotors [19, 22].

Chapter 3

Methods and Formulations in Rotor Broadband Noise Predictions: UCD-QuietFly

The previous chapter provided the general aeroacoustic theories. In this chapter, the detailed implementations of those theories into computer program will be provided. First, the formulations in UCD-QuietFly are provided, which predict broadband noise from multi-rotor aircraft. The coordinate transformations from the blade section local frame to the observer global frame are presented. The methods to calculate amplitude modulations, psychoacoustic metrics, and broadband noise of small-scale rotors are given. Second, the prediction methods for rotor aerodynamics, tonal noise, and broadband noise in forward flights are demonstrated. Third, broadband noise of rotors with serrated trailing edges is predicted using a modified analytic model. Forth, the implementations for leading-edge noise predictions in UCD-QuietFly are presented. Lastly, the training methods for two machine-learning models are given to achieve fast predictions of rotor broadband noise.

3.1 Multi-Rotor Trailing-Edge Noise Predictions in Hovering Flight

Using the Schwarzschild solution [85], Amiet's power spectral density (PSD) \bar{S}_{pp} [28] at an observer location (X, Y, Z) with respect to each of the two surfaces of an airfoil is written as

$$\bar{S}_{pp} = \frac{1}{32\pi^2} \left(\frac{\omega_d c Z}{c_o \epsilon^2} \right)^2 \Delta r |L|^2 l_r \Phi_{pp} \quad (3.1)$$

The overbar on S_{pp} means the acoustic power spectrum density from an airfoil section. In Eq. (3.1), $\epsilon^2 = X^2 + \beta^2 (Y^2 + Z^2)$, $\beta^2 = 1 - M^2$, ω_d is the Doppler-shifted frequency, c is the chord length, c_o is the speed of sound, Δr is the blade sectional span, L is the loading term, l_r is the spanwise turbulence correction length, and Φ_{pp} is the wall pressure spectrum at 99% of c . The local coordinates used in Eq. (3.1) is shown in Fig. 2.4. On a rotor blade, the origin of the local coordinate of each section is located at its mid-span.

Figure 3.1 shows the coordinates of a blade section on a rotor relative to an observer. The coordinate transformation matrices for each rotor are essentially the same as the multi-rotor UCD-QuietFly method [16] as shown in Eqs. (3.2) and (3.3), where the tilt angle matrix M_t is modified to include multiple rotors on a vehicle, since each rotor can have different tilt angles. The definitions of t_v and t_r are described in the next paragraph. It should be noted that Eqs. (3.2) and (3.3) be performed on each rotor. These matrices transform the rotor coordinate (X_1, Y_1, Z_1) at the rotor hub to the local coordinate (X, Y, Z) on a blade section. The flowchart of UCD-QuietFly programmed in FORTRAN is given in Fig. 3.2.

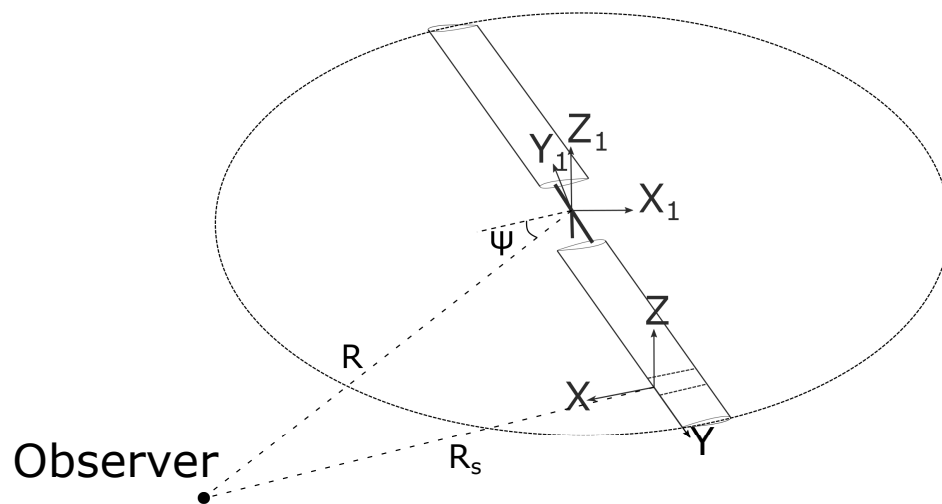


Figure 3.1: Airfoil local and global coordinates for an observer [16]. Positive elevation angle is defined as above the rotor.

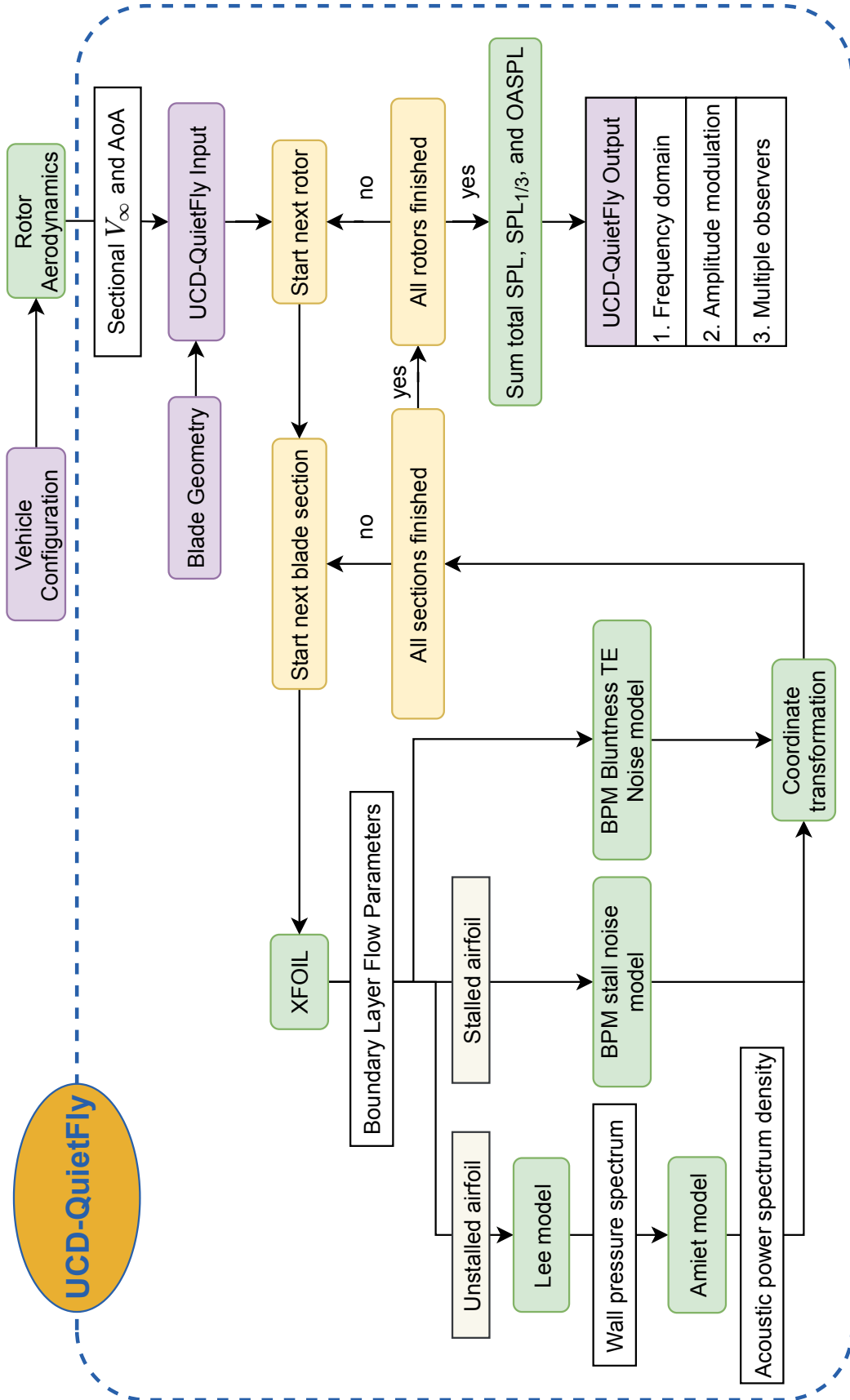


Figure 3.2: Rotor broadband noise prediction code UCD-QuietFly flowchart.

$$\begin{bmatrix} X \\ Y \\ Z \end{bmatrix} = M_\theta M_\phi \begin{bmatrix} M_t \begin{bmatrix} X_1 \\ Y_1 \\ Z_1 \end{bmatrix} + M_{\beta_p} \end{bmatrix} \quad (3.2)$$

$$\begin{aligned} M_\theta &= \begin{bmatrix} \cos(\theta_0 + \theta) & 0 & \sin(\theta_0 + \theta) \\ 0 & 1 & 0 \\ -\sin(\theta_0 + \theta) & 0 & \cos(\theta_0 + \theta) \end{bmatrix} \\ M_\phi &= \begin{bmatrix} \sin \phi & -\cos \phi & 0 \\ \cos \phi & \sin \phi & 0 \\ 0 & 0 & 1 \end{bmatrix} \\ M_t &= \begin{bmatrix} \cos(t_v + t_r) & 0 & \sin(t_v + t_r) \\ 0 & 1 & 0 \\ -\sin(t_v + t_r) & 0 & \cos(t_v + t_r) \end{bmatrix} \\ M_{\beta_p} &= \begin{bmatrix} -r \sin \beta_p \cos \phi \\ -r \sin \beta_p \sin \phi \\ r \cos \beta_p \end{bmatrix} \end{aligned} \quad (3.3)$$

θ_0 describes the collective pitch angle that varies with the rotor thrust, θ describes the twist angle, ϕ describes the azimuth angle, t describes the tilt angle with positive angle tilting up, r describes the blade sectional distance from the hub, and β_p describes the flapping angle. To the authors' best knowledge, none of the earlier research included the entire blade motions, with the flapping, collective pitch, cyclic pitch, and twist angles, in the prediction

of rotor trailing-edge noise. Even though cyclic flapping and pitch angles are not present in hover, they should be included in forward flight to accurately prescribe blade motion and trailing-edge location. Cyclic flapping and cyclic pitch angles are combined into β_p and θ_0 as the time-dependent quantities. The angles are described in Figs. 3.1 and 3.3. With the directions of positive angles defined the counter-clockwise direction, the collective pitch angle is between the rotor hub plane and the blade root chord plane, and the twist angle is between the root chord plane and the section chord plane. In other words, the collective pitch angle is a pilot's control input that adjusts the blade's feathering motion, while the twist angle varies for different blade sections.

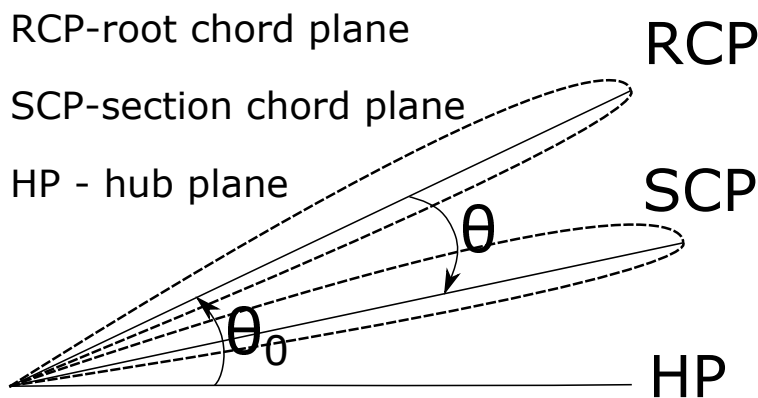


Figure 3.3: Blade collective pitch and twist. Collective pitch angle (θ_0) measures from the rotor hub plane to the root chord plane, and twist angle (θ) measures from the root chord plane to the section chord plane, with positive angles in the counter-clockwise direction.

In addition to a single-rotor prediction capability of UCD-QuietFly presented in Ref. 16, the multi-rotor broadband noise prediction capability is included in this dissertation to investigate UAM VTOL vehicles. In addition, the amplitude modulation capability is employed to study the time-dependent characteristics of the UAM VTOL broadband noise.

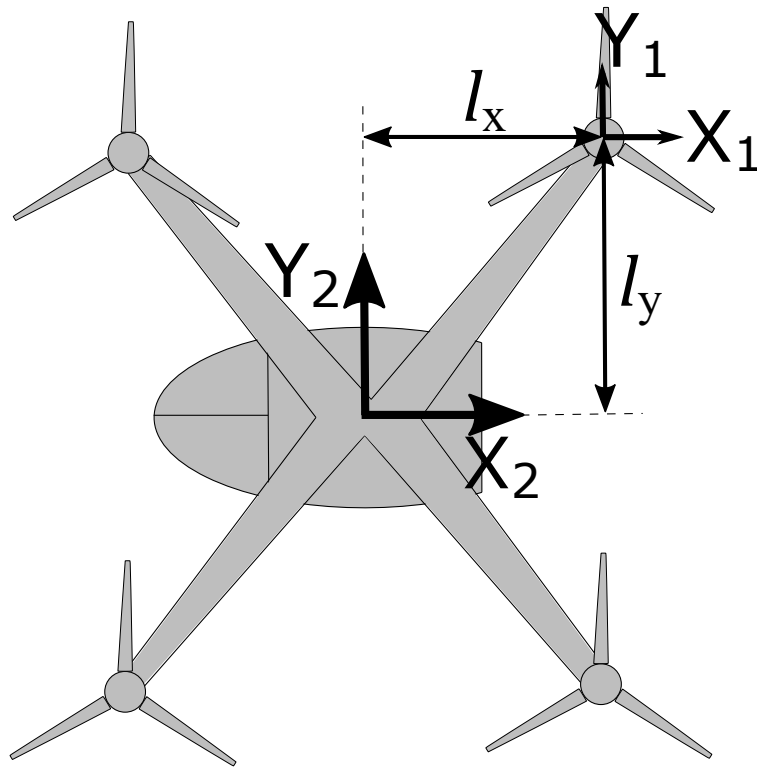
UCD-QuietFly is a physics-based method that relates the far-field acoustics with the turbulent pressure fluctuations near the trailing edge through the theory of edge scattering

[29]. Therefore, UCD-QuietFly not only predicts rotor broadband noise but also contains fundamental flow physics of the noise generation, which helps improve the physical understanding of noise generation and incorporate noise reduction techniques, such as trailing-edge serrations, into the model.

Besides the rotor trailing-edge noise, a capability of predicting the trailing-edge blunt noise and the stall noise is added using the semi-empirical BPM model [24]. It is important to note that the separation noise described in the BPM model still physically describes trailing-edge noise at non-zero angles of attack. For airfoils that are not stalled, this effect is also captured in our trailing-edge prediction based on the Amiet model [28]; the BPM stall noise model is only used on the stalled blade sections, which rarely occur in normal conditions. These capabilities are intended to cover more noise sources belonging to rotor broadband noise, although trailing-edge noise is found to be the dominant source. However, the current UCD-QuietFly does not include a model for predicting turbulent wake/blade interaction broadband noise, which is more prominent at low frequencies during the onset. As for the amplitude modulation, the azimuthal averaging of the rotor trailing-edge noise is replaced by recording the narrow-band sound pressure level in the history of time steps. Since the blade sections have different positions with respect to the observer at an observer time, the retarded-time effect is also considered.

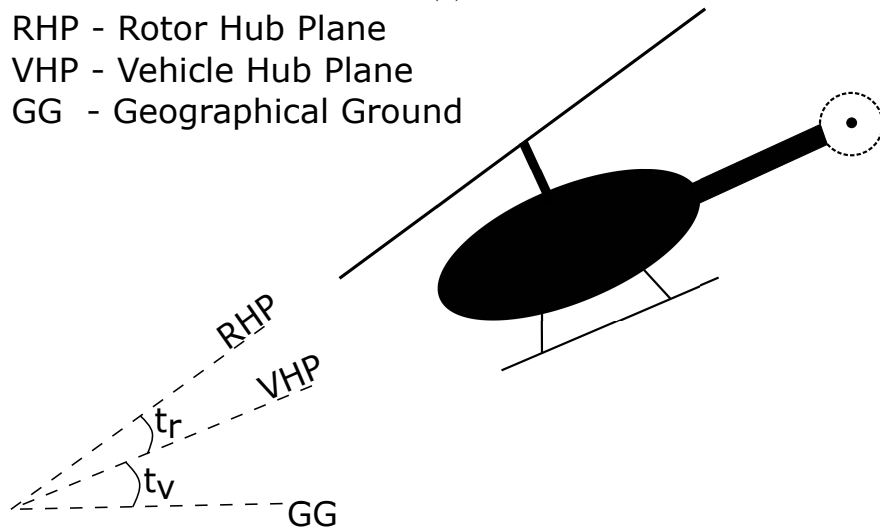
Chapter 6 extends the rotor broadband noise prediction capability from a single rotor [16] to multiple rotors on a vehicle. Equations (3.4)-(3.5) describe the coordinate transformations from the vehicle's global coordinate (X_2, Y_2, Z_2) with an origin at the vehicle hub to the rotor coordinate (X_1, Y_1, Z_1) with an origin at the rotor hub. Therefore, a user can conveniently input the global coordinate (X_2, Y_2, Z_2) relating a vehicle hub to an observer, and the program

will perform the coordinate transformations internally to find the local coordinate (X, Y, Z) from Eqs. (3.2)-(3.5), which is necessary for the Amiet model [28]. The X_2Y_2 plane is parallel to the geographical ground shown in Fig. 3.4(a). Figure 3.4(b) shows the definitions of t_v and t_r , which were used in Eqs. (3.3) and (3.5). t_v is the vehicle tilt angle between the vehicle hub plane and the geographical ground and t_r is the rotor tilt angle between the rotor hub plane and the vehicle hub plane.



(a)

RHP - Rotor Hub Plane
 VHP - Vehicle Hub Plane
 GG - Geographical Ground



(b)

Figure 3.4: Multi-rotor vehicle coordinates: (a) Rotor coordinate (X_1, Y_1, Z_1) and vehicle coordinate (X_2, Y_2, Z_2) . The distance from rotor hub to vehicle hub is described by (l_x, l_y, l_z) , and (b) Rotor hub plane, vehicle hub plane, and geographical ground.

$$\begin{bmatrix} X_1 \\ Y_1 \\ Z_1 \end{bmatrix} = M_{t_v} \begin{bmatrix} X_2 \\ Y_2 \\ Z_2 \end{bmatrix} + M_{hub} \quad (3.4)$$

$$M_{t_v} = \begin{bmatrix} \cos t_v & 0 & \sin t_v \\ 0 & 1 & 0 \\ -\sin t_v & 0 & \cos t_v \end{bmatrix} \quad \text{and} \quad M_{hub} = \begin{bmatrix} l_x \\ l_y \\ l_z \end{bmatrix} \quad (3.5)$$

The PSD of each section changes with the azimuth angle; hence, it is azimuthally averaged by Eq. (3.6). Note that the azimuthal averaging is not used for the calculations of amplitude modulation, which will be explained in the next section.

$$S_{pp} = \frac{N_B}{2\pi} \int_0^{2\pi} \left(\frac{\omega}{\omega_d} \right)^2 \bar{S}_{pp} d\phi, \quad (3.6)$$

in which the Doppler-shifted frequency ω_d at the observer is related to the source frequency ω using

$$\frac{\omega_d}{\omega} = \frac{1}{1 + M_r \left(\frac{X}{R_s} \right)}. \quad (3.7)$$

Note that $M_r = \Omega r / c_o$ is the rotational Mach number of the blade section. X has the direction pointing from leading edge to trailing edge shown in Fig. 3.1 and computed by Eq. (3.2), and R_s is the distance between the blade section and an observer. Substituting Eq. (3.1) and Eq. (3.7) into Eq. (3.6) and expanding the terms gives the acoustic PSD generated from a single side of each blade section as

$$S_{pp} = \left(\frac{\omega}{c_o}\right)^2 c^2 \Delta r \left(\frac{1}{32\pi^2}\right) \frac{N_B}{2\pi} \int_0^{2\pi} D_\phi |L|^2 l_r \Phi_{pp} d\phi. \quad (3.8)$$

The directivity term is given as $D_\phi = (Z/\epsilon^2)^2$, where ϵ is defined in Eq. (3.1). The local coordinate of Z and ϵ must be found by taking the coordinate transformations in Eqs. (3.2) and (3.3) from the global coordinate. A detailed equation of the directivity term D_ϕ in terms of the global coordinate system (X_2, Y_2, Z_2) are provided in the Appendix.

The loading term L is given by Schlinker and Amiet [30] as

$$|L| = \frac{1}{\Lambda} |e^{i2\Lambda} [1 - (1+i) E^* (2(\bar{K} + \bar{\mu}M + \bar{\gamma})) + e^{-i2\Lambda} \sqrt{\frac{K + \mu M + \gamma}{\mu x/\epsilon + \gamma}} (1+i) E^* (2(\bar{\mu}x/\epsilon + \bar{\gamma}))]| \quad (3.9)$$

where $\Lambda = \bar{k}_x - \bar{\mu}x/\epsilon + \bar{\mu}M$, $K = \omega_d/U_c$, $\mu = \omega_d M/U\beta^2$, $\gamma^2 = (\mu/\epsilon)^2(x^2 + \beta^2 z^2)$, and E^* represents the complex conjugate of a Fresnel integral. In this study, the turbulence convective velocity and spanwise turbulence length scale are defined as $U_c = 0.8U_\infty$ and $l_r = 1.6U_c/\omega$, respectively.

The remaining wall pressure spectrum Φ_{pp} is obtained by a recently developed empirical wall pressure spectrum model for non-zero gradient flows, Lee's model [36], as

$$\frac{\Phi_{pp}(\omega)U_e}{\tau_w^2 \delta^*} = \frac{\max(a, (0.25\beta_c - 0.52)a) \left(\frac{\omega \delta^*}{U_e}\right)^2}{[4.76 \left(\frac{\omega \delta^*}{U_e}\right)^{0.75} + d^*]^e + [8.8 R_T^{-0.57} \left(\frac{\omega \delta^*}{U_e}\right)]^{h^*}} \quad (3.10)$$

where $\beta_c = (\Theta/\tau_w) |dp/dx|$, $a = 2.28\Delta^2(6.13\Delta^{-0.75} + d)^e [4.2(\Pi/\Delta) + 1]$, $\Delta = \delta/\delta^*$, $\Pi = 0.8(\beta_c + 0.5)^{3/4}$, $e = 3.7 + 1.5\beta_c$, $d = 4.76(1.4/\Delta)^{0.75} [0.375e - 1]$, $R_T = (\delta/U_e)(\nu/u_\tau^2)$,

$h^* = \min(3, (0.139 + 3.1043\beta_c)) + 7$, and if $(\beta_c < 0.5)$, $d^* = \max(1.0, 1.5d)$, otherwise $d^* = d$.

Finally, the far-field SPL for one side of the i^{th} section is calculated from the power spectral density S_{pp} as

$$\text{SPL}_{i(U/L)} = 10 \log_{10} \left(\frac{2\pi S_{pp}}{(2 \times 10^{-5})^2} \right), \quad (3.11)$$

where U and L represent the upper and lower surfaces of an airfoil, respectively. The j^{th} rotor's total SPL is logarithmically summed to be

$$\text{SPL}_{\text{rotor},j} = 10 \log_{10} \sum_{i=1}^{N_S} (10^{0.1\text{SPL}_{iU}} + 10^{0.1\text{SPL}_{iL}}), \quad (3.12)$$

where N_S is the total number of sections. Likewise, the total SPL of a vehicle with multiple rotors is given in Eq. (3.13), where N_R is the number of rotors.

$$\text{SPL}_{\text{vehicle}} = 10 \log_{10} \sum_{j=1}^{N_R} (10^{0.1\text{SPL}_{\text{rotor},j}}) \quad (3.13)$$

3.2 Amplitude Modulation of Rotor Broadband Noise

Theoretically, the noise level is low when the blade is away from the observer and the level is high when the blade is close to the observer, so in the time duration, the noise level is fluctuating periodically, which is the logic of amplitude modulation. However, depending on its relative position to the observer, each section on a blade has a different corresponding observer time and noise level. Therefore, broadband noise from each blade section needs to

be individually predicted before summing up to the total noise. Figure 3.5 shows the blade sections as the noise sources, where τ is the noise emission time and $\tau + R_s/c_0$ is the observer time. The emission time is associated with the angular velocity Ω and azimuthal angle ϕ by

$$\tau = \frac{\phi}{\Omega} \quad (3.14)$$

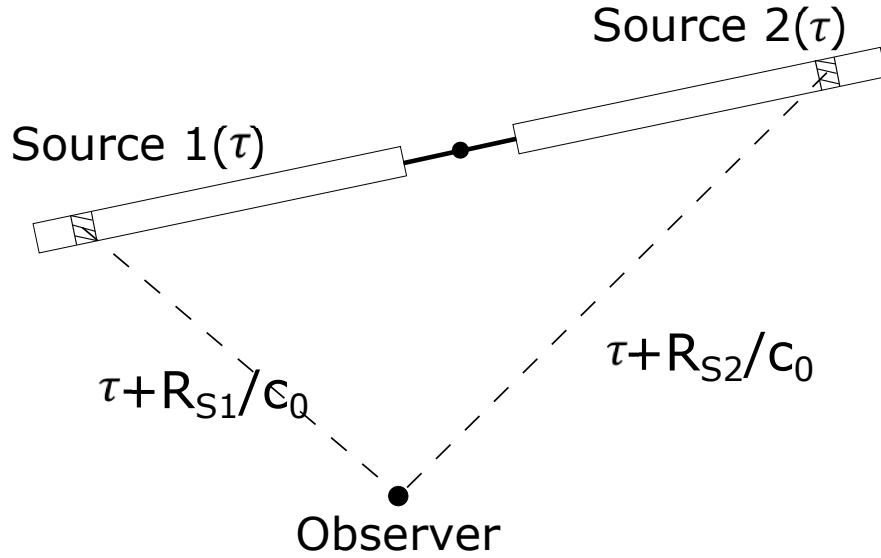


Figure 3.5: Retarded time effect on amplitude modulation from each blade section as a noise source.

For the calculation of amplitude modulation, the azimuthal averaging is removed and the broadband noise of each blade section is recorded in time history, so Eq. (3.8) becomes Eq. (3.15), where $S_{pp,\phi}$ is the acoustic power spectrum density of one blade section at an azimuth angle.

$$S_{pp,\phi} = \left(\frac{\omega}{c_o}\right)^2 c^2 \Delta r \left(\frac{1}{32\pi^2}\right) D_\phi |L|^2 l_r \Phi_{pp} \quad (3.15)$$

In UCD-QuietFly, the observer time duration is a user's option, based on which the program determines the ending emission time while the starting emission time is kept at zero.

At every emission time step, the broadband noise from each blade section is calculated from Eq. (3.15), and based on the section's location its corresponding observer time is calculated. After the calculation of all sections and time steps, the total vehicle broadband noise as a function of observer time is interpolated and summed. As the output, the program generates the broadband noise sound pressure level as a function of both frequency and observer time.

3.3 Rotor Airloads and Inflow Predictions in Forward Flight

The inflow distribution of a trimmed forward flight is calculated using the Peters-He dynamic inflow model [78]. The normalized inflow velocity w shown in Eq. (3.16) is written as a combination of multiple states,

$$w(\bar{r}, \psi, \bar{t}) = \sum_{r=0}^{\infty} \sum_{j=r+1, r+3, \dots}^{\infty} \phi_j^r(\bar{r}) [\alpha_j^r(\bar{t}) \cos r\psi + \beta_j^r(\bar{t}) \sin r\psi] \quad (3.16)$$

where ϕ is the radial expansion shape function, ψ is the azimuth angle, \bar{t} is the non-dimensional time, \bar{r} is the non-dimensional radial location, and α and β are the induced flow coefficients to be determined in the model. The radial shape function $\phi(\bar{r})$ is described as

$$\phi_j^r(\bar{r}) = \sqrt{(2j+1)H_j^r} \sum_{q=r, r+2, \dots}^{j-1} \bar{r}^q \frac{(-1)^{(q-r)/2} (j+q)!!}{(q-r)!! (q+r)!! (j-q-1)!!} \quad (3.17)$$

with

$$H_j^r = \frac{(j+r-1)!! (j-r-1)!!}{(j+r)!! (j-r)!!} \quad (3.18)$$

where r and j are the harmonic and polynomial numbers. The double factorial is defined as $(n)!! = n(n-2)(n-4)\dots$

The induced flow coefficients are formulated in Eq. (3.19), where $*$ means the time derivative, and the τ_n^m vectors contain the rotor loading coefficients. In a trimmed steady forward flight, the unsteady coefficients α^* and β^* are zeros, and the loading coefficients are averaged over one rotor revolution. $[M]$ and $[L]$ are the apparent mass matrix and the influence matrix that can be found in Ref. 78.

$$\begin{aligned}
 [M] \begin{bmatrix} \vdots \\ \{\alpha_j^r\} \\ \vdots \end{bmatrix}^* + [L^c]^{-1} \begin{bmatrix} \vdots \\ \{\alpha_j^r\} \\ \vdots \end{bmatrix} &= \begin{bmatrix} \vdots \\ \{\tau_n^m\}^c \\ \vdots \end{bmatrix} \\
 [M] \begin{bmatrix} \vdots \\ \{\beta_j^r\} \\ \vdots \end{bmatrix}^* + [L^s]^{-1} \begin{bmatrix} \vdots \\ \{\beta_j^r\} \\ \vdots \end{bmatrix} &= \begin{bmatrix} \vdots \\ \{\tau_n^m\}^s \\ \vdots \end{bmatrix}
 \end{aligned} \tag{3.19}$$

On the right-hand side of Eq. (3.19), the loading coefficient matrices can be expressed in Eq (3.20), where q is the blade index, i is the blade element index, and L_i^q is the rotor normal force on the q_{th} blade and i_{th} section. The same shape function shown in Eq. (3.17) is used in Eq. (3.20) with r and j replaced by m and n . The rotor normal force and the inflow ratio are interdependent and solved iteratively to find a solution in trimmed forward flights.

$$\begin{aligned}
\tau_n^{0c} &= \frac{1}{2\pi\rho_0\Omega^2 R^4} \sum_{q=1}^{N_q} \left[\sum_{i=1}^{N_i} L_i^q \phi_n^m(\bar{r}_i) \right] \\
\tau_n^{mc} &= \frac{1}{\pi\rho_0\Omega^2 R^4} \sum_{q=1}^{N_q} \left[\sum_{i=1}^{N_i} L_i^q \phi_n^m(\bar{r}_i) \right] \cos(m\psi) \\
\tau_n^{ms} &= \frac{1}{\pi\rho_0\Omega^2 R^4} \sum_{q=1}^{N_q} \left[\sum_{i=1}^{N_i} L_i^q \phi_n^m(\bar{r}_i) \right] \sin(m\psi)
\end{aligned} \tag{3.20}$$

The helicopter control settings or trim solutions for the various designs and flight operations are found using the force-moment-balance method [79], which is a low-fidelity model for trim flights.

3.4 Tonal Noise Prediction

The exact equations of Farassat's Formulation 1A that consist of thickness noise p'_T and loading noise p'_L are given as

$$p'(\vec{x}, t) = p'_T(\vec{x}, t) + p'_L(\vec{x}, t) \tag{3.21}$$

$$\begin{aligned}
4\pi p'_T(\vec{x}, t) &= \int_{f=0} \left[\frac{\rho_0(\dot{v}_n + v_{\dot{n}})}{r_0|1 - M_r|^2} \right]_{ret} dS \\
&+ \int_{f=0} \left[\frac{\rho_0 v_n (r_0 \dot{M}_r + c(M_r - M^2))}{r_0^2 |1 - M_r|^3} \right]_{ret} dS
\end{aligned} \tag{3.22}$$

$$\begin{aligned}
4\pi p'_L(\vec{x}, t) &= \frac{1}{c} \int_{f=0} \left[\frac{\dot{l}_r}{r_0 |1 - M_r|^2} \right]_{ret} dS \\
&+ \int_{f=0} \left[\frac{l_r - l_M}{r_0^2 |1 - M_r|^2} \right]_{ret} dS \\
&+ \frac{1}{c} \int_{f=0} \left[\frac{l_r (r_0 \dot{M}_r + c(M_r - M^2))}{r_0^2 |1 - M_r|^3} \right]_{ret} dS
\end{aligned} \tag{3.23}$$

The acoustics software PSU-WOPWOP [54] will be used to predict the compact loading noise and compact thickness noise. The blade local loading l that is integrated along the chord, which is a function of the blade radial location and the azimuth angle, is calculated by the blade element theory (BET) for the trimmed forward flight condition using the dynamic inflow model described in the previous section. The azimuthally varying loading yields the unsteady loading derivative, \dot{l} , at each time step. To calculate the thickness noise, the dual-compact thickness noise formulation [121] is used. The loading noise term shown in Eq. (3.23) can be used to calculate the thickness noise by integrating the constant loading ($\rho_0 c_0^2$) on two lines that represent a rotor blade [121]. This approach essentially follows the Isom's thickness noise computation [122]. This dual-compact thickness noise formulation was implemented in PSU-WOPWOP [54], where rotor thickness noise can be calculated given the blade motion, airfoil shape, and radial location. Therefore, rotor thickness noise is conveniently predicted without calculating the blade surface integral.

3.5 Rotor Broadband Noise Predictions in Forward Flight

Obtained from the trimmed rotor forward flight analysis, the time-dependent blade local velocity $U_\infty(r_1, \psi, q)$ and angle of attack $AoA(r_1, \psi, q)$ are the inputs to UCD-QuietFly, where r_1 is the blade radial position, ψ is the azimuth angle, and q is the blade index.

The source time τ of each blade section is associated with the angular velocity Ω and azimuthal angle ψ by

$$\tau = \frac{\psi}{\Omega} \quad (3.24)$$

At the given source time and location, the observer time and location are obtained in the following equation

$$t - \frac{|\vec{x}(t) - \vec{y}(\tau)|}{c} - \tau = 0 \quad (3.25)$$

where $\vec{x}(t)$ is the observer coordinate at the observer time t , and $\vec{y}(\tau)$ is the blade section coordinate at the source time τ . A schematic of a two-bladed rotor in forward flight and a moving observer with the same forward velocity are shown in Fig. 3.6.

According to Fig. 3.6, the distance of $|\vec{x}(t) - \vec{y}(\tau)|$ required in Eq. (3.25) is calculated as

$$|\vec{x}(t) - \vec{y}(\tau)| = \sqrt{[(X_2 - r_1 \cos \psi \cos \alpha_{sh}) + V_\infty(t - \tau)]^2 + [Y_2 - r_1 \sin \psi \cos \alpha_{sh}]^2 + [Z_2 - r_1 \cos \psi \sin \alpha_{sh}]^2} \quad (3.26)$$

where ψ and α_{sh} are the rotor azimuth angle and shaft angle of attack, respectively.

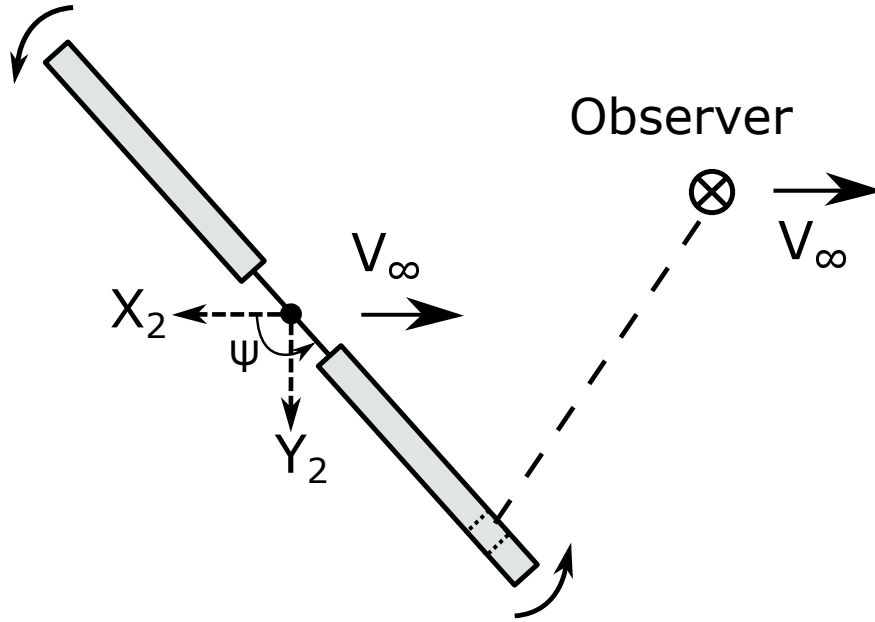


Figure 3.6: Top view of a two-bladed rotor in forward flight.

To calculate the observer time of each blade section, the quadratic equation shown in Eq. (3.25) is solved using the Newton-Raphson root finding method. Although Eq. (3.25) can be applicable to a stationary or arbitrarily moving observer, we use an observer that moves along with the vehicle throughout Chapter 7.

The broadband noise of each blade section is calculated in terms of the sound pressure level $SPL(f, \tau)$ at the source time (τ), and the sound pressure level $SPL(f, t)$ at the observer time is saved at the observer time (t), which is found in Eq. (3.25). This observer time would be different at each blade section. After the calculations of SPL at every time step and blade section, the sound pressure levels at the same observer time t are interpolated and summed to have total broadband noise. As a result, we obtain broadband noise as a function of the observer time, which is necessary to evaluate amplitude modulation of noise and psychoacoustic metrics.

3.6 Psychoacoustic Metrics

A time variation of broadband noise causes the fluctuations of noise amplitude, which affect the subjective human annoyance. Understanding and quantifying subjective annoyance is important for designing a new low-noise helicopter. In order to assess the annoyance levels, we use two psychoacoustic metrics: fluctuation strength and roughness. Based on the psychoacoustic models developed by Fastl and Zwicker [123], the noise fluctuations with the modulation frequency under 20 Hz are categorized as the amplitude modulations, while the fluctuations with the modulation frequency over 20 Hz are categorized as roughness.

The fluctuation strength is calculated using Eq. (3.27).

$$\mathbf{F} = \frac{5.8(1.25m - 0.25)[0.05(L_{BBN}) - 1]}{(f_{mod}/5)^2 + (4/f_{mod}) + 1.5} \text{ vacil} \quad (3.27)$$

where L_{BBN} is the broadband noise overall sound pressure level (OASPL), f_{mod} is the modulation frequency in Hertz, and m is the modulation factor determined from the overall modulation depth, or the peak-to-peak amplitude, $\Delta L = 20 \log[(1 + m)/(1 - m)]$. The modulation frequency is taken as the blade passing frequency. When the modulation depth is less than 3.52 dB, the fluctuation strength \mathbf{F} becomes negative and negligible.

The roughness is calculated using Eq. (3.28).

$$\mathbf{R} = 0.3 \frac{f_{mod}}{1000} \int_0^{24 \text{Barks}} \Delta L_E(z) dz \text{ asper} \quad (3.28)$$

where $\Delta L_E(z)$ is the specific modulation depth at the z_{th} critical band, which is integrated on the 24 bands (Barks) of the frequency spectrum. In the current study, the critical bands

are approximated by the one-third-octave bands.

3.7 Broadband Noise Predictions of Small-Scale Rotors

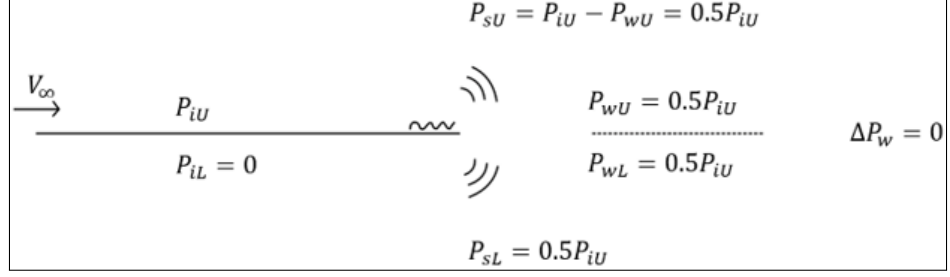
Roger and Moreau’s trailing-edge noise model [84] reads

$$S_{pp}(\vec{x}, \omega) = \left(\frac{kcZ}{4\pi S_0^2} \right)^2 2\Delta r |\mathbf{L}|^2 \Phi_{pp}(\omega) l_y(\omega) \quad (3.29)$$

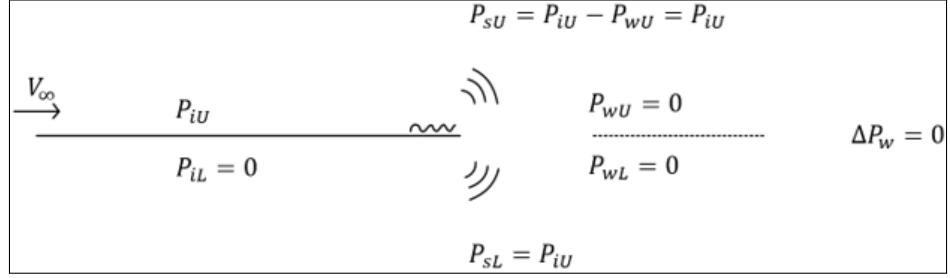
where $S_0^2 = X^2 + \beta^2 (Y^2 + Z^2)$, $\beta^2 = 1 - M^2$, k is the acoustic wavenumber, c is the chord length, Δr is the blade sectional span, L is the loading term, l_y is the spanwise turbulence correction length, and Φ_{pp} is the wall pressure spectrum [36]. The X, Y, Z coordinates are shown in Fig. 2.4

Note that Eq. (3.29) is four times in magnitude of the original Amiet model [28, 114]. While the original Amiet model assumes the zero pressure jump at the trailing edge, Roger and Moreau [86] assumed zero pressure, which makes the scattered pressure twice of the incident pressure. As a different explanation, the scattering from one surface influences both the upper and lower surfaces. The remaining factor of two comes from the expected value of the complex conjugates. This updated trailing-edge noise model raises the noise levels by 6 dB and was shown to provide improved agreement with experiments [71]. The flow field of this modification is sketched in Fig. 3.7.

The loading term L includes the contributions from the trailing-edge scattering L_1 and the leading-edge back-scattering L_2 , such that $L = L_1 + L_2$. In Roger and Moreau’s formulations [84, 86], the entire trailing-edge scattering term L_1 was multiplied by a factor of four,



(a)



(b)

Figure 3.7: Incident and scattered pressure field theories in (a) original Amiet's model [28] and (b) Roger and Moreau's modification [84].

including the incident field and the scattered field. However, the incident field should not be affected by the factor of four since the incident field is not affected by the trailing edge boundary condition or the Kutta condition. Thus, we propose a slight modification in Eq. (3.30), where the last term accounts for the incident field.

$$L_1 = -\frac{e^{2iC}}{iC} \left\{ (1+i)e^{-2iC} \sqrt{\frac{B}{B-C}} E^*[2(B-C)] - (1+i)E^*[2B] + 1 - e^{-2iC} + \frac{e^{-2iC}}{4} \right\} \quad (3.30)$$

$$B = \bar{K}_x + M\bar{\mu} + \bar{\kappa} \quad (3.31)$$

$$C = \bar{K}_x - \bar{\mu}(X/S_0 - M) \quad (3.32)$$

Small-scale rotors have small chord lengths that result in the small reduced wavenumber kc , where the leading-edge back-scattering L_2 can be important at low frequencies. The Roger and Moreau's leading-edge back-scattering correction [84] reads

$$\begin{aligned} \frac{1}{H}L_2 = & \left\{ e^{4i\bar{\kappa}}[1 - (1+i)E^*(4\bar{\kappa})] \right\}^c - e^{2iD} \\ & + i[D + k_x^* + M\bar{\mu} - \bar{\kappa}]G \end{aligned} \quad (3.33)$$

where

$$H = \frac{(1+i)e^{-4i\bar{\kappa}}(i - \Theta^2)}{2\sqrt{\pi}(\alpha - 1)k_x^*\sqrt{B}} \quad (3.34)$$

$$D = \bar{\kappa} - \bar{\mu}X/S_0; \quad \alpha = V/V_c \quad (3.35)$$

$$\Theta = \sqrt{\frac{\bar{K}_x + \bar{\mu}M + \bar{\kappa}}{k_x^* + \bar{\mu}M + \bar{\kappa}}} \quad (3.36)$$

$$\begin{aligned} G = & (1 + \epsilon)e^{i(2\bar{\kappa}+D)}\frac{\sin D - 2\bar{\kappa}}{D - 2\bar{\kappa}} + (1 - \epsilon)e^{i(-2\bar{\kappa}+D)}\frac{\sin D + 2\bar{\kappa}}{D + 2\bar{\kappa}} \\ & + \frac{(1 + \epsilon)(1 - i)}{2(D - 2\bar{\kappa})}e^{4i\bar{\kappa}}E^*(4\bar{\kappa}) - \frac{(1 - \epsilon)(1 + i)}{2(D + 2\bar{\kappa})}e^{-4i\bar{\kappa}}E^*(4\bar{\kappa}) \\ & + \frac{e^{2iD}}{2}\sqrt{\frac{2\bar{\kappa}}{D}}E^*(2D)\left[\frac{(1 + i)(1 - \epsilon)}{D + 2\bar{\kappa}} - \frac{(1 - i)(1 + \epsilon)}{D - 2\bar{\kappa}}\right] \end{aligned} \quad (3.37)$$

and the imaginary part of $\{\}^c$ in Eq. (3.33) is multiplied by $\epsilon = (\sqrt{1 + 1/(4\bar{\mu})})^{-1}$.

3.8 Predictions of Other Airfoil-Self Noise Sources

The LBL-VS equations in the BPM model [24] are implemented in UCD-QuietFly to predict vortex-shedding noise for low-Reynolds number conditions. The one-third-octave-band sound pressure level ($SPL_{1/3}$) is explicitly calculated in Eq. (3.38), where G_1 , G_2 , and G_3 are empirically determined functions of Strouhal number, Reynolds number, and angle of attack. \bar{D}_h is the directivity function in the BPM airfoil-self noise models.

$$\begin{aligned} SPL_{LBL-VS} = & 10 \log \left(\frac{\delta_p M^5 \Delta r \bar{D}_h}{r_o^2} \right) + G_1 \left(\frac{St'}{St'_{peak}} \right) \\ & + G_2 \left[\frac{R_c}{(R_c)_0} \right] + G_3(\alpha^*) \end{aligned} \quad (3.38)$$

3.9 Trailing-Edge Noise Due to Serrated Edges

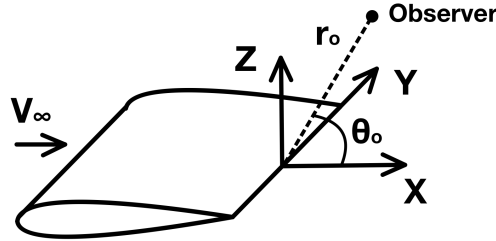


Figure 3.8: Observer distance and angle in the blade local coordinates.

For the serrated blade sections, the original Lyu and Ayton model [90] reads

$$S_{pp} \approx \frac{\bar{k}}{2\pi r_o} \sin^2 \theta_o \frac{\chi + \bar{k}}{2} \frac{1}{2(\chi - \bar{k} \cos \theta_o)^2} \sum_{n=-\infty}^{+\infty} \Pi(\omega, k_y) |E_n(\lambda)|^2 \quad (3.39)$$

where the observer location, in terms of r_o and θ_o are shown in Fig. 3.8. The observer angle, θ_o , is defined in the $X - Z$ plane, and the spanwise location is not considered in the

original model.

We propose corrections to this equation to implement Lyu and Ayton's model in rotor cases. First, the limitation of this model is the assumption of the unit span length, and the blade section span length, Δr , should be multiplied in Eq. (3.39). Second, to match the attenuation rate of the acoustic propagation, Eq. (3.39) is divided by the observer distance, r_o . Third, the effect of the spanwise observer location is included in $r_o^2 = (x/\beta)^2 + y^2 + z^2$ as well as in the spanwise wavenumber, such that $k_y = 2\pi n/l + ky/S_0$. In the original model, r_o^2 and k_y were defined as $(x/\beta)^2 + z^2$ and $2\pi n/l$, respectively [90]. Fourth, a factor of four is added to correct the scattering effect on the upper and lower surfaces, which is similar to Eq. (3.29). The new equation used in Chapter 9 is given as

$$S_{pp} \approx \frac{4\Delta r \bar{k}}{2\pi r_o^2} \sin^2 \frac{\theta_o}{2} \frac{\chi + \bar{k}}{2(\chi - \bar{k} \cos \theta_o)^2} \sum_{n=-\infty}^{+\infty} \Pi(\omega, k_y) |E_n(\lambda)|^2 \quad (3.40)$$

where the wavenumber-frequency wall pressure spectrum is

$$\Pi(\omega, k_y) = \frac{1}{\pi} \Phi_{pp}(\omega) l_y(\omega, k_y) \quad (3.41)$$

$\bar{k} = k\beta$ is the the mean-flow-corrected acoustic wavenumber; θ_o the observer angle; $\chi = \bar{k}_x\beta$ the corrected convective wavenumber; $\bar{k}_x = k_x + kM/\beta^2$ and $\lambda = (\bar{k}_x - \bar{k} \cos \theta)\bar{c}/4$ are the inputs to the radiation function $E_n(\lambda)$ [124]; $\bar{c} = 2h/\beta$ the corrected serration amplitude. Note that the fundamental mode of $n = 0$ is the most important modal term, and the effects of the higher modes appear when $k/\beta > 2n\pi$.

$$E_n(\lambda) = \int_0^1 e^{i\bar{c}F(\eta)(\bar{k}_x+\lambda)} e^{-i2\pi n\eta} d\eta \quad (3.42)$$

The radiation function of the serrated geometry is given in Eq. (3.42), where $F(\eta)$ is the non-dimensional height of the serrations, η is zero at the root and one at the tip of a blade section. We use $2h$ and l to denote the dimensional peak-to-peak amplitude of the serration and the serration wavelength, respectively, for future usages in the chapter, as shown in Fig. 3.10. This function provides the flexibility to describe arbitrary serration geometries, including a blend of straight and serrated trailing edges.

The selected trailing-edge serrated geometries are plotted in Fig. 3.9, where their corresponding equations are given in Eq. (3.43). The geometry equations describe the serration height $F(\eta)$ as a function of the η coordinate within a wavelength of l , where the origin of the $F - \eta$ coordinate is located at the lower-left corner.

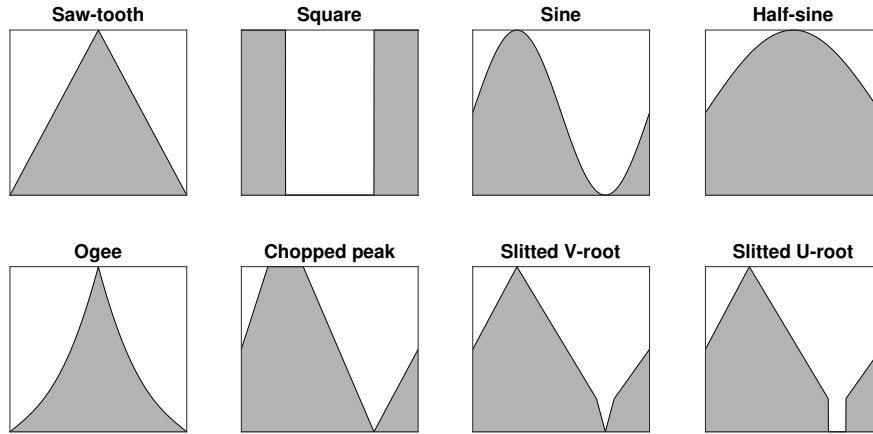


Figure 3.9: Trailing-edge serrated geometries. The $\eta - F$ serration coordinate has the origin at the lower-left corner, with the serration wavelength of l .

In UCD-QuietFly, the starting blade radial location and shape of the serration can be customized, as shown in Fig. 3.10. Although a straight blade can be calculated in Lyu and Ayton’s model, Amiet’s trailing-edge noise model is much faster when used on straight

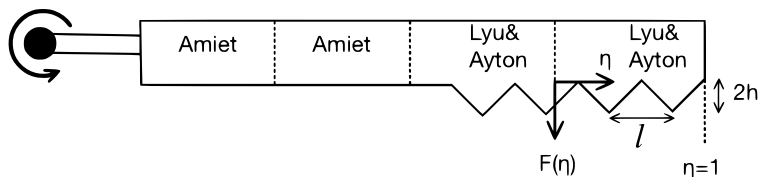


Figure 3.10: Serrated rotor blade geometry.

sections. In the current study, a rotor blade is segmented into 40 sections of equal length. The rotor design and operational parameters, such as the collective and cyclic pitch, blade twist, forward speed, multi-rotor hub locations, etc., are included in the blade section coordinate transformations [15]. For the current calculations of trailing-edge serrations in UCD-QuietFly, the serration geometries are attached to the rotor blade edges instead of cut-in.

In the current study, the boundary layer parameters are calculated using the XFOIL panel method code [35], the wall pressure spectrum near the blade trailing edge using Lee's model [36], the hovering flights using blade element momentum theory (BEMT), the forward flights using an in-house low-fidelity rotor comprehensive code [21], and trailing-edge noise using UCD-QuietFly (Refs. [15–17, 20]).

$$F_{Saw-tooth} = \begin{cases} 2\eta - 0.5, & 0 < \eta < 0.5 \\ 1.5 - 2\eta, & 0.5 < \eta < 1 \end{cases} \quad (3.43a)$$

$$F_{Square} = \begin{cases} 0.5, & 0 < \eta < 0.25 \\ -0.5, & 0.25 < \eta < 0.75 \\ 0.5, & 0.75 < \eta < 1 \end{cases} \quad (3.43b)$$

$$F_{Sine} = 0.5 \sin 2\pi\eta, \quad 0 < \eta < 1 \quad (3.43c)$$

$$F_{Half-sine} = 0.5 \sin \pi\eta, \quad 0 < \eta < 1 \quad (3.43d)$$

$$F_{Ogee} = \begin{cases} 4\eta - 0.5 - \sin \pi\eta, & 0 < \eta < 0.5 \\ 3.5 - 4\eta - \sin \pi\eta, & 0.5 < \eta < 1 \end{cases} \quad (3.43e)$$

$$F_{Chopped\ peak} = \begin{cases} 10/3\eta, & 0 < \eta < 0.15 \\ 0.5, & 0.15 < \eta < 0.35 \\ 11/8 - 5/2\eta, & 0.35 < \eta < 0.75 \\ 2\eta - 2, & 0.75 < \eta < 1 \end{cases} \quad (3.43f)$$

$$F_{Slitted\ U-root} = \begin{cases} 2\eta, & 0 < \eta < 0.25 \\ 0.94 - 1.78\eta, & 0.25 < \eta < 0.7 \\ 2.5 - 4\eta, & 0.7 < \eta < 0.75 \\ -3.5 + 4\eta, & 0.75 < \eta < 0.8 \\ -1.5 + 1.5\eta, & 0.8 < \eta < 1 \end{cases} \quad (3.43g)$$

$$F_{Slitted\ U-root} = \begin{cases} 2\eta, & 0 < \eta < 0.25 \\ 0.94 - 1.78\eta, & 0.25 < \eta < 0.7 \\ -0.5, & 0.7 < \eta < 0.8 \\ -1.5 + 1.5\eta, & 0.8 < \eta < 1 \end{cases} \quad (3.43h)$$

3.10 Airfoil-Turbulence Interaction or Leading-Edge Noise

Following the similar derivations of Amiet's trailing-edge noise model, Amiet's leading-edge noise model can be written as

$$S_{pp}(\mathbf{x}, \omega) = \left(\frac{\rho_0 k c z}{2S_0^2} \right)^2 \pi U_0 \frac{L}{2} \Phi_{ww} |L_{le}|^2 \quad (3.44)$$

where Φ_{ww} is the vertical velocity fluctuation spectrum that can be calculated in Eq. (3.45) using the empirical Von Karman isotropic turbulence model [125], with the high-frequency correction factor β_1 suggested by Moreau and Roger [126]. $\beta_1 = 8 \times 10^{-4}$ is selected for the current study.

$$\Phi_{ww} = \Phi_{ww}^{VK} e^{-\beta_1 \hat{k}_1^2} \quad (3.45)$$

The Von Karman spectrum is computed as

$$\Phi_{ww}^{VK}(k_1, k_2) = \frac{4}{9\pi} \frac{\bar{u}^2}{k_e^2} \frac{\hat{k}_1^2 + \hat{k}_2^2}{(1 + \hat{k}_1^2 + \hat{k}_2^2)^{7/3}} \quad (3.46)$$

where $\hat{k}_{1,2} = k_{1,2}/k_e$, $k_e = \sqrt{\pi}\Gamma(5/6)/\Lambda\Gamma(1/3)$. \bar{u}^2 is the mean-square turbulent velocity, and Λ is the turbulence integral scale at the blade leading edges.

The modified loading function $L_{le} = L_{le1} + L_{le2}$ for supercritical gust [127] is given as

$$L_{le1} = -\frac{1}{\pi} \sqrt{\frac{2}{(k_1^* + \beta^2 \bar{\kappa})\Theta_4}} e^{-i\Theta_2} E[2\Theta_4], \quad (3.47)$$

$$L_{le2} = \frac{e^{-i\Theta_2}}{\pi\Theta_4 \sqrt{2\pi(k_1^* + \beta^2 \bar{\kappa})}} \left\{ i(1 - e^{2i\Theta_2}) - (1 + i) \left[E(4\bar{\kappa}) - e^{2i\Theta_4} \sqrt{\frac{2\bar{\kappa}}{\bar{\kappa} + \bar{\mu}x/S_0}} E[2(\bar{\kappa} + \bar{\mu}x/S_0)] \right] \right\}, \quad (3.48)$$

where

$$\Theta_2 = \bar{\mu}(M - x/S_0) - \pi/4; \quad \Theta_4 = \bar{\kappa} - \bar{\mu}x/S_0 \quad (3.49)$$

3.11 Machine-Learning Based Rotor Noise Prediction Model

This section presents two methods to compute broadband noise quickly. First, an Artificial Neural Network (ANN) model is trained on the Google TensorFlow [118] platform, which takes a comprehensive data collection of rotorcraft broadband noise with the selected labels. These labels are the fundamental rotorcraft parameters, such as the rotor tip Mach number, in the ANN model that can affect the target outputs. The second method involves the linear regression of the selected variables on the noise data. Both methods require a large amount of noise data as functions of rotorcraft design and operating parameters relevant to the broadband noise. Therefore, an inexpensive computational method is important to obtain the noise data.

The dominant factors of rotor broadband noise have been shown to be the rotor rotational speed, collective pitch angle, blade twist, rotor solidity, and rotor radius [15]; hence, these five variables are chosen in Chapter 10 to construct the models using machine learning ANN or linear regression. Two data sets are obtained for overall sound pressure level (OASPL) and narrow-band sound pressure level (SPL), where OASPL is a function of the five selected rotor parameters and SPL is a function of the five parameters as well as frequency. Based on the data sets, the fast-predicting models are trained using each data-driven method.

From UCD-QuietFly, the OASPL and SPL are predicted at each combination of the parameters. Table 3.1 shows the starting and ending values of the five selected variables, and each variable has four points in its range. The frequency range for the SPL is from 0.1 to 10 kHz. Other rotor operating conditions are also shown in Table 3.1. Specifically, the

five parameters are analyzed in UCD-QuietFly for all the possible combinations, which are $4^5 = 1024$ points in total. This data set was used to train both the ANN model and the linear regression model.

For the ANN model, two important characteristics determining the accuracy of the trained model are the data size and the number of epochs. The data size is varied by changing the number of points between the starting and ending value of each rotor parameter, and the number of epochs is varied by changing the number of internal iterations in the ANN training process. Theoretically, a larger data size and a larger number of epochs will give more accurate trained models but consume more computational time. Therefore, convergence studies are performed to determine the improvement of the model’s accuracy with the increasing number of data points and the number of epochs, respectively, to determine the optimum data size and an optimum number of epochs. We use three-layer ANN model; each of the first two layers has 64 nodes and the third layer has one node since the output is a scalar value, the OASPL or the SPL. The configuration of the ANN model is shown in Fig. 3.11. Among the total data of 1024 points, 80% are used to train the model, and 20% are used to validate the trained model. The training process is repeated at each epoch until the training error and validation error converge.

Table 3.1: Variables and Constants

Variable	Start	End	Constant	Value
M_{tip}	0.2	0.7	Number of rotors	1
θ_0 (deg)	10	17	Number of blades	2
θ (deg)	-13	-4	Airfoil	NACA0012
σ	0.0507	0.1200	Observer distance	2R
R (m)	1.9	7.0	Elevation angle	-90°

The trained ANN model is capable of providing fast predictions of the rotorcraft broad-

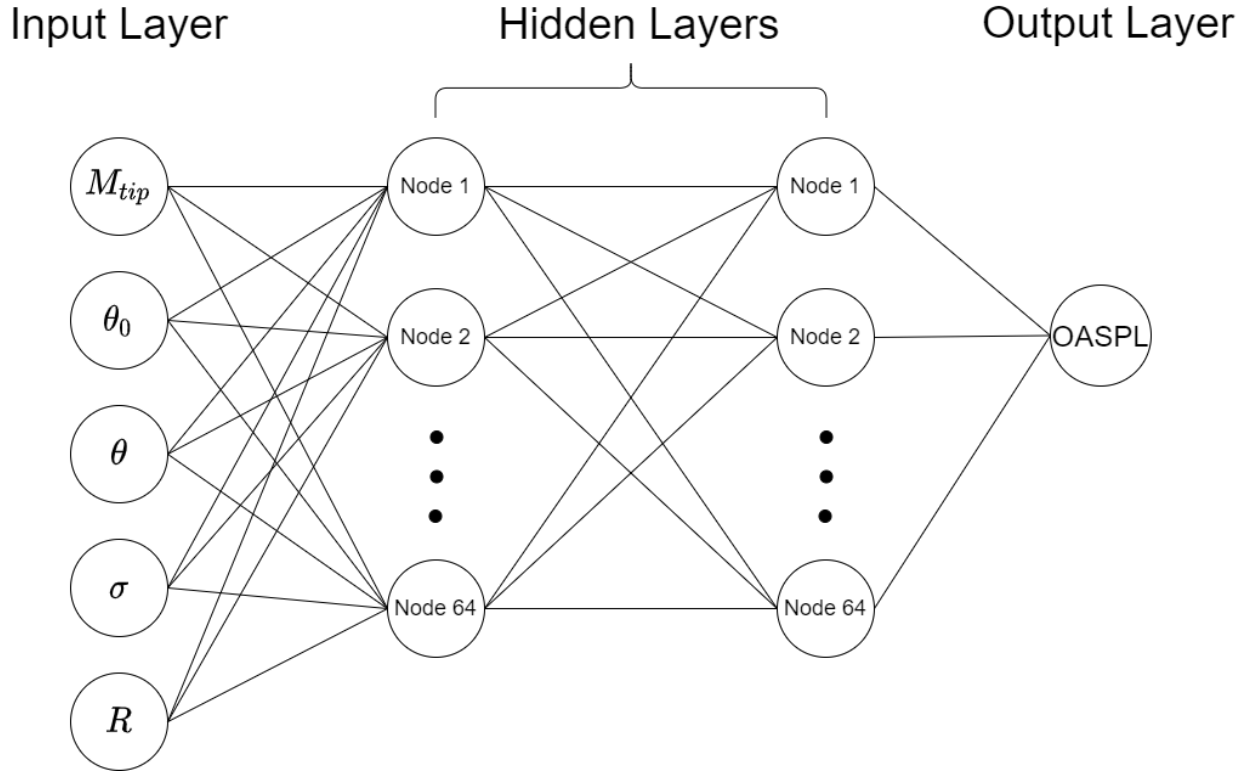


Figure 3.11: ANN model configuration.

band noise, but the model involves many internally associated nodes and activation functions, on which extracting an equation is not feasible. Therefore, the second method of linear regression is performed to obtain a polynomial formula of rotorcraft broadband noise as a function of the five variables. The 1024-point data set introduced above is used in the linear regression. The target polynomial equation forms are shown in Eq. (3.50) and Eq. (3.51), where M_{tip} , θ_0 , σ , θ , and R are the tip Mach number, collective pitch angle, rotor solidity, blade twist, and rotor radius. The difference between these two equations is that the SPL equation has an additional variable of frequency, and the different coefficients are expected. It should be noted that interactions between parameters are not considered so that the model may not be perfect. The constants α 's and β 's are the coefficients to be determined in the linear regression. As a result of the linear regression, the p-value of each coefficient, which

indicates the significance of the corresponding term in the polynomial equation, is obtained to eliminate the negligible terms. Since the linear regression model is intended to be easy to use, it takes the simplification that the variables are linearly associated with the OASPL the SPL.

$$\text{OASPL} = \alpha_1 + \alpha_2 M_{tip} + \alpha_3 \theta_0 + \alpha_4 \theta + \alpha_5 \sigma + \alpha_6 R + \alpha_7 M_{tip}^2 + \alpha_8 \theta_0^2 + \alpha_9 \theta^2 + \alpha_{10} \sigma^2 + \alpha_{11} R^2 \quad (3.50)$$

$$\text{SPL}(f) = \beta_1 + \beta_2 M_{tip} + \beta_3 \theta_0 + \beta_4 \theta + \beta_5 \sigma + \beta_6 R + \beta_7 f + \beta_8 M_{tip}^2 + \beta_9 \theta_0^2 + \beta_{10} \theta^2 + \beta_{11} f^2 + \beta_{12} \sigma^2 + \beta_{13} R^2 \quad (3.51)$$

For both the ANN model and the linear regression models, the observer location is kept at one rotor diameter and -90° elevation angle, which is denoted as a reference position. Note that the noise level at other locations can be easily obtained based on the noise level at the reference position using a semi-analytical formula [15], as shown in Eq. (3.52), where $\text{OASPL}_{\text{ref}}$ is the OASPL at one rotor diameter with a -90° elevation angle, ϕ is the observer elevation angle, R_0 is the observer distance, and d is the rotor diameter.

$$\text{OASPL} = (\sin^{0.0209} |\phi|) \text{OASPL}_{\text{ref}} - [18.2429 + 6.7267 (1 - \sin |\phi|)] \log \left(\frac{R_0}{d} \right) \quad (3.52)$$

Chapter 4

Validations of Rotorcraft Noise Predictions

This chapter first shows the validations of airfoil trailing-edge noise predictions to demonstrate the accuracy of the numerical method on the airfoil sections. Second, two experimental cases of hovering helicopters are used to demonstrate the validity of UCD-QuietFly. Third, broadband noise of the mid- and small-scale rotors in hovering and forward flights is predicted and validated against the experimental data. Forth, rotor forward-flight inflow distributions are validated on two rotors, and tonal noise predictions are validated in forward flights. Fifth, the predictions of turbulence-ingestion noise on an airfoil section are validated.

The computational time to obtain the hovering noise level for one observer is 65 seconds on a personal desktop computer with an Intel i7-9700 Processor, 8 cores and 16 GB RAM.

4.1 Airfoil Sections

4.1.1 Case 1: BANC case airfoil section

Airfoil trailing-edge noise is predicted and compared with the measurement, which was reported in Benchmark Problems for Airframe Noise Computations (BANC) [128]. Table 4.1

describes the airfoil test conditions. For this airfoil validation case, the turbulence convective velocity $U_c = 0.7U_\infty$ and spanwise turbulence lengthscale $l_r = 1.0U_c/\omega$ are used [129].

Table 4.1: Conditions of airfoil section validations.

Airfoil Section Case	Case 1	Case 2
Experiment	Ref. 128	Ref. 130
Airfoil	NACA0012	NACA0012
Chord Length (m)	0.4	0.61
Span (m)	1.0	0.46
(X, Y, Z) (m)	(0.0, 0.0, 1.0)	(0.0, 0.0, 1.2)
Transition ¹	S ² : 0.06, P ² :0.07	Natural
U_∞ (m/s)	53.0	69.5/38.6
Angle of Attack (deg)	6.0	0.0

¹Fixed Transition Position (x/c); ²S: Suction Side, P: Pressure Side

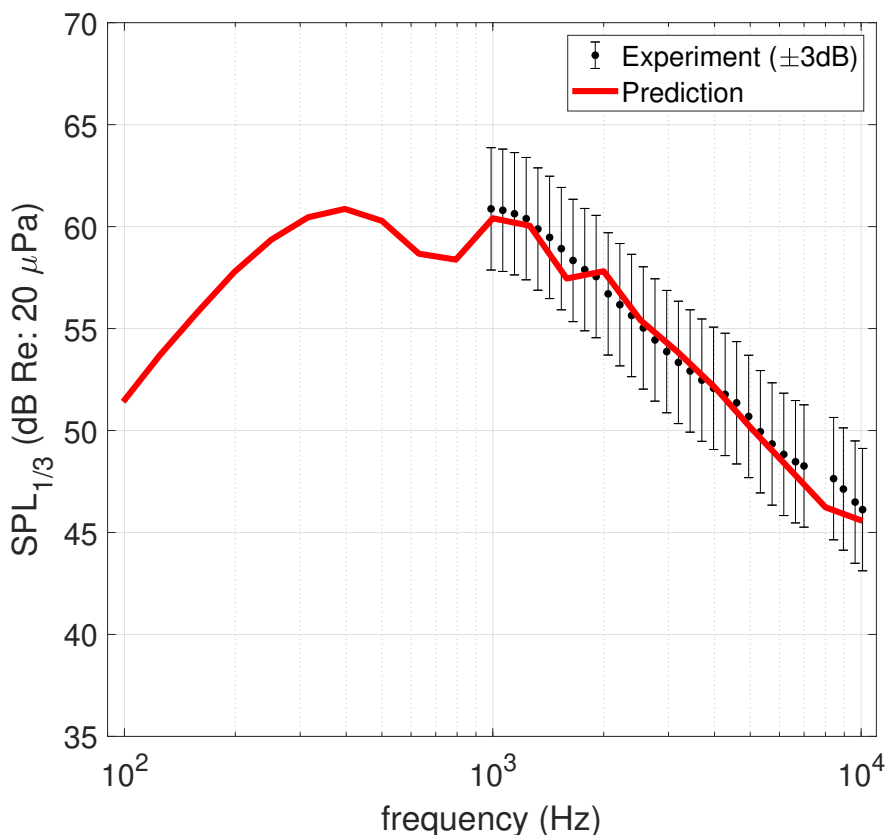


Figure 4.1: Validation of airfoil trailing-edge noise prediction against measurement [128].

One-third octave band sound pressure levels (SPLs) of airfoil trailing-edge noise prediction and the measurement are presented in Fig. 4.1 in which error bars of $\pm 3\text{dB}$ are included.

The prediction has a good match with the measurement at an entire frequency range, which demonstrates the validity of the numerical approach involving the boundary-layer flow parameters from XFOIL, Lee’s wall pressure spectrum model in Eq. (3.10), and the Amiet model in Eq. (3.1).

4.1.2 Case 2: NACA0012 airfoil section

The modified model of airfoil trailing-edge noise, as shown in Eq. (3.29), is first validated against the airfoil-self noise experiments [130] shown in Fig. 4.2. The tested blade section has a NACA0012 airfoil, with a chord length of 0.61 m, a span of 0.46 m, an observer distance of 1.2 m, and an observer angle of 90° directly above the airfoil section. The predictions agree well with the experiments for the entire frequency range, and the effect of flow speed is captured. It is seen that the modified scattering factor [84] and the corrected incident field suggested in this dissertation give excellent trailing-edge noise predictions on various flow speeds. With the modified theories validated in this 2-dimensional flow case, the following sections will present the validations of broadband noise predictions on various small-scale rotors in hovering and forward flight conditions.

4.2 Full-Scale Helicopter Rotors

4.2.1 Case 1: Leverton full-scale model rotor

In Table 4.2, the helicopter configuration in the experiment conducted by Johnson and Katz [131] is shown, where the observer is 5 rotor diameters from the hub with an elevation angle of $\Psi = 26.7^\circ$. In the experiment, a UH-1B helicopter was used.

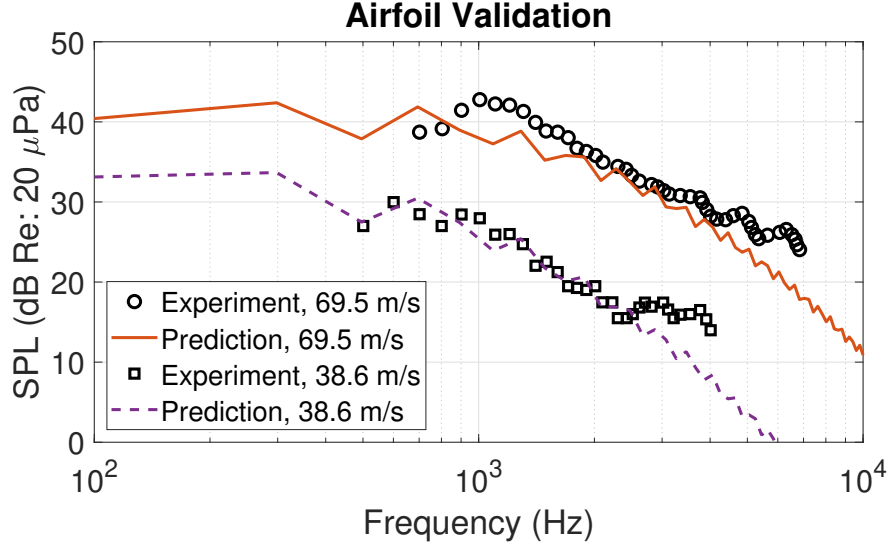


Figure 4.2: Predictions of airfoil trailing-edge noise using the current model compared to the experimental data in Ref. 130.

Table 4.2: Conditions of Helicopter Rotor validations.

Rotor Case	Case 1	Case 2
Experiment	Ref. [131]	Ref. [132]
Radius (m)	6.7056	8.5
Airfoil	NACA0012	NACA0012
Number of Blade	2	2
Linear Twist (deg)	-10	-8
Solidity	0.0506	0.0312
(X_1, Y_1, Z_1) (m)	(60.69, 0, -30.48)	(19.7, 0, -73.6)
(R_o, Ψ) (m, deg)	(67.91, -26.7)	(76.19, 75)
C_T	0.0036	0.002
M_{tip}	0.67	0.47

The UCD-QuietFly prediction of the Johnson case is presented in Fig. 4.3 along with the measurement and the prediction by Kim and George [31]. The results show that UCD-QuietFly has a good match with the measurement in the mid- and high-frequency range in which trailing-edge noise is expected to be the dominant noise source. In addition, Fig. 4.3 shows that UCD-QuietFly is more accurate than Kim and George’s prediction for the entire frequency range.

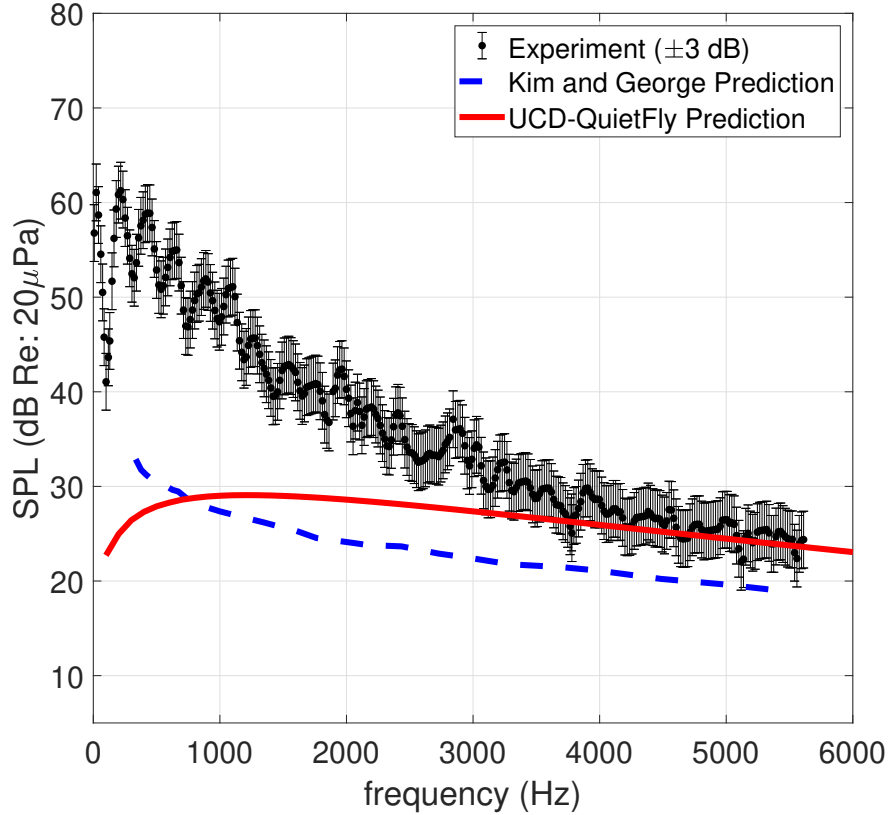


Figure 4.3: Comparison of UCD-QuietFly prediction with measurement by Johnson and Katz [131] and prediction by Kim and George [31]

4.2.2 Case 2: UH-1B helicopter rotor

Table 4.2 includes Leverton’s [132] measured noise from a model rotor at an observer located at 4.5 rotor diameters from the hub with an elevation angle of $\Psi = 75^\circ$.

The prediction of the Leverton case is presented in Fig. 4.4. Note that the SPL in Fig. 4.4 has a constant frequency bandwidth of 100 Hz and sums the 1-Hz energy in each band. It is also shown that the prediction exhibits similar trends with the data. It is shown that the prediction is in good agreement with the data at high frequencies. The prediction does not capture the local noise maximum at 2.5-4 kHz. It is thought that this local noise maximum is generated from different noise sources such as trailing-edge bluntness noise, which can be predicted by the semi-empirical trailing-edge bluntness noise term in the BPM model

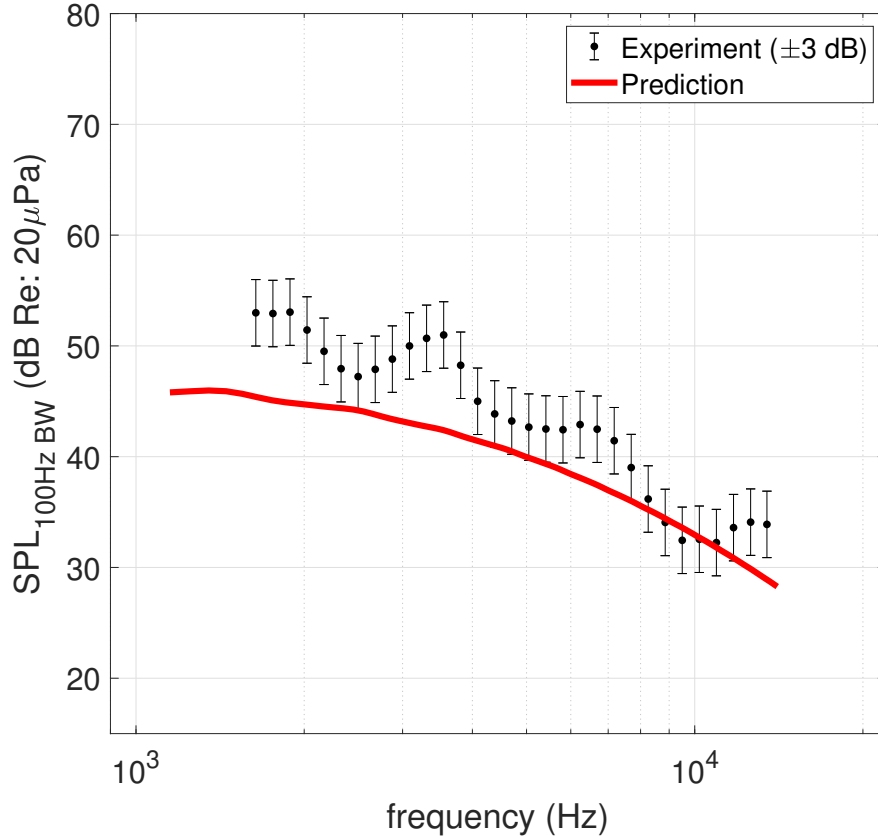


Figure 4.4: Comparison of UCD-QuietFly prediction with measurement by Leverton [132] developed by Brooks et al. [24].

4.3 Mid- and Small-Scale Rotors

4.3.1 Cases 1 and 2: APC drone rotor and BO-105 model rotor

Table 4.3: Specifications of the rotors used for UCD-QuietFly validation.

Rotor name	APC Slow Flyer 11X4.7	BO-105 40% scale
Rotor radius (m)	0.14	2.0
Number of blades	2	4
Observer distance to hub (m)	1.095	7.14
Observer elevation angle (deg)	- 45	90
Airfoil	E63(root)/ClarkY(tip)	NACA 23012

Due to the lack of noise measurements of actual VTOL vehicles with multiple rotors, the validation of UCD-QuietFly in this section is performed on a small-scale two-bladed rotor and

a mid-scale four-bladed rotor that are representations of VTOL rotors, while the validation of UCD-QuietFly on full-scale helicopters has been presented in Refs. 16 and 15. Table 4.3 shows the test conditions for the two rotors, the APC Slower Flyer 11X4.7 rotor and the 40% scale BO-105 rotor, and the predictions for the two rotors at various operating conditions are presented in Figs. 4.5. The APC rotor was tested in the NASA Langley’s Structural Acoustic Loads and Transmission (SALT) anechoic chamber by Zawodny et al. [9], who mounted the single rotor on a test stand and positioned the microphone in the acoustic far-field with an elevation angle of -45° . The acoustics measurements of the 40% scale BO-105 rotor was acquired by Brooks et al. [4] in the Duits-Nederlandse Wind Tunnel (DNW), where the model was tested in the forward and hover flights. The narrow-band spectra of both measurements [4, 9] were post-processed using the Fast Fourier Transformation (FFT). The good comparisons of UCD-QuietFly and the measurements at various speeds demonstrate the validity of UCD-QuietFly’s prediction on different scaled rotors. The predictions catch the noise spectrum from the mid- to high-frequency range, where rotor broadband noise is dominant; in Fig. 4.5(b)-(d), they also follow a trend of an increase in noise levels from low to high rotational speeds for the BO-105 rotor. In the APC rotor prediction in Fig. 4.5(a), a sharp peak in the predictions and measurements at high frequencies is attributed to the trailing-edge bluntness noise. It is expected that the predictions do not match the data at low frequencies at which other noise sources are important, including loading noise [12] and turbulence ingestion noise [4, 113]. The computational time to obtain the noise level of one rotor for one observer is 65 seconds on a personal desktop computer with an Intel i7-9700 Processor, 8 cores and 16 GB RAM.

Since UCD-QuietFly has been extensively validated on various rotor cases with different

scales [15, 16, 20, 70] in hover flights, the validation case shown in Fig. 4.5(d) is the forward flight configuration for the BO-105 40 % scale rotor. The narrow-band SPL prediction of broadband noise is compared with the wind tunnel acoustic measurements [4]. The comparison confirms that the predictions from UCD-QuietFly well capture the measured noise levels in the mid- to high-frequency range (2-15 kHz) on the noise spectrum, where airfoil-self broadband noise, such as trailing-edge noise, is dominant. The frequency range below 2 kHz is dominated by other noise sources, such as blade-wake-interaction (BWI) noise and tonal noise. While the prediction method of tonal noise is presented in the previous section, BWI noise is not included in this study.

The frequency f (in Hz) of the energetic fluctuations in the boundary layer approaching the trailing-edge scales as $f\delta^*/U_\infty = 0.06 - 0.08$ [133]. For the APC rotor, this scaling law results in 16.9 KHz using the boundary layer thickness and flow velocity at the blade tip. On a 40 % scale BO-105 rotor with the rotor radius of 2 m, this scaling law provides the peak frequency of trailing-edge noise of above 4.5 kHz based on the blade tip. This peak frequency is slightly higher than the peak frequency in Fig. 4.5(a). Although this scaling law cannot be directly used to estimate the peak frequency of rotor trailing-edge noise since rotor noise is contributed from multiple airfoil segments, it still provides a rough estimate of a frequency region of interest in terms of rotor trailing-edge noise. This frequency range is designated as mid- to high-frequency region in this section since other broadband noise, such as turbulence ingestion noise or blade-wake interaction noise, typically occurs at lower frequencies than trailing-edge noise. It is obvious this frequency region is case-dependent since the peak frequency is different based on the velocity and boundary-layer displacement thickness. In addition, the peak frequency range can also be different depending on operating

conditions. Although we do not argue that these noise sources are always the dominant sources at certain frequency ranges, their audible levels that exceeds community background noise present a clear community disturbance.

It should be noted that the narrow-band measurement data [4, 113] for the validation problems show that broadband noise is dominant at this frequency range with an absence of tonal noise so that the predicted results represent the measured airfoil-self noise very well.

4.3.2 Cases 3: NASA Ideally-Twisted rotor

Three different drone rotors are studied in UCD-QuietFly for their broadband noise. Table 4.4 shows the parameters and operating conditions of NASA ideally twisted rotor, SUI Endurance rotor, and DJI-CF rotor. The tip Mach number and Reynolds number are also given in Table 4.4, where all the rotor cases have the Reynolds numbers under 2×10^5 . Although these low Reynolds numbers suggest that laminar flows occur on the entire blade span, the rotation-induced Coriolis force [74] and the wake generated by the previous blade [6] can destabilize the boundary layers to transit to turbulent flows. However, instead of investigating the case-dependent flow transitions on the individual rotors, the research interest of this section is to explore a low-fidelity broadband noise method that can be practically generalized on small-scale rotors.

As the inputs to UCD-QuietFly, the blade radial distributions of the angle of attack and flow velocity are calculated in the blade element momentum theory (BEMT). For the ideally twisted rotor, the angle of attack and induced velocity distributions are shown in Fig. 4.6. It is seen that the induced velocity remains approximately unchanged in the radial direction

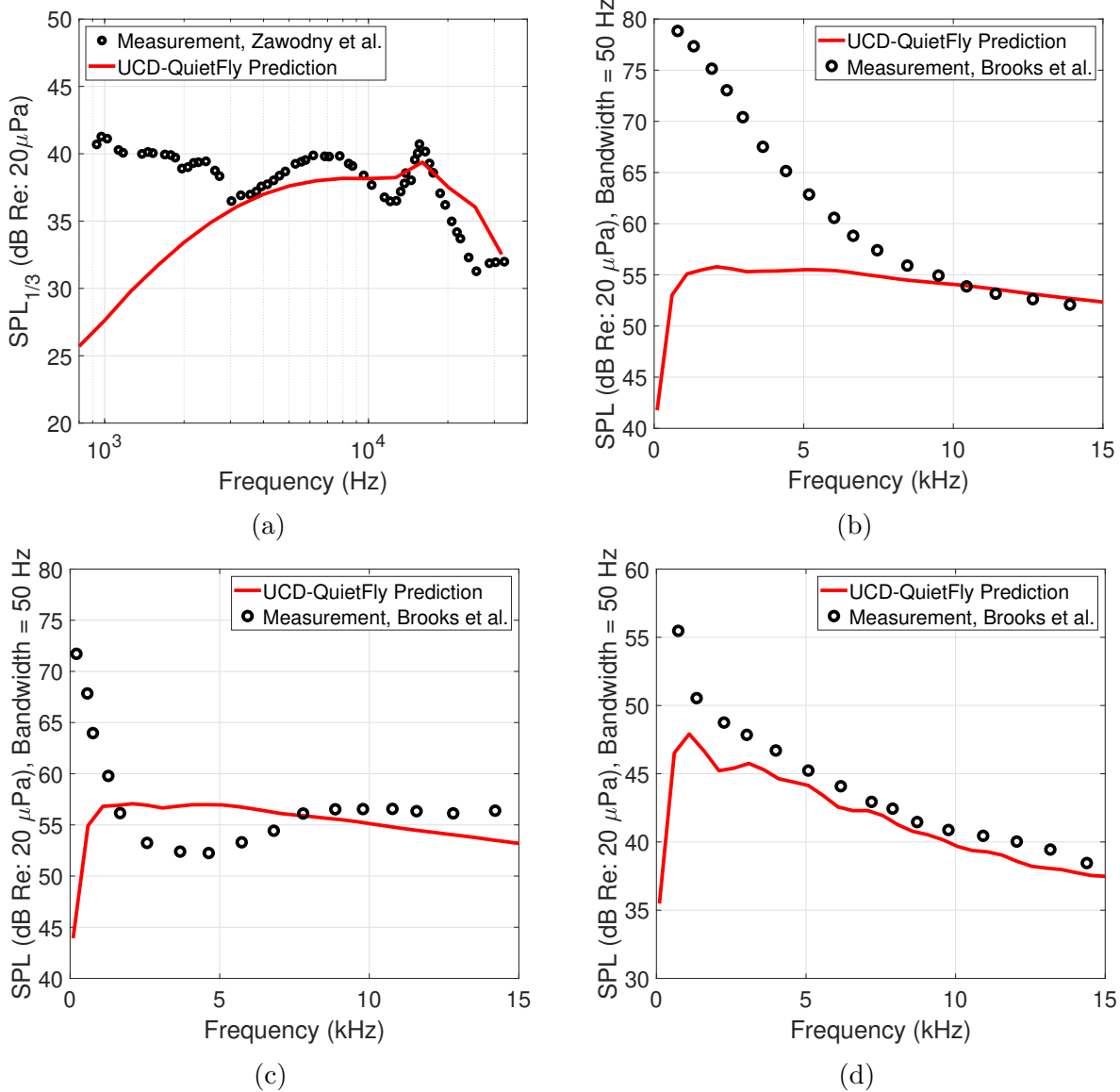


Figure 4.5: Validations of UCD-QuietFly on rotors. (a) APC Slow Flyer 11 \times 4.7, RPM=3600, $\mu = 0.0$, (b) BO-105 40% scale, RPM=1050, $\mu = 0.0$, $\alpha_{tpp} = -20^\circ$, $C_T = 0.0$, (c) BO-105 40% scale, RPM=1050, $\mu = 0.086$, $\alpha_{tpp} = -20^\circ$, $C_T = 0.0044$, and (d) BO-105 40% scale, RPM=525, $\mu = 0.173$, $\alpha_{tpp} = -10^\circ$, $C_T = 0.044$.

except for the blade tip due to the ideal twist, which is desired to yield the minimum induced power. The angle of attack decreases at the hub and tip regions due to the tip loss effect. The broadband noise predictions of an ideally twisted small-scale rotor are shown in Figs 4.7 and 4.8 for two different rotational speeds on rough blades and smooth blades. The broadband noise components are shown in the noise spectrum, including trailing-edge (TE)

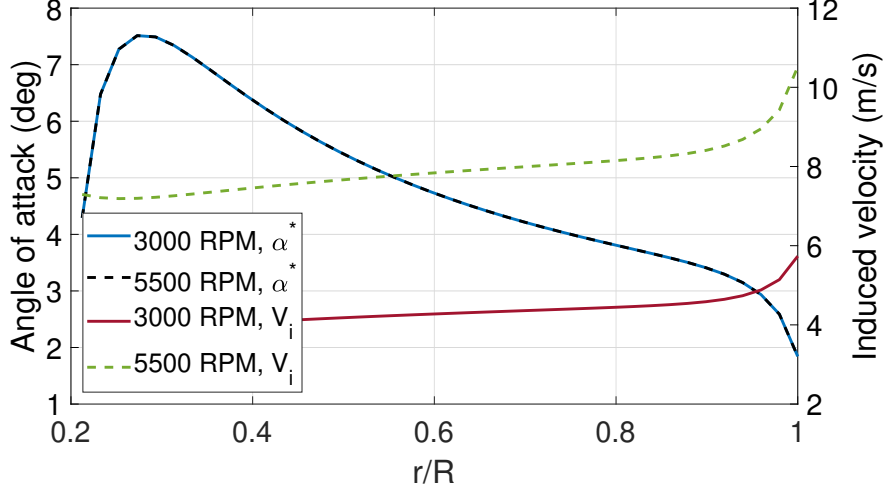


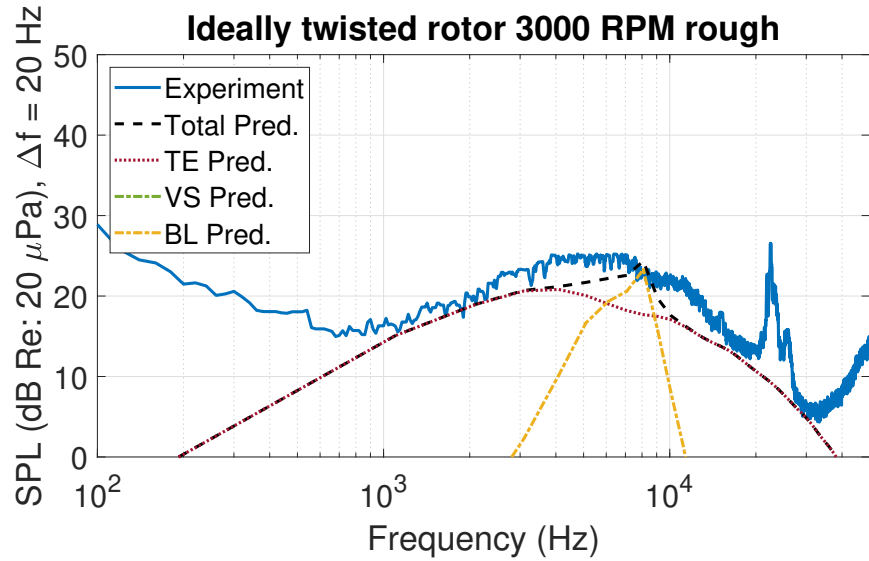
Figure 4.6: Predictions of angle of attack and induced velocity from the blade element momentum theory (BEMT) on the ideally twisted rotor.

noise, vortex-shedding (VS) noise, trailing-edge bluntness (BL) noise, and airfoil-stall (ST) noise. The measurements were taken in the Small Hover Anechoic Chamber (SHAC) at the NASA Langley Research Center [5].

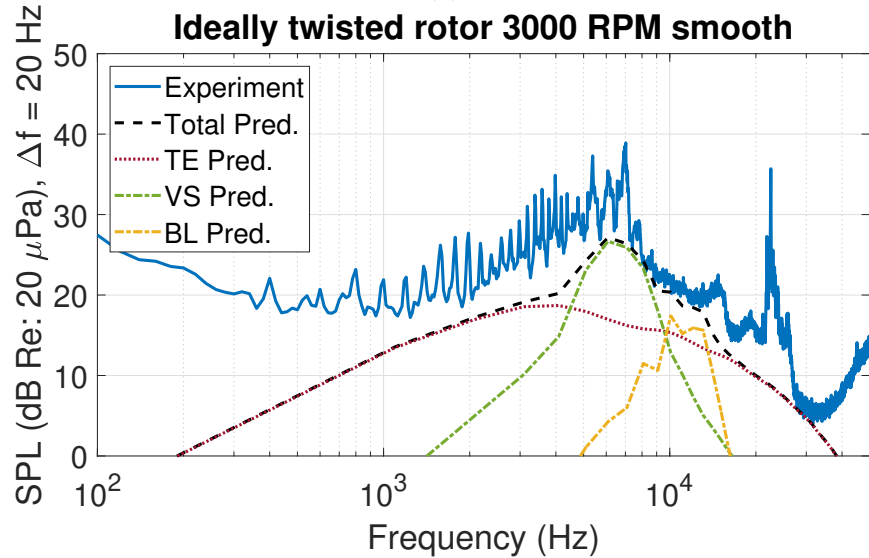
Table 4.4: Parameters of small-scale rotors

Parameters	NASA ideally twisted rotor	SUI Endurance	DJI-CF
R (m)	0.1588	0.1904	0.12
σ (m)	0.255	0.0712	0.07
N_b	4	2	2
RPM	3000/5500	4800	4800/5400/6000
Tip M	0.1467/0.2690	0.2815	0.1774/0.1996/0.2218
Tip R_c (10^5)	1.0719/1.9652	0.7227	0.4244/0.4775/0.5305
C_T	0.0137	0.01	0.009
Airfoil	NACA0012	SUI	DJI-CF
r_o (m)	2.27	5.507	1.905
ϕ_o (deg)	-35	-40	-45

For the 3000 RPM case in Fig. 4.7, the predictions have excellent agreement with the experiments above 1 kHz, in which the broadband noise sources are dominant. The rough blade has a fully turbulent flow, which is well captured by the TBL-TE noise. The smooth blade induces an LBL-VS noise peak at 7 kHz that is captured by the LBL-VS noise model



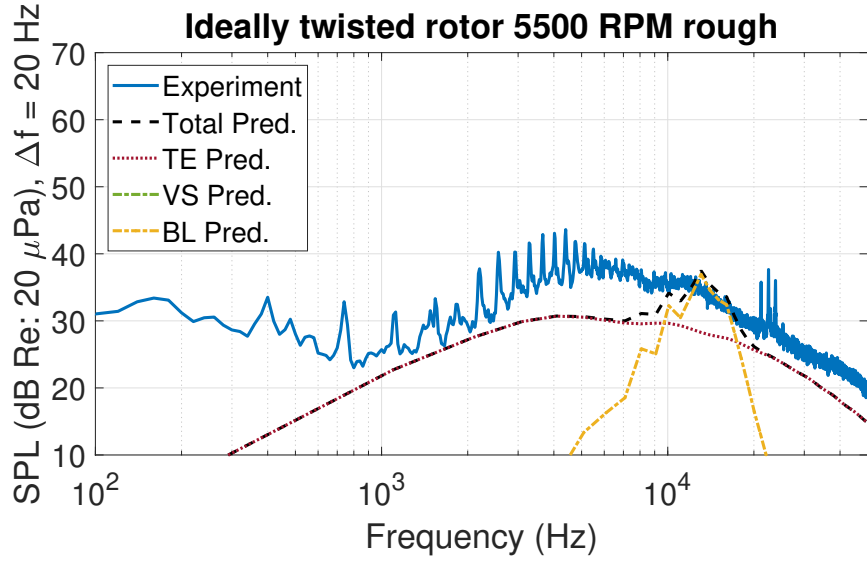
(a)



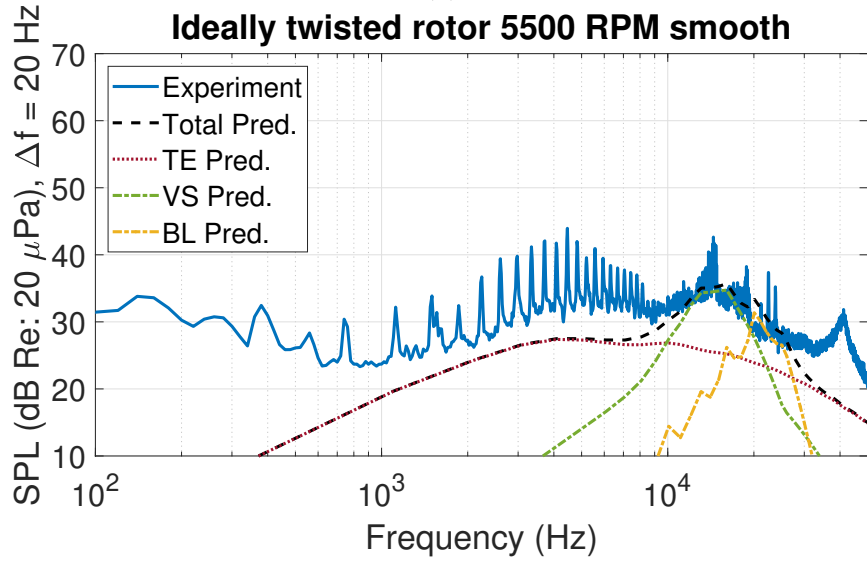
(b)

Figure 4.7: Broadband noise predictions of the ideally twisted small rotor at 3000 RPM using UCD-QuietFly for: (a) rough blade surface, and (b) smooth blade surface. The experiment data is given in Ref. 5.

in Eq. (3.38). In a higher rotational speed of 5500 RPM, the UCD-QuietFly under-predicts noise levels. However, the predictions well capture the noise increases in the entire frequency range for both the rough and the smooth blades with higher RPM. The 3000 RPM rotor has a higher noise level on the smooth blade, while the 5500 RPM rotor has a higher noise level on the rough blade. This trend is also predicted in UCD-QuietFly. Note that the LBL-VS



(a)



(b)

Figure 4.8: Broadband noise predictions of the ideally twisted small rotor at 5500 RPM using UCD-QuietFly for: (a) rough blade surface, and (b) smooth blade surface. LBL-VS noise model is limited to $R_c < 1.8 \times 10^5$. The experiment data is given in Ref. 5.

noise model in Fig. 4.8(b) is manually limited for Reynolds number under 1.8×10^5 , lower than the tip R_c in Table 4.4, to give the best prediction of LBL-VS noise level. Although this ad hoc method is impractical when measured data is not available, it is physically reasonable because flows near rotor tip regions can transit to turbulent flows at low Reynolds numbers due to Coriolis and wake effects [6, 74]. The discrepancies between the predictions and the

experiments for the ideally twisted rotor may come from the noise sources not included in our method, including blade-wake-interaction noise (broadband component below 0.6 kHz), motor noise, and tonal noise (discrete-frequency peaks).

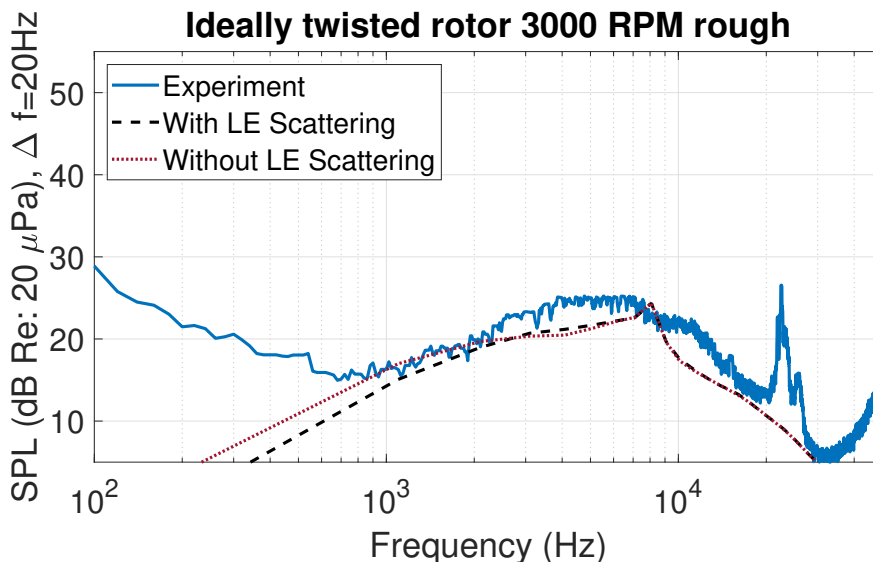


Figure 4.9: Comparisons of the effects of the leading-edge back-scattering correction. The experiment data and BPM predictions are given in Ref. 25.

The effects of the leading-edge (LE) back-scattering correction are shown in Fig. 4.9 on the ideally twisted rotor with a rough surface and 3000 RPM. It is seen that including the leading-edge scattering gives about a 3 dB difference in the predictions at the low frequencies. The leading-edge scattering effect becomes important for the frequencies below 2 kHz, corresponding to the reduced frequency of $kc = 1.17$.

4.3.3 Cases 4: SUI Endurance drone rotor

Broadband noise predictions and experimental data of SUI Endurance rotor in hovering flight are shown in Fig. 4.10. The acoustic experiment was conducted in the NASA Langley Low Speed Aeroacoustic Wind Tunnel (LSAWT)[25], and the BPM model [24] was used

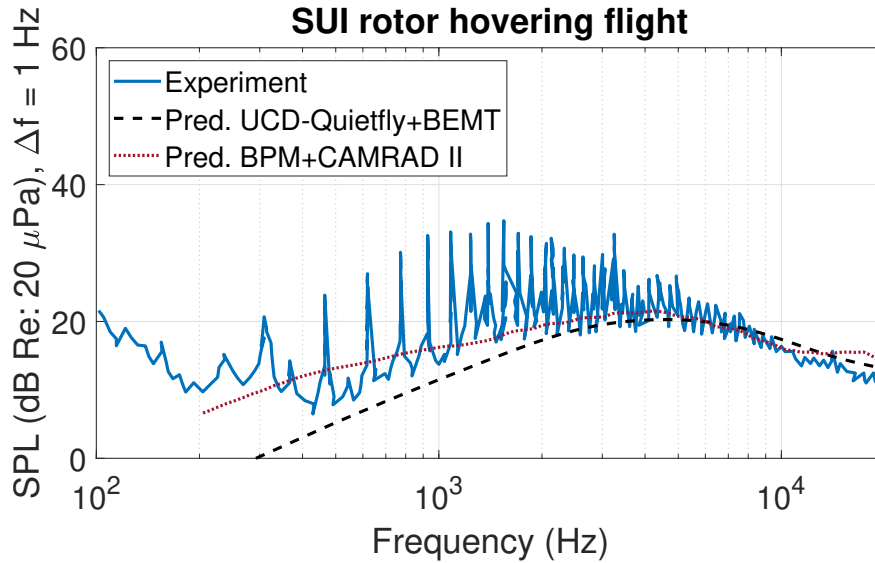


Figure 4.10: Broadband noise predictions of the SUI Endurance rotor using UCD-QuietFly. The experiment data and BPM predictions are given in Ref. 25.

with CAMRAD II [134] to obtain the BPM predictions [25]. The UCD-QuietFly predictions are obtained using the models presented in this section, with the aerodynamics predicted in the BEMT. It is seen that UCD-QuietFly gives excellent broadband noise predictions for the entire frequency range, and the peak-level frequency is captured. Note that the broadband noise in the experiments is considered to be the bottom of the data where the effect of tonal noise is removed. In other words, our predictions are targeted to reach the bottom of the test data. Although the BPM prediction shows good overall agreement with the experiment, it gives about 5 dB over-predictions (above the bottom of the data) in the frequency range below 1 kHz. Note that in the BPM model, the acoustic results are empirically tuned based on NACA 0012 experiments, while UCD-QuietFly was developed based on the wall pressure spectrum modeling and physics-based acoustic scattering process. The SUI rotor uses cambered airfoils. Therefore, the discrepancies between the BPM and UCD-QuietFly predictions are possibly due to the airfoil effects, where a different airfoil profile can significantly change the boundary layer parameters near the airfoil trailing edge

[74].

The acoustic measurements of an isolated SUI single rotor in forward flight are shown in Fig. 4.11, which is given in [25]. The predicted angle of attack and flow velocity at each blade section and each azimuthal angle are used in UCD-QuietFly to obtain the noise spectrum shown in Fig. 4.11, where time-averaging is taken in one rotor revolution. It is seen that the current models give excellent predictions in the frequency range (2-15 kHz) dominated by the airfoil-self noise sources, which covers the most sensitive range of human hearing (2-5 kHz).

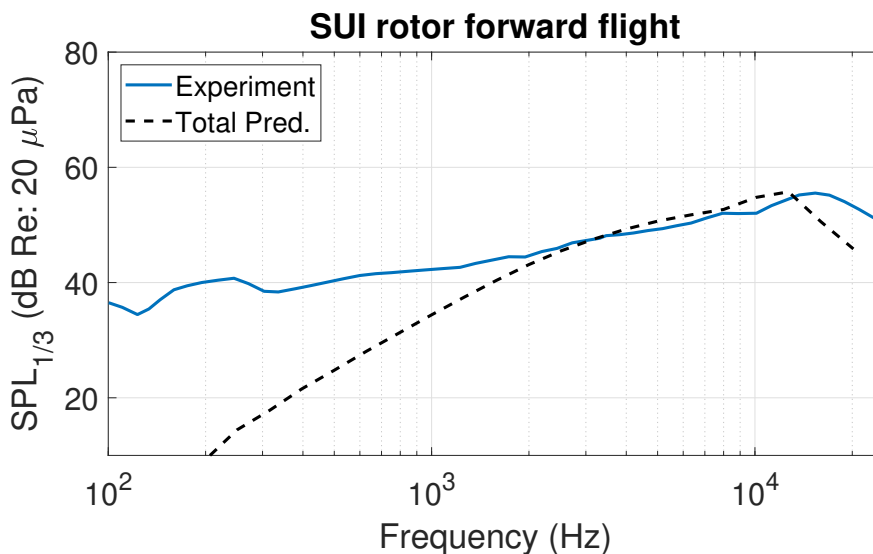
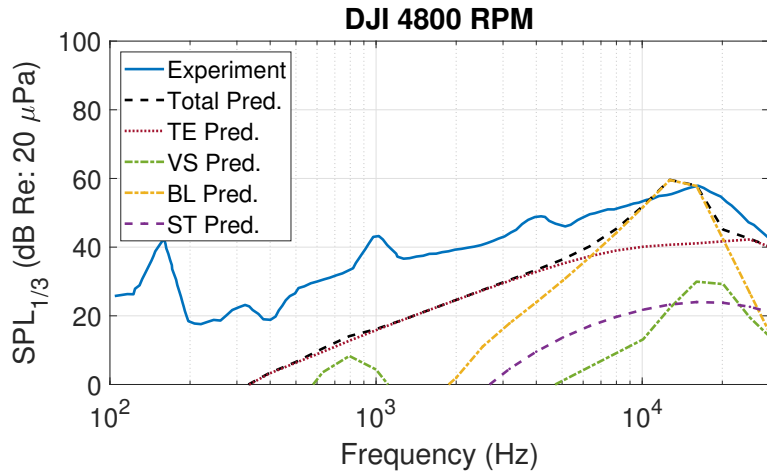


Figure 4.11: Broadband noise predictions of the SUI rotor in forward flight using UCD-QuietFly. $\alpha_{sh} = -10^\circ$, $M_\infty = 0.045$, $\phi_o = -90$, $r_o = 3.54$ m. The experiment data is given in Ref. 25.

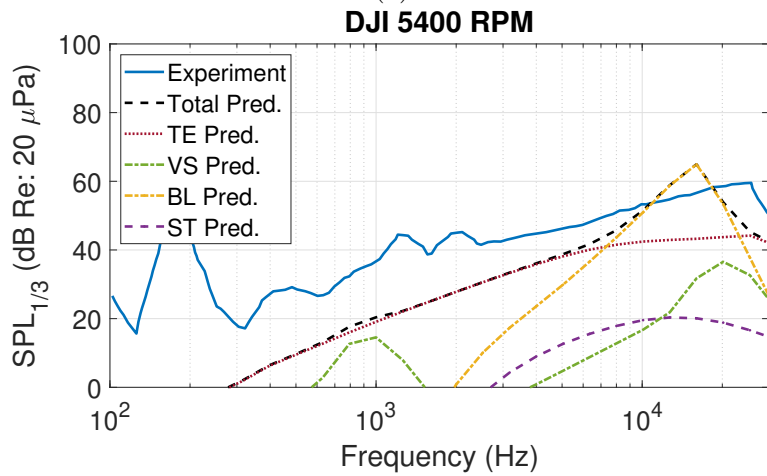
4.3.4 Cases 5: DJI-CF rotor

Figure 4.12 shows the broadband noise validations of the DJI rotor in three rotational speeds. The angle of attack and the flow speed at each blade section are calculated using the BEMT, and the broadband noise components are predicted in UCD-QuietFly. The experimental data

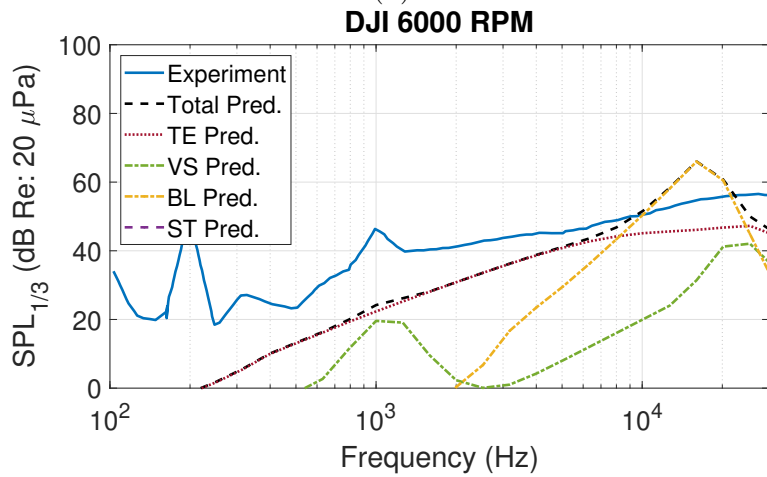
were measured in the Structural Acoustic Loads and Transmission (SALT) anechoic chamber facility at the NASA Langley Research Center [9]. The noise peaks levels are captured by the trailing-edge bluntness noise predictions. The predictions show good agreement with the experiments at 6000 RPM, but worse agreements at 4800 RPM and 5400 RPM. The predicted noise level increases with increasing rotational speed. However, the broadband components of the measured data remain the same at different RPMs, which might be due to the aeroelastic deflections of the rotor blades [9]. Therefore, the comparisons between the predictions and the experiments at different RPMs suggest that aeroelastic effects can be important in rotor broadband noise predictions and should be investigated in the future.



(a)



(b)



(c)

Figure 4.12: Broadband noise predictions of the DJI-CF rotor using UCD-QuietFly at the rotational speeds of (a) 4800 RPM, (b) 5400 RPM, and (c) 6000 RPM. The experiment data is given in Ref. 9.

The predictions from UCD-QuietFly agree well with the experiments in various small-scale rotor conditions. Laminar boundary layer-vortex shedding (LBL-VS) noise is shown to be an important broadband noise source for untripped small-scale rotors. The current LBL-VS noise calculation in the BPM model requires an ad hoc adjustment of the Reynolds number limit, which is impractical without experimental data. Future efforts are needed to develop more robust LBL-VS noise predictions. The effect of leading-edge back-scattering is important when the reduced frequency (kc) is below 1.17, and this effect should be included for the broadband noise predictions on small-scale rotors.

4.4 Rotor Inflow Distribution

4.4.1 Case 1: 2MRTS rotor

Figure 4.13 shows the validation of the inflow on the rotor disk in forward flight for a 2MRTS rotor using the Peters-He model [78]. The prediction is validated against the inflow measured by the laser velocimeter [135]. It is shown that the predicted inflow distribution agrees well with the measurement, especially on the blade tip sections that significantly contribute to broadband noise. The validation of the inflow distribution is also important for tonal noise predictions since the inflow velocity determines the local angle of attack, which provides the blade sectional loading from the 2-D airfoil aerodynamics.

The inflow predictions at the hub region shows some discrepancies to the experiment, but due to the low speed and lower loading, the inboard sections are considered less important to tonal noise and broadband noise. The discrepancies at the hub region are mainly due to the flow separation and reverse flow on the retreating blade's inboard sections. More validations

of the current model can be found in Ref. 21. At the tip region, which is important in tonal and broadband noise, the predictions show good agreement with the experimental data.

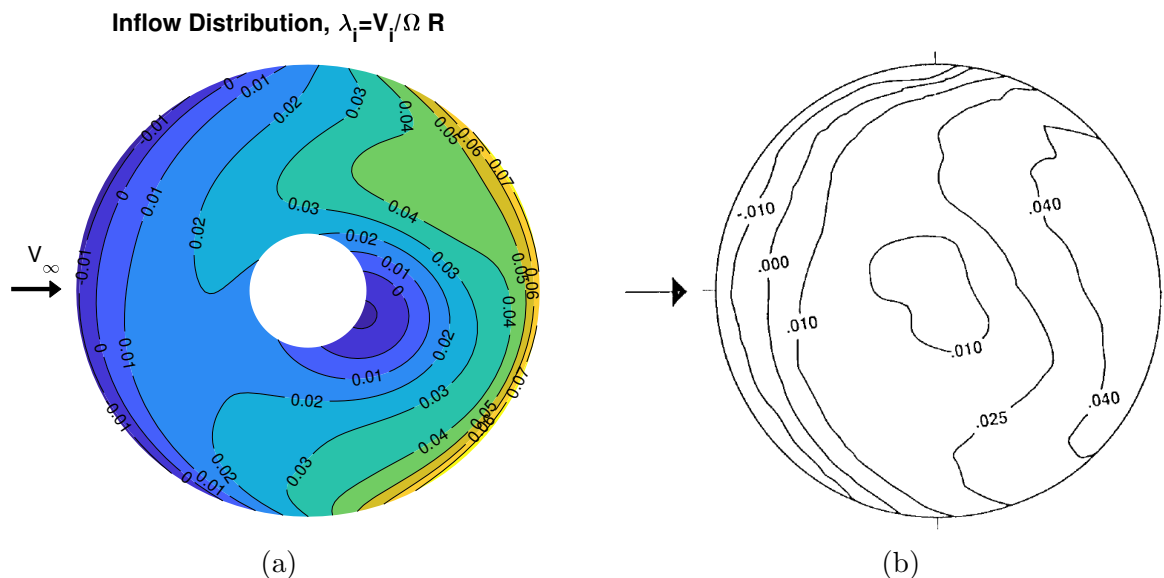


Figure 4.13: Validation of rotorcraft forward flight inflow distributions on 2MRTS rotor at $\mu = 0.15$: (a) prediction, and (b) measurement [78, 135].

4.4.2 Case 2: SUI Endurance drone rotor

This section presents the validations of rotor broadband noise predictions on a small-scale SUI Endurance rotor in forward flight. The rotor parameters are shown in Table 4.4, with rotor forward Mach number of 0.045 and shaft angle of attack of -10° . The SUI rotor forward flight analysis is carried out using an in-house BET code [21, 83], which includes the Peters-He dynamic inflow model [78], the moment-balance trim solution [79], and the blade element theory (BET). The predicted angle of attack distribution on the rotor disc is given in Fig. 4.14(a), and Fig. 4.14(b) shows the results from CAMRAD II [25]. It is seen that the in-house BET code agrees well with CAMRAD II, especially in the rotor tip regions that are acoustically important. The regions of high angles of attack are well predicted in the first

quadrant and near 270° azimuthal angle.

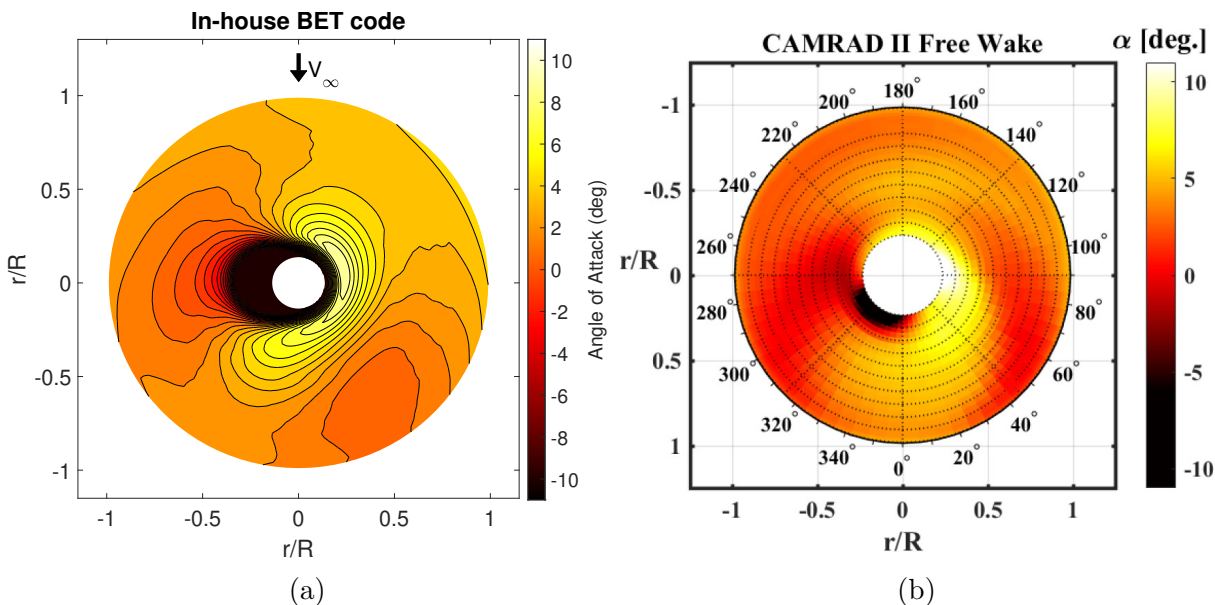


Figure 4.14: Predictions of the SUI rotor forward flight angle of attack distribution at $\alpha_{sh} = -10^\circ$ and $M_\infty = 0.045$ using: (a) in-house BET code, and (b) CAMRAD II [25].

4.5 Tonal Noise

This section briefly presents the validations of the tonal noise predictions using the in-house BET code [21] and PSU-WOPWOP [11].

Figure 4.15 shows the validations of the tonal noise predictions by using the rotor airloads in forward flight obtained from the BET code above in PSU-WOPWOP. The validations are performed on the BO105 and Bell430 rotors, whose properties are shown in Table 4.5. The three rotor cases are selected to validate noise in different ranges of the rotor scale, the tip speed, and the advance ratio. The 40% scale BO105 rotor acoustic measurements (cases 1 and 2) were carried out by Brooks et al. [4] in the Duits–Nederlandse Wind Tunnel in the forward flight conditions. The helicopter flight test of Bell430 (case 3) was performed by Snider et al. [7] to obtain the measured noise data. Since the forward flight analysis does not

include blade-vortex interactions, only the first blade passing frequency (BPF) noise level is compared between simulations and measurements. It is shown that the predictions agree well with the experimental data for all the three cases.

Table 4.5: Validation rotor cases.

Tonal Noise Case	Case 1	Case 2	Case 3
Experiment	Ref. 4	Ref. 4	Ref. 7
Rotor name	BO105	BO105	Bell430
Scale	40%	40%	full
Rotor radius (ft)	6.56	6.56	21
Number of blades	4	4	4
RPM	1050	525	349
Advance ratio	0.086	0.173	0.27
Thrust coefficient	0.0044	0.0044	0.0047
Observer-hub distance (ft)	23.4	23.4	492
Observer elevation angle (deg)	90	90	-90

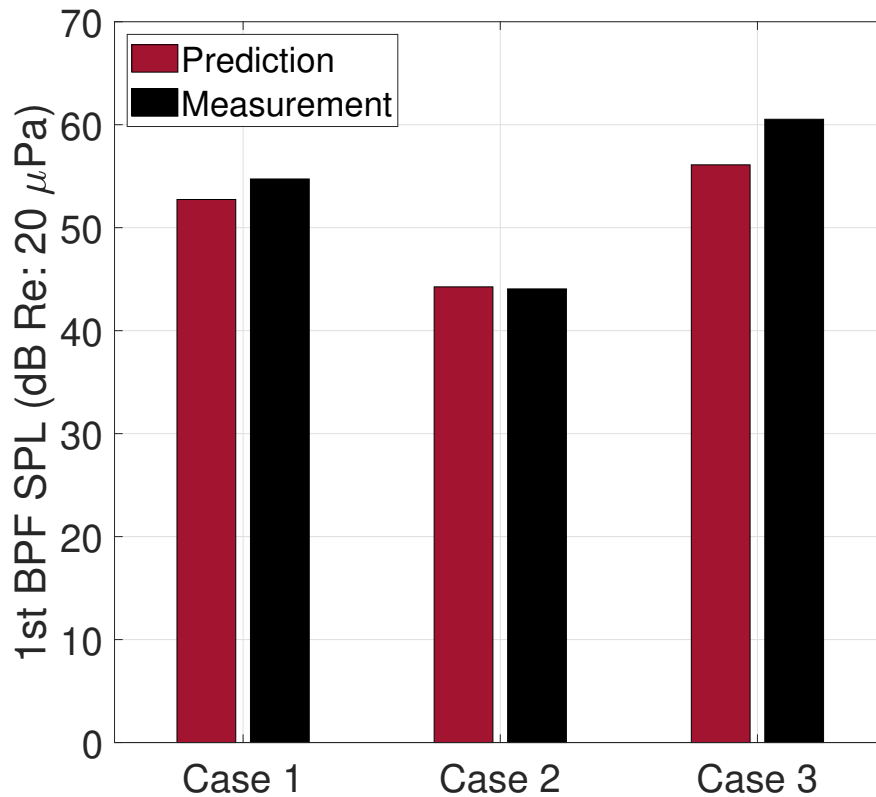


Figure 4.15: Validations of tonal noise predictions, compared with the measurements of Brooks et al. [4] and Snider et al. [7]. Rotor specifications and observer locations are given in Table 4.5.

4.6 Turbulence-Ingestion Noise

Turbulence-ingestion (leading-edge) noise on an airfoil section is predicted using Amiet’s leading-edge noise model [114] with Roger and Moreau’s modification [127] shown in Chapter 3.10. Figure 4.16 shows the turbulence-ingestion noise predictions on an airfoil section at various flow speeds. The turbulence integral scale Λ was found to be independent of the flow speed and it’s value was measured to be 3 cm [115]. The averaged turbulence intensity of at the flow speeds of 40, 60, 90, and 120 m/s were measured to be 4.5, 3.9, 4.8, and 4.1 percent, which are 1.18, 2.34, 4.32, and 4.92 m/s, respectively [115].

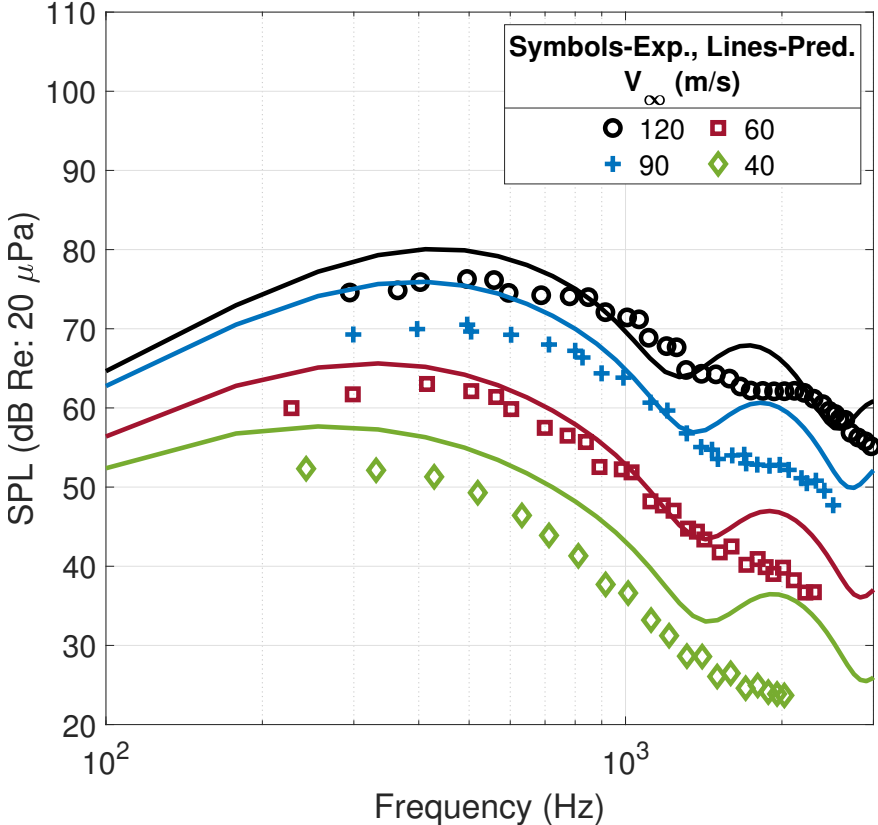


Figure 4.16: Validation of the predictions of turbulence-ingestion noise on an airfoil section with the observer at 2.25 m directly above. Experimental data are given in Ref. [115]

It is seen on Fig. 4.16 that the predictions matches well with the experiments at the flow speeds of 60, 90, and 120 m/s, but the prediction at 40 m/s shows about 5 dB over-prediction.

The discrepancies at 40 m/s is likely due to its small gust wavelength that induces significant scattering by a finite thickness of the leading edge. Fortunately, typical rotorcraft tip speeds are much higher than 40 m/s (except for drones at low RPMs), and the good predictions at the high-speed cases demonstrates the validity of using Amiet’s leading-edge noise model on rotorcraft.

Due to the lack of rotor turbulence data from computational fluid dynamics (CFD), rotor BWI noise is not validated in this dissertation. The validations of rotor BWI noise can be a research topic for future researchers.

4.7 Summary

In this chapter, UCD-QuietFly was validated against various acoustic measurements on rotorcraft in multiple scales. The airfoil-self noise sources on rotorcraft were well-captured, including trailing-edge noise, trailing-edge bluntness noise, and vortex-shedding noise. Furthermore, rotor aerodynamics in forward flight is calculated in an in-house BET code [21], and it’s results are validated against experiments and other prediction codes. Finally, tonal noise predictions using the in-house BET code and PSU-WOPWOP [11] validated for the first blade passing frequency.

It is important to note that trailing-edge noise of the full- and mid-scale rotors was calculated using the original Amiet’s model [28] in Eq. (3.1), while the modified Amiet’s model with Roger and Moreau’s corrections [84] in Eq. (3.29) was used to calculate trailing-edge noise on the small-scale rotors, including NASA Ideally-Twisted rotor, SUI Endurance rotor, and DJI-CF rotor. The difference between these two equations is a factor of four

in the acoustics power spectral density S_{pp} that results in 6 dB in sound pressure level. Although the selection of Roger and Moreau's corrections is controversial in the aeroacoustics community, it is physically reasonable in the current dissertation to use the original Amiet's model for full-scale rotors and Roger and Moreau's corrections for small-scale rotors. First, experiments [136, 137] showed that the convection velocity and the spanwise coherence length varied with Reynolds number and Mach number, and the conventional Corcos's model [138] may not be generalized into all flow conditions. Therefore, the flexibility of using Roger and Moreau's corrections serves as a convenient approach to account for the flow physics that are lack in the theories. Second, the goal of this dissertation is to explain the broadband noise mechanisms on rotorcraft and explore the noise differences among different aircraft designs, rather than finding a generalized trailing-edge noise theory for all flow conditions. Due to the un-accounted variations of flow conditions in the currently insufficient theories for varied rotor scales, a single generalized model for all rotor scales is not appropriate. Thus, UCD-QuietFly gives its users the flexibility to choose the suitable models based on the rotor scales.

The validations of the leading-edge noise predictions on an airfoil section were considered good for flow Mach numbers above 0.26. Future work can be carried out to predict turbulence-ingestion noise of rotorcraft using the turbulence obtained from CFD.

Chapter 5

Parameter Sensitivity Study of Rotorcraft Broadband Trailing-Edge Noise

This chapter presents trend analyses of trailing-edge noise associated with rotor design and operating parameters, such as the rotor tip Mach number, ascending speed, radius, blade collective pitch angle, twist angle, rotor solidity, disk loading, and number of blades. The detailed flow physics behind this noise trend is also discussed. A semi-analytic equation is obtained from a noise map on the plane observers.

5.1 Rotor Parameters Trend Analysis

In this section, UCD-QuietFly is used to investigate the trend of rotor trailing-edge noise with different parameters. The six parameters studied are listed in Table 5.2, and other constant conditions are shown in Table 5.1. Each parameter is analyzed from the start to the end values while other parameters are kept at the base values. For each parameter, 20 values were selected. An observer is located at one base rotor diameter from the hub with

-90° degree elevation angles.

Table 5.1: Constant Conditions.

Item	Value
Airfoil	NACA0012
R_o, Ψ (m, deg)	13.4112, -90
N_B	2

Table 5.2: Range of Parameters.

Parameter	Start	End	Base
M_{tip}	0.45	0.8	0.67
θ_0 (deg)	11	18	13.52
θ (deg)	-13	-4	-10
σ	0.0507	0.1200	0.0507
R (m)	2.3	8.0	6.7056
V_c (m/s)	0	9	0

First, the trends of the overall sound pressure level (OASPL) associated with the rotorcraft design and operating parameters are presented in Fig. 5.1. It is seen that the OASPL increases with increasing tip Mach number, collective pitch angle, blade twist angle, rotor solidity, rotor radius, and disk loading, but the ascending speed and the number of blades with the constant solidity have negligible effects on rotor trailing-edge noise. The blade pitch angle, twist angle, and rotor solidity changes OASPL only by about 2 dB within the specified ranges. The rotor radius changes OASPL by about 5 dB. Among the studied parameters, the tip Mach number is found to be the dominant factor in rotorcraft trailing-edge noise. Detailed studies of the parameters are provided in the following sections to show the narrow-band sound pressure levels and the flow physics in terms of the boundary layer parameters.

With a constant rotor radius, the OASPL contribution from each blade section is plotted in Fig. 5.1(i). Since the tip sections have a higher velocity than the root sections, the

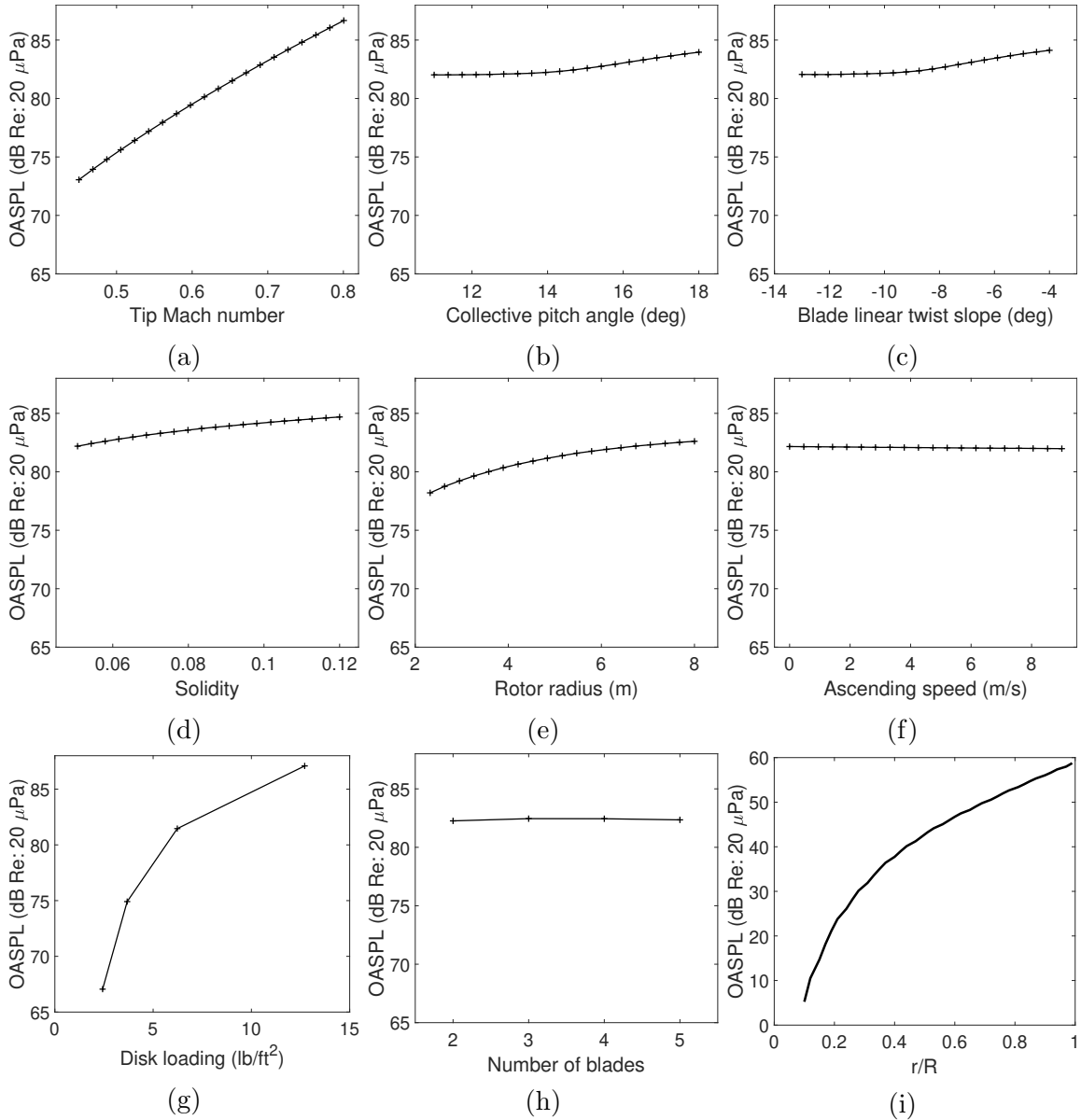


Figure 5.1: OASPL trend with parameters: (a) tip Mach number, (b) collective pitch angle, (c) blade linear twist slope, (d) rotor solidity, (e) rotor radius, (f) rotor ascending speed, (g) disk loading, (h) number of blades, and (i) sectional noise contribution from one blade.

trailing-edge noise level from the tip sections is higher.

5.1.1 Effect of rotor tip Mach number:

The trend of narrow-band sound pressure level associated with the rotor tip Mach number is shown in Fig. 5.2(a). It is shown that the narrow-band SPL increases with increases to the

tip Mach number for the entire frequency range. This trend is explained by the boundary layer parameters measured near the trailing edge ($x/c = 0.99$) at 90% rotor radius position as shown in Fig. 5.3. The noise increase is mainly accounted for by the increase in the boundary layer edge velocity U_e and the pressure gradient dp/dx near the trailing edge. The higher tip Mach number gives a higher boundary layer edge velocity and higher convection velocity. According to Eq. (3.10), the strength of the wall pressure spectrum is proportional to the boundary layer edge velocity; hence, the higher wall pressure spectrum results in a higher noise level. In addition to the increase in the magnitude of SPL, the increased tip Mach number shifts the spectral peak to a higher frequency.

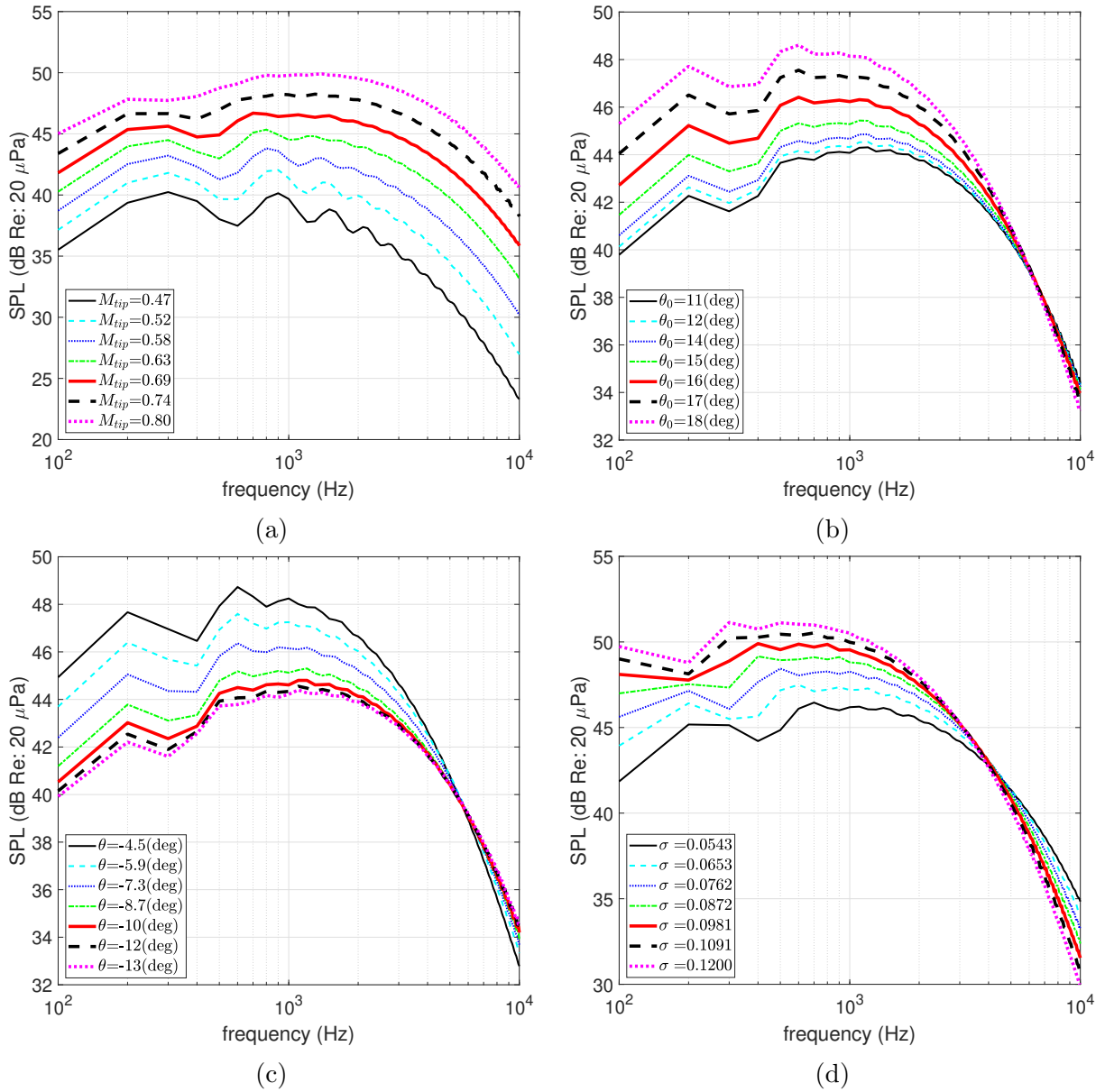


Figure 5.2: Narrow-band SPL trends with design parameters: (a) tip Mach number, (b) collective pitch angle, (c) twist slope, and (d) chord length.

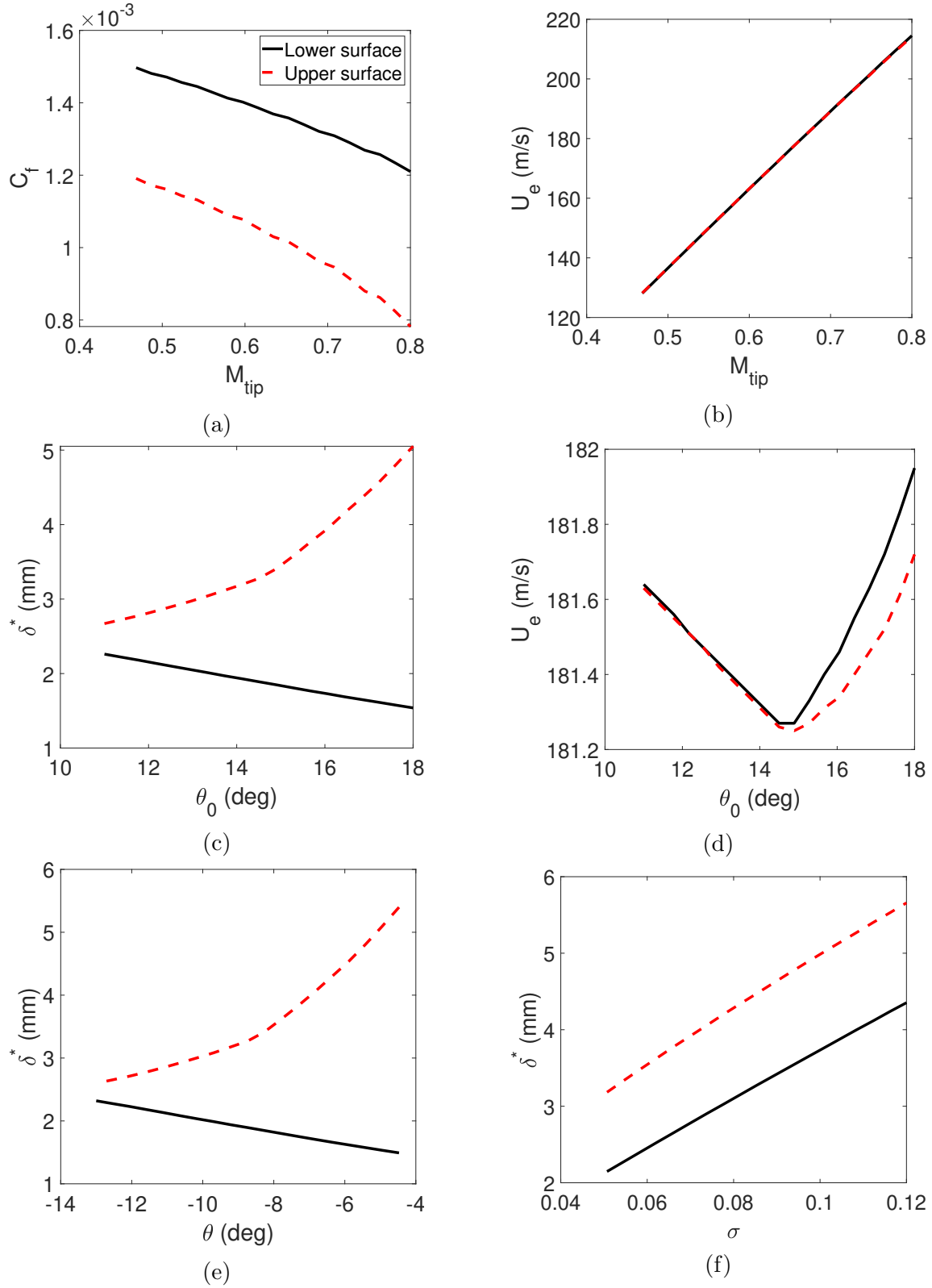


Figure 5.3: Boundary layer parameters measured near the trailing edge ($x/c = 0.99$) at 90% rotor radius: (a) M_{tip} vs. C_f , (b) M_{tip} vs. U_e , (c) θ_0 vs. δ^* , (d) θ_0 vs. U_e , (e) θ vs. δ^* , and (f) σ vs. δ^* .

In Fig. 5.4(a), the sound pressure level is scaled with the tip Mach number, and the frequency is normalized with the tip Mach number to collapse the maximum peak frequency. It is found that SPLs collapse very well into a single line, especially for high Mach number cases with the 4.7th power of the tip Mach number and the frequency scaling of $f * 0.8/M_{tip}$. This frequency scaling has the same physical meaning as the Strouhal number (fL/U_∞); however, on a rotor blade, the characteristic length (L) and freestream velocity (U_∞) are not constant values for different sections. Therefore, a frequency scaling of $f * 0.8/M_{tip}$ is chosen over the Strouhal number, where $0.8/M_{tip} = 0.8c_0/U_{tip}$ is a consistent reference value for the blade sections, which also serves the same purpose as L/U_∞ in Strouhal number. The rotor tip Mach number scaling between two rotors is provided in Eq. 5.1, which is close to the flow Mach number's 5th power scaling for airfoil trailing-edge noise as suggested by Hatcheson and Brooks [42].

$$\text{SPL}_{\text{rotor}} = \text{SPL}_{\text{rotor,ref}} + 10 \log_{10} \left[\left(\frac{M_{tip}}{M_{tip,\text{ref}}} \right)^{4.7} \right] \quad (5.1)$$

It is also found that the scaling factor varies in the approximate range of 4.5 to 5.0 as a function of the collective pitch angle as shown in Fig 5.4(c), and it has the local maximum of 5.0 at $\theta_0 = 10^\circ$ as presented in 5.4(b) where the rotor tip has the angle of attack close to 0 degree since $\theta = -10^\circ$. Therefore, regarding the typical collective pitch and blade twist for the operation and design of helicopters, the tip Mach number scaling ranges from 4.5 to 5.0 with an average of 4.7.

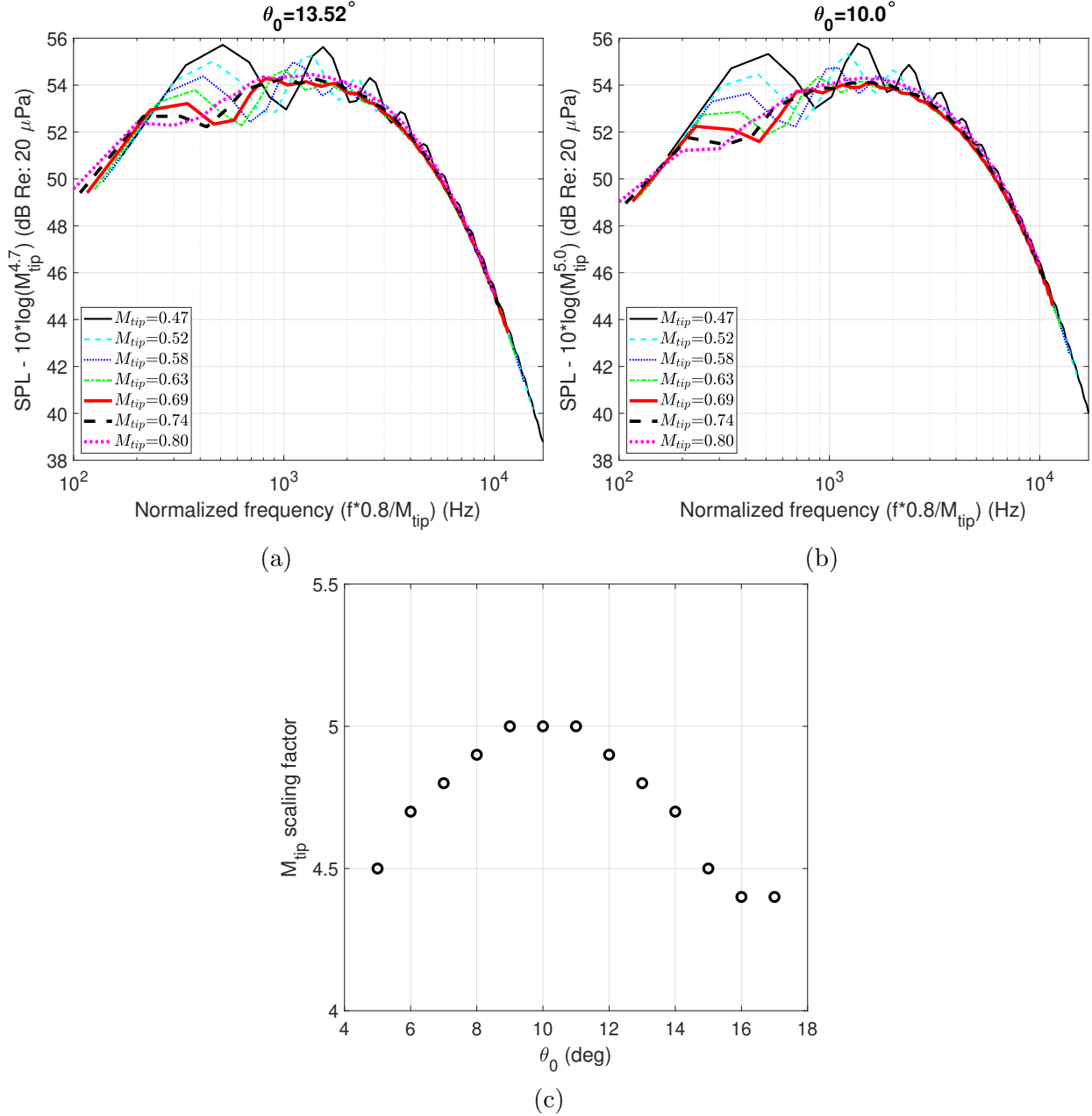


Figure 5.4: Scaled SPL with tip Mach number: (a) $\theta_0 = 13.52^\circ$, (b) $\theta_0 = 10.0^\circ$, and (c) scaling factor for various collective pitch angles with blade twist fixed at -10° .

5.1.2 Effect of blade collective pitch

Collective pitch angle changes the angle of attack on the entire blade. Figure 5.2(b) shows that increasing collective pitch angle gives higher low-frequency noise while high-frequency (larger than 5kHz) noise remains unchanged. In Fig. 5.3(c), as the angle of attack increases,

the boundary-layer displacement thickness increases on the upper surface and decreases on the lower surface. It is also found that the change in the edge velocity U_e is small. Although Hutcheson and Brooks [42] showed that the angle of attack only affects noise with frequencies lower than 1kHz, Fig. 5.2(b) demonstrates the collective pitch angle's influence on frequency lower than 5kHz for rotorcraft noise.

Chou and George's results [44], based on the Kim and George method [31], showed that the effect of the collective pitch on the low-frequency (100 Hz) and the mid-frequency (1000 Hz) noise were the same. However, it is shown that the effect on low-frequency noise is larger than that on mid-frequency noise.

5.1.3 Effect of blade twist

Unlike the collective pitch angle, blade linear twist angle varies with the blade radial position. Figure 5.2(c) shows the SPL as a function of the linear twist slope from the root to the tip. The noise trend with the twist angle is similar to the trend for the collective pitch angle. In fact, the behaviors of the boundary-layer parameters, shown in Fig. 5.3(e), are similar to those for the collective pitch angle.

5.1.4 Effect of rotor solidity

Figure 5.2(d) shows the SPLs for the various rotor solidity, which is varied by the chord length as the rotor radius and number of blades are fixed. The increase in chord length results in higher low-frequency noise, while the high-frequency noise remains unchanged. Since the boundary layer develops further with a longer chord length, the boundary layer

becomes thicker, especially on the upper surface, as shown in Fig. 5.3(f), which accounts for the increase in low-frequency noise. In addition, the peak level shifts to lower frequencies as the rotor solidity is increased, which agrees with the effect of a chord length on airfoil noise [24].

5.1.5 Effect of rotor radius

Figure 5.5(a) shows the SPLs as a function of the blade radius with the same tip Mach number. It is shown that the increased rotor radius gives higher sound pressure levels in the entire frequency range. The boundary-layer parameter changes measured near the trailing edge ($x/c = 0.99$) at 90% rotor radius are small, as shown in Fig. 5.6, since the tip Mach number is kept constant. The main factor accounting for the noise increase is the span increase with increasing the rotor radius. In other words, the source region is increased by increasing the blade radius.

5.1.6 Effect of rotor ascending speed

Figure 5.5(b) shows the SPLs as a function of the rotor climb or ascending speed. An increased ascending speed slightly increases the noise level. The effect is small compared to the other rotor parameters since the variation of the local angle of attack is small within the limited realistic ascending speed range, which is 9 m/s for this rotor. Figure 5.6 confirms that the changes in the boundary-layer parameters are small with the ascending speed.

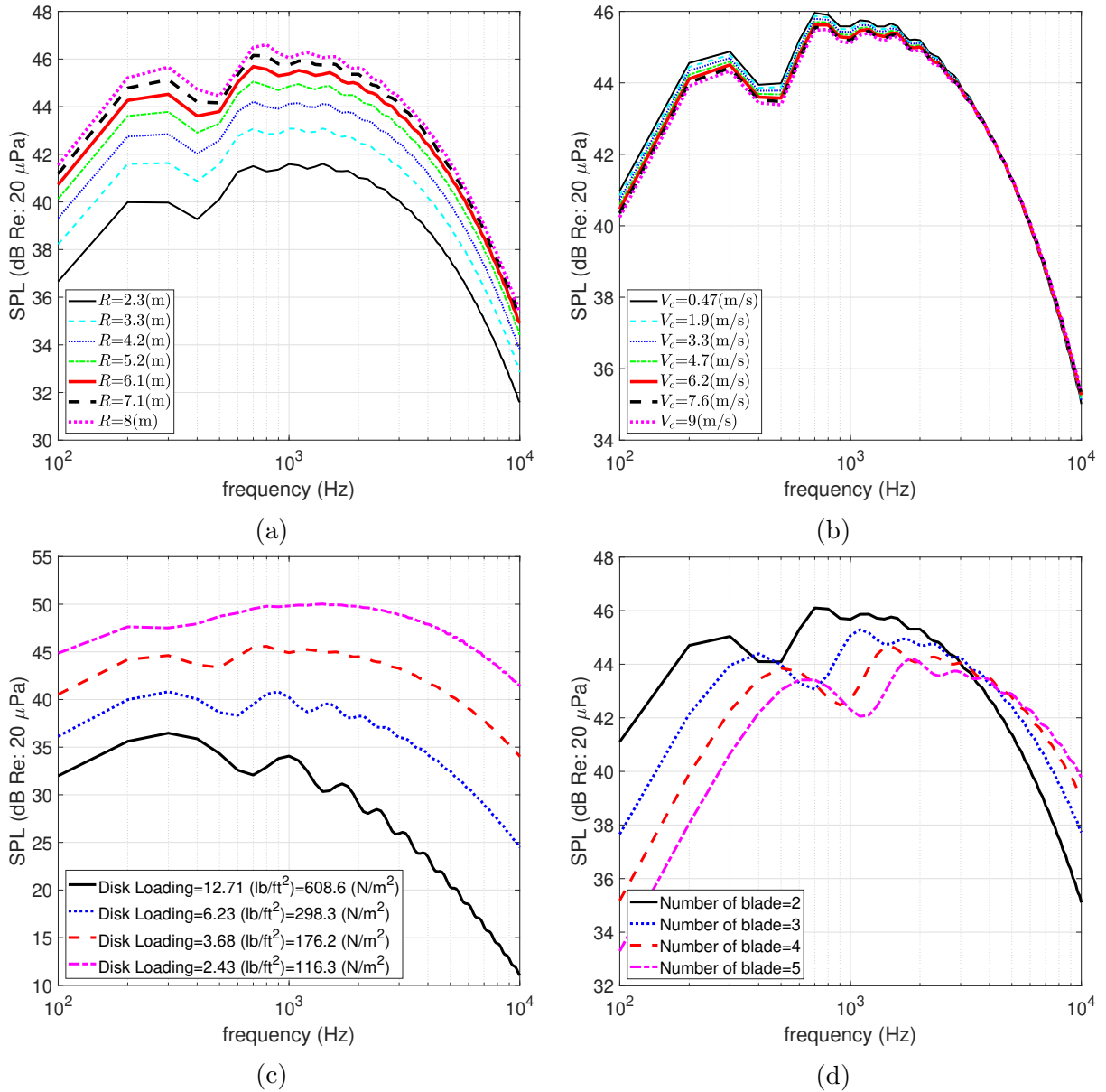


Figure 5.5: Narrow-band SPL trends with design parameters: (a) rotor radius, (b) rotor ascending speed, (c) disk loading, and (d) number of blades.

5.1.7 Effect of disk loading

As for the investigation of the effect of rotor disk loading, the rotor thrust is fixed at 23,000N, while the rotor radius and the collective pitch are varied to match the four selected disk loading values, which is essentially the effect of a combination of rotor radius and collective pitch. The effect of disk loading on the rotor trailing-edge noise is presented in Fig. 5.5(c)

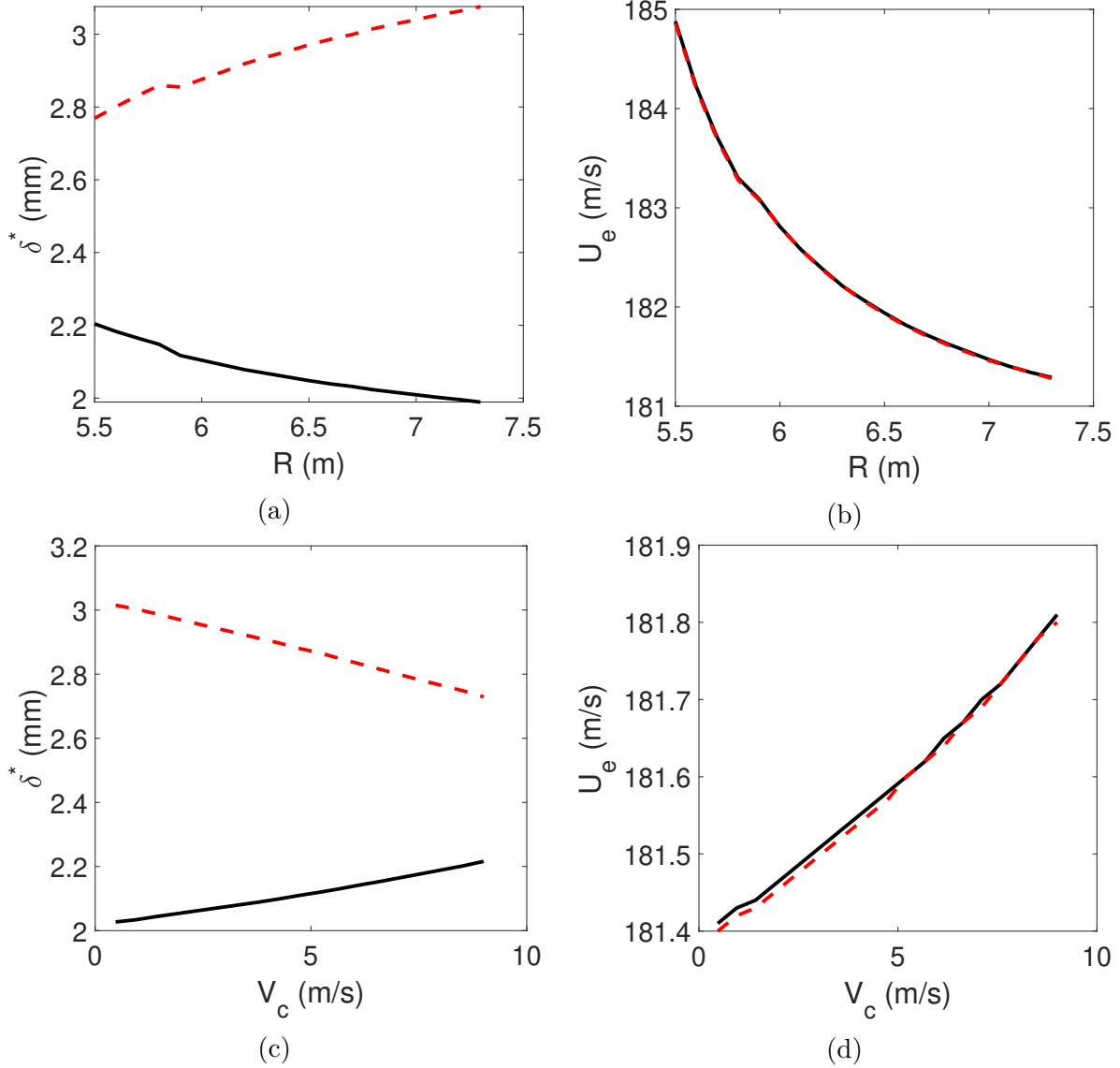


Figure 5.6: Boundary layer parameters measured near the trailing edge ($x/c = 0.99$) at 90% rotor radius: (a) R vs. δ^* , (b) R vs. U_e , (c) V_c vs. δ^* , (d) V_c vs. U_e .

where the noise level increases with the decreasing disk loading since the lower disk loading results in the larger rotor radius and therefore, the larger airfoil span. It is worthwhile noting that tonal noise is increased with the increasing disk loading [139] due to the increased loading on the blades, which is opposite to the observation of rotor trailing-edge noise.

5.1.8 Effect of number of blades

In the study of the effect of the number of blades on rotor trailing-edge noise, all the parameters in Table 5.2 are fixed at the base values while the chord length is varied for the different number of blades to ensure the solidity to be the same. Figure 5.5(d) shows that when the number of blades is increased, or the chord length decreased, the low- to mid-frequency trailing-edge noise is decreased while the high-frequency noise is increased. OASPL does not change noticeably with the number of blades, as shown in Fig. 5.1(h), since the decrease of the low-frequency noise level is offset by the increase of the high-frequency, but the narrow-band SPL change is large, and human perception of noise could be different depending on the number of blades. It is interesting to note that rotor tonal noise is decreased by increasing the number of blades since the loading noise is decreased as the lifting force is distributed on more blades [82].

5.2 Rotor Geometric Attenuation and Directivity

The geometric attenuation and directivity pattern of rotor trailing-edge noise are studied, and a semi-analytic equation is obtained to relate the OASPL at any observer location to a reference location of one rotor diameter with a -90° elevation angle. Using the base values in Table 5.2, the OASPL is predicted by UCD-QuietFly on the X_1Y_1 and X_1Z_1 planes shown in Fig. 5.7(a)-(b). Table 5.3 provides the detailed coordinate ranges about these two planes. The dipole directivity is shown in Fig. 5.7(a) when the noise levels are viewed from the side of rotorcraft. When the noise levels are viewed from the top in Fig. 5.7(b), the noise contours have a monopole directivity.

Table 5.3: Geometric Attenuation and Directivity.

Parameters	X_1Y_1	X_1Z_1
X_1 Range (m)	[-70,70]	[-30,30]
Y_1 Range (m)	[-70,70]	NA
Z_1 Range (m)	NA	[-100,-10]
Grid Size (m)	10	5
Distance to Hub (m)	-26.8	0

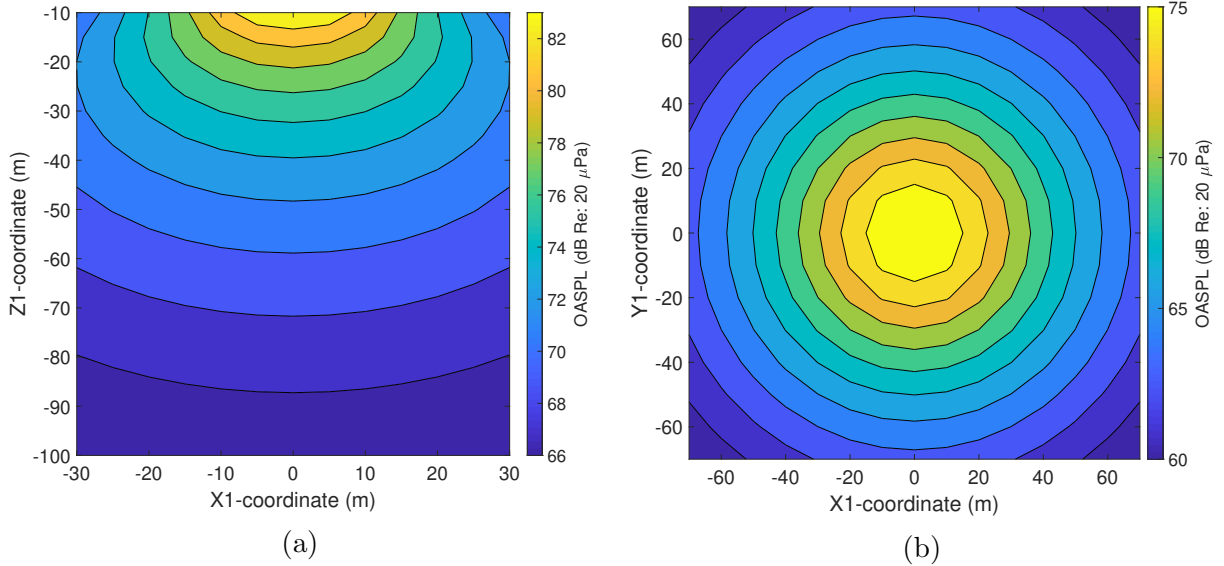


Figure 5.7: OASPL obtained from UCD-QuietFly on: (a) X_1Z_1 plane, and (b) X_1Y_1 plane.

The ISO standard [140] gives the geometric attenuation of a point source as shown in Eq. (5.2) where PWL_{ref} is sound power level at a point source.

$$\text{SPL} = \text{PWL}_{\text{ref}} - [20 \log(R) + 11] \quad (5.2)$$

However, Eq. (5.2) cannot be directly applied to predict rotorcraft noise in the far field since the noise source is not a point source. In addition, rotor trailing-edge noise has a dipole directivity, which should be included in far-field noise predictions. The rotor geometric attenuation equation is proposed to be a form of Eq. (5.3) in which the first term accounts for the directivity at one rotor diameter distance while the second term couples the effect of

the attenuation and directivity.

$$\text{OASPL} = (\sin^{\beta_1} |\phi|) \text{OASPL}_{\text{ref}} - [\beta_2 + \beta_3 (1 - \sin |\phi|)] \log \left(\frac{R_0}{d} \right) \quad (5.3)$$

The constants β_1 , β_2 , and β_3 are determined by minimizing the difference between this equation and the noise predicted on the X_1Y_1 and X_1Z_1 planes. $\text{OASPL}_{\text{ref}}$ is the OASPL at one rotor diameter with a -90° elevation angle. Based on the prediction results shown in Fig. 5.7(a)-(b), the Quasi-Newton minimization method is used to find the three constants as

$$\beta_1 = 0.0209; \quad \beta_2 = 18.2429; \quad \beta_3 = 6.7267 \quad (5.4)$$

It is worthwhile noting that it is possible to predict noise levels at the entire observer plane with only one noise level at a reference position and using Eqs. (5.3) and (5.4). Since the noise level at the reference location is used to propagate the sound to far-field observers, Eq. (5.3), along with Eq. (5.4), only accounts for sound propagation effects. In other words, Eqs. (5.3) and (5.4) are expected to work for any rotorcraft designs or operating conditions as long as the noise level at the reference location is provided.

Figure 5.8 shows the OASPL calculated by Eq. (5.3) where its average difference in comparison with the direct UCD-QuietFly predictions is 0.0147 dB, or 0.018% of the OASPL. Such a small difference demonstrates a good representation of the combination of rotor noise attenuation and directivity in the proposed semi-analytic equation form. The difference between the UCD-QuietFly and Eq. (5.3) are presented in Fig. 5.8 (c)-(d), demonstrating a close match except for small elevation angles. Comparing the computation time of about

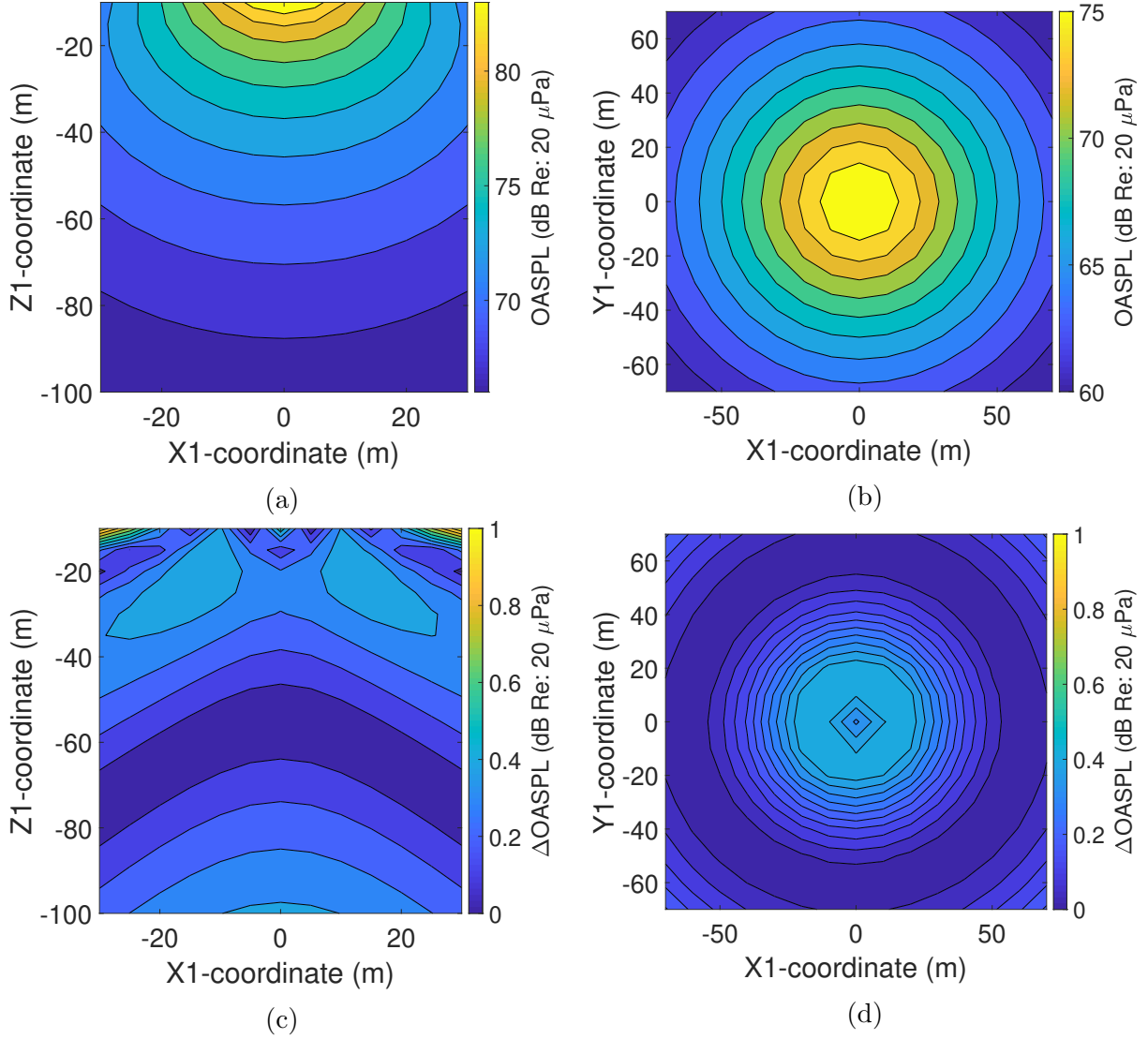


Figure 5.8: OASPL calculated from rotor attenuation equation, and its difference to UCD-QuietFly: (a) OASPL calculated by Eq. (5.3) on the X_1Z_1 plane, (b) OASPL calculated by Eq. (5.3) on the X_1Y_1 plane, (c) absolute difference between Fig. 5.8(a) and Fig. 5.7(a) on the X_1Z_1 plane, and (d) absolute difference between Fig. 5.8(b) and Fig. 5.7(b) on the X_1Y_1 plane.

1 min at a single observer location using UCD-QuietFly with instant calculations of Eq. (5.3), the computational time saved using this approach is a factor of N , where N denotes the number of observers.

SPL predicted by Eq. (5.3) is compared with UCD-QuietFly results at multiple elevation

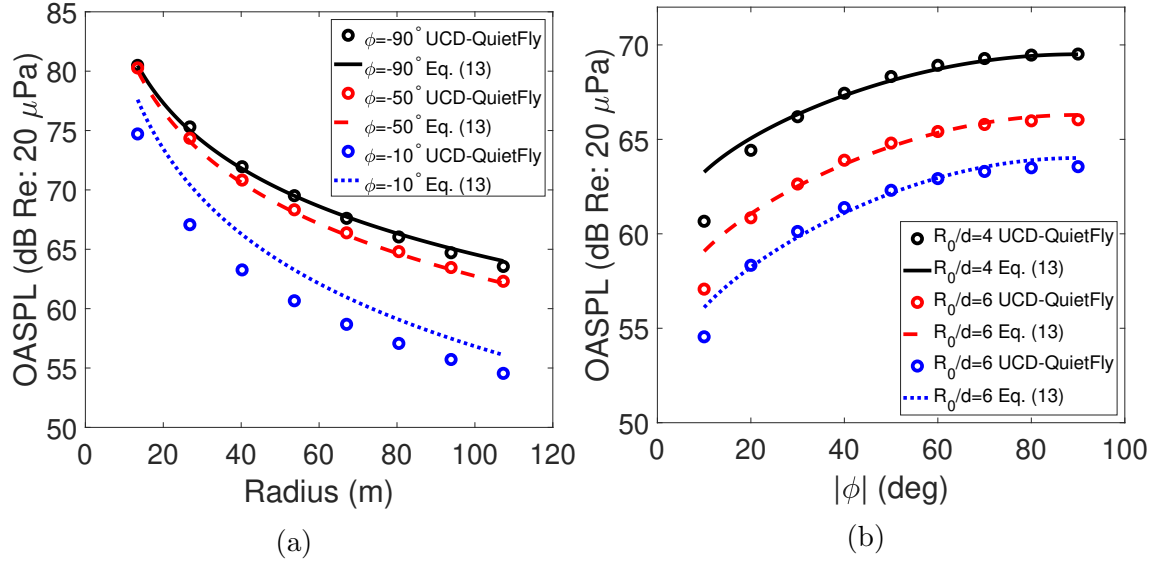


Figure 5.9: Comparison of UCD-QuietFly and Eq. (5.3): (a) OASPL vs. observer distance, (b) OASPL vs. elevation angle.

angles and distances in Fig. 5.9. As expected, it is clearly shown that the OASPL decreases with increasing the distance and increases with increasing the elevation angle. It is shown that Eq. (5.3) accurately predicts the attenuation and directivity trends except for small elevation angle. Figure 5.9 also shows that at low elevation angles, the noise reduction is steeper with increasing the observer distance.

5.3 Summary

This chapter first investigated the effects of rotor parameters on broadband noise. A scaling law that associates rotor broadband noise with tip Mach number is created. The broadband noise directivity of a helicopter rotor is calculated. An empirical equation was developed to calculate geometric attenuation of rotor broadband noise. Key findings are summarized as follows:

1. Rotor trailing-edge noise is scaled with the 4.5^{th} to 5.0^{th} power of the tip Mach number

for typical helicopter collective pitch and blade twist angles, and the frequency is scaled with $f * 0.8/M_{tip}$.

2. Although rotational speed still significantly affects the rotor trailing-edge noise, neglecting other parameters results in considerable inaccuracies. For example, an increased collective pitch angle increases the noise levels at low- to mid-frequencies while maintaining high-frequency noise. The blade twist angle was observed to have a similar effect as the collective pitch angle. An increased rotor solidity only increases low- to mid-frequency noise levels. An increased rotor radius with the constant tip Mach number results in higher noise for all frequencies mainly due to the increased source region. In addition, an increased ascending speed shows the negligible effect on rotor trailing-edge noise due to the operational limit of the helicopter maximum ascending speed. Increasing disk loading is found to decrease rotor trailing-edge noise for the entire frequency. Finally, for the increasing number of blades, low- to mid-frequency noise is decreased while high-frequency noise is increased.

3. For a hovering helicopter, the vertical plane (X_1Y_1) has a dipole shape directivity pattern while the horizontal plane (X_1Y_1) has a circular monopole directivity pattern. A semi-analytic equation was proposed to represent the geometric attenuation and directivity of rotor trailing-edge noise. This equation requires SPL at one reference observer location, which can be obtained by UCD-Quietfly or any other methods including measurement. It should be noted that this semi-analytic equation is independent of helicopter designs or operation conditions since it only accounts for the attenuation and directivity of sound propagation. The effect of helicopter designs and operating

conditions should be accounted for noise levels at the reference location. It was shown that this proposed equation provided good agreement with direct noise computations on the observer plane except shallow elevation angles. The computational time saving of an order of the number of observers can be achieved using this semi-analytic equation.

4. Considering the high-frequency noise dominance, trailing-edge noise is important in terms of human perception, which should be accounted for rotorcraft blade design. In a preliminary rotorcraft design process, for example, UCD-QuietFly can be used to compare trailing-edge noise generated on various vehicle and blade designs. In addition, the design parameters can be optimized for trailing-edge noise by performing a parameter sweep in UCD-QuietFly.
5. More work is recommended to obtain the scaling of other parameters, beyond Mach number, on rotor trailing-edge noise, from which a rotor trailing-edge noise scaling law can be deduced.

Chapter 6

Broadband Noise Predictions of VTOL Multi-Rotors in Urban Air Mobility

To investigate the importance of broadband noise for UAM VTOL aircraft, three 6-passenger UAM VTOL vehicle designs [37] are studied, and their broadband noise is compared to background noise measurements [23]. Regarding noise perception, the amplitude modulation of broadband noise is studied for single-rotor and multi-rotor configurations. Finally, the broadband noise contours from an urban vertiport are predicted.

6.1 Prediction of UAM VTOL Aircraft

Figures 6.1-6.3 show the one-third octave band broadband noise predictions from UCD-QuietFly for the three different 6-passenger VTOL designs: quadcopter, side-by-side, and lift+cruise. The broadband noise from these three designs is compared to investigate the noise levels for the same mission specifications. Five different altitudes, from 50 ft to 1500 ft, are studied for the hover flight with the observer straightly underneath the rotor (elevation

angle of -90°). Due to the dipole directivity shape of rotor broadband noise [15], this overhead position has the maximum broadband noise level. Although the ground noise reflection effect is not included in this research, this may increase the noise levels further. In each figure, the community background noise measurements [23] is included for reference. For the quadrotor at the highest studied altitude of 1500 ft, the broadband noise is audible above 0.7 kHz in a rural area, above 2 kHz in a community park, above 3.5 kHz in a residential community, and above 6 kHz in a highway area. Compared to that at 1500 ft, as the quadrotor altitude is decreased, the noise level is increased by about 4 dB at 1000 ft, 10 dB at 500 ft, 15 dB at 250 ft, and 30 dB at 50 ft. At the typical altitude of a vertiport of 50 ft, quadcopter noise is not masked for a large frequency range (>0.4 kHz) even in the freeway environment. Note that broadband noise is predicted from one quadrotor, and a higher noise level is observed with multiple vehicles, which is presented in the next section. In sum, broadband noise of multi-rotor VTOL vehicles stands out in the mid- to high-frequency range, where VTOL broadband noise is not masked by the community background noise.

Compared to the quadrotor design, the side-by-side VTOL generates slightly less broadband noise (2 dB) in the entire frequency range, but the high-frequency noise is important to human perception for its audibility in urban areas. Regarding the lift+cruise design, its high-frequency broadband noise remains the same importance as the quadrotor design while low- to mid-frequency broadband noise is increased.

To make more direct comparisons, Figure 6.4 shows the community equivalent sound exposure level (L_{eq}) measured by Begault [23] and the overall sound pressure level (OASPL) predicted from UCD-QuietFly for the three UAM VTOL designs, where L_{eq} and OASPL are mathematically the same since the broadband is statistically stationary or not time-

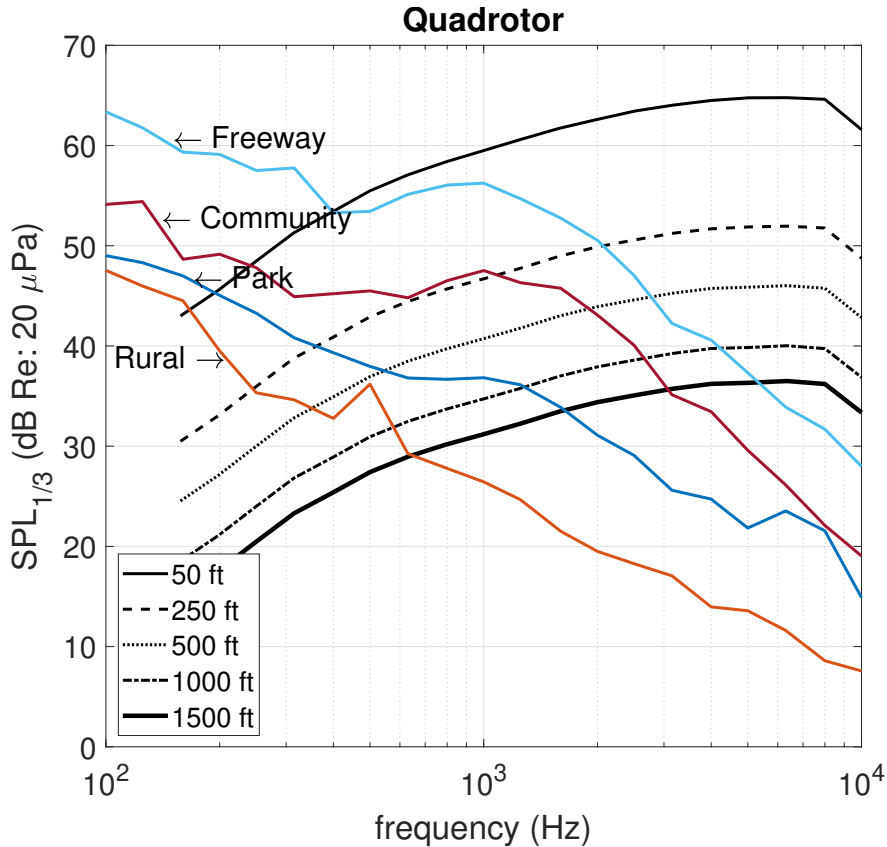


Figure 6.1: Quadrotor VTOL broadband noise prediction from UCD-QuietFly compared to community background noise [23]. Peak-level frequency = 6 kHz.

varying. In this work, the OASPL is calculated in the frequency range from 0.1 kHz to 10 kHz. Comparing the overall sound pressure level, in the freeway environment, broadband noise from the UAM VTOL vehicles are important at 50 ft altitude, or a vertiport’s height. In the residential community, broadband noise is important at an altitude of 250 ft. In the community park, broadband noise is important for the quadcopter vehicle at 1000 ft, the side-by-side vehicle at 500 ft, and the lift+cruise vehicle at 1000 ft. Finally, in the rural area, broadband noise is important for all vehicles at 1500 ft. However, OASPL represents the general importance, while the importance of high-frequency noise compared to all measured environments cannot be neglected as shown in Figs. 6.1-6.3. Although our research demonstrates the importance of high-frequency UAM VTOL broadband noise, low-frequency UAM

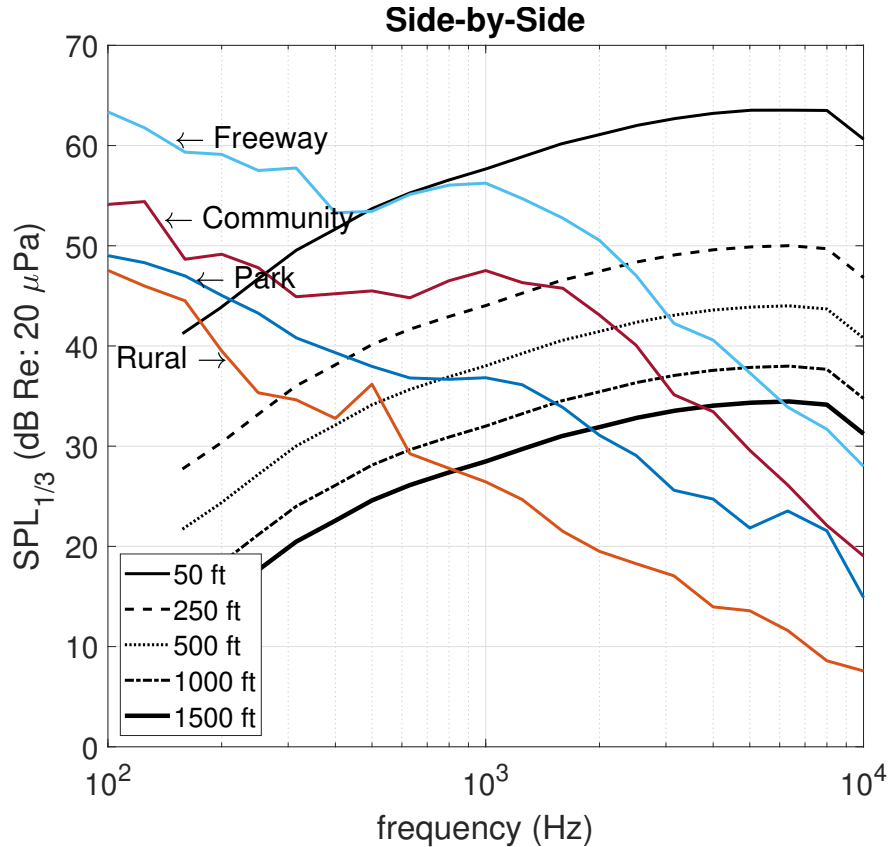


Figure 6.2: Side-by-side VTOL broadband noise prediction from UCD-QuietFly compared to community background noise [23]. Peak-level frequency = 7 kHz.

VTOL noise can also be audible from other noise sources, such as blade-vortex-interaction noise [2, 3].

Comparing the broadband noise levels from the three UAM VTOL designs, it is shown that the design with more rotors generates higher broadband noise in the same mission specifications. To further investigate the effect of the number of rotors on broadband noise, the number of rotors is varied with the lift+cruise VTOL being a base design, where the rotor tip speed and total swept area from multiple rotors are kept the same. As the number of rotors increases, the blade radius of each rotor is reduced and rotational speed is increased. The one-third octave band sound pressure levels from a various number of rotors are shown in Fig. 6.5(a). While the increasing number of rotors increases high-frequency broadband noise,

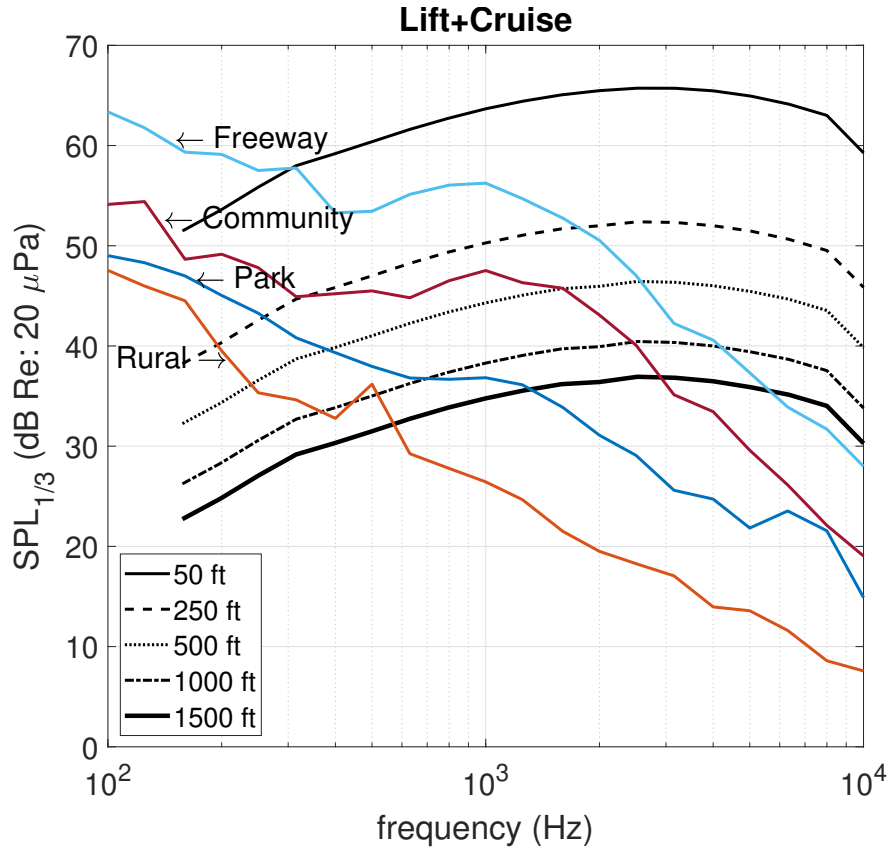


Figure 6.3: Lift+cruise VTOL broadband noise prediction from UCD-QuietFly compared to community background noise [23]. Peak-level frequency = 3 kHz.

low-frequency noise is decreased. This trend can be explained by the fact that reducing the blade radius with multi-rotors results in decreasing low-frequency noise while maintaining the same high-frequency noise on a single rotor [15]. However, high-frequency noise increases as added rotors generate more trailing-edge noise. As noise from multiple rotors with reduced blade radius is combined, the overall effect gives an increase in high-frequency noise and a decrease in low-frequency noise. In Fig. 6.5(b), the three UAM VTOL conceptual designs are seen to have lower broadband noise than the conventional helicopter Bell 430 that has a similar payload as the conceptual designs. Hovering at the altitude of 250 ft, the broadband noise of a Bell 430 helicopter is about 10 dB higher than that of the UAM VTOL conceptual designs, which indicates the noise benefit of operating multi-rotor VTOL at low tip speeds.

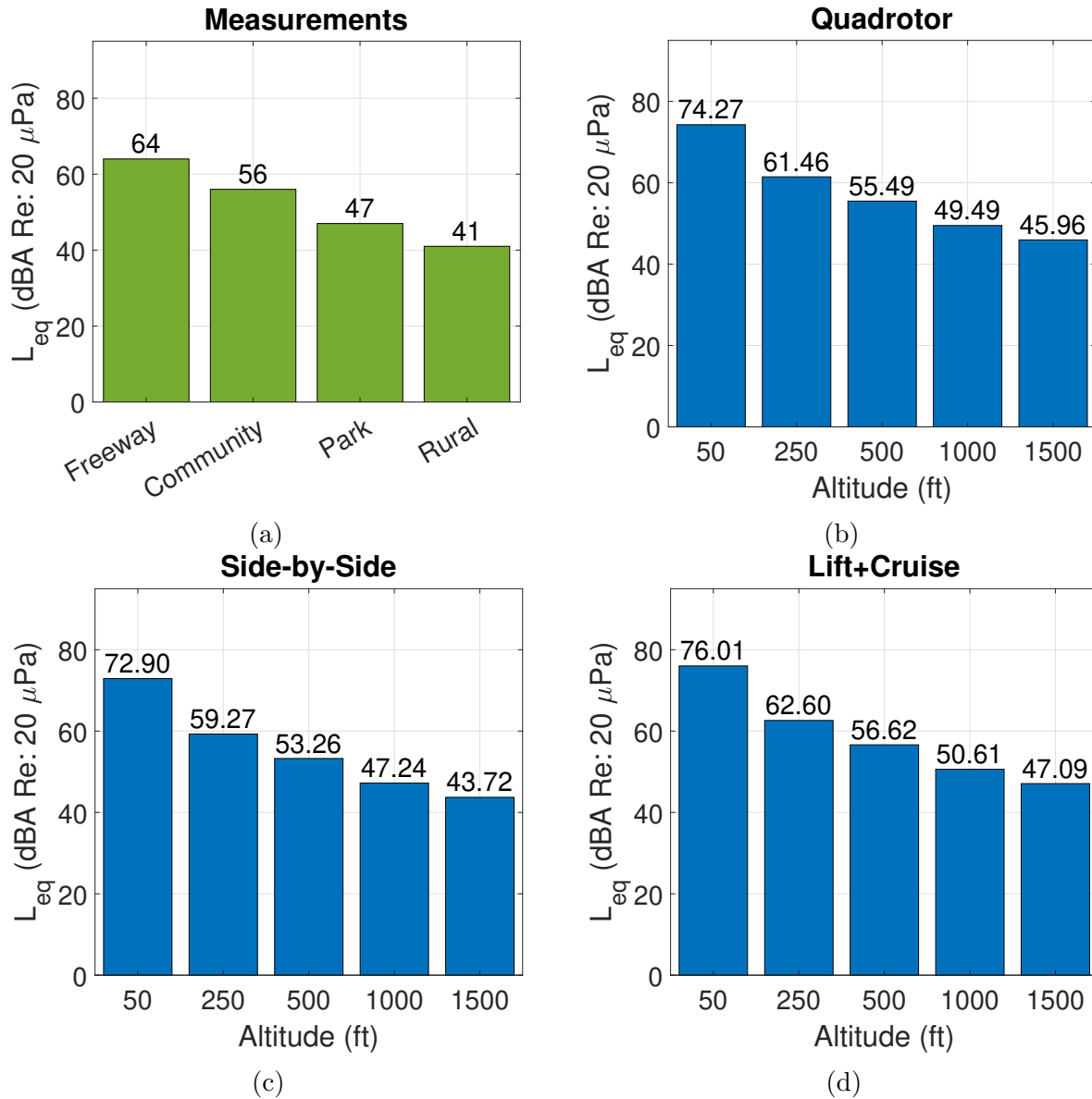


Figure 6.4: Equivalent sound exposure level measurement and overall sound pressure level prediction for: (a) community background noise [23], (b) quadrotor, (c) side-by-side, and (d) lift+cruise.

Uber recommended a UAM noise requirement of 15 dB lower than helicopter noise [141].

This 15 dB noise reduction requirement might be challenging in terms of trailing-edge noise.

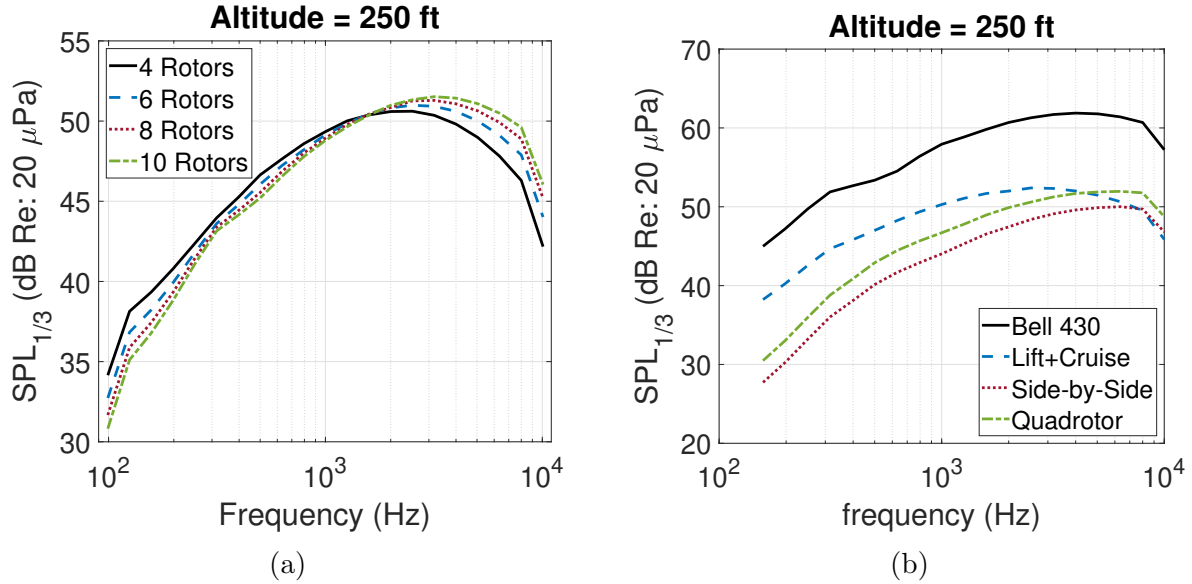


Figure 6.5: Comparisons of UAM VTOL designs: (a) effect of changing the number of rotors by keeping the same tip Mach number and the same total swept area from multiple rotors, and (b) broadband noise of conventional helicopter Bell 430 compared to multi-rotor UAM VTOLs.

6.2 Amplitude Modulation

The amplitude modulation of UAM VTOL aircraft broadband noise is investigated to find its importance for various observer distances and vehicle designs. In the current study, the rotors on a vehicle are assumed to be in phase. It would be interesting to study the amplitude modulations with varying rotor phases. On a 2-bladed UH-1B single rotor, the broadband noise spectrum in time history is presented for various observer distances in Fig. 6.6, where the elevation angle is fixed at -45° . The ending time is 1 second for the four cases, and the starting time is 0.4 second. Figure 6.6 shows that the broadband noise level periodically varies with time for the entire frequency range. As the observer distance is increased, the overall noise level is decreased while the amplitude modulation remains the same patterns. In addition, within the same time duration, the number of peaks present remains unchanged for different observer radial distances. Such periodic variations are caused by the variation

of source-to-observer distance as well as the Doppler effect; the blade moves away from the observer with decreasing noise and towards the observer with increasing noise. Therefore, the period of amplitude modulation is associated with the number of blades and the number of rotors, as well as the rotational speed.

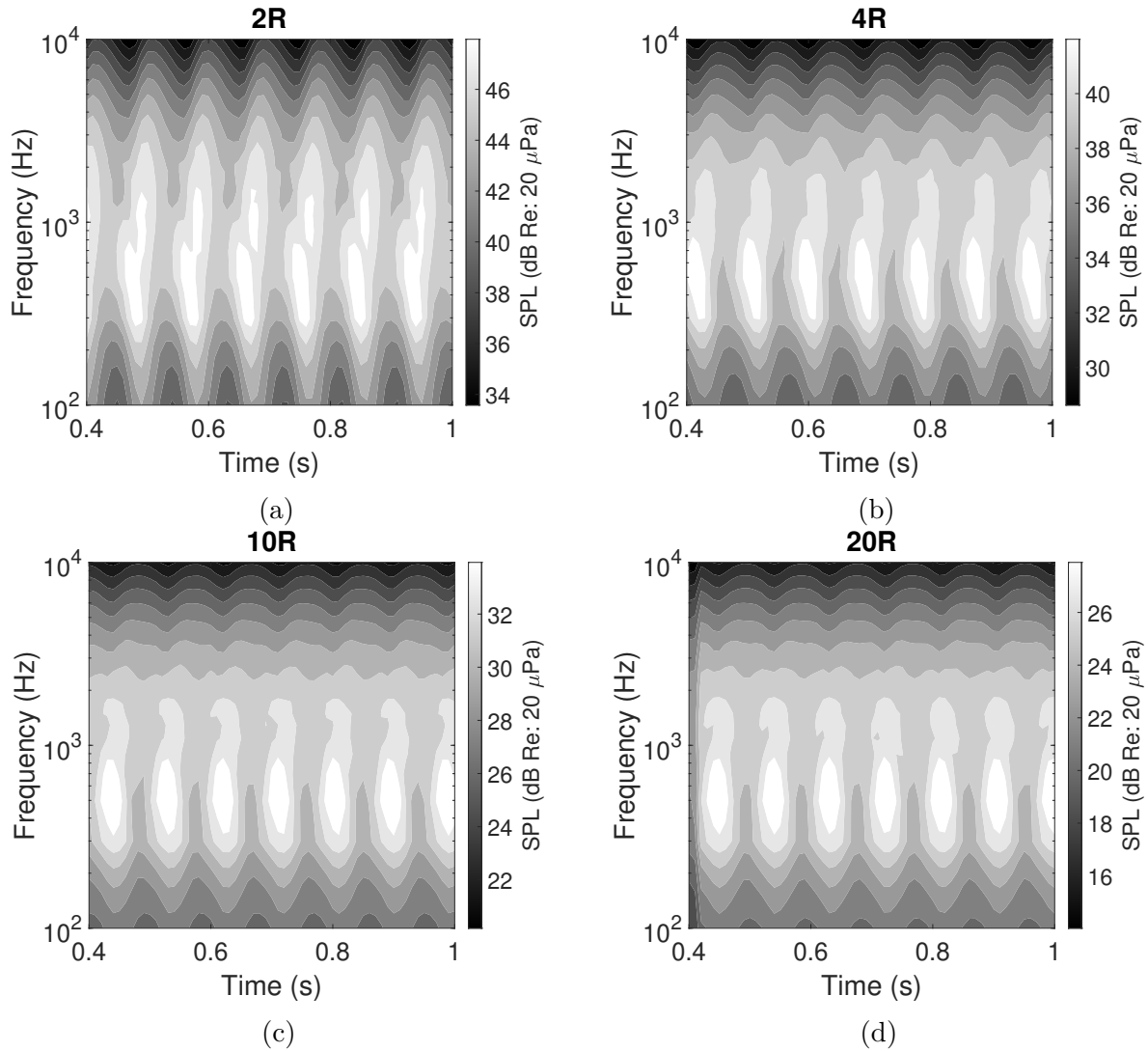


Figure 6.6: Broadband noise spectrum of a UH-1B helicopter in time history for observer distances at an elevation angle of -45 deg: (a) 2R, (b) 4R, (c) 10R, and (d) 20R.

To further investigate the effects of the number of blades and the number of rotors on the broadband noise amplitude modulation at the same rotational speed, broadband noise in the time history is predicted for the three VTOL designs in Fig. 6.7. The side-by-side,

quadrotor, and lift+cruise VTOLs have 2, 4, and 8 rotors, and 8, 12, and 16 blades in total. The observer is located at 44 ft (R_0) and -45° elevation angle from the vehicle hub.

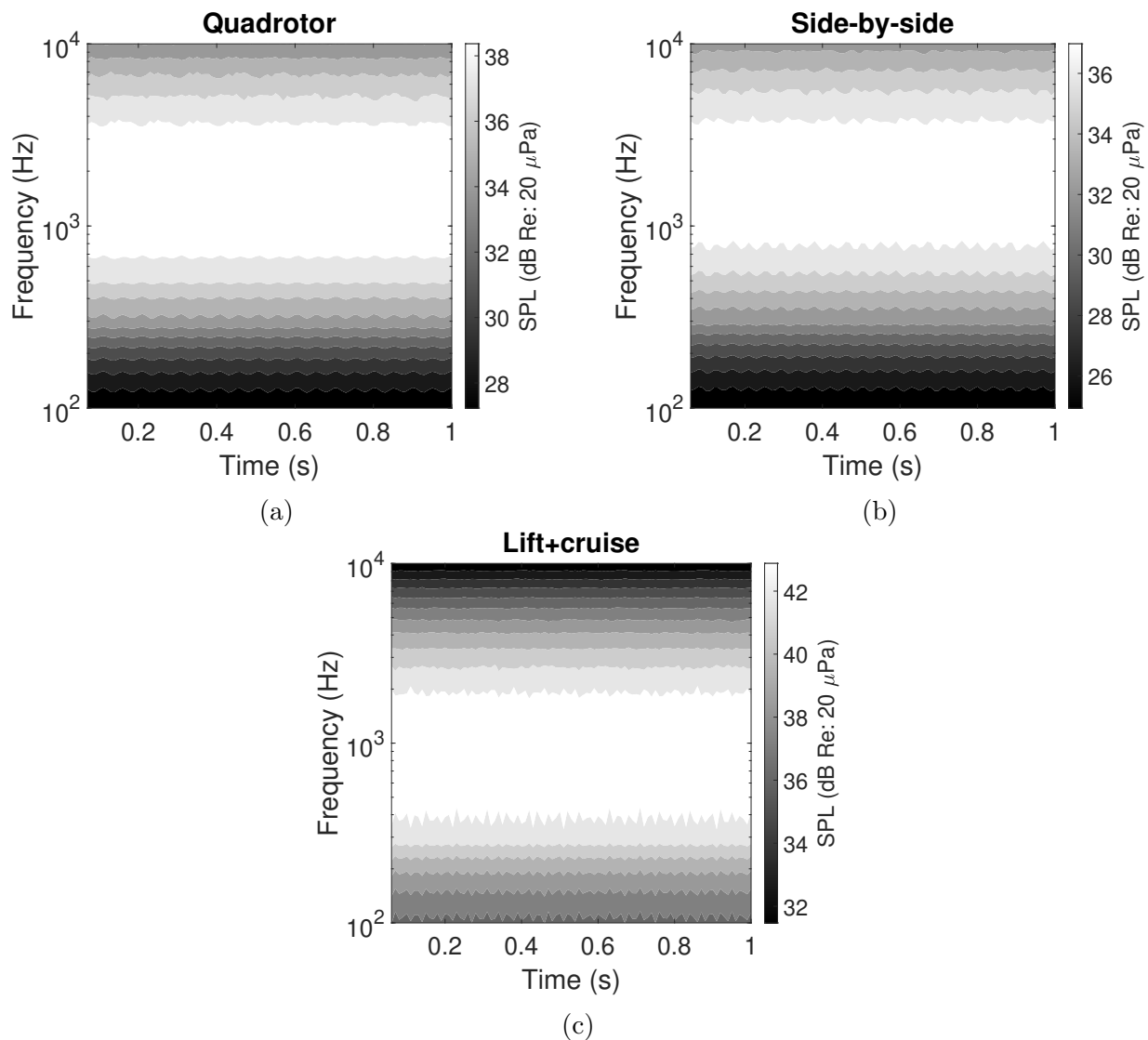


Figure 6.7: Broadband noise spectrum of multi-rotor vehicles in time history: (a) quadcopter, (b) side-by-side, and (c) lift+cruise.

Figure 6.8 shows the OASPL peak-to-peak amplitudes and time history of OASPL of the UH-1B single rotor at various observer distance. It is found that increasing an observer distance reduces the amplitude while the period remains the same. To explain this observation, as the observer-hub distance is increased, the relative difference between the

observer-source 1 distance and the observer-source 2 distance in Fig. 3.5 becomes smaller. For a fixed observer-hub distance (R_0), Fig. 6.9 shows the OASPL peak-to-peak amplitudes and time history of OASPL for different vehicle configurations, which include the UH-1B helicopter and the three UAM VTOL designs. It is demonstrated that the multi-rotor designs have much smaller OASPL peak-to-peak amplitudes than the single rotor. Figure 6.9(b) shows that as the number of blades increases, the modulation period and the peak-to-peak amplitude are both reduced. Within a time duration of 0.2 seconds, the single rotor has 2 periods, the side-by-side VTOL has 6 periods, the quadrotor VTOL has 7 periods, and the lift+cruise VTOL has 9 periods, although they are not clearly shown in Fig. 6.9(b). Therefore, increasing the number of blades increases the number of amplitude modulations, which is similar to the blade passing frequency of tonal noise being increased with the number of blades. Since the observer location is kept at 44 ft, however, a rotor blade with a smaller radius with multiple rotors has a smaller difference between the largest and smallest source-to-observer distances as the blade rotates away and towards the observer, so the peak-to-peak amplitude is smaller. Therefore, more blades result in more noise peaks but smaller amplitudes of the modulation. Different from the simple periodic amplitude modulations for the single rotor, the multi-rotors have the irregular peaks, since their amplitude modulations are combined from multiple periodic modulations of each rotor with phase differences. In conclusion, the amplitude modulation of rotorcraft broadband noise becomes weak when the source-to-observer distance is large; in our case, the peak-to-peak amplitude of OASPL is less than 1 dB when an observer is 4 rotor radii from the rotor hub. For a fixed observer location, the amplitude modulation is less important for a larger number of blades. Thus, one acoustic advantage of VTOL designs with more rotors and more blades is that they have

less annoying broadband noise characteristics associated with amplitude modulation.

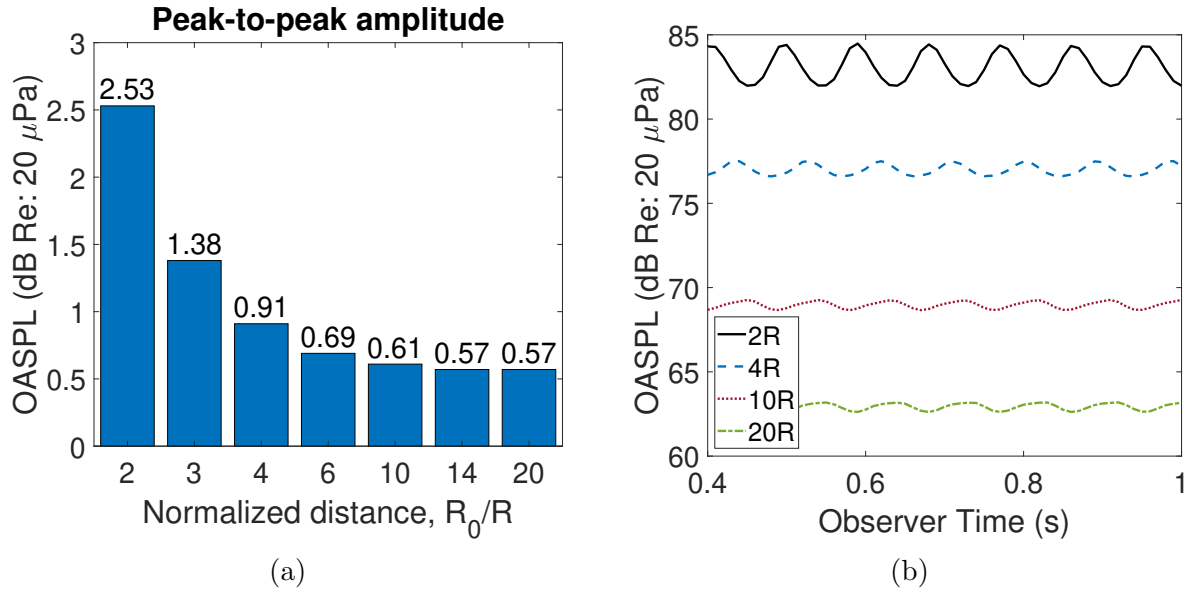


Figure 6.8: Predicted UH-1B helicopter amplitude modulation: (a) peak-to-peak amplitude vs. observer distance, and (b) OASPL in time history for different observer distances.

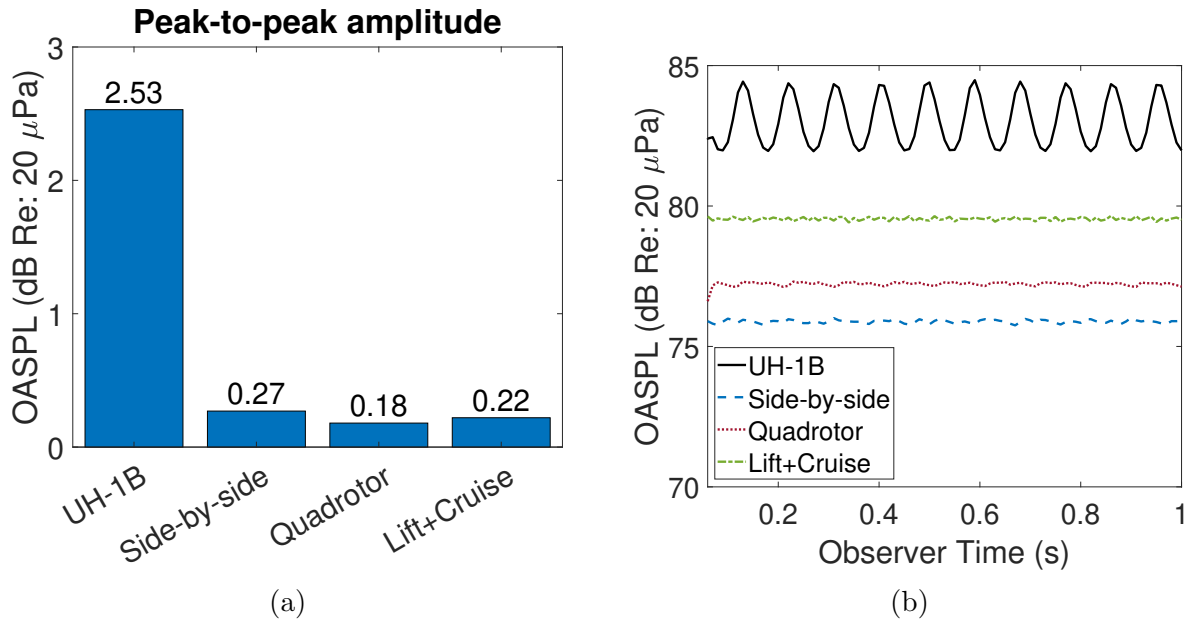


Figure 6.9: Predicted amplitude modulations of different vehicle designs: (a) peak-to-peak amplitudes for four designs, and (b) OASPL in time history for four designs.

6.3 Vertiport

Built in urban areas for vehicles to vertically take-off and land, vertiports are relevant to the communities' noise perception for their vicinities of residential areas. The Gannett Fleming vertiport [40] is considered for the evaluation of broadband noise from multiple UAM VTOL designs. Four UAM VTOL vehicles are operated simultaneously at the four final approach and takeoff areas (FATO) [142] at the altitude of 40 ft, and the overall sound pressure levels are predicted for a map of observer locations on the ground, where the noise scattering effects from the vertiport building are neglected. The noise predictions for quadcopter, side-by-side, and lift+cruise VTOLs are shown in Fig. 6.10, respectively. The lift-cruise design has higher broadband noise than the quadrotor design, and the side-by-side design has the lowest broadband noise. This result is consistent with an earlier finding that more blades generate a higher amplitude of broadband noise. Directly below the FATOs are the four local noise maxima, with each vehicle accounting for each noise maximum.

6.4 Summary

Urban air mobility VTOL broadband noise has been studied using an updated UCD-QuietyFly program [143], which includes the coordinate transformations from single to multiple rotors. The broadband noise amplitude modulation is analyzed to study the noise characteristics. UCD-QuietyFly is validated against measured noise levels for two scaled rotors. Key findings are concluded as follows:

1. Broadband noise of UAM VTOL vehicles is important in the mid- to the high-frequency range (frequency > 1 kHz). Comparing to the noise measurements shows that mid-

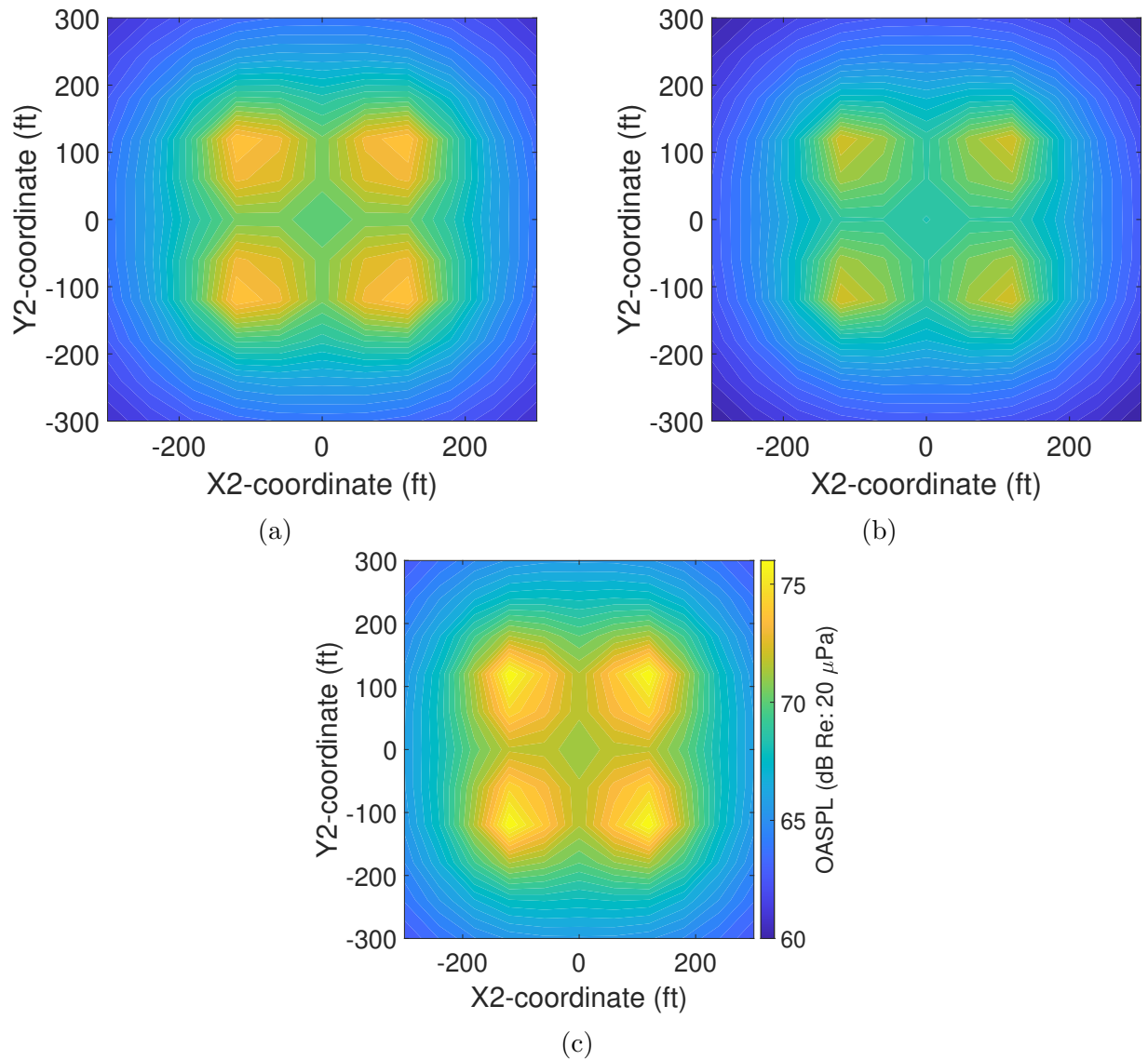


Figure 6.10: Predicted broadband noise OASPL from the 4-FATO Gannett Fleming [40] vertiport: (a) quadcopter, (b) side-by-side, and (c) lift+cruise.

to high-frequency broadband noise of UAM VTOL aircraft is not masked in urban community environments, and future investigation on broadband noise reduction is recommended for UAM VTOLs.

2. With the same payload operating at the altitude of 250 ft, multi-rotor UAM vehicle broadband noise is about 10 dB lower than conventional single rotor helicopter noise. However, 10 dB noise reduction may not be sufficient to meet public acceptance of

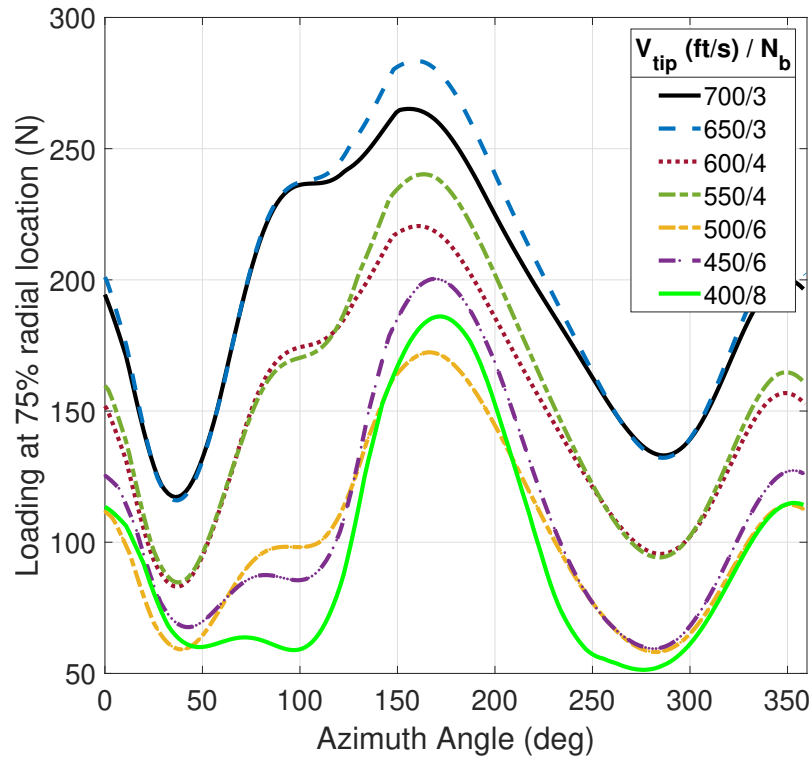
UAM vehicles. For the same mission specifications, broadband noise of the quadrotor design is slightly higher than that of the side-by-side design, and the lift-cruise design has a considerable broadband noise increase compared to the other two designs.

3. Amplitude modulation of broadband noise on a single rotor is weak when the observer distance is larger than 4 rotor radii at an elevation angle of -45° . Increasing the number of blades increases the number of amplitude modulations, but with reduced amplitudes. Multi-rotor vehicles have weaker amplitude modulations, since the blade radius is decreased compared to the single rotors with the same swept area, which is a benefit of choosing multi-rotor designs.
4. Noise contours from a vertiport design demonstrate the increase in broadband noise level when multiple UAM VTOL vehicles are operated simultaneously.

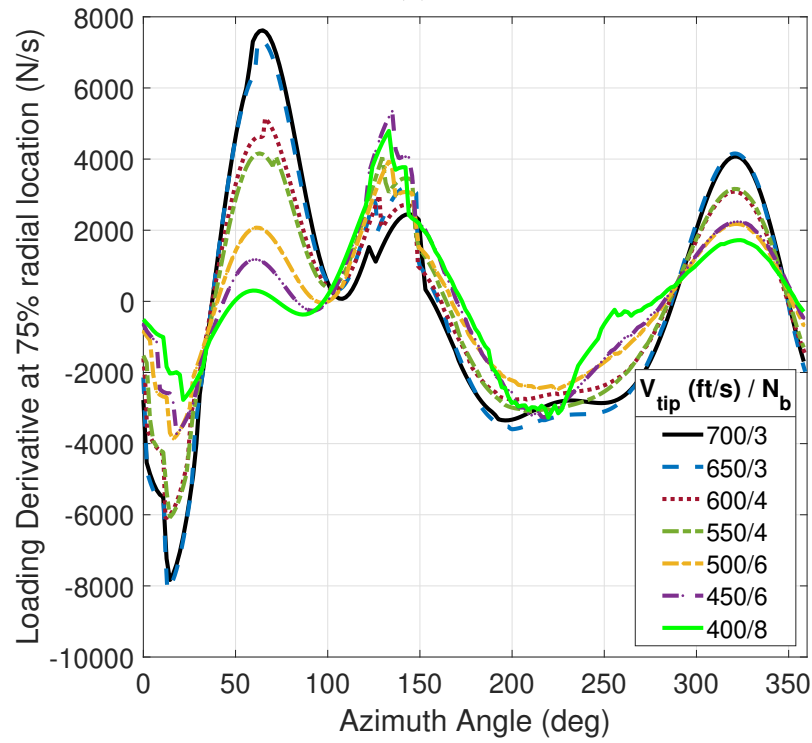
Chapter 7

Forward Flight Rotor Tonal Noise, Broadband Noise, and Psychoacoustics

The quiet air taxi designs are investigated in this chapter for their tonal noise, broadband noise, and psychoacoustic analyses in forward flight. Table 7.1 shows the quiet air taxi conceptual configurations designed by Johnson [45] with different rotational tip speeds while maintaining the same disk loading and forward speed. With the reduced blade tip speed, the rotor solidity is increased by increasing the number of blades to maintain the same payload. Therefore, the acoustics analysis in this research includes the combined effects of multiple design and operating parameters. The current study shows the acoustic analysis at the same mission specification with different rotor blade designs. The blade sectional loading force and derivative at 75% radial location are shown in Fig. 7.1 for the seven configurations. As the number of blades increases, the loading force on one blade decreases. With the same number of blades, the lower tip speed design has the slightly higher loading force because of the larger chord length. The higher tip speed design gives the higher loading derivative, which results in the higher loading noise from one blade.



(a)



(b)

Figure 7.1: Aerodynamic predictions for seven designs over one revolution of the single blade at the 75% radial section: (a) loading force, and (b) loading derivative.

Table 7.1: Quiet air taxi rotor design configurations [45].

Rotational Tip Speed (ft/s)	700	650	600	550	500	450	400
Rotor radius (ft)	16.96	17.07	17.09	17.25	17.27	17.64	18.39
Number of blades	3	3	4	4	6	6	8
Solidity	0.0411	0.0477	0.0559	0.0666	0.0805	0.0994	0.1258
Advance ratio	0.246	0.269	0.29	0.319	0.361	0.395	0.411
Blade passing frequency (Hz)	19.7	18.2	22.4	20.3	27.6	24.4	27.7

7.1 Tonal and Broadband Noise Comparison

The tonal and broadband noise predictions at the downward position are shown in Fig. 7.2, where A-weighting is applied for the adjustment of human hearing. The total noise level is the logarithmic summation of tonal and broadband noise. It is seen that the high tip speed designs of 700, 650, 600, and 550 ft/s rotors have higher tonal noise levels than the lower tip speed designs due to the increased blade loading derivative and the associated loading noise. Thickness noise is weak when the observer is directly beneath the rotor. However, an increase in tonal noise is observed from the tip speed of 650 to 600 ft/s, and from 500 to 450 ft/s, due to the acoustic destructive and constructive interferences between the blades, which will be discussed later. On the other hand, since broadband noise is highly dependent on the tip speed, the broadband noise level is observed to decrease linearly with decreasing the rotor tip speed. For the designs with the tip speeds of 550 ft/s and 600 ft/s, the tonal noise OASPL is higher than that of broadband noise, while the broadband noise level significantly exceeds tonal noise for the low tip speed designs. In the current study, since tonal noise is dominated by the first BPF, which is less than 100 Hz, A-weighting significantly reduces the tonal noise levels as shown in Fig. 7.2(b). However, since broadband noise has its peak levels

near 2 kHz frequency, A-weighting has little effect on its noise levels. Therefore, broadband noise is demonstrated to be the dominant noise source in terms of human hearing at the downward position.

A recent study by Silva and Johnson, which examined these seven helicopter designs in flyover, showed that reducing the tip speed significantly reduces the effective perceived noise level (EPNL) until 500 ft/s, while the noise reduction is less effective below that tip speed [45, 77]. However, they did not show the detailed breakdown of noise levels or an in-depth study on the noise trends. We observed a similar trend in Fig. 7.2, where the noise level is greatly reduced from the tip speed of 550 ft/s to 500 ft/s, and the noise reduction is ineffective below 500 ft/s tip speed. This sudden noise drop at 500 ft/s is due to the change of the number of blades from 4 blades to 6 blades, which significantly reduces the blade loading and the associated loading noise. Our study provides more in-depth analyses on the noise trends of the quiet helicopter in flyover and the detailed breakdown of noise contributions, which will continue to be discussed in the subsequent paragraphs and sections.

The acoustic pressures of the loading noise predicted on the cases of design tip speeds of 600 ft/s (4 blades) and 650 ft/s (3 blades) are shown in Figs. 7.3 and 7.4, where the time windows of one rotor revolution are used. The loading noise acoustic pressure contributions from each individual blade as well as the total acoustic pressure are shown in the same observer time range. It is observed that although the acoustic pressure peak of a single blade of the 600 ft/s tip speed case is lower than that of the 650 ft/s tip speed case, the 600 ft/s tip speed case has the higher total loading noise acoustic pressure when including all the blades due to the constructive interference. The destructive interference is seen on the 650 ft/s tip speed case, where the positive pressure peak of one blade is superimposed

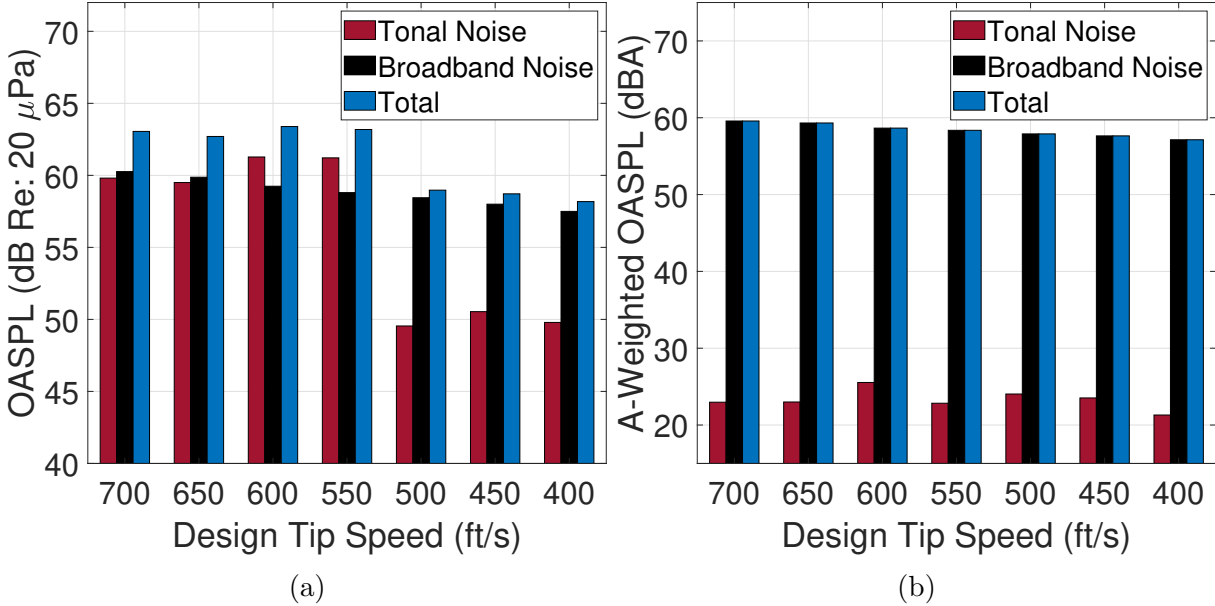


Figure 7.2: Predictions of tonal and broadband noise of the quiet air taxi designs at -90° elevation angle and 492 ft observer-hub distance: (a) OASPL, and (b) A-weighted OASPL.

with the negative pressure peak of another blade at the same observer time. Note that the destructive interference depends on the observer position, and this effect may not appear at other observer positions.

The narrow-band SPL predictions of broadband noise for the air taxi conceptual designs are given in Fig. 7.5, where the high-frequency noise level increases with the higher design tip speeds. Below 1 kHz, the minimum broadband noise level is found at the tip speed of 500 ft/s, which resulted from the combined effects of the number of blades and the design tip speeds. However, the difference of the broadband noise level at low frequencies among various designs is small. It is also confirmed that the broadband noise peaks are near 2 kHz frequency, which is the most sensitive frequency range for human hearing.

At a different observer location of -45° elevation angle and observer-hub distance of 492 ft in front of the rotor, tonal noise and broadband noise are predicted for the seven conceptual designs as shown in Fig. 7.6. Compared to the observer directly beneath the

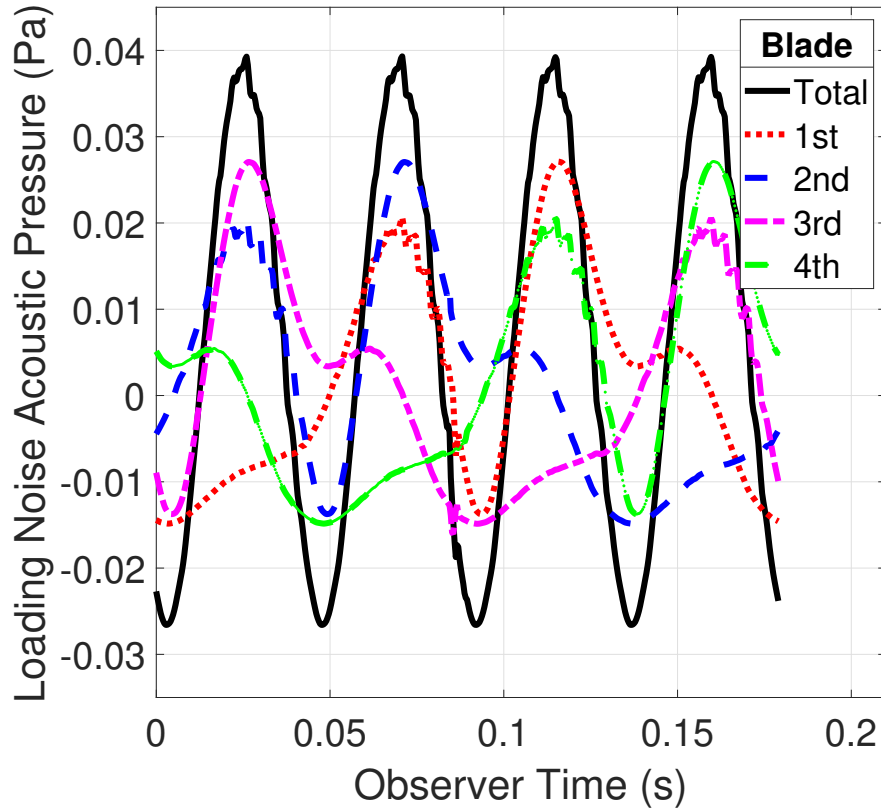


Figure 7.3: The loading noise acoustic pressure time histories from each blade and from the entire rotor (total) for the design tip speed of 600 ft/s. The observer is at -90° elevation angle and 492 ft observer-hub distance.

rotor, the observer at -45° elevation angle experiences significantly higher tonal noise due to the presence of the thickness noise that propagates in the forward direction. Broadband noise level is reduced at -45° elevation angle compared to -90° since rotor broadband noise has the dipole directivity pattern with the maximum noise level at -90° elevation angle [15]. Broadband noise is significantly higher than tonal noise at 400 ft/s. A-weighting still shows the dominance of broadband noise in Fig. 7.6(b). Figure 7.7 shows that as the design tip speed is increased, low-frequency broadband noise decreases while high-frequency broadband noise increases. When the design tip speed is reduced, the blade chord length and the number of blades are increased, and the larger chord length results in the increase in the boundary layer thickness near the trailing edge and increases low-frequency broadband noise. Although

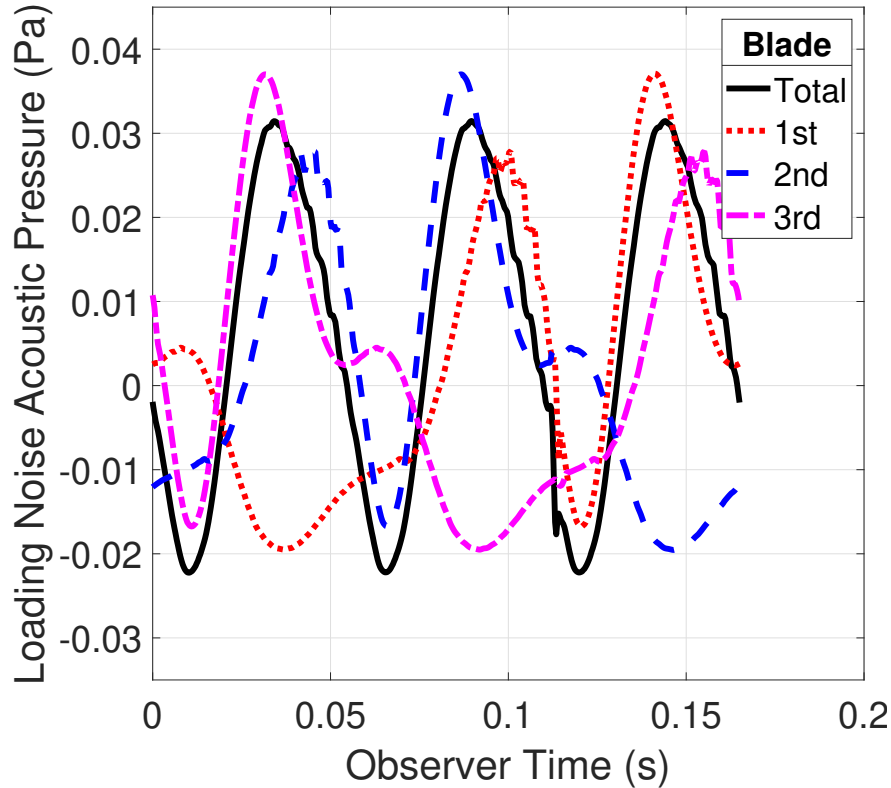


Figure 7.4: The loading noise acoustic pressure time histories from each blade and from the entire rotor (total) for the design tip speed of 650 ft/s. The observer is at -90° elevation angle and 492 ft observer-hub distance.

Fig. 7.7 shows the opposite trends for the low- and high-frequency ranges, the broadband noise OASPL uniformly increases with increasing the tip speed.

The tonal and broadband noise directivities of the 450 ft/s tip speed design are shown in Fig. 7.8 where the observer-hub distance is 5 rotor radii or 88.2 ft. This observer distance is much larger than the acoustics wavelength of 5.62 ft at 0.2 kHz, well below the frequency of interest in this study, and hence the far-field assumption in the broadband predictions is satisfied. With the same observer-hub distance, it is shown that the rear side has a higher broadband noise level than the forward side, since the motion of a source and an observer reduces the noise propagation distance towards the rear side and increases the propagation distance towards the forward side as the observer is attached to the rotor in forward flight. In

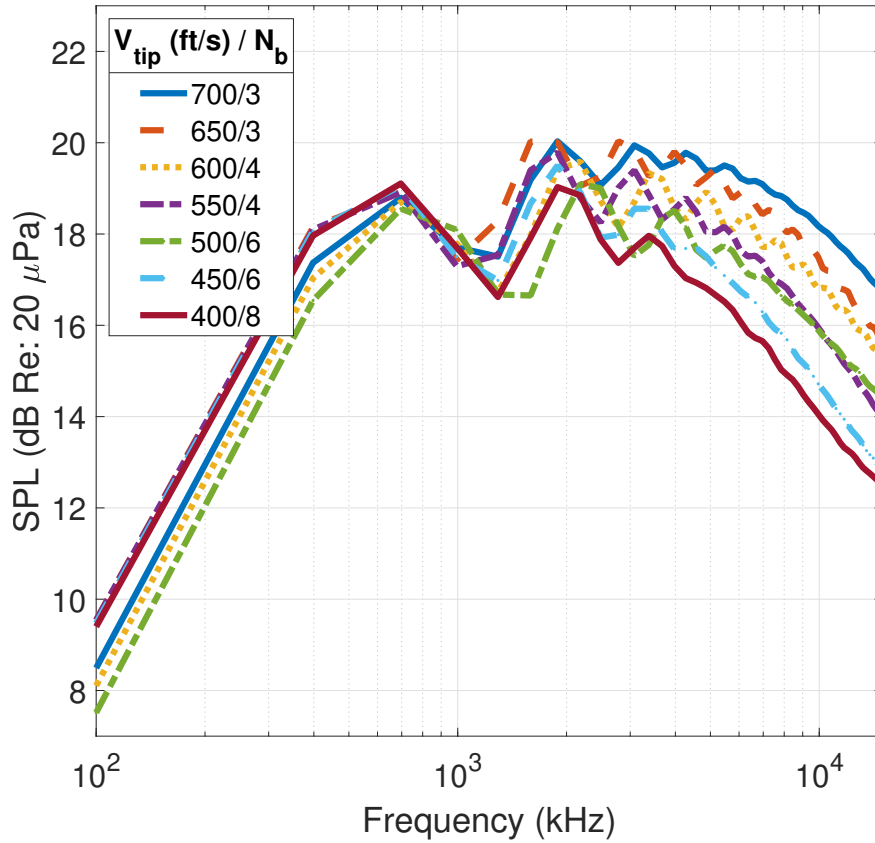


Figure 7.5: Narrow-band SPL predictions of broadband noise for the seven design cases at the elevation angle of -90° and 492 ft observer-hub distance.

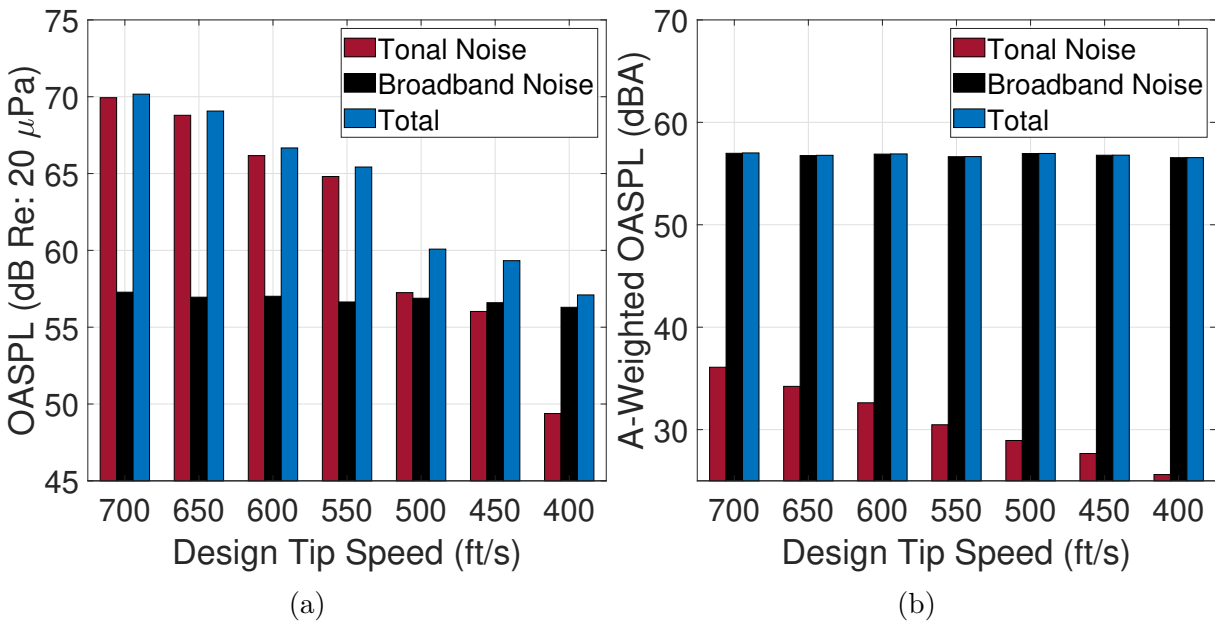


Figure 7.6: Predictions of tonal and broadband noise of the quiet air taxi designs at -45° elevation angle and 492 ft observer-hub distance: (a) OASPL, and (b) A-weighted OASPL.

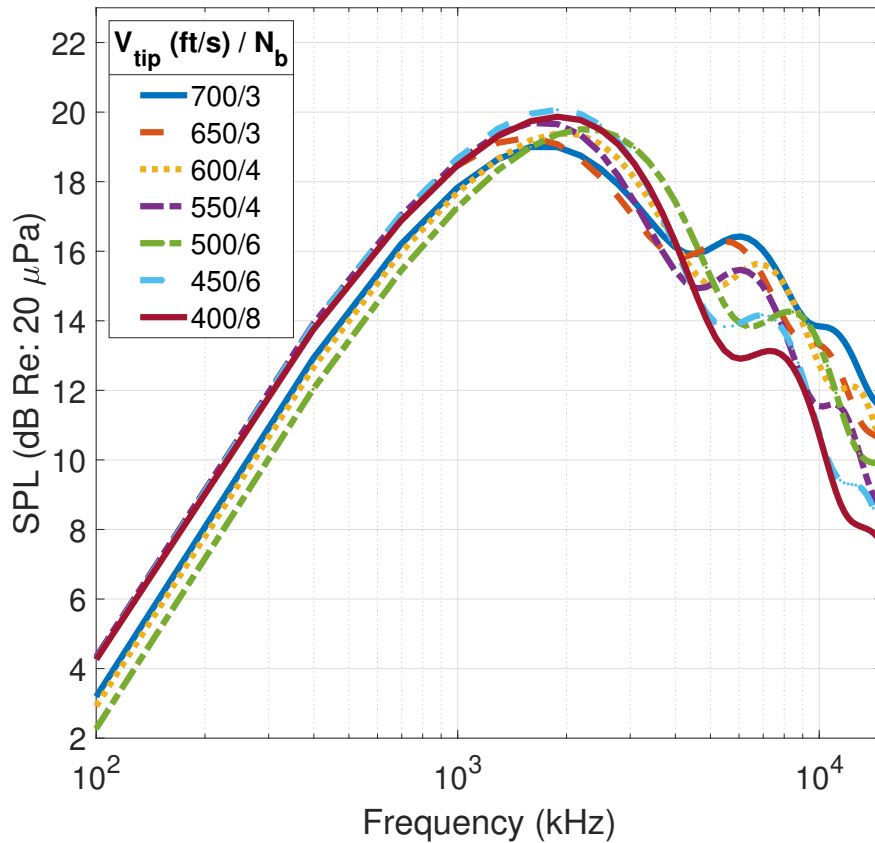


Figure 7.7: Narrow-band SPL predictions of broadband noise for the seven design cases at the elevation angle of -45° and 492 ft observer-hub distance at the forward position of the vehicle.

Fig. 7.8(b), broadband noise is biased towards the starboard side since the advancing blade has a higher local velocity (tip speed) than the retreating blade. Although the retreating blade experiences a higher local angle of attack, broadband noise does not increase much since the flow velocity effect is more dominant than the angle of attack for broadband noise. Tonal noise is observed to be dominant in the in-plane directions, primarily contributed by the presence of the thickness noise. Comparing their relative importance, broadband noise is more important to the observer underneath the vehicle while tonal noise is dominant in the forward direction. Tonal noise is shown to have the same directivity patterns in the forward and rear directions. Note that the broadband noise OASPL shown in Fig. 7.8 is not

weighted, and A-weighting will greatly reduce the tonal noise level. However, tonal noise is expected to maintain its dominance for the in-plane observers at a long observer distance since atmospheric absorption attenuates high-frequency broadband noise at large distances, which is not considered in the current study.

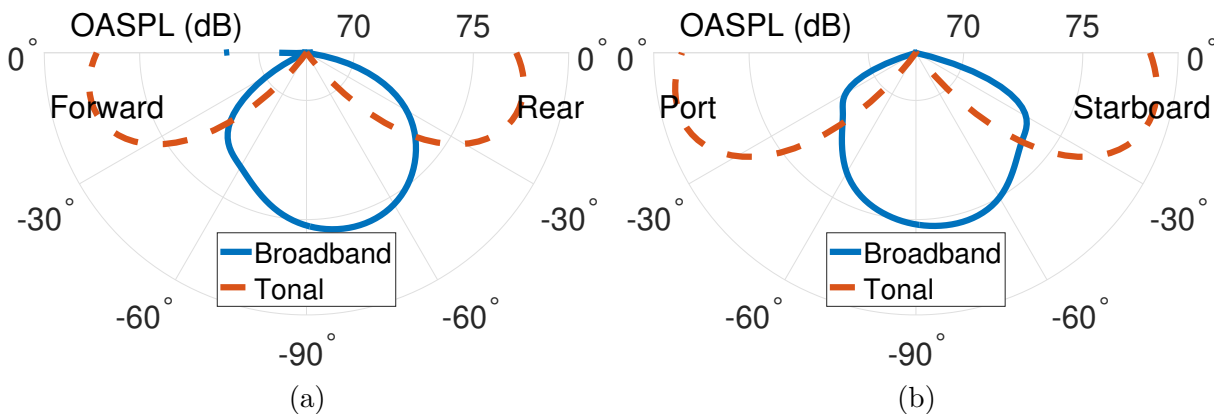


Figure 7.8: Noise directivity in the vehicle downward region of the design tip speed of 450 ft/s and the observer-hub distance of 5 rotor radii, with elevation angle in the longitudinal and lateral directions shown in the polar angle: (a) port side view, and (b) rear view.

The sectional OASPL contours of broadband noise generated by one blade over the rotation are shown in Fig. 7.9 to understand the noise distribution on the rotor disk. The rotor flight conditions are given in Table 7.1, and the observer is 492 ft away from the rotor hub at the elevation angle of -90° . The noise contours show that the OASPL increases with increasing the design tip speed. The starboard side generates broadband noise of about 10 dB higher than the retreating blade due to the higher flow speed on the advancing blade. Although Fig. 7.9 shows the noise contribution from one blade, the overall broadband noise from all the blades will provide the same conclusion that the lower design tip speed rotor with more blades results in lower broadband noise as shown in Fig. 7.2.

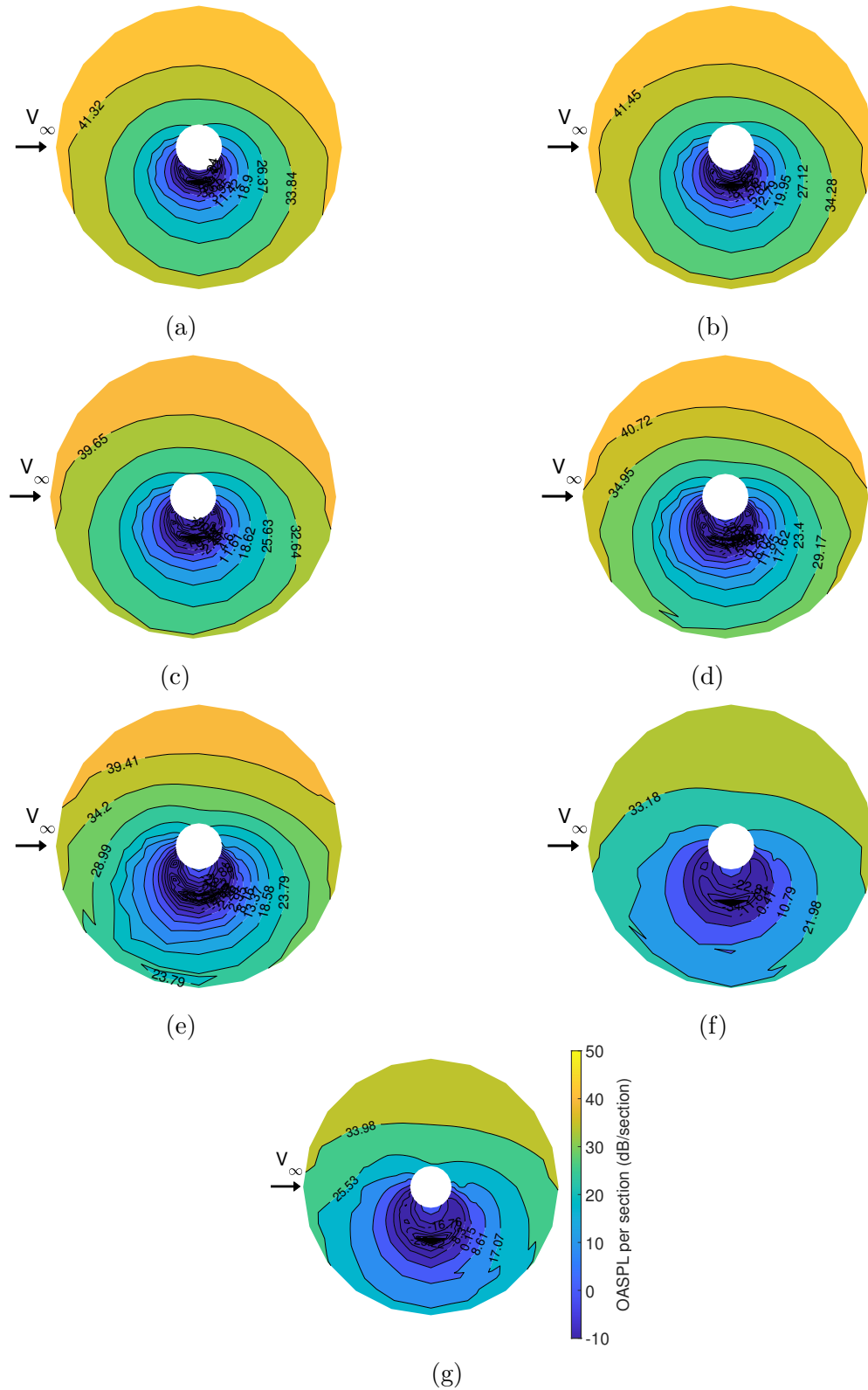


Figure 7.9: Sectional OASPL contours at the observer-hub distance of 492 ft and the elevation angle of -90° : (a) 700 ft/s, (b) 650 ft/s, (c) 600 ft/s, (d) 550 ft/s, (e) 500 ft/s, (f) 450 ft/s, and (g) 400 ft/s.

The contours of the boundary layer parameters for the 700 ft/s tip speed case are shown in Fig. 7.10 to understand the broadband noise source distributions. Note that the boundary layer parameters, such as the boundary layer edge velocity, boundary layer thickness, pressure gradient, skin friction coefficient, etc., are used in Lee's empirical wall pressure spectrum model [36], which is an input to the Amiet trailing-edge noise model [28]. The parameters are taken at 99% of the chord length, which are used to calculate trailing-edge noise. The advancing side is shown to have significantly larger boundary layer edge velocity than the retreating side, which makes the higher broadband noise level on the advancing side as shown in Fig. 7.8. The upper surface of the advancing side has smaller displacement thickness values than the retreating side due to the lower cyclic pitch or lower angle of attack. The inboard region on the retreating side shows the large displacement thickness due to the reverse flow, but the noise contribution from this inboard region is relatively small due to the smaller velocity. The pressure gradient contours show a similar trend as the boundary layer edge velocity since the two parameters are proportionally related. The pressure gradient contours show a discontinuity at the blade tip section where the two different airfoils are connected at the 90% radial position: VR12 airfoil inboard of 90% and SSCA09 airfoil outboard. Since the values of the skin friction coefficient are not in the same order of magnitude on the rotor disk, especially in the inboard region of the retreating side, the contours of $\log(C_f)$ are depicted in Fig. 7.10. It is shown that the skin friction coefficient has a complex trend on the upper surface, and the discontinuity near the tip region comes from the change of the airfoils. The effect of the boundary layer edge velocity is more dominant than the skin friction coefficient for trailing-edge noise.

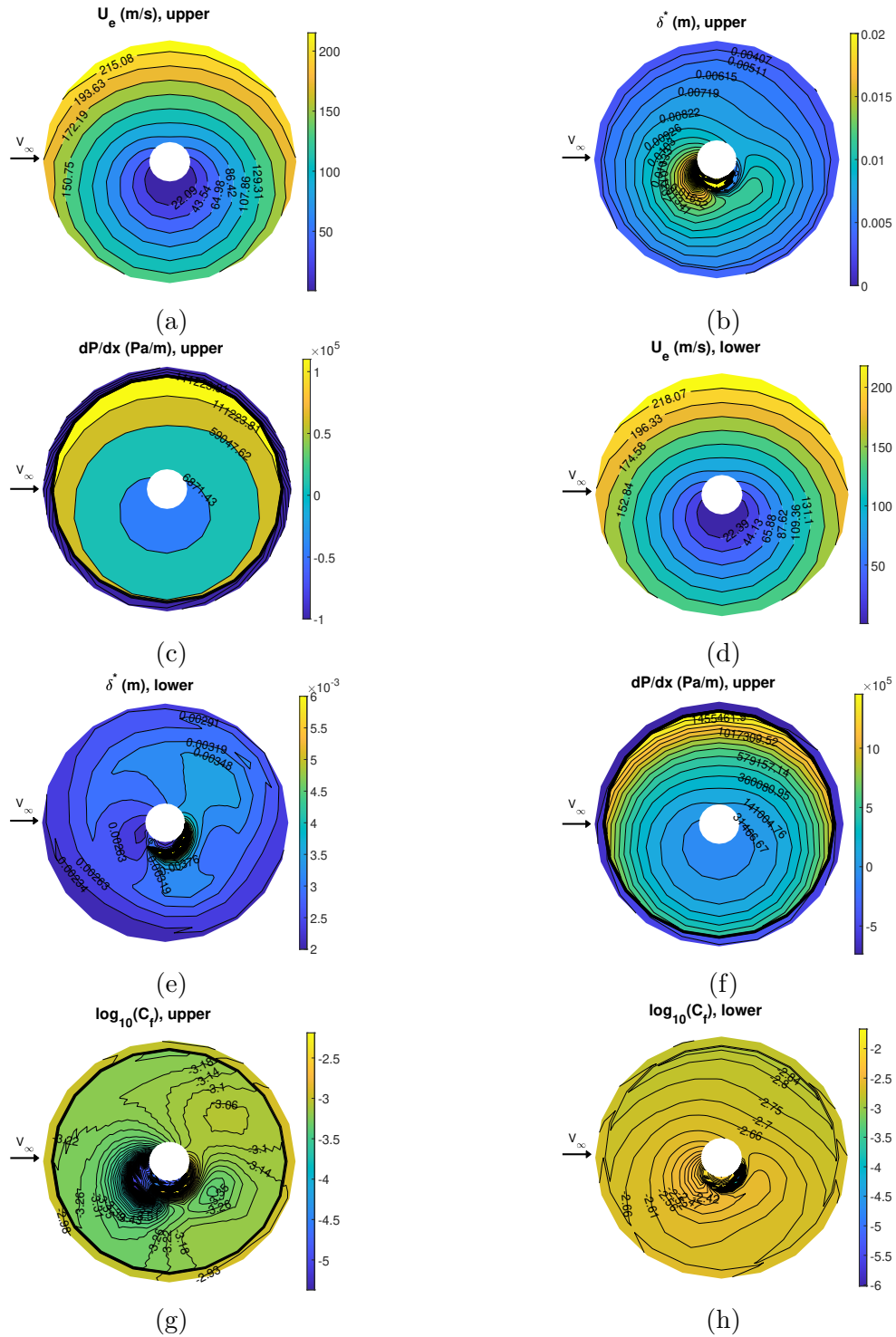


Figure 7.10: Contours of the boundary layer parameters taken at 99% of the blade chord length for the 700 ft/s tip speed case: (a) boundary layer edge velocity on the upper surface, (b) displacement thickness on the upper surface, (c) chord-wise pressure gradient on the upper surface, (d) boundary layer edge velocity on the lower surface, (e) displacement thickness on the lower surface, (f) chord-wise pressure gradient on the lower surface, (g) skin friction coefficient on the upper surface, and (h) skin friction coefficient on the lower surface.

7.2 Effect of Advance Ratio

The air taxi configuration of 450 ft/s blade tip speed is used to study the effect of advance ratio on its acoustics. The observer is 492 ft from the rotor hub with the elevation angle of -90° (downward position), and the observer moves along with the vehicle. The advance ratio is varied from 0.25 to the maximum design advance ratio of 0.442. As we use fixed-RPM with variable pitch for the rotor, the higher advance ratio represents the higher forward speed. The rotor trim solutions are found for each value of the advance ratio. It is seen in Fig. 7.11 that both tonal noise and broadband noise increase proportionally with increasing the advance ratio, and the relative importance between tonal noise and broadband noise remains unchanged. It is interesting to observe that the difference between tonal and broadband noise remains the same for the varied advance ratios, which suggests the same forward-speed scaling for the two noise sources. The narrow-band SPL of broadband noise is shown in Fig. 7.12 where broadband noise increases in the entire frequency range with increasing the advance ratio. According to the lateral moment balance of the vehicle, the increasing advance ratio results in a higher local velocity and a lower angle of attack on the advancing side, and a lower local velocity and a higher angle of attack on the retreating side. Since the flow speed is the primary effect on broadband noise, the increased velocity on the advancing side contributes to higher broadband noise. In addition, tonal noise increases with the higher forward speed due to the larger blade loading and loading derivative on the advancing blade.

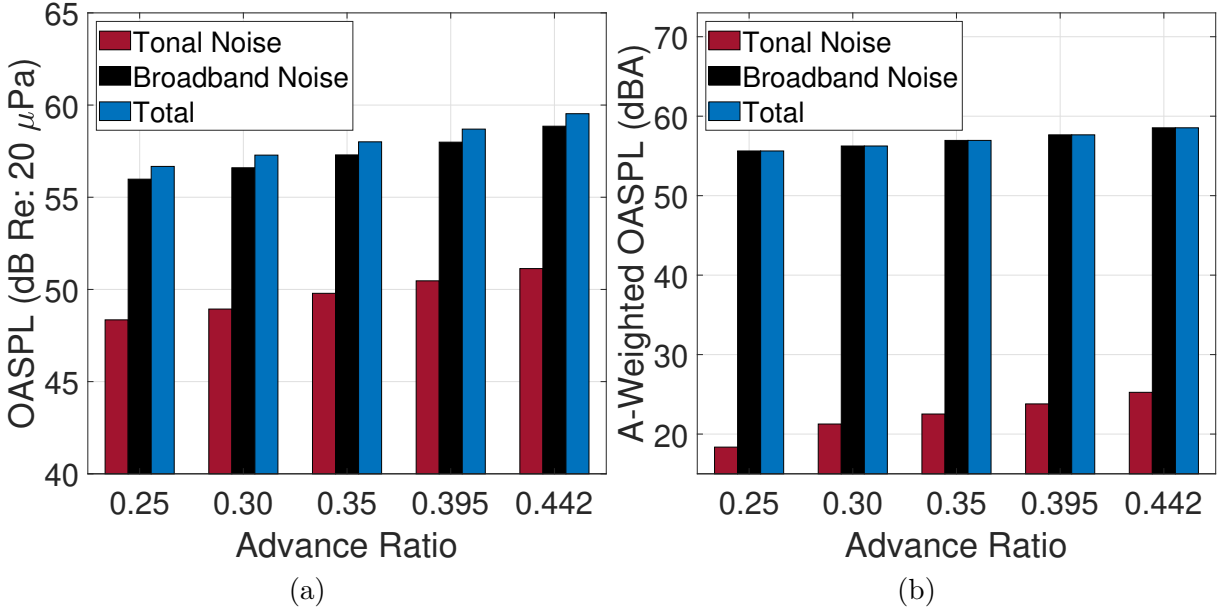


Figure 7.11: Predictions of tonal and broadband noise of the 450 ft/s tip speed design for varied advance ratios at -90° elevation angle and 492 ft observer-hub distance: (a) OASPL, and (b) A-weighted OASPL.

7.3 Broadband Noise Amplitude Modulation and Psychoacoustics

The amplitude modulations of broadband noise are calculated on the seven air taxi designs listed in Table 7.1, and the time range for all the test cases is 2 rotor revolutions. The observer is 5 rotor radii from the rotor hub, and the elevation angle is -45° in the forward direction. The time variations of the noise spectrum are shown in Fig. 7.13, where the number of noise peaks corresponds to the number of blade passages in two revolutions. The noise spectrum shows that the characteristics of the modulations diminishes with increasing the number of blades and decreasing the design tip speed. To quantify the significance of the fluctuations in psychoacoustic perspective, the fluctuation strength and the roughness of the seven cases are calculated using Eqs. (3.27) and (3.28) in and shown Figs. 7.14 and 7.15. Although the 650 ft/s tip speed design has lower noise levels than the 700 ft/s case,

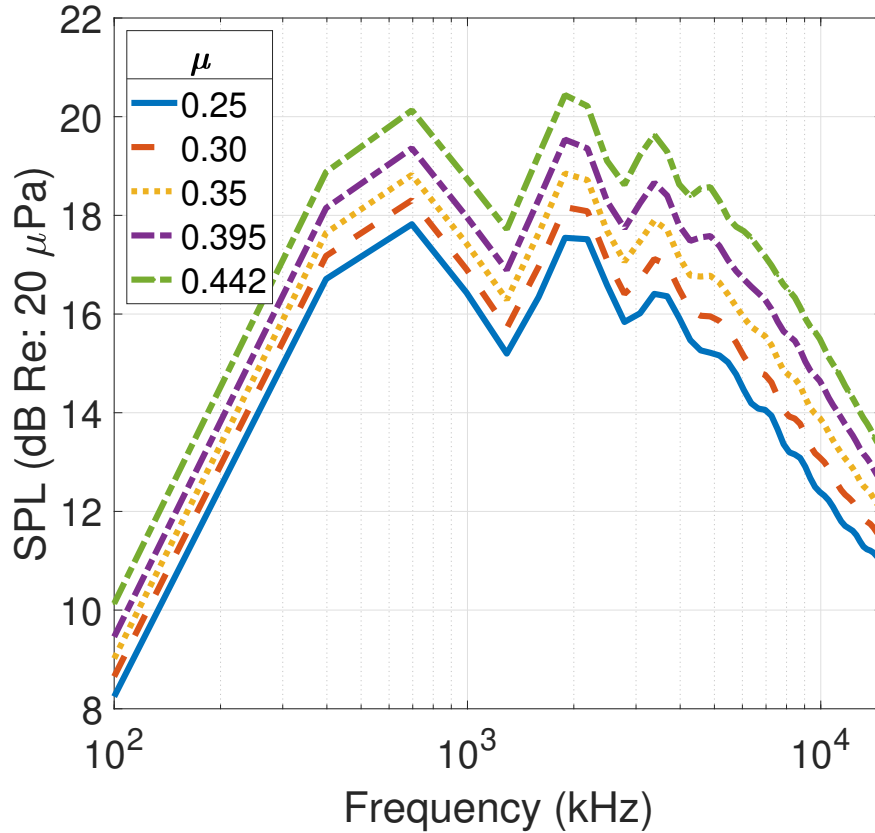


Figure 7.12: Narrow-band SPL predictions of broadband noise of the 450 ft/s tip speed design for varied advance ratios at -90° elevation angle and 492 ft observer-hub distance.

its blade passing frequency is lower than the latter, hence its fluctuation strength is higher in Fig. 7.14. Figure 7.14 also shows that the fluctuation strength becomes negative, or negligible, for the design tip speed lower than 600 ft/s, which occurs when the modulation depth ΔL is less than 3.52 dB as discussed in to Eq. (3.27). These small modulation depths are attributed to two factors. First, the maximum noise peaks are reduced for the low tip speed cases. Second, the high modulation frequencies with more blades make the edge of the noise signature of one blade closely overlap with those of its adjacent blades so that the modulation events are less visible as shown in Fig. 7.13. Figure 7.15 shows that the rotor designs with the higher tip speeds and fewer blades create a more severe sensation of roughness. Given that all seven cases achieve the same missions, low-RPM rotors with

more blades are preferable from a psychoacoustic point of view. Note that fluctuation and roughness considered in this chapter are two factors to evaluate the annoyance of rotorcraft noise, and other factors, such as loudness and tonality, can also affect the annoyance level [144].

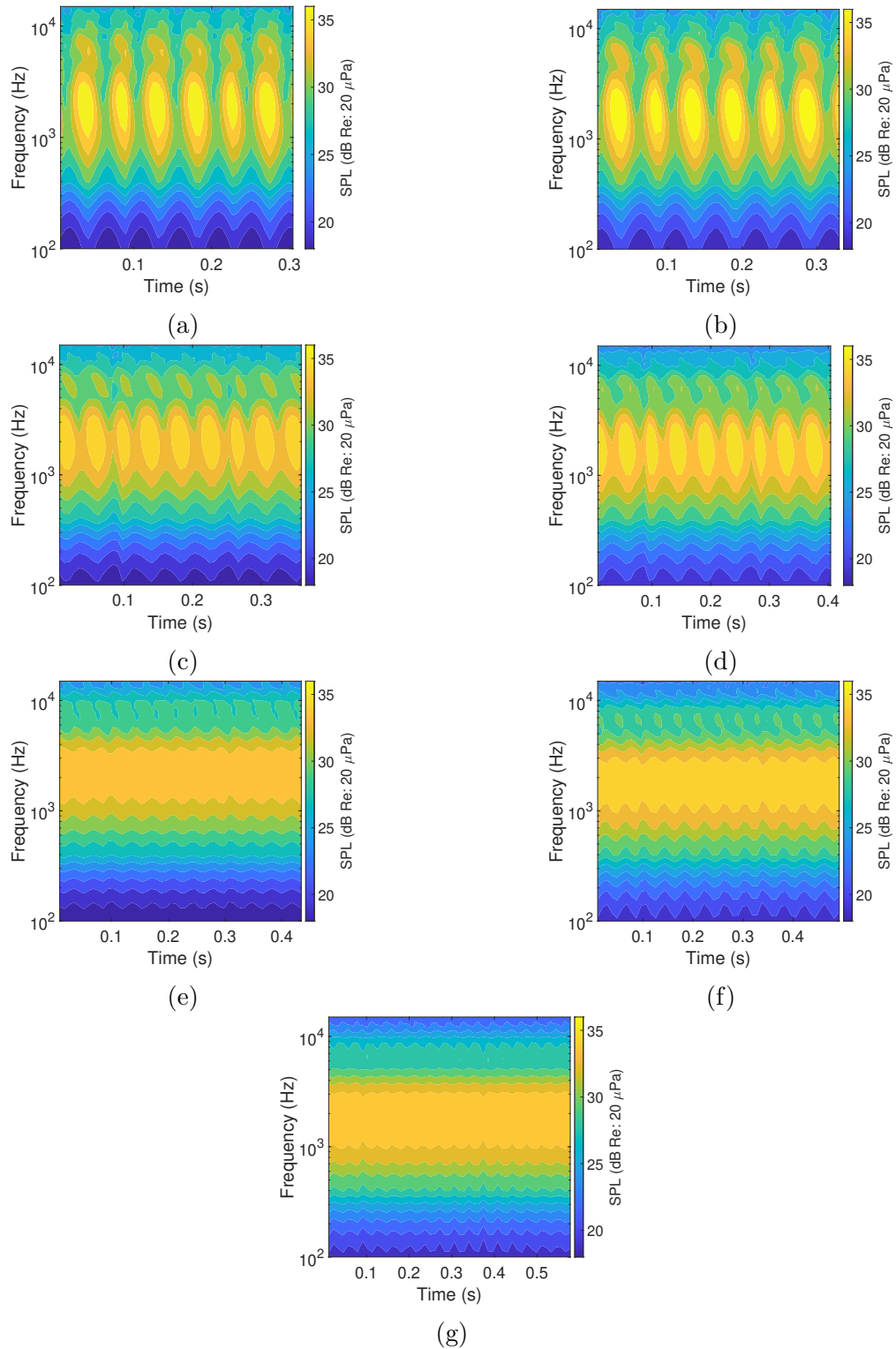


Figure 7.13: Time variation of the broadband noise spectrum at 5 rotor radii observer distance and -45° forward elevation angle for the design tip speeds of: (a) 700 ft/s, (b) 650 ft/s, (c) 600 ft/s, (d) 550 ft/s, (e) 500 ft/s, (f) 450 ft/s, and (g) 400 ft/s.

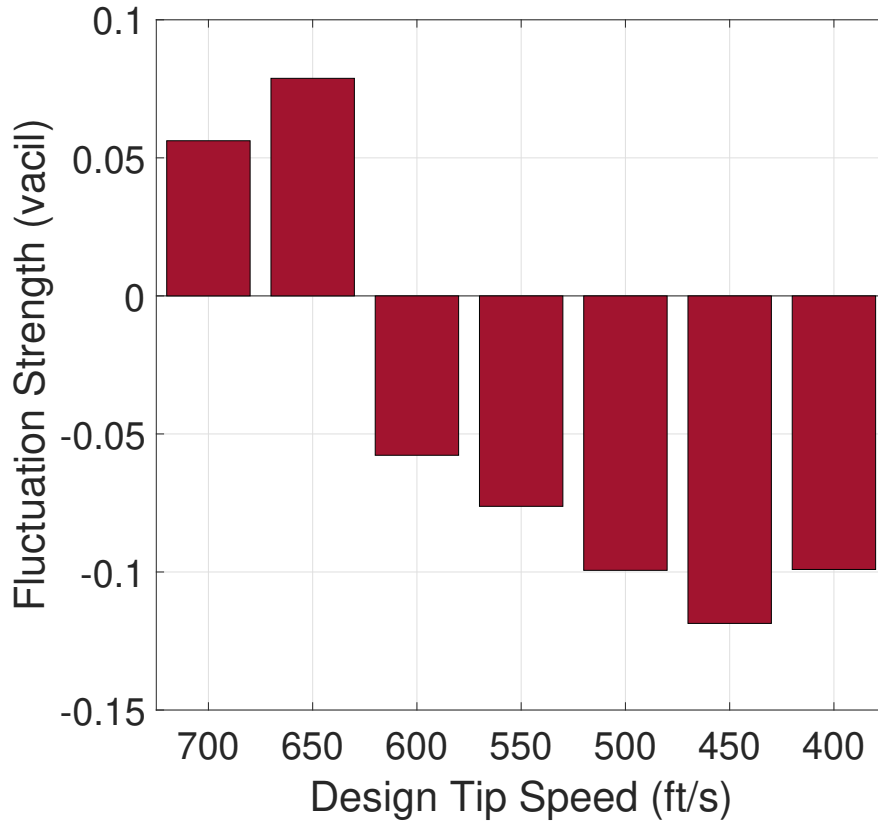


Figure 7.14: Fluctuation strengths of the rotor designs at 5 rotor radii observer distance and -45° forward elevation angle.

7.4 Summary

The rotorcraft acoustics analysis procedure in forward flight was developed to predict both tonal noise and broadband noise as well as psychoacoustics. This method couples the dynamic-inflow blade element theory, PSU-WOPWOP, and UCD-QuietFly. The acoustic sources included in this study are the thickness noise, loading noise, trailing-edge noise, trailing-edge bluntness noise, and stall noise. The numerical method was applied to investigate acoustics of a quiet helicopter with seven rotor designs. The major findings are summarized as follows:

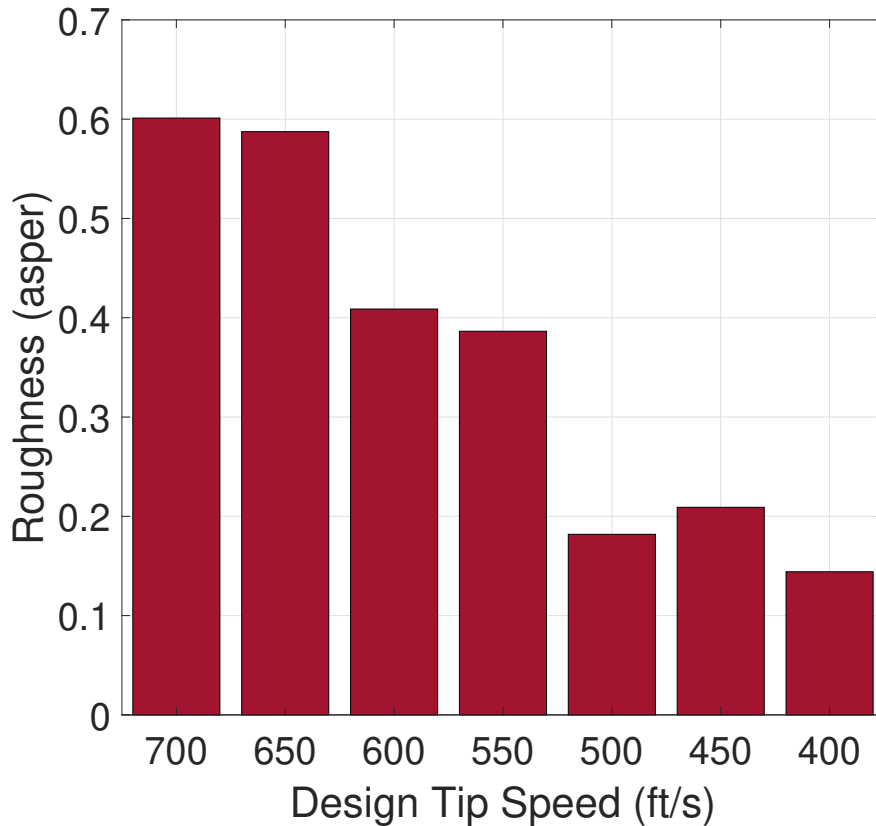


Figure 7.15: Roughness of the rotor designs at 5 rotor radii observer distance and -45° forward elevation angle.

- At the downward observer, broadband noise is the dominant noise source for the rotor designs with low tip speeds and more blades, while broadband noise and tonal noise have comparable noise levels for the rotors with high tip speeds and fewer blades. In the forward region of the rotor, tonal noise is the dominant noise source for the high-tip-speed design, while broadband noise and tonal noise have comparable noise levels for the rotors with low tip speeds.
- On the A-weighted sound pressure spectrum, broadband noise is demonstrated to be the dominant noise source in the out-of-plane directions. Note that blade-vortex-interaction noise and atmospheric absorption are not included in the current study, which may alter this conclusion when these effects are important.

- Broadband noise is demonstrated to be biased towards the rear and starboard directions due to the motion of a source and an observer and the higher velocity on the advancing blade. The noise contribution contours show the higher broadband noise contributions from the advancing side, primarily due to the boundary layer edge velocity.
- In the study of the effect of the advance ratio on the rotor acoustics, the relative importance of tonal noise and broadband noise remains unchanged for varying forward speeds. Both the tonal and broadband noise levels are shown to increase proportionally with increasing the advance ratio.
- Psychoacoustic metrics of the fluctuation strength and roughness were calculated based on the amplitude modulation of broadband noise. It was shown that the fluctuation strength was negligible when the modulation depth is less than 3.52 dB, which is more distinct at the high blade passing frequency with more blades. The sensations of both the fluctuation and roughness reduce with the decrease in the design tip speed. Therefore, the rotor designs with a low tip speed and more blades are preferable in terms of psychoacoustic metrics.

Chapter 8

Effects of Rotor Blade Ideal Twist and Tip Taper on Broadband Noise

At the same thrust coefficient, rotor blade twist and taper are varied to find their effects on broadband noise. This chapter compares the broadband noise differences between ideal twist and linear twist, and between tip taper and constant chord length.

8.1 Ideal Twist and Tip Taper

The effects of the blade twist and taper on rotor broadband noise are investigated, where the baseline case is the 5500 RPM ideally twisted rotor with the rough surface shown in Table 4.4. The baseline case has an ideal twist and a constant chord length. The parameters and performance coefficients of the three rotor cases are given in Table 8.1. The second rotor case has the same parameters as the baseline, except it has a linear twist of -10° . The third rotor case has a linear twisted of -10° and a 0.75 taper starting at $0.9 r/R$. The collective pitch angle of the three rotor cases is adjusted to maintain the constant thrust coefficient. The radial distributions of the blade section pitch angle are shown in Fig. 8.1 for the three rotor cases. The performance data are calculated using the BEMT, where the linearly twisted

rotor has a lower figure of merit than the ideally twisted rotor, and the tapered rotor has a higher figure of merit than the non-tapered rotors. Therefore, the designs of ideal twist and taper provide better performance. The three rotors have the same RPM in hovering conditions, and the observer is at -35° elevation angle and 2.27 m from the rotor hub.

Table 8.1: Parameters of twisted and tapered rotors

Rotor case	θ_{tw}	θ_0	taper location	taper ratio	RPM	C_T	FM	C_P	OASPL
Ideal twist + const. chord	Ideal	34.5	No	No	5500	1.37E-2	0.649	1.75E-3	69.78
Linear twist + const. chord	-10	19.09	No	No	5500	1.37E-2	0.640	1.77E-3	68.25
Linear twist + tip taper	-10	19.17	0.9 r/R	0.75	5500	1.37E-2	0.647	1.75E-3	64.82

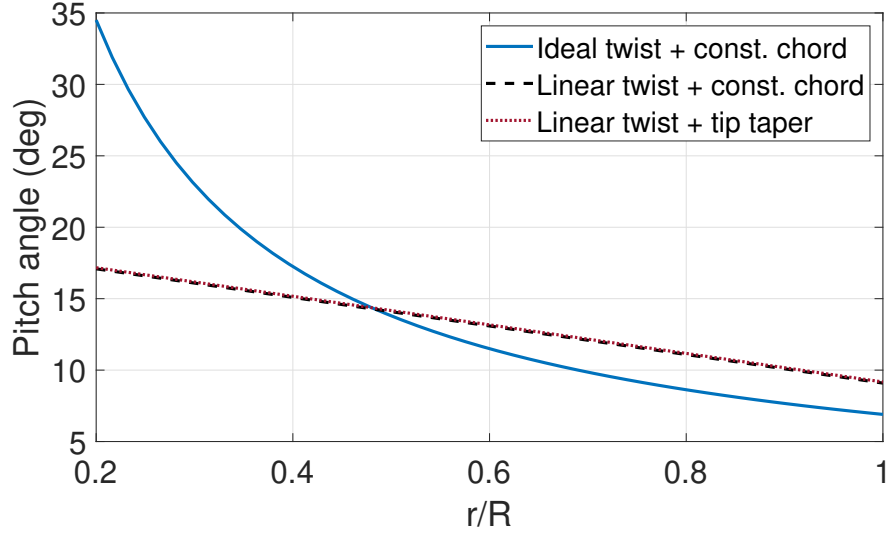


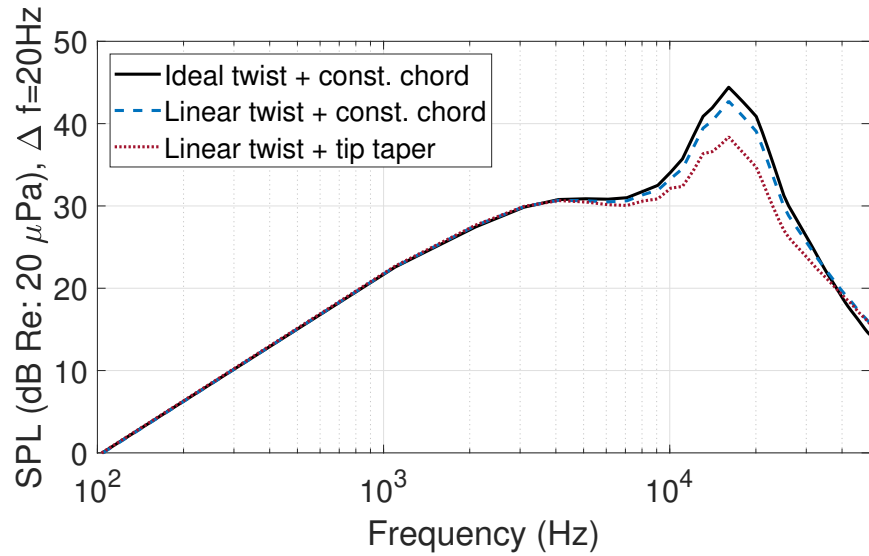
Figure 8.1: Spanwise distributions of pitch angle for the three rotor cases.

The broadband noise predictions from UCD-QuietFly are shown in Fig. 8.2, and the overall sound pressure levels (OASPLs) of the three rotors are given in Table 8.1. The ideally twisted rotor has the highest noise level, and the linearly twisted and tapered rotor has the lowest noise level. As shown in Fig. 8.2(a), the noise differences among the three rotors are primarily in the frequency range covered by LBL-VS noise (15 kHz). Figure 8.2(b) shows the sectional contributions of OASPL. Although the root sections of the ideally twisted rotor generate lower noise than the other two cases, its tip sections give higher noise levels. As seen in Fig. 8.3(b), the radial distribution of the boundary layer displacement thickness on the pressure side indicates that the ideally twisted rotor has the highest δ^* at the tip region due to higher angles of attack. This thicker pressure side boundary thickness explains the higher LBL-VS noise on the ideally twisted rotor according to Eq. (3.38), where the suction side boundary layer thickness is not used. The tapered rotor generates lower LBL-VS noise due to its small chord length and small pressure side boundary layer thickness at the blade tip regions. Figure 8.2(b) shows that the ideally twisted rotor generates lower noise at the

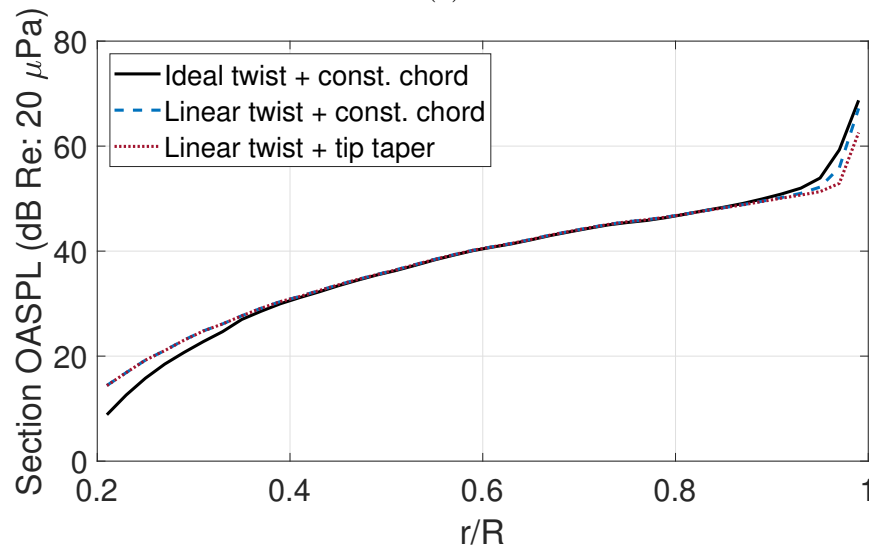
inboard regions, but its boundary layer displacement thickness on the suction side is large at the inboard regions. Although larger boundary layer displacement contributes to larger trailing-edge noise, the ideally twisted rotor has the large blade section pitch angle at the inboard regions, which results in its lower inboard sectional OASPL due to the directivity effect (away from the dipole directivity direction). Therefore, the effect of the ideal twist gives a slight increase of 1.53 dB in broadband noise level. On the other hand, the tip taper significantly reduced the broadband noise level by 3.43 dB.

8.2 Summary

This chapter presents the effects of rotor blade twist and taper on broadband noise. At the same thrust, the ideally twisted rotor is shown to have a slightly higher broadband noise level than the linearly twisted rotor. The tapered rotor blade tips can significantly reduce the broadband noise levels compared to the non-tapered blades.

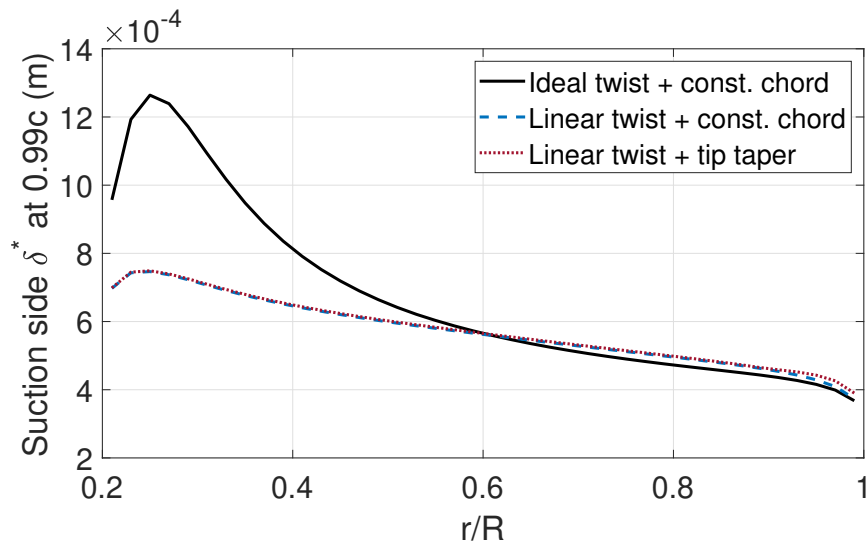


(a)

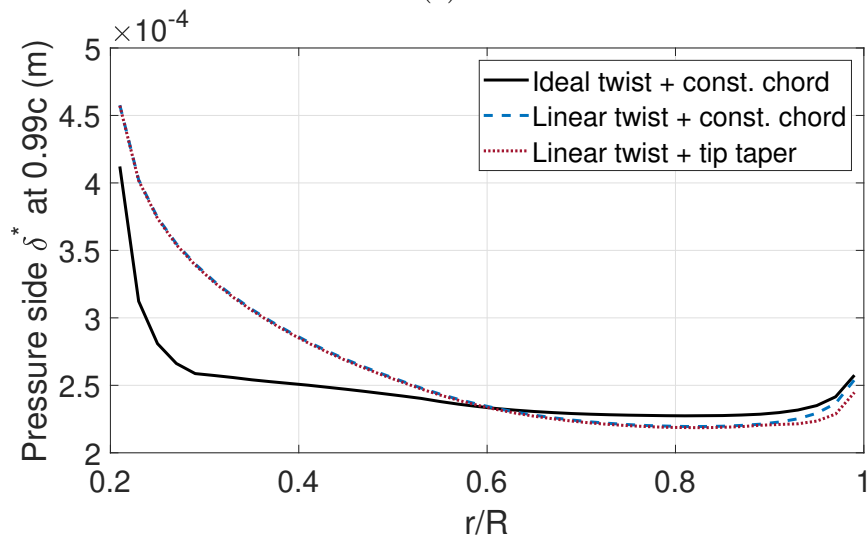


(b)

Figure 8.2: Comparisons of the acoustic effects of the blade ideal twist, linear twist, and taper on the rotor at a constant thrust: (b) sound pressure level (SPL) spectrum, and (c) overall sound pressure level (OASPL) contributions of the radial sections.



(a)



(b)

Figure 8.3: Comparisons of the boundary layer displacement thickness at a 0.99 chord location for the blade ideal twist, linear twist, and taper on the rotor at a constant thrust for: (a) suction side, and (b) pressure side.

Chapter 9

Applications of Trailing-Edge Serrations

Trailing-edge serrations are effective in reducing broadband noise. This chapter first presents the validations of the new prediction method for serrated rotors. The validation cases include an airfoil section, a hovering rotor, and a forward-flight rotor. The effects of the serration parameters on rotor broadband noise are studied, including the number of serrations, serration height, serration shape, serrations' starting r/R , and tip-to-root height ratio. Finally, the noise reductions using trailing-edge serrations are investigated on a UAM eVTOL quadrotor and a quiet helicopter.

9.1 Validations

This section first compares Amiet's model [28] and the modified Lyu and Ayton's model [90] on the calculations of trailing-edge noise on the straight wing section. The prediction of noise reduction on a serrated wing section is validated against the experiment. Second, broadband noise of two serrated-blade rotors, one in hovering flight and the other in forward flight, is calculated in UCD-QuietFly and validated against the experiments.

9.1.1 Serrated Wing Section

This section presents validations of the broadband noise predictions for straight and serrated wing sections and straight and serrated rotors. Table 9.1 shows the two cases of wing section validations. The first case is given in Fig. 9.1, where the modified Lyu and Ayton’s model is used to predict trailing-edge noise of a straight wing section, which is compared to the results of Amiet’s model. The overlapping of these two models demonstrates the correctness of our improvements shown in Eq. (3.40).

Table 9.1: Parameters for Validation of Trailing-Edge Noise from a Wing Section

Parameters	Verification (Fig. 9.1)	Verification (Fig. 9.2)	Validation (Fig. 9.3)
Airfoil	NACA 0012	NACA 0012	NACA 0018
TE geometry	straight	straight	serrated
V_0 (m/s)	241	241	34
α (deg)	1.8	1.8	0.0
c (m)	0.2	0.2	0.2
Δr (m)	0.15	0.15	0.4
r_o (m)	1 & 13	14.35	1.0548
θ_o (deg)	90	85.6	90
y (m)	0	6	0

Figure 9.2 shows the effect of the spanwise wavenumber k_y on a straight wing, where the original Lyu and Ayton’s model used $k_y = 2n\pi/l$ that did not account for the change of observer locations in the spanwise direction. The modified spanwise wavenumber of $k_y = ky/S_0 + 2\pi n/l$ is shown to give better agreements with the Amiet model on a straight trailing edge for observers at non-zero spanwise locations. This modification is important in rotorcraft applications, since the observers of interest can be located in the in-plane directions.

The predictions of trailing-edge noise of a serrated wing and a straight wing are provided in Fig. 9.3, where the experiment data is given [145]. The noise reduction, ΔSPL (sound

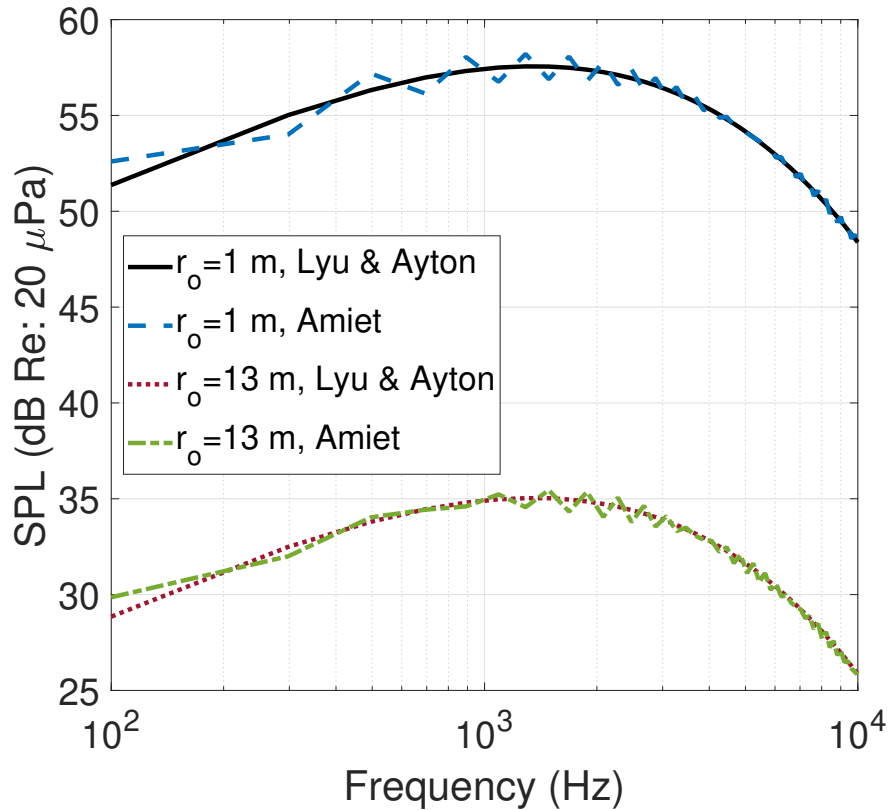


Figure 9.1: Comparison of Amiet’s model and Lyu and Ayton’s model on a straight wing section at different observer distances.

pressure level), is the Decibel difference between a straight blade and a serrated blade in the same conditions. Amiet’s model was used on the straight blade, while Lyu and Ayton’s model was used on the serrated blade in this validation study. It is seen that the noise reduction is predicted well at middle frequencies. The over-predictions of the noise reduction are observed in the high-frequency range, which is likely due to other noise sources in the experiment that are not included in the current acoustic model, such as misaligned small vortical flows at the serration root sections [146]. The existence of these additional sources is case-dependent.

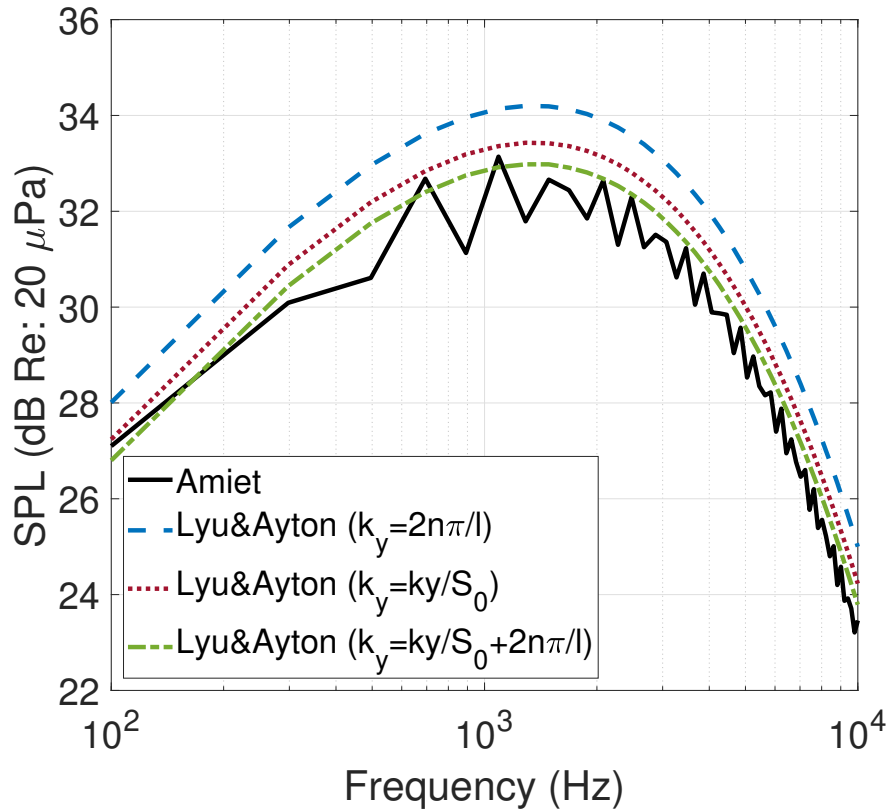


Figure 9.2: Effect of the spanwise wavenumber in Lyu & Ayton’s model on a straight wing section.

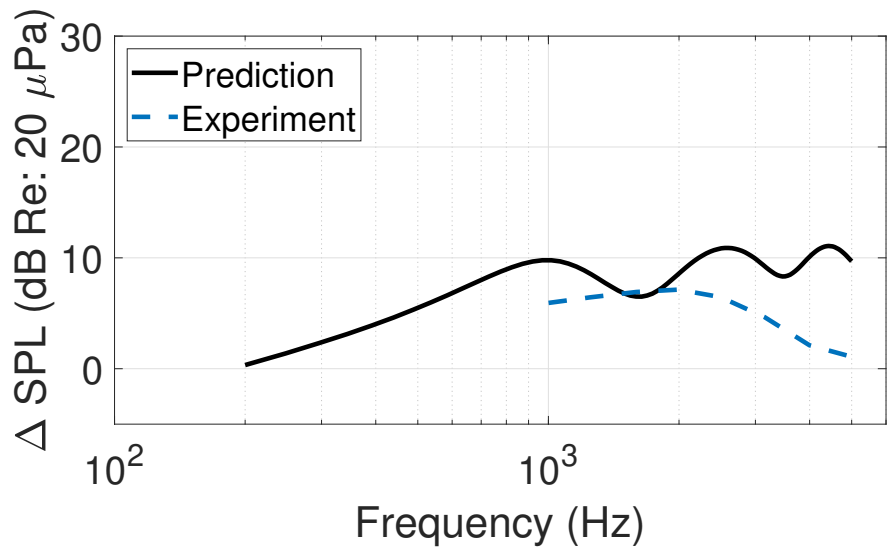


Figure 9.3: Noise reduction validation of the serrated trailing-edge noise model on the wing section. The serration shape is sawtooth, $2h = 0.04$ m, and $l = 0.02$ m. Experiment data is given in Ref. [145]

Table 9.2: Hovering Rotor Validation Parameters

Parameters	APC Slow Flyer 11X4.7
R (m)	0.14
N_b	2
RPM	3000
Airfoil	E63(hub)/ClarkY(tip)
ϕ_o (deg)	90
r_o (m)	1.65
Shape	Sawtooth
$2h$ (m)	0.006
l (m)	0.00322
serration r/R range	0.5-1.0

9.1.2 Serrated Rotor

A hovering rotor validation case is provided in Table 9.2, where an APC drone rotor is serrated from the mid-span to the tip. The experiment of a hovering rotor was conducted in an acoustic wind tunnel [104]. The microphone is 1.65 m directly above the rotor hub. The predictions of the rotor noise with straight and serrated trailing edges are given in Fig. 9.4. The predictions of the straight-blade rotor noise match the experiment very well. At the middle to high frequencies, the predictions of the serrated rotor noise give reasonable noise reductions compared to the experiment, while some under-predictions appear. In the low-frequency range, the serrated-rotor broadband noise is over-predicted, due to the limitation of Lyu and Ayton’s model in a small chord length. We found that blades with chord lengths larger than 0.1 m do not have this over-prediction issue at low frequencies. Overall, although the serrated trailing-edge noise predictions are not perfect compared to the experiment, they give reasonable predictions in noise reduction.

In addition to the broadband noise validation of a hovering rotor, broadband noise is predicted on a forward-flight eHANG rotor with serrated trailing edges. The eHANG drone

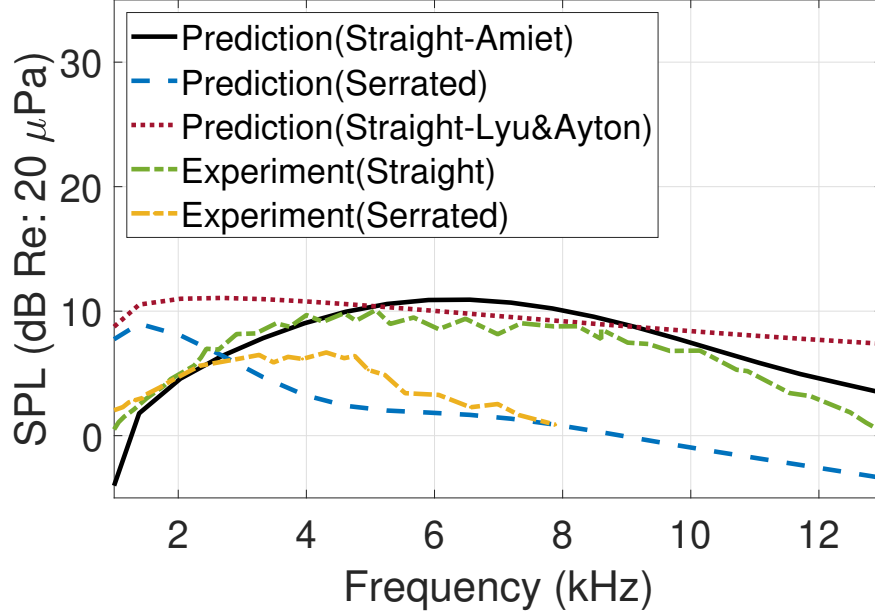


Figure 9.4: Validation of UCD-QuietFly on the serrated drone rotor. Experiment data is given in Ref. [104], with broadband components extracted.

Table 9.3: Forward Rotor Validation Parameters

Parameters	eHANG Ghost 3.0
R (m)	0.13
N_b	2
RPM	7200
μ	0.1931
α_{sh} (deg)	15
Airfoil	A18
ϕ_o (deg)	-56.31
ψ_o (deg)	180
r_o (m)	1.49
Shape	Saw-tooth
$2h$ (m)	0.00326
l (m)	0.00652
serration r/R range	0.2-1.0

rotor parameters are provided in Table. 9.3, where the acoustic measurements were taken in an anechoic wind tunnel [105]. The microphone is in the forward direction of the rotor, with an elevation angle of -56.31° , azimuthal angle of 180° , and a distance of 1.49 m. The tested rotor has saw-tooth serrations with a height to wavelength ratio, $2h/l$, of 0.5. The

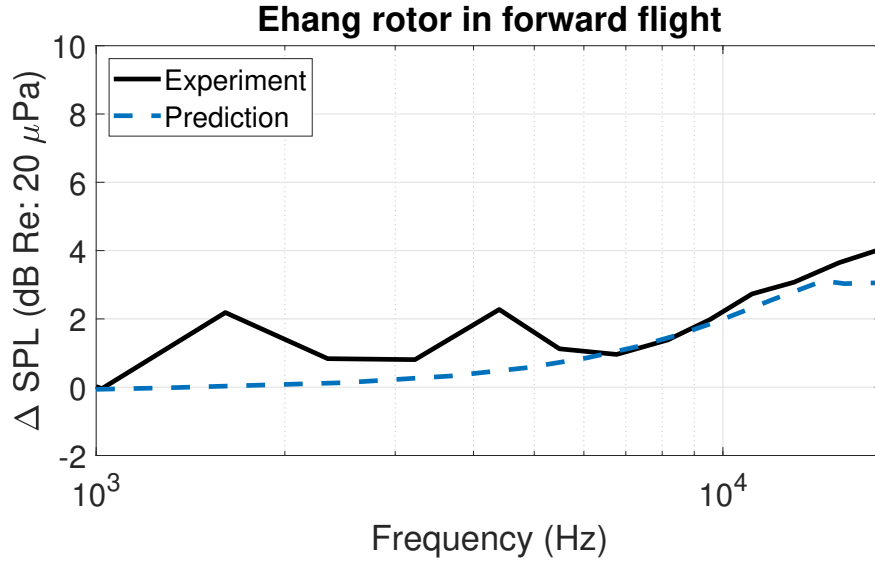


Figure 9.5: Validation of UCD-QuietFly on the serrated drone rotor in forward flight. Experiment data is given in Ref. [105], with broadband components extracted.

noise reduction between a serrated-blade rotor and a straight-blade rotor is predicted in Fig. 9.5 and compared against the experimental data. It is seen that the prediction has good agreement with the measurements, especially above 5 kHz, where apparent noise reductions are present.

9.2 Results

First, the serration effects on rotor broadband noise are assessed by varying the trailing-edge serration parameters: number of serrations, serrations' starting radial location, serration geometry, serration height, and tip-to-root height ratio. Next, the trailing-edge serrations are applied to NASA's UAM eVTOL quadcopter designs with varying tip speeds and blade numbers. The directivity of the serrated-blade quadrotor in hover is compared to the quadrotor with straight blades.

9.2.1 Effects of Serration Parameters

The baseline rotor case is an APC Slow Flyer drone rotor with serrated trailing edges, whose parameters are given in Table. 9.2. For each parameter studied, other parameters are kept as the baseline values. In this parameter study, the straight-blade rotor noise prediction is used as a reference, which is calculated using Lyu and Ayton’s model from the corresponding serration region outboard, and using Amiet’s model inboard. The purpose of this practice is to reduce computational time using the faster Amiet’s model for the inboard sections, which are less important acoustically. The noise difference between the straight-blade rotor and serrated-blade rotor (Δ OASPL) is calculated. Note that we use Lyu and Ayton’s model even for the straight blade at the outboard sections where the serrations would be located so that the noise comparison between the straight blade and the serrated blade is fair. The frequency range of summation for the OASPL (overall sound pressure level) is 0.1-13 kHz.

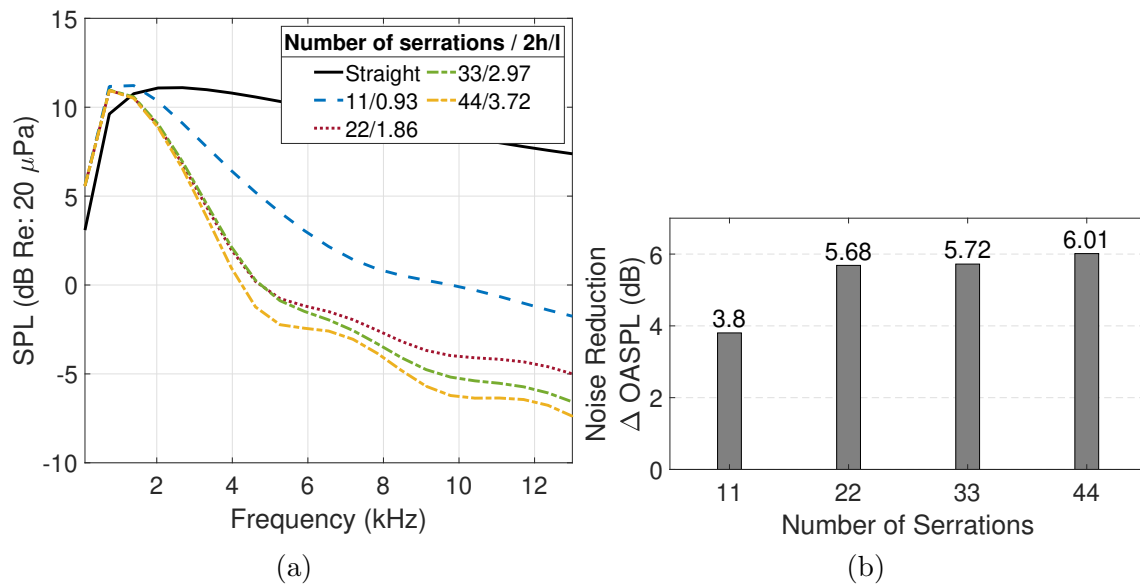


Figure 9.6: The effect of the number of serrations on rotor broadband noise: (a) sound pressure level spectrum and (b) noise reduction compared to the straight-blade rotor.

The effect of varying the number of serrations is shown in Fig. 9.6, where the rotor

trailing edges have saw-tooth serrations from its 50 % radial position to the tip. As the number of serrations increases, the serration wavelength is shortened, which can also be seen as the effect of changing the serration wavelength. The frequency spectrum of SPL in Fig. 9.6(a) shows that noise reductions occur in the mid- to high-frequency range (above 2.5 kHz), while noise increases are seen in the low frequencies. Increasing the number of serrations (or reducing the serration wavelength) reduces the noise level. However, as more serration shapes are added, the effectiveness of noise reduction is reduced. With more serrations or the shorter wavelength, the destructive interference on the rotor blade is increased, since the modal coefficient in Eq. (3.42) gets more oscillations with more serrations on the blade span. Therefore, considering the manufacturing and structural challenges, 22 serrations ($2h/l=2$) are desirable although more serrations slightly improve the noise reduction.

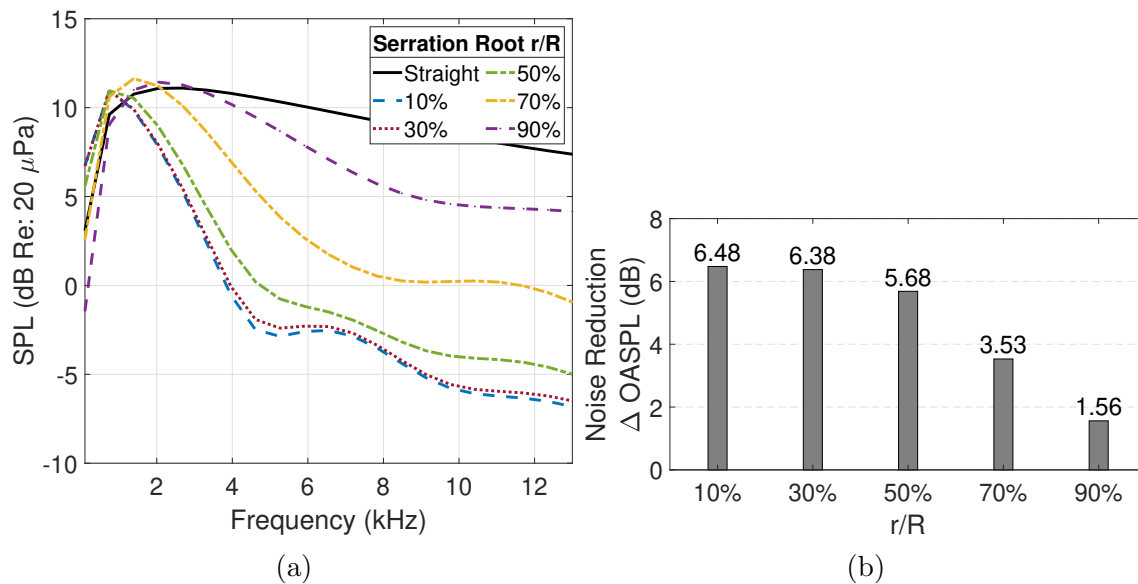


Figure 9.7: The effect of starting radial locations of the serrations on rotor broadband noise: (a) sound pressure level spectrum and (b) overall sound pressure level reduction compared to the straight-blade rotor.

Figure 9.7 shows the effects of changing the starting radial position of the serrations, where the inboard of the starting position has straight edges, as shown in Fig. 3.10. The

frequency spectrum indicates that the noise levels at the mid and high frequencies (above 2 kHz) are reduced with the increasing span portion of the serrated blade, while the low-frequency range has a slight noise increase. This noise increase might result from the model difference when blending Amiet's model and Lyu and Ayton's model on the same blade, where some discrepancies at the low frequencies are present in Fig. 9.4. The benefit of using Amiet's model for the straight portion of a blade is to reduce the computational time. The trend of the noise reduction shows that the noise level of the serrated rotor keeps decreasing as the starting position of the serrations moves to the root, but the tip serrations are more effective in reducing noise, since the higher flow speeds at the tip sections give the higher noise levels. The most outboard 10% sections provide a noise reduction of 1.56 dB, and the 70-90% and the 50-70% sections each provide noise reductions of about 2 dB. However, the 30-50% sections give a noise reduction of less than 1 dB, and the inboard 30% sections have minimal noise reduction benefits. Thus, it is suggested that using trailing-edge serrations starting from 50% r/R is preferred.

Figure 9.8 demonstrates the effect of increasing the serration height on broadband noise. The APC Slow Flyer rotor has a chord length of about 28 mm at 75% r/R , so attaching too large serration heights is unrealistic. Since the serrations are attached to the blade trailing edges, this approach results in increasing the blade chord length, and the impacts of varying the chord length on the boundary layer condition are neglected in this study. It is observed that increasing the serration height has noticeable benefits of noise reduction, but this benefit is reduced at the larger serration heights. As the serration height increases, the incline angle between the serration and the blade span also increases to create stronger destructive interference between the serration tip and the root regions. The trend of changing

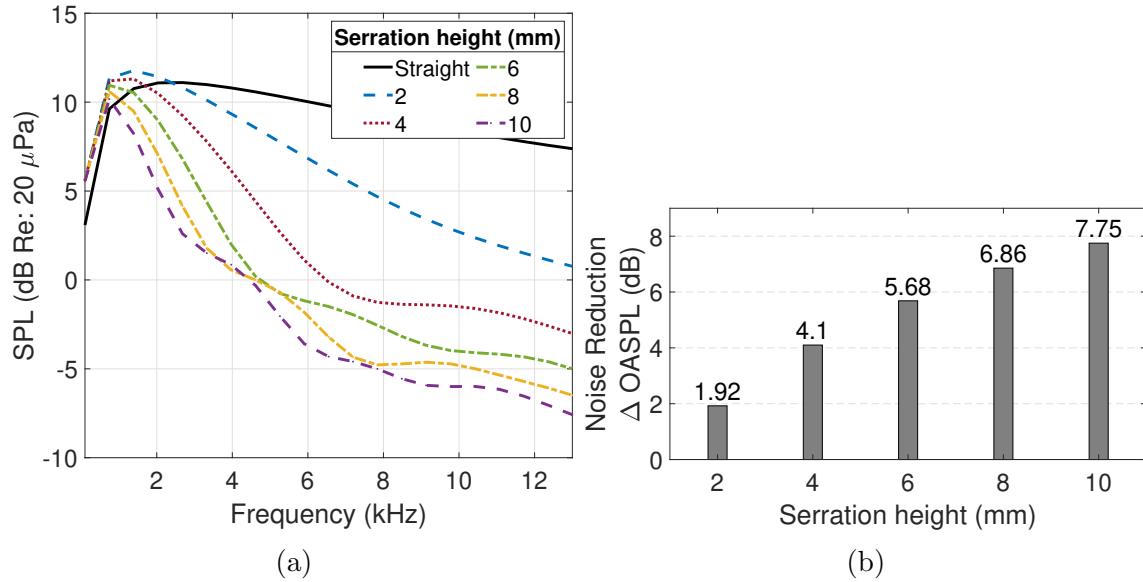


Figure 9.8: The effect of serration heights on rotor broadband noise: (a) sound pressure level spectrum and (b) overall sound pressure level reduction compared to the straight-blade rotor.

the height to wavelength ratio $2h/l$ in Fig. 9.8 is the same as in Fig. 9.6; the higher $2h/l$ increases the noise reduction in a decreasing rate. In addition, more acoustic energy is redistributed to the higher-frequency cut-off modes (imaginary part of E_n) since the shape coefficient in Eq. 3.42 is a function of $k\bar{c} = 2kh/\beta$, which is proportional to the serration height.

The different serration shapes shown in Fig. 3.9 and Eq. (3.43) are used on the rotor to study their noise reduction capabilities. Figure 9.9 shows that the sine-wave shape gives the largest noise reduction, and the chopped peak and the saw-tooth shapes give similarly excellent noise reductions. The square and the half-sine shapes give the least noise reductions of about 3 dB. This trend is accounted for in the shape coefficient in Eq. (3.42), where the saw-tooth shape gives an increasing noise reduction as the frequency increases, but the square shape provides an up-and-down noise reduction behavior as a function of frequency. Note that the saw-tooth shape in Fig. 9.9(a) appears to have more noise reduction than the sine

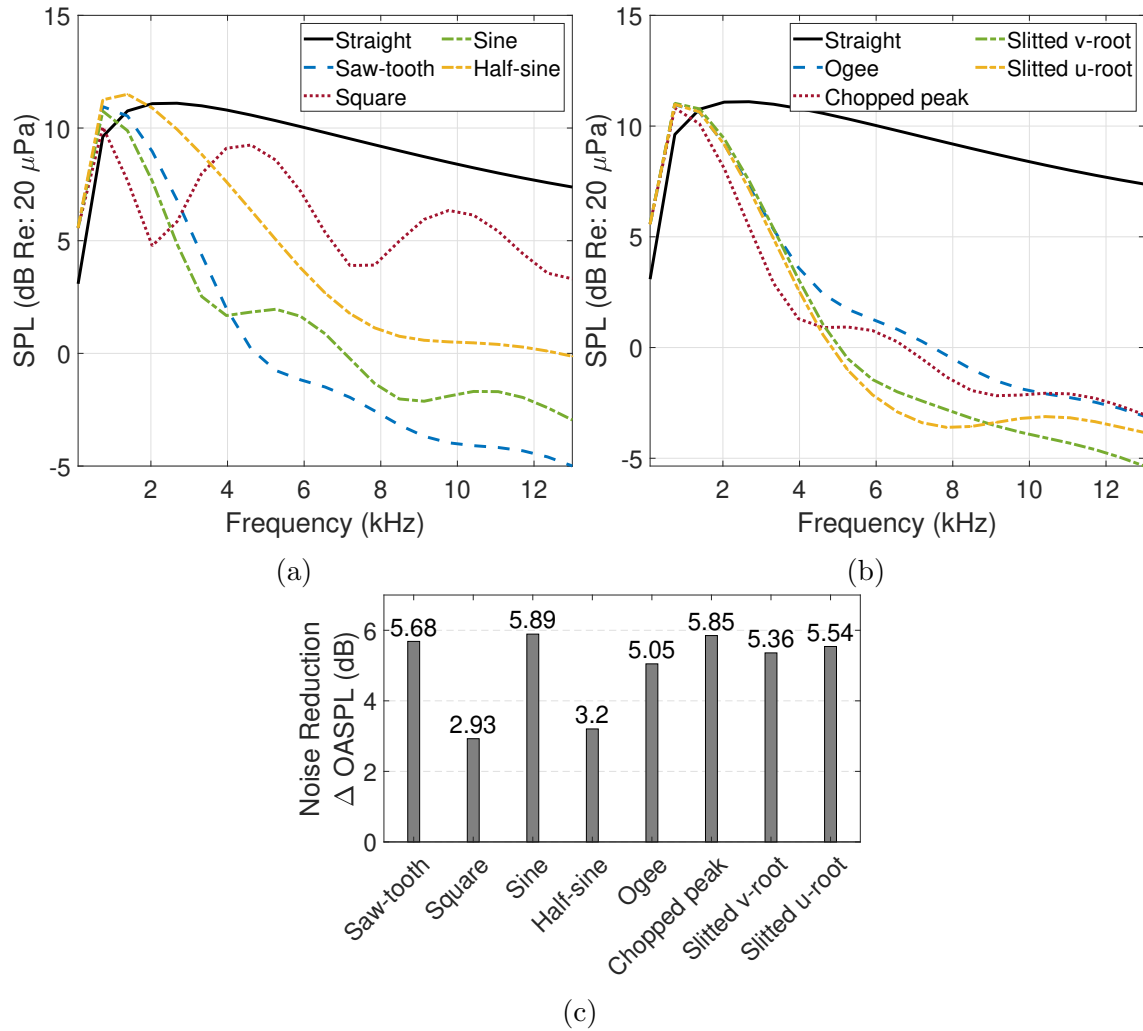


Figure 9.9: The effect of serration shapes on rotor broadband noise: (a) (b) sound pressure level spectrum of the shapes in Eq. (3.43), and (c) overall sound pressure level reduction compared to the straight-blade rotor.

shape, specifically above 4 kHz. This trend is not reflected in the Δ OASPL plot, since the noise levels above 4 kHz for the saw-tooth and sine shapes are very small compared to the low-frequency noise.

For some rotor designs, different sizes of serrations may be preferred along the blade span. The effect of changing the serration height's tip-to-root ratio is given in Fig. 9.10. For the tip-to-root ratio of 0.5, the tip serration height is half of the starting r/R serration height, which is 0.5. The serration height linearly varies in between. The larger tip-to-root

ratio creates a larger serration height at the tip to reduce noise. The tip-to-root ratio of 0.5 still provides a considerable noise reduction of 4.23 dB, although it is 1.45 dB lower than the constant geometries on the blade, as shown in Fig. 9.9(b). For tapered rotor blades with the reduced chord length at the tip, a smaller serration height at the tip region may be required for structural reasons.

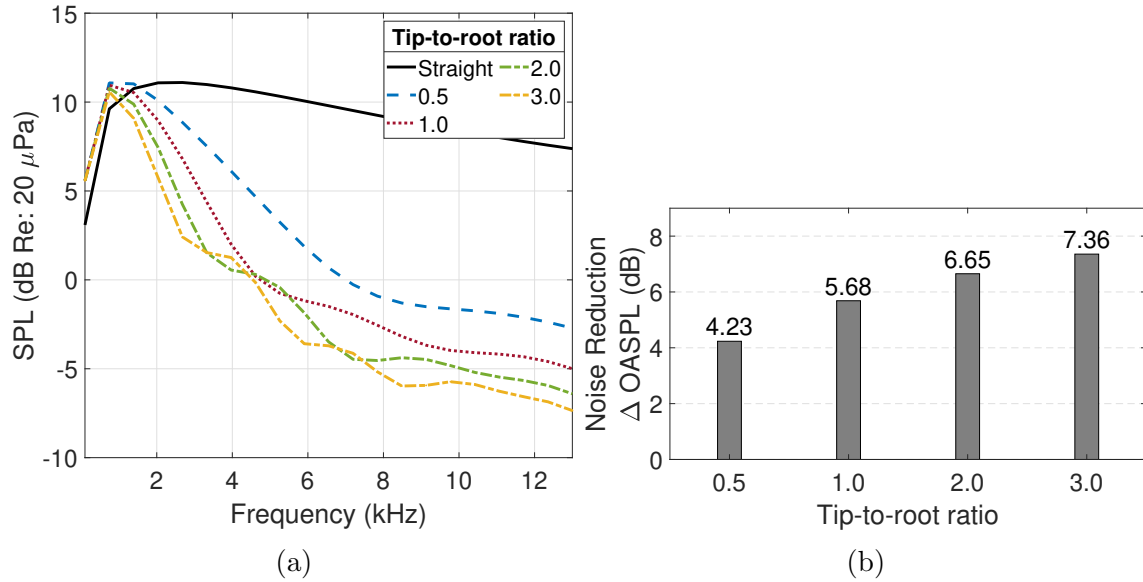


Figure 9.10: The effect of starting radial locations of the serrations on rotor broadband noise: (a) sound pressure level spectrum and (b) overall sound pressure level reduction compared to the straight-blade rotor.



Figure 9.11: Conceptual design of an electric quadrotor [77].

Table 9.4: UAM eVTOL Quadrotor Parameters ([77])

Parameters	6-passenger eVTOL quadrotor
R (m)	2.808
N_r	4
N_b	3/3/7
V_{tip} (ft/s) [m/s]	700/550/375 [213.4/167.6/114.3]
Airfoil	VR-12/SSC-A09
ϕ_o (deg)	-90
r_o (m)	150
Shape	Sawtooth
$2h$ (m)	0.0702
l (m)	0.0351
serration r/R range	0.5-1.0

9.2.2 Noise Reduction on an eVTOL Quadcopter

The UAM quadrotor conceptual designs shown in Fig. 9.11 are studied for their noise reduction potentials using trailing-edge serrations. The vehicle is operated in hovering condition, and the observer is 492 ft (150 m) directly below the quadrotor center. The detailed parameters of the vehicle can be found in Table. 9.4. In this study, the blade trailing edges of the quadrotor are serrated from mid-span to the tip with the saw-tooth geometry, whose serration height is $2h=0.0702$ m and serration wavelength is $l=0.0351$ m so that $2h/l$ becomes 2. For the straight-blade quadrotors, Amiet’s model is used on the entire blade span. For reference, the blade chord length at 75% span is about 0.17 m. For this chord length, we found that Amiet’s model and Lyu and Ayton’s model provide almost the same results on the straight blade as demonstrated in Fig. 9.1. Thus, we have selected Amiet’s model for its fast calculation. Three designs, with different tip speeds and numbers of blades, are studied in Fig. 9.12. The community background noise measured in a neighborhood in Sunnyvale, California [23] is added in the figure as reference. The noise spectrum shows that the noise reductions appear in the entire frequency range. The Δ OASPL shows that the trailing-

edge serrations have more noise reductions on the higher-tip-speed and fewer-blade designs. Trailing-edge serrations are effective in reducing noise in the mid-frequency range (1-5 kHz), which is masked by the community background noise. Although the high-frequency noise with serrations is not entirely masked by the background noise, the noise level even in the loudest condition is lower than 40 dB, which will help have the UAM aircraft much more favorably received by the public. In sum, using trailing-edge serrations as a noise reduction technique, multi-rotor eVTOL aircraft have the potential to reduce broadband noise by more than 9 dB as shown in Fig. 9.12(b), which is significant considering the unmasked eVTOL noise in the urban environment [16].

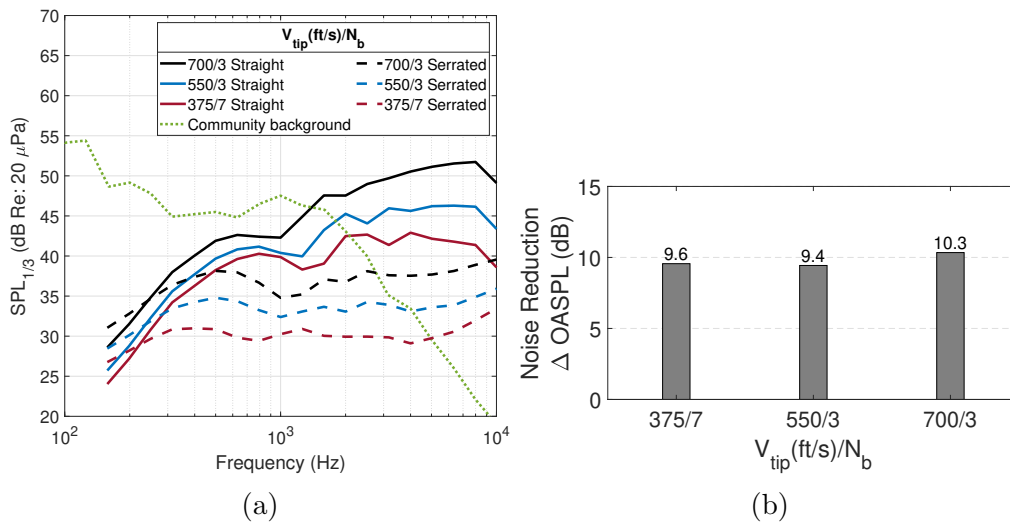


Figure 9.12: Effects of using serrated blades on broadband noise of a eVTOL quadrotor, with various design tip speeds and numbers of blades. The observer is located at 492 ft directly underneath the vehicle. The serration height is $2h=0.0702$ m and the serration wavelength is $l=0.0351$ m. The community background noise is given in [23]. (a) sound pressure level spectrum and (b) overall sound pressure level reduction compared with the straight-blade rotor.

The hemispheric broadband noise directivities of the UAM eVTOL quadrotor are calculated in Fig. 9.13, including the straight-blade quadrotor, the serrated-blade quadrotor, and the noise reduction. The vehicle parameters are given in Table 9.4, and the radius of

the observer hemisphere is 150 m. The quadrotor selected for this directivity study has three blades and the tip speed of 700 ft/s. The blue dot in Fig. 9.13 represents the vehicle position. The straight-blade quadrotor noise is calculated using Amiet’s model. It is seen that both the straight-blade and the serrated-blade quadrotors have dipole directivity, where the highest noise level is found directly below the quadrotor. The noise reduction is observed for all observer locations on the hemisphere, except for the very small elevation angles (in-plane) due to the model difference at low frequencies. This directivity pattern on serrated-blade rotorcraft is consistent with the directivity on a serrated airfoil section, where noise reductions are observed for all observer angles [69, 147].

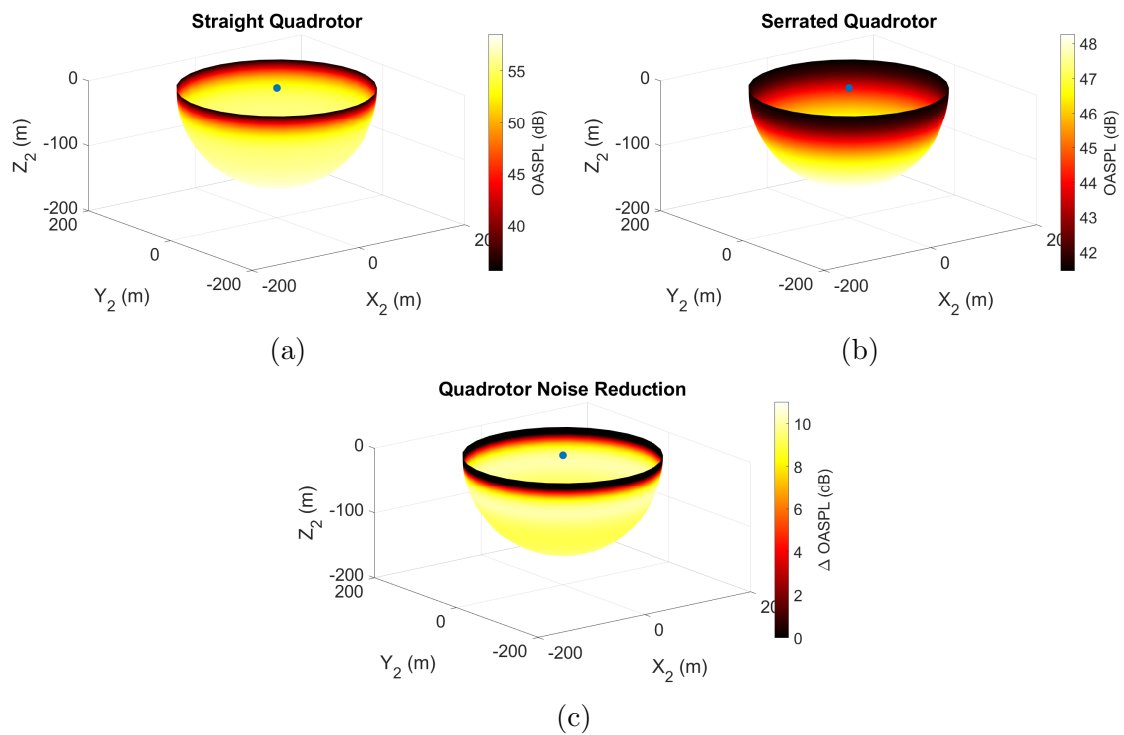


Figure 9.13: Hemispheric directivity of broadband noise OASPL (0.1-13 kHz) of the UAM eVTOL quadrotor with three blades and the tip speed of 700 ft/s: (a) straight blade, (b) serrated blade, and (c) noise reduction.

9.2.3 Noise Reduction of a Helicopter in Cruise

The single rotor helicopter in forward flight shown in Fig. 1.6(a) is analyzed for its broadband noise reduction using serrated trailing edges. The quiet helicopter [45] parameters are given in Table 9.5, where the design of 700 ft/s tip speed is studied.

Table 9.5: Quiet helicopter design [45].

Parameters	Quiet helicopter
V_{tip} (ft/s)[m/s]	700 [213.4]
R (m)	5.17
N_b	3
σ	0.0411
μ	0.246
ϕ_o (deg)	-90
r_o (m)	150
Shape	Sawtooth
$2h$ (m)	0.258
l (m)	0.129
serration r/R range	0.5-1.0

The broadband noise hemisphere directivities of the quiet helicopter are given in Fig. 9.14, where $-X_2$ is the forward direction. It is seen that due to the forward tilting angle, the hemisphere directivities are tilted in the forward direction. Both the straight rotor and the serrated rotor have the dipole directivity. Figure 9.14(c) shows that the highest noise reduction occurs in the forward direction (-45° elevation angle), although the downward direction also shows a significant noise reduction of 10 dB.

9.3 Summary

This chapter presented a state-of-the-art approach to predict broadband noise on rotors with serrated trailing edges. The original Lyu and Ayton's serrated airfoil section model, based on the Wiener-Hopf solution, was extended in this chapter to include the finite span,

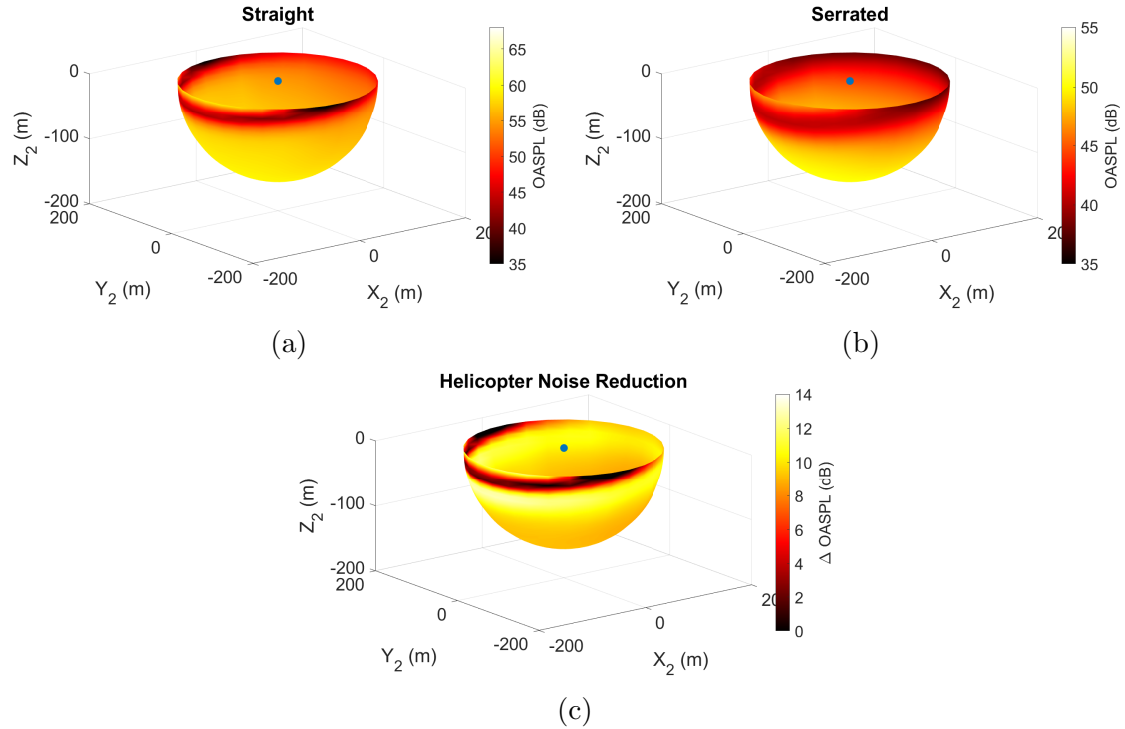


Figure 9.14: Hemispheric directivity of broadband noise OASPL (0.1-13 kHz) of a quiet helicopter design in forward flight with three blades and the tip speed of 700 ft/s: (a) straight blade, (b) serrated blade, and (c) noise reduction.

the modified scattering coefficient, and the spanwise observer distance. These extensions were verified with Amiet’s model and validated for serrated trailing-edge noise of a wing section, a hovering rotor, and a forward rotor. The effects of serration parameters on rotor broadband noise were studied. The broadband noise directivity of a serrated-blade quadrotor is investigated. The potential noise reduction using serrated trailing edges on an eVTOL quadrotor was analyzed. Important findings are summarized as follows:

- The serration height to wavelength ratio of 2 is a desirable selection to reduce rotor broadband noise, since further increasing the ratio only has slight noise reduction benefits. The preferred radial range to install trailing-edge serrations on a rotor blade is 50% to the tip, where the noise reduction increases linearly with the spanwise serrations added. However, adding serrations on the inboard 50% of the rotor blade only

gives minimal noise reductions. The sine-wave, chopped peak, and saw-tooth serration shapes provide the largest noise reductions, and the square shape provides the least noise reduction among the studied shapes. A linearly decreasing serration height from the root to the tip slightly decreases the noise reduction compared to a constant height.

- On an eVTOL quadrotor, more than 9 dB noise reduction was found with serrated trailing edges. Higher noise reductions are observed on the serrated quadrotors with higher tip speeds and fewer blades. The serrated-blade UAM eVTOL quadrotor have the dipole broadband noise directivity, and noise reductions are observed at all observer angles with a primary noise reduction toward downward direction.
- For single-rotor helicopter in forward flight, about 10 dB noise reduction was observed in the downward direction, and noise reduction occurs for all observer angles.

Although this research is focused on analytic and low-fidelity predictions of serrated trailing-edge noise, the results provide insights into important serration parameters in the context of rotor broadband noise and the significant potential to reduce UAM aircraft noise. It is suggested in the future study that the serration parameters or geometries are optimized to maximize the noise reduction and the predictions are further validated against experimental data or high-fidelity computational fluid dynamics (CFD) predictions. Finally, we note that the analytic model only considered the destructive interferences and it did not account for the acoustic source change due to the add-on serrations. This assumption and limitation can be revisited with more fundamental aeroacoustic research development.

Chapter 10

Machine Learning Model on Rotorcraft Broadband Noise Predictions

This chapter presents an Artificial Neural Network (ANN) model and a linear regression model to predict rotor trailing-edge noise. The training history of the ANN model and the statistics of the linear regression model are demonstrated. Finally, the two models are validated against the validation results directly obtained from UCD-QuietFly.

10.1 Artificial Neural Network Model

As mentioned in Chapter 3, two convergence studies are performed to determine the reasonable number of points for each variable and the number of epochs in the training process. First, Fig. 10.1 shows the decrease in the mean absolute error of OASPL as the total number of points increases, which indicates the convergence of the mean absolute error as the total number of points goes to infinity. Specifically, further increasing the total number of points beyond 1024 will require substantial computational power while slightly increasing the ac-

curacy. Second, the convergence study of the number of epochs is shown in Fig. 10.2, which includes the training records of the OASPL model and the SPL model. For the OASPL training in Fig. 10.2(a), the training error and the validation error decrease as the number of epochs increases, and the solution is seen to be converged around 150000 epochs, where the final OASPL model is achieved. However, for the SPL training in Fig. 10.2(b), the training and validation error first converge and fluctuate around 100000 epochs, possibly due to the numerical instability. To obtain the optimal results, the final SPL model is taken at 500000 epochs.

On the other hand, as seen in the training history of the ANN models shown in Fig. 10.2, where the training error and validation mean absolute error overlaps and converges to less than 0.5 dB for the OASPL model 1.5 dB for the SPL model, which indicates a well-trained machine learning model.

Figure 10.3 shows the distribution of the predicted values from the trained machine learning model compared to the true values obtained from UCD-QuietFly. The true values are the 20% data used for validation, while the model is trained from the rest 80% data. It is shown that the predictions from the machine learning model have low errors, in which the OASPL errors and the SPL errors are normally distributed around 0.04 dB and 0.3 dB, respectively. Therefore, the model has a comparable accuracy as UCD-QuietFly. It is important to note that the machine learning model gives instant results of rotor OASPL based on the five parameters, while UCD-QuietFly takes about 60 seconds to predict one rotor parameter case.

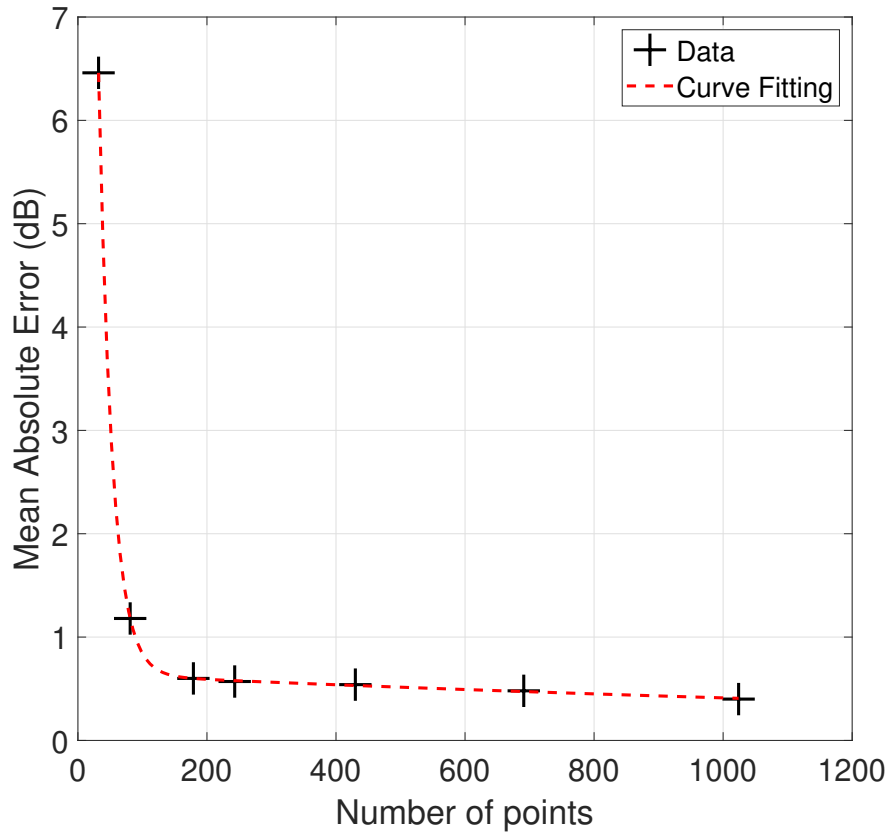


Figure 10.1: Number of points in data vs. mean absolute error of OASPL, which shows the convergence of the model’s accuracy with an increasing data size.

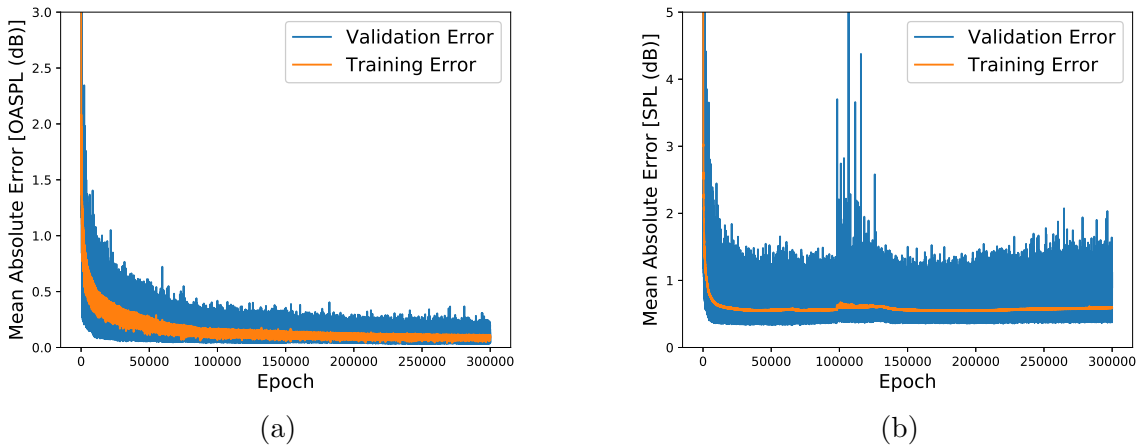


Figure 10.2: Convergence study of the number of epochs in the training of the ANN model: (a) overall sound pressure level, and (b) narrow-band sound pressure level.

10.2 Linear Regression Model

The polynomial equations obtained from linear regression is shown in Eqs. (10.1)-(10.2).

The statistics of the models are shown in Table 10.1, and the detailed statistics of each

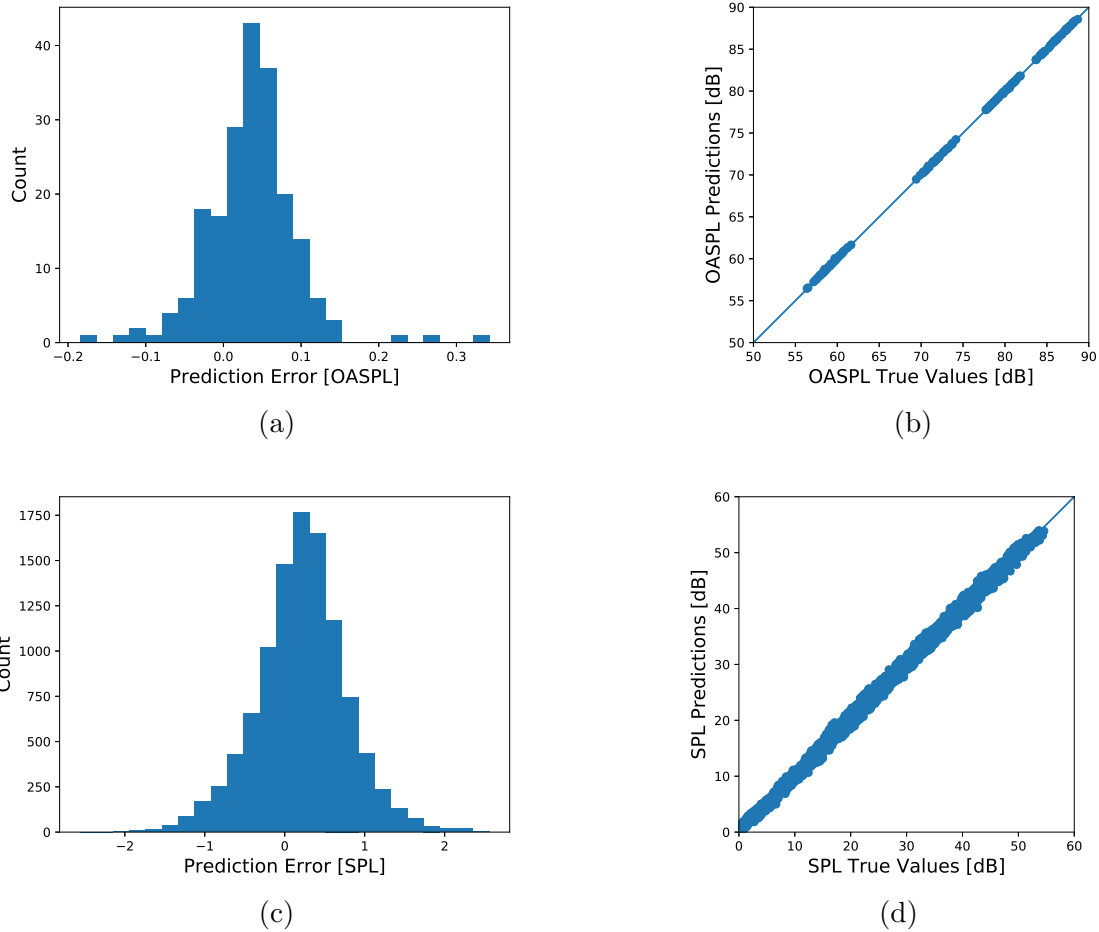


Figure 10.3: Distribution of validation errors: (a) Comparison between true OASPL and predicted OASPL, (b) Histogram of OASPL validation error distribution, (c) Comparison between true SPL and predicted SPL, and (d) Histogram of SPL validation error distribution.

variable in the models are given in Table A.1 and A.2 in the Appendix. A small p-value indicates that the term has a strong association with the target OASPL or SPL, hence the term is important. For example, the tip Mach number is the most important factor for the rotor broadband noise. As for the accuracy of the linear regression model, the OASPL model and the SPL model has the mean absolute errors of 0.81 dB and 1.85 dB, respectively, which are acceptable considering the simplicity of the polynomial equations.

$$\text{OASPL} = 81.80 + 41.95M_{tip} - 1.81\theta_0 + 0.07\theta_0^2 - 8.33\sigma + 0.91\theta + 0.05\theta^2 - 0.71R \quad (10.1)$$

$$\begin{aligned} \text{SPL}(f) = & 7.18 + 135.4M_{tip} - 0.338\theta_0 + 0.139\theta - 13.6\sigma - 1.28R - 2.45 \times 10^{-3}f \\ & - 77.3M_{tip}^2 + 0.013\theta_0^2 + 0.139\theta^2 + 6.97 \times 10^{-8}f^2 \end{aligned} \quad (10.2)$$

Table 10.1: Statistics of the linear regression model (Continued)

Item	OASPL Model	SPL Model
Number of observations	1024	52224
Error degrees of freedom	1015	52213
Mean Absolute Error	0.81 dB	1.85 dB
R-squared	0.996	0.941
Model p-value	3.9E-47	1.1E-163

10.3 Validations of the ANN model and the linear regression model

This section presents the comparison between the ANN models and the linear regression models against the noise predictions from UCD-QuietFly, and the validation of the ANN models are presented by the 20% validation data. First, the validations of the OASPL models are shown in Fig. 10.4, where each rotor parameter is varied with other parameters fixed at the UH-1B helicopter values in Table 4.2. For example, in Fig. 10.4(a), the tip Mach number is varied from 0.2 to 0.7 while the other four parameters are fixed, and the OASPL is predicted using UCD-QuietFly, the ANN model, and the linear regression model.

Note that these validation data are not used in the training process.

As seen in Fig. 10.4, both the ANN model and the linear regression model well capture the noise trend for the variation of the tip Mach number, which is the dominant factor for trailing-edge noise[15]. For the other four parameters, the ANN model predictions match well with the UCD-QuietFly predictions, which demonstrates the small validation error. Regarding the linear regression model, although the OASPL trend of the rotor solidity is well predicted, the OASPL of the collective pitch, twist angle, and rotor radius is over-predicted with the correct trends.

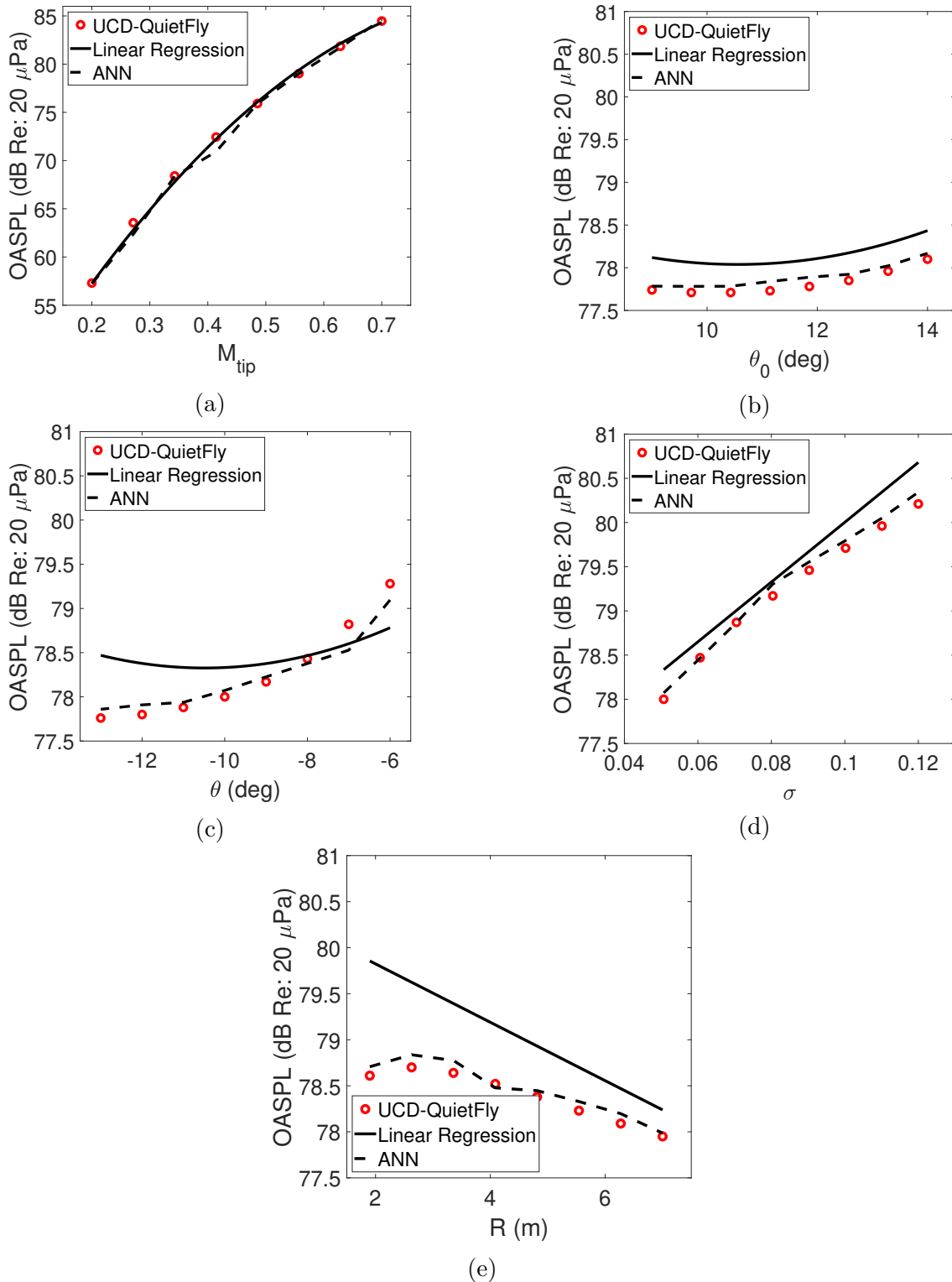


Figure 10.4: The OASPL validation of the ANN model and the linear regression model for the parameters: (a) Tip Mach number, (b) Collective pitch angle, (c) Twist angle, (d) Rotor solidity, and (e) Rotor radius.

In addition to the OASPL predictions, the validations of the narrow-band SPL from the ANN model and linear regression model are shown in Fig. 10.5, where the two cases are different in the tip Mach number and the rotor solidity. As seen in the two cases, the ANN prediction overlaps with the UCD-QuietFly prediction in the entire frequency domain, including the peak-level frequency. On the other hand, the linear regression model is capable of predicting the general noise trend, but the peak-level frequency region is not captured and the discrepancies in the high-frequency range are observed.

The validation difference between the ANN model and linear regression model can be explained as follows. While the ANN model considers the non-linear effects among the five parameters, the linear regression model takes the linear combinations of the parameters. The regression model is expected to improve its prediction if the non-linear terms are considered, but this addition will make the equation more complicated for the rotorcraft preliminary design purpose.

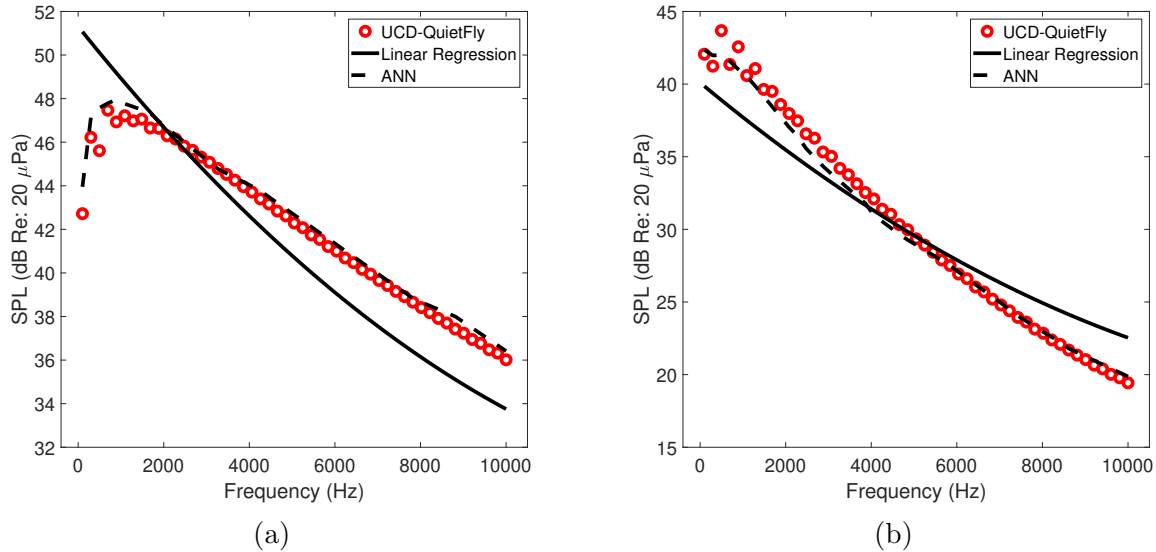


Figure 10.5: The narrow-band SPL validation of the for the ANN model and the linear regression model in frequency domain: (a) $M_{\text{tip}}=0.67$, $\theta_0=13.52^\circ$, $\theta=-10^\circ$, $\sigma=0.0506$, and $R=6.71\text{m}$, and (b) $M_{\text{tip}}=0.45$, $\theta_0=13.52^\circ$, $\theta=-10^\circ$, $\sigma=0.0853$, and $R=6.71\text{m}$.

10.4 Summary

A rotorcraft broadband noise prediction program UCD-QuietFly was used as a tool to obtain a comprehensive noise data set with the variables of five rotor parameters, which are the tip Mach number, collective pitch angle, twist angle, rotor solidity, and rotor radius. From UCD-QuietFly the overall sound pressure level and the narrow-band sound pressure level were used to train the artificial neural network models and the linear regression models that directly predict the rotor broadband noise from the five rotor parameters. Key findings are concluded as follows:

1. The ANN models are trained with converged training and validation errors. The trained OASPL model and SPL model have the mean absolute validation errors of 0.3 dB and 1.3 dB, respectively. While UCD-QuietFly takes around 60 seconds to calculate the broadband noise for one rotor case, the trained ANN model instantly gives the results.
2. The linear regression models for the OASPL and SPL are trained to give the polynomial equations that are easy to use for the rotorcraft preliminary design purpose. Based on the training data, the linear regression models for the OASPL and SPL have the mean absolute error of 0.91 dB and 1.85 dB, respectively.
3. From the validations against the UCD-QuietFly predictions, the ANN models are demonstrated to well capture the variations of the parameters and noise trends in the frequency domain. On the other hand, the linear regression models predict the general trends of the parameters and frequency variation but are less accurate than the ANN models.

Chapter 11

Concluding Remarks and Future Directions

This chapter presents a summary of this dissertation research. The major contributions are listed. Some recommendations for future work are suggested.

11.1 Summary of Research Work

This dissertation research has developed a state-of-the-art method to predict rotorcraft broadband noise. This physics-based method was used to investigate the noise impacts of conventional helicopters, UAM eVTOL aircraft, and small-scale drone rotors. The noise reductions of rotor broadband noise were investigated using trailing-edge serrations. The selected psychoacoustic metrics of rotorcraft were analyzed.

11.1.1 Validations of Rotorcraft Noise Predictions

A multi-rotor broadband noise prediction method was first developed. Rotor trailing-edge noise was predicted using the aerodynamics and the turbulence wall pressure spectrum

near the trailing edge on airfoils, which were obtained by a combination of the standard blade element momentum theory, a viscous boundary layer panel method, and a recently developed empirical wall pressure spectrum model. The coordinate transformations were combined with Amiet's model to predict far-field noise. Other airfoil-self noise sources, such as trailing-edge bluntness noise and stall noise, were included using the semi-empirical Brooks-Pope-Marcolini (BPM) model. A modified trailing-edge noise model was presented for small-scale drone rotors that have small chord lengths, low Reynolds numbers, and high rotational speeds. These unique characteristics, different from conventional full-scale rotors, were studied in the improved noise prediction models presented in Chapter 4. The Roger and Moreau's trailing-edge boundary condition and leading-edge back-scattering correction were included in the Amiet's trailing-edge noise model in UCD-QuietFly. An incident field correction was proposed in this chapter to account for the modified trailing-edge boundary condition. The laminar boundary layer-vortex shedding (LBL-VS) noise prediction was implemented in UCD-QuietFly using the BPM model. The theoretical predictions were validated against the experiments on three small-scale drone rotors in hovering and forward flights. LBL-VS noise was found to be an important noise source for untripped blades, but the BPM model required an ad hoc tuning for good predictions. The effect of leading-edge back-scattering in broadband noise was found to be important for small-scale rotors at low frequencies when the reduced frequency (kc) is below 1.17. Finally Amiet's leading-edge noise model with Roger and Moreau's modifications was used to predict turbulence-ingestion noise on an airfoil section

In Chapter 4, validations were provided for the predictions rotor broadband noise, rotor tonal noise, and forward-flight inflow distributions. Predictions of rotor broadband noise

was validated against experimental data for full-scale helicopter rotors, mid-scale rotors, and small-scale drone rotor. The predictions of turbulence-ingestion noise on an airfoil section showed good agreements with the acoustic measurements.

11.1.2 Parameter Sensitivity Study of Rotorcraft Broadband Trailing-Edge Noise

Chapter 5 investigated the effects of rotorcraft design and operating parameters on trailing-edge noise. A rotor trailing-edge noise prediction method was first developed where the aerodynamics and the turbulence wall pressure spectrum near the trailing edge on airfoils were predicted by a combination of the standard blade element momentum theory (BEMT), a viscous boundary-layer panel method, and a recently developed empirical wall pressure spectrum model. The coordinate transformations were combined with the Amiet model to predict far-field noise. Compared to experimental data, the validation of this method demonstrated its advantages and validity for airfoil and rotorcraft broadband noise predictions. Then, this method was used to study the effects of rotorcraft design and operating parameters on rotor trailing-edge noise. It was found that helicopter broadband noise scales with the 4.5th to 5.0th power of the tip Mach number in which the range was determined by the typical helicopter collective pitch angle in operation. Detailed trend analyses of noise levels as a function of frequency were presented in terms of the collective pitch angle, twist angle, rotor solidity, rotor radius, disk loading, and number of blades. It was found that the collective pitch angle, twist angle, and chord length make noticeable impacts on low- and mid-frequency noise. Finally, a semi-analytic model was presented to predict the directivity and geometric attenuation of rotor trailing-edge noise.

11.1.3 Broadband Noise Predictions of VTOL Multi-Rotors in Urban Air Mobility

Chapter 6 investigated broadband noise of multi-rotor urban air mobility (UAM) vertical take-off and landing (VTOL) vehicles. Based on an earlier single-rotor trailing-edge noise prediction method, a multi-rotor broadband noise prediction program was developed, where the multi-rotor coordinate transformation was included, and the amplitude modulation capability was introduced. Thereafter, the program was used to predict broadband noise from three UAM VTOL conceptual designs and a vertiport conceptual design. It was found that UAM VTOL vehicles' broadband noise is important in the high-frequency range, where the community background noise level is typically low. For the same mission specifications, broadband noise was found to be higher for VTOL designs with more rotors. UAM vehicle noise was compared to conventional helicopter noise. It was found that the amplitude modulation of broadband noise of a single rotor is insignificant when the observer distance is larger than 4 rotor radii. Multi-rotor vehicles at the same rotational speeds had weaker amplitude modulations than a single rotor, which demonstrated the benefits of using multiple rotors in terms of noise annoyance. Finally, noise contours from a vertiport design showed an increase in the broadband noise level when multiple VTOL vehicles are operated simultaneously.

11.1.4 Forward Flight Rotor Tonal Noise, Broadband Noise, and Psychoacoustics

Chapter 7 investigated tonal and broadband noise for rotor designs used on urban air mobility vehicles. Quiet helicopter rotor designs with varying tip speeds and blade numbers were studied for the tonal and broadband noise at the same mission specification. The

rotor aerodynamics in edge-wise forward flight were calculated using the blade element theory coupled with a dynamic inflow model and the moment-balance trim analysis. Loading noise and thickness noise were obtained using the lifting-line loading distribution and the dual-compact thickness noise model in PSU-WOPWOP. With the forward flight capability developed in UCD-QuietFly, broadband noise, including trailing-edge noise, trailing-edge bluntness noise, and airfoil stall noise was predicted. Psychoacoustic metrics, such as fluctuation and roughness, were used to quantify the human subjective annoyance levels. The relative importance between tonal noise and broadband noise was investigated for various design cases and operating conditions. It was found that broadband noise is the dominant noise source for the rotor designs with low tip speeds and fewer blades, while tonal noise is dominant for the high-tip-speed designs. A low tip speed and more blades were found to be the preferable design features in terms of psychoacoustic metrics.

11.1.5 Effects of Rotor Blade Ideal Twist and Tip Taper on Broadband Noise

In Chapter 8, broadband noise was compared for different blade designs. At the same thrust, the ideally twisted rotor generated slightly higher broadband noise than the linearly twisted rotor, while the tapered blade tip was shown to reduce the broadband noise levels significantly.

11.1.6 Applications of Trailing-Edge Serrations

Trailing-edge serrations are known to be an effective way to reduce broadband noise on wing sections, but their noise reduction capabilities on rotorcraft have not been fully understood.

Chapter 9 developed a new approach to analytically predicting and investigating broadband noise of rotors with serrated trailing edges. To achieve rotorcraft broadband noise predictions, we extend Lyu and Ayton’s semi-infinite serrated wing model to include the finite blade span, the modified scattering coefficient, and the spanwise observer distance. The validations showed good agreements with experimental data for serrated trailing-edge noise of a wing section, a hovering rotor, and a forward-flight rotor. Next, the effects of serration parameters on rotor broadband noise were studied. For optimal and realistic rotor broadband noise reduction, the desirable design of a serrated-blade rotor had the serration height to wavelength ratio of 2, the radial range of serrations from 50% blade span to the tip. It was also found that the sine-wave, chopped peak, or saw-tooth serration shapes reduce noise most among various shapes that were considered. Finally, noise reduction with serrations was applied to urban air mobility (UAM) aircraft. A 6-passenger eVTOL quadrotor was found to have more than 9 dB noise reduction potential with serrated trailing edges, where higher noise reductions were observed with higher tip speeds and fewer blades. Serrated-blade quadrotors were found to have the dipole broadband noise directivity, and noise reductions were observed at all observer angles.

11.1.7 Machine Learning Model on Rotorcraft Broadband Noise Predictions

Chapter 10 developed the data-driven fast-predicting models of rotorcraft trailing-edge broadband noise. The models were capable of predicting noise for the overall sound pressure level and the frequency-domain sound pressure level from basic rotor parameters, such as the tip Mach number, collective pitch angle, twist angle, rotor solidity, and rotor radius. A compre-

hensive noise data set used to train the models were generated from the rotorcraft broadband noise prediction program UCD-QuietFly, whose validations were presented against the measurements. The fast-predicting models were trained using two data-driven methods. First, the artificial neural network (ANN) was used to train the machine learning-based model. Second, the linear regression was used in which a polynomial equation along with linear combinations of the parameters was obtained. From the validations against UCD-QuietFly, it was found that the ANN model accurately captured the variations of the noise levels according to the rotor parameters and frequency. The linear regression models were also capable of predicting the general trends of noise levels with the rotor parameters.

11.2 Contributions

The critical contributions of this dissertation to the study of rotorcraft broadband noise are highlighted below. This research has developed the first physics-based rotorcraft broadband noise analysis method UCD-QuietFly, including comprehensive rotorcraft operating conditions. Up to the completion of this dissertation, UCD-QuietFly has been extensively utilized by more than ten leading research institutions and companies to predict rotorcraft broadband noise. Advanced Air Mobility (AAM) is on its way to revolutionizing humankind's transportation, logistics, and recreation. The studies in this dissertation advanced our understanding of rotorcraft broadband noise, a field vital and critical to the international goal of AAM implementation. Through this Doctoral research, the effects of the rotor operations on broadband noise were understood. The UAM eVTOL high-frequency noise was shown to be unmasked in the urban environment. Quiet rotor designs were investigated for their

broadband and tonal noise impacts on human hearing. The potential to reduce broadband noise using trailing-edge serrations was explored. Finally, this research work has initiated a new trend of studying broadband noise in the rotorcraft community, which will assist future researchers in continuing exploring rotorcraft broadband noise.

11.3 Recommendations for Future Work

The ultimate goal of studying rotorcraft noise is to alleviate its impact on humans. Acoustics studies include three parts: source, propagation, and receiver. Rotorcraft research efforts are heavily weighted on investigating the source and propagation, but the receiver receives less attention. The acoustical designs of UAM vehicles should focus on minimizing the psychoacoustic impacts on human perceptions and sensations, but the current designers only focus on the numerical interpretations of noise, such as the noise level. For example, A-weighting is regularly used to emphasize the frequency range of 2-5 kHz, which is considered a sensitive frequency range for human hearing. However, children's ear canal is smaller than adults, leading to a different sensitive frequency range from A-weighting. Therefore, it is suggested that future rotorcraft acoustics research takes an annoyance-oriented approach, which includes not only the source and the propagation but also the receiver.

Although the physics-based acoustic model is used in this research, the theory has many assumptions and limitations that can be improved. For example, the theory of wake pressure given in Fig. 3.7 is hypothetical and requires further investigation. Experimental or high-fidelity computational studies are required to provide correlations between the acoustics model and the flow conditions. The convection velocity and spanwise coherence length

were experimentally shown to vary with different flow conditions, and more sophisticated prediction models for these parameters are required.

Blade-wake-interaction (BWI) noise or turbulence-ingestion (TI) noise is an important broadband noise source for rotorcraft in level forward or descent flights [113]. Predictions of BWI noise require turbulence information at the leading edge of rotorcraft, which can only be obtained through high-fidelity computations or experiments. Future research can obtain the turbulence spectrum near the leading edge from computational fluid dynamics (CFD) and use UCD-QuietFly to predict rotor BWI noise.

Improvements of the wall pressure spectrum (WPS) model are suggested for future research. The current WPS models are limited to un-stalled airfoils and certain ranges of flow conditions, due to the lack of experimental and computational data. This insufficiency limits the potential of the physics-based acoustics models, such as Amiet's model, to only the prediction of turbulent-boundary-layer trailing-edge noise for in a limited range. In light of more comprehensive WPS models, the acoustics models will also have the capabilities to predict stall noise and laminar-boundary-layer vortex-shedding noise. Machine-learning based WPS models can be developed to expand the prediction capabilities of the acoustics models.

The current research has taken the assumption that each rotor blade section encounters clean and 2-D flows to simplify the simulation, which is sufficient when blade-to-blade interactions are weak. However, as more complex rotorcraft designs emerge, high-fidelity methods are required to capture the more complex flow fields. These designs and conditions include wing-propeller aircraft, compound helicopters, and fast maneuvering and descending flights. CFD can be used in the future to obtain boundary layer parameters on rotorcraft

blades as the inputs to UCD-QuietFly.

The current UCD-QuietFly program in FORTRAN only supports serial computing, which limits its capabilities to handle multi-vehicle and flight path. Future research should develop parallel computing in UCD-QuietFly for multiple observers because each observer's calculation is independent. Such faster computations will make flight-trajectory optimization possible.

Appendix A

Expanded Terms

The expanded form of the directivity term D_ϕ is shown in Eq. (3.2), which is obtained by performing the coordinate transformations in Eqs. (3.2)-(3.5).

$$\begin{aligned} D_\phi = A_1 / \{ & [\sin(\theta_0 + \theta) \cdot A_3 - \cos(\theta_0 + \theta) \cdot \cos \beta_p \cdot A_4 \\ & + \cos(\theta_0 + \theta) \sin \beta_p \cdot A_2]^2 + A_1 \\ & + [\sin \beta_p \cdot A_4 + \cos \beta_p \cdot A_2]^2 \}^2 \end{aligned} \quad (\text{A.1})$$

A_1 , A_2 , A_3 and A_4 in Eq. (A.1) are shown as follows for clarity.

$$\begin{aligned} A_1 = & [\cos(\theta_0 + \theta) \cdot A_3 + \sin(\theta_0 + \theta) \cos \beta_p \cdot A_4 \\ & - \sin(\theta_0 + \theta) \sin \beta_p \cdot A_2]^2 \end{aligned} \quad (\text{A.2})$$

$$\begin{aligned}
A_2 &= \cos(t_r + t_v)[\cos t_v(l_x + X_2) + \sin t_v(l_z + Z_2)] \\
&\quad + \sin(t_r + t_v)[\cos t_v(l_z + Z_2) - \sin t_v(l_x + X_2)] \\
&\quad - r \cos \phi \sin \beta_p
\end{aligned} \tag{A.3}$$

$$\begin{aligned}
A_3 &= \cos(t_r + t_v)[\cos t_v(l_z + Z_2) - \sin t_v(l_x + X_2)] \\
&\quad - \sin(t_r + t_v)(\cos t_v(l_x + X_2) + \sin t_v(l_z + Z_2)) \\
&\quad + r \cos \beta_p
\end{aligned} \tag{A.4}$$

$$A_4 = l_y + Y_2 - r \sin \beta_p \sin \phi \tag{A.5}$$

Appendix B

Calculation of Sound Pressure Level

The conversion from the narrow-band sound pressure level (SPL) to one-third octave band sound pressure level ($\text{SPL}_{1/3}$) are provided in Eq. (B.1), f_n is the mid-band frequency, $m_{l,n}$ and $m_{u,n}$ are the lower and upper bounds frequency indices of the n^{th} band, and $\text{SPL}_{rotor,i}$ is the narrow-band sound pressure level in Eq. (3.12) that is interpolated into 1-Hz intervals.

$$\text{SPL}_{1/3,n} = 10 \log_{10} \left(\int_{f_{l,n}}^{f_{u,n}} \frac{2\pi S_{pp}}{(2 \times 10^{-5})^2} df \right) = 10 \log_{10} \sum_{i=m_{l,n}}^{m_{u,n}} 10^{0.1 \text{SPL}_{rotor,i}} \quad (\text{B.1})$$

$$f_n = 1000 \times 2^{(n-30)/30}; \quad f_{l,n} = f_n / 2^{1/6}; \quad f_{u,n} = f_n \times 2^{1/6} \quad (\text{B.2})$$

The conversion from the narrow-band sound pressure level (SPL) to overall sound pressure level (OASPL) are provided in Eq. (B.3). In Chapters 5 and 10, the OASPL is integrated from the SPL in the frequency range of $f_0 = 0.1$ kHz to $f_1 = 10$ kHz. Before computing OASPL and $\text{SPL}_{1/3}$, narrow-band SPL is interpolated into 1-Hz intervals.

$$\text{OASPL} = 10 \log_{10} \left(\int_{f_0}^{f_1} \frac{2\pi S_{pp}}{(2 \times 10^{-5})^2} df \right) = 10 \log_{10} \sum_{i=1}^{n_f} 10^{0.1 \text{SPL}_{rotor,i}} \quad (\text{B.3})$$

where n_f is the number of 1-Hz frequency intervals from f_0 to f_1 .

Appendix C

Training Statistics

The training statistics of the machine learning model in Chapter 10 are provided. Table A.1 and A.2 show the detail training statistics of each coefficient in the OASPL and the SPL linear regression models.

Table A.1: Statistics of the OASPL linear regression model

Coeff. in Eq. (3.50)	Corresponding Term	Estimates	Squared Error	t-stat	p-value
α_1	Intercept	45.071	1.012	44.54	5.55E-241
α_2	M_{tip}	103.564	0.665	155.68	0.00E+00
α_3	θ_0	-0.705	0.168	-4.20	2.93E-05
α_4	θ	0.475	0.071	6.66	4.35E-11
α_5	σ	33.830	0.785	43.09	1.79E-231
α_6	R	-0.317	0.011	-29.72	3.52E-140
α_7	M_{tip}^2	-54.947	0.729	-75.35	0.00E+00
α_8	θ_0^2	0.033	0.007	4.58	5.18E-06
α_9	θ^2	0.023	0.004	6.08	1.75E-09

Table A.2: Statistics of the SPL linear regression model

Coeff. in Eq. (3.50)	Corresponding Term	Estimates	Squared Error	t-stat	p-value
β_1	Intercept	7.176E+00	0.747	9.61	7.93E-22
β_2	M_{tip}	1.355E+02	0.490	276.26	0.00E+00
β_3	θ_0	-3.389E-01	0.124	-2.74	6.23E-03
β_4	θ	1.394E-01	0.053	2.66	7.93E-03
β_5	σ	-1.369E+01	0.579	-23.65	4.84E-123
β_6	R	-1.280E+00	0.008	-162.83	0.00E+00
β_7	f	-2.453E-03	0.000	-119.47	0.00E+00
β_8	M_{tip}^2	-7.736E+01	0.537	-143.94	0.00E+00
β_9	θ_0^2	1.347E-02	0.005	2.51	1.22E-02
β_{10}	θ^2	8.989E-03	0.003	3.27	1.07E-03
β_{11}	f^2	6.967E-08	0.000	35.40	3.14E-271

REFERENCES

- [1] Zawodny, N., and Boyd, D., “Investigation of Rotor-Airframe Interaction Noise Associated with Small-Scale Rotary-Wing Unmanned Aircraft Systems,” *Journal of the American Helicopter Society*, Vol. 65, No. 1, 2020, pp. 1–17.
- [2] Jia, Z., and Lee, S., “Computational Study of Aerodynamics and Acoustics for Quadrotor eVTOL Aircraft,” *Proceedings of the 2020 VFS Aeromechanics for Advanced Vertical Flight Technical Meeting*, San Jose, CA, January 21-23, 2020.
- [3] Jia, Z., and Lee, S., “Acoustic Analysis of a Quadrotor eVTOL Design via High-Fidelity Simulations,” *Proceedings of the 25th AIAA/CEAS Aeroacoustics Conference*, Delft, The Netherlands, May 20-23, 2019.
- [4] Brooks, T., Marcolini, M., and Pope, D., “Main Rotor Broadband Noise Study in the DNW,” *Journal of the American Helicopter Society*, Vol. 34, No. 2, 1989, pp. 3–12.
- [5] Pettingill, N., Zawodny, N., Thurman, C., and Lopes, L., “Acoustic and Performance Characteristics of an Ideally Twisted Rotor in Hover,” *2021 AIAA SciTech Forum*, VIRTUAL EVENT, 19–21 January 2021.
- [6] Thurman, C., Zawodyn, N., Pettingill, N., Lopes, L., and Baeder, J., “Physics-Informed Broadband Noise Source Identification and Prediction of an Ideally Twisted Rotor,” *2021 AIAA SciTech Forum*, VIRTUAL EVENT, 19–21 January 2021.
- [7] Snider, R., Samuels, T., Goldman, B., and Brentner, K., “Full-Scale Rotorcraft Broadband Noise Prediction and Its Relevance to Civil Noise Certification Criteria,” *Proceedings of the 69th Annual Forum of the American Helicopter Society*, Phoenix, AZ, May 21-23, 2013.
- [8] Intaratap, N., Alexander, W., and Devenport, W., “Experimental Study of Quadcopter Acoustics and Performance at Static Thrust Conditions,” *Proceedings of 22nd AIAA/CEAS Aeroacoustics Conference*, Lyon, France, May 30-June 1, 2016.
- [9] Zawodny, N., Boyd, D., and Burley, C., “Acoustic Characterization and Prediction of Representative, Small-Scale Rotary-Wing Unmanned Aircraft System Components,” *Proceedings of the 72nd Annual Forum of the American Helicopter Society*, West Palm Beach, FL, May 17-19, 2016.
- [10] Brentner, K., and Farassat, F., “Modeling Aerodynamically Generated Sound of Helicopter Rotors,” *Progress in Aerospace Sciences*, Vol. 39, No. 2, 2003, pp. 83–120.
- [11] Brentner, K., and Holland, P., “An Efficient and Robust Method for Computing Quadrupole Noise,” *Journal of the American Helicopter Society*, Vol. 42, No. 2, 1997, pp. 172–181.
- [12] Jia, Z., Lee, S., Sharma, K., and Brentner, K., “Aeroacoustic Analysis of a Lift-Offset Coaxial Rotor Using High-Fidelity CFD/CSD Loose Coupling Simulation,” *Journal of the American Helicopter Society*, Vol. 65, No. 1, 2020, pp. 1–15.

- [13] Jia, Z., and Lee, S., “Aeroacoustic Analysis of a Side-by-Side Hybrid VTOL Aircraft,” *Proceedings of the Vertical Flight Society 76th Annual Forum*, Virtual Event, October 5-8, 2020.
- [14] Sagaga, J., and Lee, S., “Acoustic Predictions for the Side-by-Side Air Taxi Rotor in Hover,” *Vertical Flight Society 77th Annual Forum*, Virtual Event, May 11-13, 2021.
- [15] Li, S., and Lee, S., “Prediction of Rotorcraft Broadband Trailing-Edge Noise and Parameter Sensitivity Study,” *Journal of the American Helicopter Society*, Vol. 65, No. 4, 2020, pp. 1–14. doi:10.4050/JAHS.65.042006.
- [16] Li, S., and Lee, S., “Prediction of Urban Air Mobility Multirotor VTOL Broadband Noise Using UCD-QuietFly,” *Journal of the American Helicopter Society*, Vol. 66, No. 3, 2021, pp. 1–13. doi:10.4050/JAHS.66.032004.
- [17] Li, S., and Lee, S., “Acoustic Analysis and Sound Quality Assessment of a Quiet Helicopter for Air Taxi Operations,” *Journal of the American Helicopter Society*, Vol. 67, No. 3, 2022, pp. 1–15. doi:10.4050/JAHS.67.032001.
- [18] Li, S., and Lee, S., “Predictions and Validations of Small-Scale Rotor Noise Using UCD-QuietFly,” *Proceedings of the Vertical Flight Society 2022 Transformative Vertical Flight - Aeromechanics for Advanced Vertical Flight Technical Meeting*, San Jose, CA, January 25-27, 2022.
- [19] Li, S., and Lee, S., “Analytic Prediction of Rotor Broadband Noise with Serrated Trailing Edges,” *Proceedings of the Vertical Flight Society 78th Annual Forum*, Fort Worth, Texas, May 10-12, 2022.
- [20] Li, S., and Lee, S., “A Machine Learning-Based Fast Prediction of Rotorcraft Broadband Noise,” *Proceedings of the 2020 AIAA Aviation Forum*, Virtual Event, June 15-19, 2020.
- [21] Li, S., “Development of Rotorcraft Forward Flight Analysis Code Using the Finite-State Dynamic Inflow Model,” Master’s thesis, University of California Davis, August 2020.
- [22] Li, S., and Lee, S., “Extensions and Applications of Lyu and Ayton’s Serrated Trailing-Edge Noise Model to Rotorcraft,” *Proceedings of the 28th AIAA/CEAS Aeroacoustics Conference*, Southampton, UK, June 14-17, 2022.
- [23] Begault, D., “Ambient Noise Measurement for UAM Metric Analysis and Research,” *Acoustics and Urban Air Mobility Technical Working Group Meeting*, Hampton, VA, April 09-11, 2019.
- [24] Brooks, T., Pope, D., and Marcolini, M., “Airfoil Self-noise and Prediction,” Tech. rep., 1989. NASA RP 1218.
- [25] Pettingill, N., and Zawodny, N., “Identification and Prediction of Broadband Noise for

- a Small Quadcopter,” *Proceedings of the Vertical Flight Society 75th Annual Forum & Technology Display*, Philadelphia, PA, May 13–16, 2019.
- [26] Ffowcs Williams, J., and Hall, L., “Aerodynamic Sound Generation by Turbulent Flow in the Vicinity of a Scattering Half Plane,” *Journal of Fluid Mechanics*, Vol. 40, No. 4, 1970, pp. 657–670.
- [27] Lighthill, M., “On Sound Generated Aerodynamically I. General Theory,” *Proceedings of the Royal Society*, Vol. A211, 1952, pp. 564–587.
- [28] Amiet, R., “Noise Due to Turbulent Flow Past a Trailing Edge,” *Journal of Sound and Vibration*, Vol. 47, No. 3, 1976, pp. 387–393.
- [29] Curle, N., “The Influence of Solid Boundaries upon Aero-Dynamic Sound,” *Proceedings of the Royal Society*, Vol. A231, 1955, pp. 505–514.
- [30] Schlinker, R., and Amiet, R., “Helicopter Rotor Trailing Edge Noise,” Tech. rep., 1981. NASA RP 3470.
- [31] Kim, Y., and George, A., “Trailing-Edge Noise from Hovering Rotors,” *AIAA Journal*, Vol. 20, No. 9, 1982, pp. 1167–1174.
- [32] Ffowcs Williams, J., and Hawkings, D., “Theory Relating to the Noise of Rotating Machinery,” *Journal of Fluid Mechanics*, Vol. 10, No. 1, 1969, pp. 10–21.
- [33] Blandeau, V., and Joseph, P., “Validity of Amiet’s Model for Propeller Trailing-Edge Noise,” *AIAA Journal*, Vol. 49, No. 5, 2011, pp. 1057–1066.
- [34] Goody, M., “Empirical Spectral Model of Surface Pressure Fluctuations,” *AIAA Journal*, Vol. 42, No. 9, 2004, pp. 1788–1794.
- [35] Drela, M., *XFOIL: An Analysis and Design System for Low Reynolds Number Airfoils*, Vol. 54, Springer, 1989. Mueller T.J. (eds) Low Reynolds Number Aerodynamics.
- [36] Lee, S., “Empirical Wall-Pressure Spectral Modeling for Zero and Adverse Pressure Gradient Flows,” *AIAA Journal*, Vol. 56, No. 5, 2018, pp. 1818–1829.
- [37] Silva, C., Johnson, W., Solis, E., Patterson, M., and Antcliff, K., “VTOL Urban Air Mobility Concept Vehicles for Technology Development,” *Proceedings of the 2018 AIAA Aviation Forum*, Atlanta, GA, June 25–29, 2018.
- [38] Christian, A., Caston, J., and Greenwood, E., “Regarding the Perceptual Significance and Characterization of Broadband Components of Helicopter Source Noise,” *Proceedings of the Vertical Flight Society 75th Annual Forum & Technology Display*, Philadelphia, PA, May 13–16, 2019.
- [39] Johnson, W., Silva, C., and Solis, E., “Concept Vehicles for VTOL Air Taxi Operations,” *Proceedings of the American Helicopter Society Technical Conference on Aeromechanics Design for Transformative Vertical Flight*, San Francisco, CA, January

16-19, 2018.

- [40] Gary, A., and Goyal, R., “Ambient Noise Measurement for UAM Metric Analysis and Research,” *Acoustics and Urban Air Mobility Technical Working Group Meeting*, Cleveland, OH, October 22-24, 2019.
- [41] Burley, C., and Brooks, T., “Rotor Broadband Noise Prediction with Comparison to Model Data,” *Journal of the American Helicopter Society*, Vol. 49, No. 1, 2004, pp. 28–42.
- [42] Hutcheson, F., and Brooks, T., “Effects of Angle of Attack and Velocity on Trailing Edge Noise,” *Proceedings of the 42nd AIAA Aerospace Sciences Meeting and Exhibit*, Reno, Nevada, January 5-8, 2004.
- [43] Lee, S., “The Effect of Airfoil Shape on Trailing Edge Noise,” *Journal of Theoretical and Computational Acoustics*, Vol. 27, No. 2, 2019, p. 1850020.
- [44] Chou, S., and George, A., “Effect of Angle of Attack on Rotor Trailing-Edge Noise,” *AIAA Journal*, Vol. 22, No. 12, 1984, pp. 1821–1823.
- [45] Johnson, W., “A Quiet Helicopter for Air Taxi Operations,” *Proceedings of the 2020 VFS Aeromechanics for Advanced Vertical Flight Technical Meeting*, San Jose, CA, January 21-23, 2020.
- [46] Scott, M., “Military Mission Suitability Assessment of eVTOL Aircraft Configurations,” *Proceedings of the Vertical Flight Society 77th Annual Forum & Technology Display*, Virtual Event, May 10-14, 2021.
- [47] Sherman, J., “Urban Air Mobility Steals the Show at CES 2020,” *Vertiflite*, Vol. 64, No. 4, 2020, pp. 62–63.
- [48] Stoll, A., Bevirt, B., Pei, P., and Stilson, E., “Conceptual Design of the Joby S2 Electric VTOL PAV,” *2014 AIAA Aviation Forum*, Atlanta, GA, June 16-20, 2014.
- [49] Hasan, S., “Urban Air Mobility (UAM) Market Study,” *NASA Report HQ-E-DAA-TN63497s*, NASA Headquarters, Washington, DC, November 1, 2018.
- [50] Holden, J., and Goel, N., “Fast-Forwarding to a Future of On-Demand Urban Air Transportation,” *White Paper, Uber*, 2016.
- [51] Thurman, C., Zawodny, N., and Baeder, J., “Computational Prediction of Broadband Noise from a Representative Small Unmanned Aerial System Rotor,” *Proceedings of the Vertical Flight Society 76th Annual Forum*, Virtual Event, October 5-8, 2020.
- [52] Smith, B., Gandhi, F., and Niemiec, R., “A Comparison of Multicopter Noise Characteristics with Increasing Number of Rotors,” *Proceedings of the Vertical Flight Society 76th Annual Forum*, Virtual Event, October 5-8, 2020.
- [53] Niemiec, R., and Gandhi, F., “Development and Validation of the Rensselaer Mul-

- ticopter Analysis Code (RMAC): A Physics-Based Comprehensive Modeling Tool,” *Proceedings of the Vertical Flight Society 75th Annual Forum & Technology Display*, Philadelphia, PA, May 13–16, 2019.
- [54] Brentner, K., Brès, G., Perez, G., and Jones, H., “Maneuvering Rotorcraft Noise Prediction: A New Code for a New Problem,” *Proceedings of the American Helicopter Society Aerodynamics, Acoustics*, San Francisco, CA, January 13–25, 2002.
- [55] Lee, S., Brentner, K., Farassat, F., and Morris, P., “Analytic Formulation and Numerical Implementation of an Acoustic Pressure Gradient Prediction,” *Journal of Sound and Vibration*, Vol. 319, No. 3, 2009, pp. 1200–1221.
- [56] Farassat, F., and Succi, G., “The Prediction of Helicopter Discrete Frequency Noise,” *Vertica*, Vol. 7, No. 4, 1983, pp. 309–320.
- [57] Lopes, L., and Burley, C., “Design of the Next Generation Aircraft Noise Prediction Program: ANOPP2,” *Proceedings of the 17th AIAA/CEAS Aeroacoustics Conference*, Portland, Oregon, June 5-8, 2011.
- [58] Lee, S., Brentner, K., and Morris, P., “Long-Range and Nonlinear Propagation of Helicopter High-Speed Impulsive Noise,” *Journal of the American Helicopter Society*, Vol. 62, No. 2, 2017, pp. 1–10.
- [59] Stephenson, J., Watts, M., Greenwood, E., and Pascioni, K., “Development and Validation of Generic Maneuvering Flight Noise Abatement Guidance for Helicopters,” *Proceedings of the Vertical Flight Society 76th Annual Forum*, Virtual Event, October 5-8, 2020.
- [60] Reboul, G., Bailly, J., Rottmann, L., Bekemeyer, P., Einarsson, G., and Guntzer, F., “Prediction of RACER’s Lateral Rotor Noise Using the CONCERTO Chain,” *Proceedings of the Vertical Flight Society 77th Annual Forum & Technology Display*, Virtual Event, May 10-14, 2021.
- [61] Sharma, K., Brentner, K., Jia, Z., Lee, S., and Anusonti-Inthra, P., “Aeroacoustic Predictions of the Free-Wake Model, Vortex Particle Method, and Computational Fluid Dynamics for a Coaxial Rotor System,” *Proceedings of the Vertical Flight Society 75th Annual Forum & Technology Display*, Philadelphia, PA, May 13–16, 2019.
- [62] Jacobellis, G., Singh, R., Johnson, C., Sirohi, J., and McDonald, R., “Experimental and Computational Investigation of Stacked Rotor Acoustics in Hover,” *Proceedings of the Vertical Flight Society 76th Annual Forum*, Virtual Event, October 5-8, 2020.
- [63] Botre, M., Brentner, K., Horn, J., and Wachspress, D., “Validation of Helicopter Noise Prediction System with Flight Data,” *Proceedings of the Vertical Flight Society 75th Annual Forum & Technology Display*, Philadelphia, PA, May 13–16, 2019.
- [64] He, C., Ware, C., Yang, S., Kim, J., Baeder, J., and Jung, Y., “eVTOL Rotor Noise Study Using Comprehensive Modeling Combined with Acoustic Analysis,” *Proceedings*

of the Vertical Flight Society 77th Annual Forum & Technology Display, Virtual Event, May 10-14, 2021.

- [65] Smith, B., Gandhi, F., and Lyrintzis, A., “An Assessment of Multi-copter Noise in Edgewise Flight,” *Proceedings of the Vertical Flight Society 77th Annual Forum & Technology Display*, Virtual Event, May 10-14, 2021.
- [66] Akiwate, D. C., Parry, A. B., Joseph, P., and Paruchuri, C. C., “On the balance between the tonal and broadband noise of uninstalled propellers,” *Proceedings of the 2021 AIAA Aviation Forum*, Virtual Event, August 2-6, 2021.
- [67] Howe, M., “Aerodynamic noise of a serrated trailing edge,” *Journal of Fluids and Structures*, Vol. 5, No. 1, 1991, pp. 33 – 45. doi:10.1016/0889-9746(91)80010-B.
- [68] Lee, S., Ayton, L., Bertagnolio, F., Moreau, S., Chong, T. P., and Joseph, P., “Turbulent boundary layer trailing-edge noise: Theory, computation, experiment, and application,” *Progress in Aerospace Sciences*, Vol. 126, 2021, p. 100737.
- [69] Ayton, L. J., “Analytic Solution for Aerodynamic Noise Generated by Plates with Spanwise-Varying Trailing Edges,” *Journal of Fluid Mechanics*, Vol. 849, 2018, p. 448–466. doi:10.1017/jfm.2018.431.
- [70] Thai, A. D., De Paola, E., Di Marco, A., Stoica, L. G., Camussi, R., Tron, R., and Grace, S. M., “Experimental and Computational Aeroacoustic Investigation of Small Rotor Interactions in Hover,” *Applied Sciences*, Vol. 11, No. 21, 2021.
- [71] Rozenberg, Y., Roger, M., and Moreau, S., “Rotating Blade Trailing-Edge Noise: Experimental Validation of Analytical Model,” *AIAA Journal*, Vol. 48, No. 5, 2010, pp. 951–962. doi:10.2514/1.43840.
- [72] Zarri, A., Christophe, J., Moreau, S., and Schram, C., “Influence of Swept Blades on Low-Order Acoustic Prediction for Axial Fans,” *Acoustics*, Vol. 2, No. 4, 2020, pp. 812–832. doi:10.3390/acoustics2040046.
- [73] Lau, A., Kim, J., Hurault, J., Vronsky, T., and Joseph, P., “Aerofoil trailing-edge noise prediction models for wind turbine applications,” *Wind Energy*, Vol. 20, 2017, p. 1727–1752.
- [74] Jung, Y., Baeder, J., and He, C., “Investigation of Empirical Rotor Broadband Prediction using CFD Boundary Layer Parameters Extraction,” *Vertical Flight Society 77th Annual Forum*, Virtual Event, May 11-13, 2021.
- [75] Gan, Z. F., Brentner, K., and Greenwood, E., “Time Variation of Rotor Broadband Noise,” *The Vertical Flight Society’s 9th Biennial Autonomous VTOL Technical Meeting*, Virtual Event, January 26–28, 2021.
- [76] Krishnamurthy, S., Rizzi, S. A., Cheng, R., Boyd, D. D., and Christian, A. W., “Prediction-Based Auralization of a Multirotor Urban Air Mobility Vehicle,” *2021*

AIAA SciTech Forum, VIRTUAL EVENT, 19–21 January 2021.

- [77] Silva, C., and Johnson, W., “Practical Conceptual Design of Quieter Urban VTOL Aircraft,” *Proceedings of the Vertical Flight Society 77th Annual Forum & Technology Display*, Virtual Event, May 10-14, 2021.
- [78] Peters, D., Boyd, D., and He, C., “Finite-State Induced-Flow Model for Rotors in Hover and Forward Flight,” *Journal of the American Helicopter Society*, Vol. 34, No. 5, 1989, pp. 5–17.
- [79] Johnson, W., *Helicopter Theory*, Dover Publication, 1994.
- [80] Colucci, F., “Unmanned Delivery Pending,” *Vertiflite Magazine*, May/June, 2020.
- [81] Air Force Research Laboratory Public Affairs, “Agility Prime announces ‘flying car’ military airworthiness, infrastructure milestones,” 2020.
- [82] Floros, M., “Performance and Acoustics of Small Rotors with Non-Uniform Blade Spacing,” *Vertical Flight Society 75th Annual Forum*, Philadelphia, Pennsylvania, May 13–16, 2019.
- [83] Li, S., and Lee, S., “Acoustics Analysis of a Quiet Helicopter for Air Taxi Operations,” *Proceedings of the Vertical Flight Society 77th Annual Forum*, Virtual Event, May 11-13, 2021.
- [84] Roger, M., and Moreau, S., “Back-Scattering Correction and Further Extensions of Amiet’s Trailing-Edge Noise Model. Part 1: Theory,” *Journal of Sound and Vibration*, Vol. 286, 2005, pp. 477 – 506. doi:10.1016/j.jsv.2004.10.054.
- [85] Landahl, M., *Unsteady Transonic Flows*, Pergamon Press, 1961.
- [86] Moreau, S., and Roger, M., “Back-scattering correction and further extensions of Amiet’s trailing-edge noise model. Part II: Application,” *Journal of Sound and Vibration*, Vol. 323, 2009, pp. 397–425.
- [87] Amiet, R., “Effect of the Incident Surface Pressure Field on Noise due to Turbulent Flow Past a Trailing Edge,” *Journal of Sound and Vibration*, Vol. 57, No. 2, 1978, pp. 305–306.
- [88] Wolf, W. R., and Lele, S. K., “Trailing-Edge Noise Predictions Using Compressible Large-Eddy Simulation and Acoustic Analogy,” *AIAA Journal*, Vol. 50, No. 11, 2012, pp. 2423–2434.
- [89] Howe, M., “Noise produced by a sawtooth trailing edge,” *The Journal of the Acoustical Society of America*, Vol. 90, No. 1, 1991, pp. 482–487. doi:10.1121/1.401273.
- [90] Lyu, B., and Ayton, L. J., “Rapid noise prediction models for serrated leading and trailing edges,” *Journal of Sound and Vibration*, Vol. 469, 2020, p. 115136. doi:10.1016/j.jsv.2019.115136.

- [91] Casalino, D., Grande, E., Romani, G., Ragni, D., and Avallone, F., “Definition of a Benchmark for Low Reynolds Number Propeller Aeroacoustics,” *Aerospace Science and Technology*, Vol. 113, 2021, p. 106707.
- [92] Page, J., “In Situ Development and Application of Fly Neighborly Noise Abatement Procedures for Helicopters,” *Vertical Flight Society 75th Annual Forum*, Philadelphia, Pennsylvania, May 13–16, 2019.
- [93] Greenwood, E., “Dynamic Replanning of Low Noise Rotorcraft Operations,” *Vertical Flight Society 75th Annual Forum*, Philadelphia, Pennsylvania, May 13–16, 2019.
- [94] Krishnamurthy, S., Aumann, A. R., and Rizzi, S. A., “A Synthesis Plugin for Auralization of Rotor Self Noise,” *2021 AIAA Aviation Forum*, Virtual Event, August 2-6, 2021.
- [95] Currier, J. M., Hardesty, M., and O’Connell, J. M., “NOTAR system - A quiet character,” *AHS International Specialists’ Meeting on Rotorcraft Basic Research*, Philadelphia, PA, October 1991.
- [96] Yu, Y., “Rotor Blade-Vortex Interaction Noise,” *Progress in Aerospace Sciences*, Vol. 36, 2000, pp. 97–115.
- [97] JanakiRam, R., Sim, B., Kitaplioglu, C., and Straub, F., “Blade-Vortex Interaction Noise Characteristics of a Full-Scale Active Flap Rotor,” *Proceedings of the American Helicopter Society 65th Annual Forum*, Grapevine, Texas, May 27-29, 2009.
- [98] Szoke, M., and Azarpeyvand, M., “Active Flow Control Methods for the Reduction of Trailing Edge Noise,” *23rd AIAA/CEAS Aeroacoustics Conference*, Denver, Colorado, June 5-9, 2017.
- [99] Shi, Y., and Lee, S., “Numerical Study of 3-D Finlets Using RANS CFD for Trailing Edge Noise Reduction,” *International Journal of Aeroacoustics*, Vol. 19, No. 1-2, 2020, pp. 95–118.
- [100] Ali, S. A. S., Szoke, M., Azarpeyvand, M., and da Silva, C. R. I., “Turbulent Flow Interaction with Porous Surfaces,” *2018 AIAA/CEAS Aeroacoustics Conference*, Atlanta, Georgia, June 25-29, 2018.
- [101] Moreau, S., Dignou, B., Jaiswal, P., Yakhina, G. R., Pasco, Y., Sanjose, M., Alstrom, B., and Atalla, N., “Trailing-Edge Noise of a Flat Plate with Several Liner-Type Porous Appendices,” *2018 AIAA/CEAS Aeroacoustics Conference*, Atlanta, Georgia, June 25-29, 2018.
- [102] Ning, Z., Wlezien, R. W., and Hu, H., “An Experimental Study on Small UAV Propellers with Serrated Trailing Edges,” *2017 AIAA AVIATION Forum*, Denver, Colorado, 5-9 June, 2017.
- [103] Oerlemans, S., Fisher, M., Maeder, T., and Kögler, K., “Reduction of Wind Turbine

- Noise Using Optimized Airfoils and Trailing-Edge Serrations,” *AIAA Journal*, Vol. 47, No. 6, 2009, pp. 1470–1481. doi:10.2514/1.38888.
- [104] Cambray, A., Pang, E., Rezgui, D., Azarpeyvand, M., and Ali, S. A. S., “Investigation Towards a Better Understanding of Noise Generation from UAV Propellers,” *2018 AIAA AVIATION Forum*, Atlanta, Georgia, June 25-29, 2018.
- [105] Yang, Y., Wang, Y., Liu, Y., Hu, H., and Li, Z., “Noise Reduction and Aerodynamics of Isolated Multi-Copter Rotors with Serrated Trailing Edges During Forward Flight,” *Journal of Sound and Vibration*, Vol. 489, 2020, p. 115688.
- [106] Letica, S., and Alexander, W. N., “Understanding the Impact of a Serrated Trailing Edge on the Unsteady Hydrodynamic Field,” *Journal of Aerospace Engineering*, Vol. 34, No. 4, 2021, p. 04021045.
- [107] Gelot, M. B., and Kim, J. W., “Broadband Noise Prediction for Aerofoils with a Serrated Trailing Edge Based on Amiet’s theory,” *Journal of Sound and Vibration*, Vol. 512, 2021, p. 116352.
- [108] Lyu, B., Azarpeyvand, M., and Sinayoko, S., “Prediction of noise from serrated trailing edges,” *Journal of Fluid Mechanics*, Vol. 793, 2016, p. 556–588.
- [109] Noble, B., *Methods Based on the Wiener–Hopf Technique for the Solution of Partial Differential Equations*, Pergamon Press, 1958.
- [110] Huang, X., “Theoretical model of acoustic scattering from a flat plate with serrations,” *Journal of Fluid Mechanics*, Vol. 819, 2017, p. 228–257.
- [111] Jones, L. E., and Sandberg, R. D., “Acoustic and hydrodynamic analysis of the flow around an aerofoil with trailing-edge serrations,” *Journal of Fluid Mechanics*, Vol. 706, 2012, p. 295–322.
- [112] Sanjosé, M., Moreau, S., Lyu, B., and Ayton, L. J., “Analytical, Numerical and Experimental Investigation of Trailing-Edge Noise Reduction on a Controlled Diffusion Airfoil with Serrations,” *25th AIAA/CEAS Aeroacoustics Conference*, Delft, The Netherlands, 20-23 May, 2019.
- [113] Brooks, T., and Burley, C., “Blade Wake Interaction Noise for a Main Rotor,” *Journal of the American Helicopter Society*, Vol. 49, No. 1, 2004, pp. 11–27.
- [114] Amiet, R., “Acoustic Radiation from an Airfoil in a Turbulent Stream,” *Journal of Sound and Vibration*, Vol. 41, No. 4, 1975, pp. 407–420.
- [115] Paterson, R., and Amiet, R., “Acoustic Radiation and Surface Pressure Characteristics of an Airfoil due to Incident Turbulence,” *3rd Aeroacoustics Conference*, Palo Alto, CA, July 20-23, 1976.
- [116] Martinez, D., Sitaraman, J., Brewer, W., Rivera, P., and Jude, D., “Machine Learning Based Aerodynamic Models For Rotor Blades,” *Proceedings of the 2020 VFS Aerome-*

- chanics for Advanced Vertical Flight Technical Meeting*, San Jose, CA, January 21-23, 2020.
- [117] Ren, X., Sadeghirad, A., Pham, D., and Lua, J., “Machine Learning based Digital Twin Simulation and Prediction of Structural Component’s Fatigue Life,” *Proceedings of the Vertical Flight Society 75th Annual Forum & Technology Display*, Philadelphia, PA, May 13–16, 2019.
- [118] Abadi, M., Agarwal, A., Barham, P., Brevdo, E., Chen, Z., Citro, C., Corrado, G. S., Davis, A., Dean, J., Devin, M., Ghemawat, S., Goodfellow, I. J., Harp, A., Irving, G., Isard, M., Jia, Y., Józefowicz, R., Kaiser, L., Kudlur, M., Levenberg, J., Mané, D., Monga, R., Moore, S., Murray, D. G., Olah, C., Schuster, M., Shlens, J., Steiner, B., Sutskever, I., Talwar, K., Tucker, P. A., Vanhoucke, V., Vasudevan, V., Viégas, F. B., Vinyals, O., Warden, P., Wattenberg, M., Wicke, M., Yu, Y., and Zheng, X., “TensorFlow: Large-Scale Machine Learning on Heterogeneous Distributed Systems,” , 2015. Software available from tensorflow.org.
- [119] Kinsler, L., Frey, A., Coppens, A., and Sanders, J., *Fundamentals of Acoustics*, Wiley, 2000.
- [120] Glegg, S., and Devenport, W., *Aeroacoustics of Low Mach Number Flows*, Wiley, 2017.
- [121] Yang, T., Brentner, K., and Walsh, G., “A Dual Compact Model for Rotor Thickness Noise Prediction,” *Journal of the American Helicopter Society*, Vol. 63, No. 2, 2018, pp. 12–23.
- [122] Isom, M., “The Theory of Sound Radiated by a Hovering Transonic Helicopter Blade,” *Polytechnic Institute of New York Report Poly-AE/AM No. 75-4*, 1975.
- [123] Fastl, H., and Zwicker, *Psychoacoustics: Facts and Models*, Springer, 2007.
- [124] Kholodov, P., and Moreau, S., “Optimization of trailing-edge serrations with and without slits for broadband noise reduction,” *Journal of Sound Vibration*, Vol. 490, 2021, p. 115736.
- [125] Hinze, J., *Turbulence*, McGraw-Hill Book Co., 1959.
- [126] Moreau, S., and Roger, M., “Competing Broadband Noise Mechanisms in Low-Speed Axial Fans,” *AIAA Journal*, Vol. 45, No. 1, 2007, pp. 48–57.
- [127] Roger, M., and Moreau, S., “Extensions and limitations of analytical airfoil broadband noise models,” *International Journal of Aeroacoustics*, Vol. 9, No. 3, 2010, pp. 273–305.
- [128] Herr, M., Ewert, R., Rautmann, C., Kamruzzaman, M., Bekiropoulos, D., Iob, A., Arina, R., Batten, P., Chakravarthy, S. R., and Bertagnolio, F., “Broadband Trailing-Edge Noise Predictions— Overview of BANC-III Results,” *Proceedings of the 21st AIAA/CEAS Aeroacoustics Conference*, Dallas, Texas, June 22-26, 2015.
- [129] Lee, S., and Shum, J., “Prediction of Airfoil Trailing-Edge Noise Using Empirical

- Wall-Pressure Spectrum Models,” *AIAA Journal*, Vol. 57, No. 3, 2019, pp. 888–897.
- [130] Brooks, T., and Hodgson, T., “Trailing Edge Noise Prediction from Measured Surface Pressures,” *Journal of Sound and Vibration*, Vol. 78, No. 1, 1981, pp. 69–117.
- [131] Johnson, H., and Katz, W., “Investigation of the Vortex Noise Produced by a Helicopter Rotor,” Tech. rep., 1972. USAAMRDL RP 72-2.
- [132] Leverton, J., “The Noise Characteristics of a Large ”Clean” Rotor,” *Journal of Sound and Vibration*, Vol. 27, 1973, pp. 357–376.
- [133] Colonius, T., and Lele, S. K., “Computational aeroacoustics: progress on non-linear problems of sound generation,” *Progress in Aerospace Sciences*, Vol. 40, No. 6, 2004, pp. 345 – 416. doi:<https://doi.org/10.1016/j.paerosci.2004.09.001>, URL <http://www.sciencedirect.com/science/article/pii/S0376042104000570>.
- [134] Johnson, W., “Technology Drivers in the Development of CAMRAD II,” *American Helicopter Society Aeromechanics Specialist Meeting*, San Francisco, California, January 1994.
- [135] Elliott, J., and Althoff, S., “Inflow Measurement Made with a Laser Velocimeter on a Helicopter Model in Forward Flight,” Tech. rep., 1988. NASA Technical Report 100541-100545.
- [136] Brooks, T., and Hodgson, T., “Trailing Edge Noise Prediction from Measured Surface Pressures,” *Journal of Sound and Vibration*, Vol. 78, No. 1, 1987, pp. 69–117.
- [137] Roger, M., and Moreau, S., “Trailing Edge Noise Measurements and Prediction for Subsonic Loaded Fan Blades,” *Proceedings of the 8th AIAA/CEAS Aeroacoustics Conference*, Breckenridge, Colorado, June 17-19, 2002.
- [138] Corcos, G. M., “The structure of the turbulent pressure field in boundary-layer flows,” *Journal of Fluid Mechanics*, Vol. 18, No. 3, 1964, p. 353–378.
- [139] Brentner, K., Zolbayar, B., and Jaworski, T., “An Investigation of Noise from Electric, Low-tip-Speed Aircraft Propellers,” *Proceedings of the AHS International Technical Meeting on Aeromechanics Design for Transformative Vertical Flight*, San Francisco, CA, January 16-18.
- [140] International Organization for Standardization, “Acoustics - Attenuation of Sound During Propagation Outdoors,” 1996.
- [141] Holden, J., and Goel, N., “Fast-Forwarding to a Future of On-Demand Urban Air Transportation,” *White Paper, Uber*, 2016.
- [142] Vasick, P., and Hansman, J., “Development of Vertiport Capacity Envelopes and Analysis of Their Sensitivity to Topological and Operational Factors,” *Proceedings of the AIAA SciTech Forum*, San Diego, CA, January 7-11, 2019.

- [143] Li, S., and Lee, S., “UCD-QuietFly: A New Program to Predict Multi-Rotor eVTOL Broadband Noise,” *Proceedings of the 2020 VFS Aeromechanics for Advanced Vertical Flight Technical Meeting*, San Jose, CA, January 21-23, 2020.
- [144] Boucher, M., Krishnamurthy, S., Christian, A., and Rizzi, S. A., “Sound Quality Metric Indicators of Rotorcraft Noise Annoyance Using Multilevel Regression Analysis,” *The Journal of the Acoustical Society of America*, Vol. 145, No. 3, 2019, pp. 1899–1899.
- [145] Leon, C., Ragni, D., Probsting, S., Scarano, F., and Madsen, J., “Flow Topology and Acoustic Emissions of Trailing Edge Serrations at Incidence,” *Experiments in Fluids*, Vol. 57, No. 91, 2016, pp. 1–17.
- [146] Chong, T. P., and Vathylakis, A., “On the aeroacoustic and flow structures developed on a flat plate with a serrated sawtooth trailing edge,” *Journal of Sound and Vibration*, Vol. 354, 2015, pp. 65–90.
- [147] Sanjose, M., Meon, C., Moreau, S., Idier, A., and Laffay, P., “Direct Numerical Simulation of Acoustic Reduction Using Serrated Trailing-Edge on an Isolated Airfoil,” *20th AIAA/CEAS Aeroacoustics Conference*, Atlanta, GA, June 16-20, 2014.